NASA/TM-1999-206572

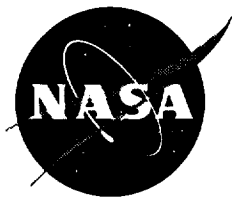

Factors Affecting Inlet-Engine Compatibility During Aircraft Departures at High Angle of Attack for an F/A-18A Aircraft

W. G. Steenken and J. G. Williams
GE Aircraft Engines
Cincinnati, Ohio

A. J. Yuhas
Analytical Services and Materials, Inc.
Edwards, California

K. R. Walsh
Dryden Flight Research Center
Edwards, California

Prepared for
NASA Dryden Flight Research Center
Edwards, California
NASA Contract NAS3-26617

National Aeronautics and
Space Administration

Dryden Flight Research Center
Edwards, California 93523-0273

February 1999

NOTICE

Use of trade names or names of manufacturers in this document does not constitute an official endorsement of such products or manufacturers, either expressed or impl ed, by the National Aeronautics and Space Administration.

Available from the following:

NASA Center for AeroSpace Information (CASI)
7121 Standard Drive
Hanover, MD 21076-1320
(301) 621-0390

National Technical Information Service (NTIS)
5285 Port Royal Road
Springfield, VA 22161-2171
(703) 487-4650

TABLE OF CONTENTS

TABLE OF CONTENTS (Concluded)

LIST OF FIGURES

LIST OF TABLES

NOMENCLATURE

AIP	Aerodynamic Interface Plane
ALF	Aft Looking Forward
ARP	Aerospace Recommended Practice
AOA	Angle of Attack
AOSS	Angle of Sideslip
CROCP	Combined Rate of Change Parameter
DP/PC	Circumferential Distortion Descriptor (See Appendix A)
DP/PR	Radial Distortion Descriptor (See Appendix A)
DPRS	Loss of Stability Pressure Ratio
DPRSF	Loss of Fan Stability Pressure Ratio
DPRSH	Loss of Compressor Stability Pressure Ratio
EFH	Engine Flight Hours
EOT	Engine Operating Time in hours
ESN	Engine Serial Number
GE	GE Aircraft Engines, Evendale, Ohio
HARV	High Alpha Research Vehicle
HAP	HARV Analysis Program
IRP	Intermediate Rated Power
INS	Inertial Navigation System
LEX	Leading Edge Extension
M	Mach number
PCM	Pulse Code Modulation
PLA	Power Lever Angle
PSI	Pressure Systems, Inc., Hampton, Virginia
QCP	Quality Check Program
RMS	Root Mean Square
deg	Degree
g	Gravitational acceleration
kft	Thousands of feet
lbf	Pounds force
lbm	Pounds mass
psi	Pounds per square inch
sec	Seconds
sps	Samples per Second

ABSTRACT

The F404-GE-400 engine powered F/A-18A High Alpha Research Vehicle (HARV) was used to examine the quality of inlet airflow during departed flight maneuvers, that is, during flight outside the normal maneuvering envelope where control surfaces have little or no effectiveness. A series of six nose-left and six nose-right departures were initiated at Mach numbers between 0.3 and 0.4 at an altitude of 35 kft. The yaw rates at departure recovery were in the range of 40 to 90 degrees per second. Engine surges were encountered during three of the nose-left and one of the nose-right departures. Time-variant inlet-total-pressure distortion levels at the engine face were determined to not significantly exceed those measured at maximum angle-of-attack and -sideslip maneuvers during controlled flight. Surges as a result of inlet distortion levels were anticipated to initiate in the fan. Analysis revealed that the surges initiated in the compressor and were the result of a combination of high levels of inlet distortion and rapid changes in aircraft motion. These rapid changes in aircraft motion are indicative of a combination of engine mount and gyroscopic loads being applied to the engine structure that impact the aerodynamic stability of the compressor through changes in the rotor-to-case clearances.

1.0 INTRODUCTION

Departed flight occurs when an aircraft is flown beyond regimes where the control surfaces no longer have the desired effectiveness or cannot accomplish the intended function In these situations, the pilot loses the ability to control the flight path of the aircraft and the aircraft enters a series of self-induced motions that represent a departure from normal trajectories. Hence, this type of flight is known as departed flight.

In general, this type of flight is only encountered by military pilots who are pushing their aircraft to extreme angles of attack and sideslip. However, inlet-compatibility engineers long have been interested in knowing the manner in which the aircraft inlet flow behaves during departures and if engine surges should occur, knowing the contributors to the cause of the surge.

The NASA High Alpha Research Vehicle (HARV) F/A18-A aircraft flown at NASA Dryden Flight Research Center provided an almost ideal test vehicle for such studies since it was configured, in part, for propulsion research. That is, the complement of Aerodynamic Interface Plane (AIP) instrumentation, aircraft attitude instrumentation, and engine instrumentation could readily provide the data needed to accomplish appropriate studies. Thus, departed flight investigations could be conducted as an extension of already planned HARV propulsion system research (References 1 and 2).

A series of twelve departures were achieved between M = 0.3 and 0.4 at 35 kft by pulling angle of attack to approximately 60 degrees and inducing the departure by left and right yaws with rates of 40 - 90 degrees per second. Engine stalls were obtained during four of the twelve departures. The data obtained during these departures provided the capability to characterize the performance of the inlet in terms of inlet recovery and dynamic distortion characteristics as well as the ability to obtain insight into the causes of the engine stalls.

It is important to note that this is the first known time in the industry that valid high-response inlet data have been obtained during departed flight maneuvers.

The following sections of this report provide a description of the HARV aircraft, the instrumentation, the departure test techniques and the types of analyses conducted, a discussion of the results, and conclusions. The types of analyses conducted during this investigation will be illustrated for one departure in an effort to maintain a degree of conciseness to this report. However, similar sets of plots are presented in the appendix for all other departures.

2.0 TEST HARDWARE, DATA ACQUISITION, AND DATA REDUCTION SYSTEM DESCRIPTIONS

The HARV aircraft, specifically configured to accomplish high angle-of-attack research, was highly instrumented and possessed state-of-the-art data acquisition and data reduction systems as described below.

2.1 HARV Aircraft Description

The HARV is a single-seat F/A-18A aircraft (pre-production aircraft Number 6) powered by two afterburning turbofan F404-GE-400 engines. The high angle-of-attack capability is obtained by thrust vectoring, in this case, by removing the divergent nozzle flaps from the convergent-divergent exhaust nozzle and deflecting the nozzle exit flow by inserting three externally mounted paddles into each exhaust stream in a controlled and coordinated manner to produce the desired thrust vectoring (Reference 3). This thrust-vectoring capability allowed a wide range of stabilized angles of attack and sideslip to be achieved at the desired Mach numbers in the range of 0.3 to 0.4. The wide range of conditions, in terms of inlet distortion to which the inlet was subjected, provided part of the database necessary for conducting the desired departed flight maneuvers study.

The F/A-18A aircraft inlets are two-dimensional, external compression inlets with 5-degree compression ramps mounted on the sides of the aircraft fuselage under the aft portion of the LEX (Leading Edge Extension of the wing) approximately 25 feet aft of the aircraft nose. Additional details of the inlet are described in Reference 4. The propulsion research was conducted on the right-hand inlet aft looking forward (ALF).

The HARV aircraft and F/A-18A inlet system are shown in Figure 1.

2.2 F404-GE-400 Engine Description and Instrumentation

The F404-GE-400 engine is a low-bypass, twin-spool, axial-flow turbofan engine with an afterburner. The 3-stage fan (low-pressure compressor) and 7-stage high-pressure compressor are each independently driven by a single-stage turbine. In the fan, the inlet guide vanes and the stators of the first stage are variable. In the high-pressure compressor, the inlet guide vanes and the first two stator stages are variable. These variable inlet guide vanes direct the inlet air at an optimum angle for efficient and stable engine operation. The through-flow annular combustor uses atomizing fuel nozzles. The mixed-flow augmentor burns air from both the bypass and the high-pressure core in the afterburner section. The engine control is an integrated system, using both hydromechanical and electronic control components. The sea level static IRP thrust of each engine is approximately 10,700 lbf, and the maximum afterburner thrust is approximately 16,000 lbf. The maximum corrected airflow through the engine is approximately 145 lbm per sec.

Engine Serial Number (ESN) 310-083 was installed on the left-hand side of the aircraft and ESN 310-051 was installed on the right-hand side of the aircraft. Both engines were equipped with an original engine control which placed the IRP flat at 87 degrees PLA.

ESN 310-051 had the standard complement of engine readout parameters as shown in Part A of Table 1. Additionally, flight test instrumentation was installed to provide additional readouts of bill-of-material parameters or additional parameters that were of interest to propulsion research. These parameters are listed in Part B of Table 1. Also of importance to this effort were the fan discharge wall-static-pressure taps located downstream of the outlet guide vanes in the Plane 2.1 borescope holes. These high-response pressures were used to determine in which compression component (fan or compressor) the surges initiated.

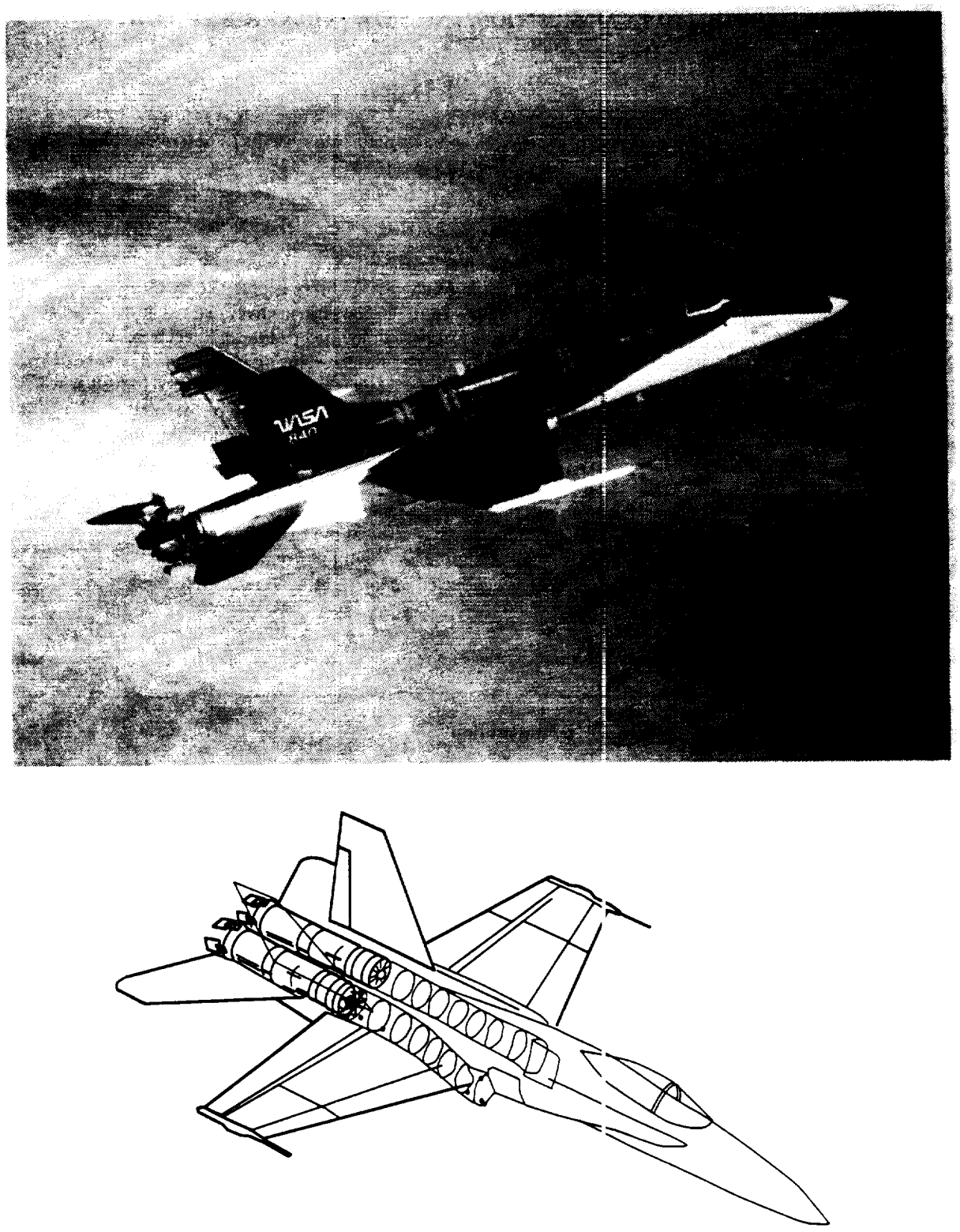

Figure 1. High Alpha Research Vehicle (HARV) and F/A-18 Inlet System.

Table 1. ESN 310-051 (Right-Hand-Side) ground and flight test instrumentation.

Part A - Bill of Material		Part B - Flight Test Instrumentation	
Instrumentation Designation	Instrumentation Description	Instrumentation Designation	Instrumentation Description
PLA*	Power Lever Angle	N1	Physical Fan Speed
TT1*	Engine Inlet Total Temperature	N2	Physical Compressor Speed
N1*	Physical Fan Speed	FGV	Fan Variable Geometry Position
N2*	Physical Compressor Speed	HPVG	Compressor Variable Geometry Position
FIGV	Fan Inlet Guide Vane Position	WFE	Engine Fuel Flow
CIGV	Compressor Inlet Guide Vane Position	WFET	Engine Fuel Temperature
CDP*	Compressor Discharge Pressure	WFABM	Afterburner Main Fuel Flow
WF*	Engine Fuel Flow	WFABMT	Afterburner Main Fuel Temperature
PT56*	Turbine Exhaust Pressure	WFABP	Afterburner Pilot Fuel Flow
EGT*	Exhaust Gas Temperature	PSFUELI	Control Inlet Fuel Pressure
A8*	VEN Position	PSFUELO	Control Outlet Fuel Pressure
		PS211, PS212	Fan Discharge Wall Static Pressures
		PSB1, PSB2	Combustor Wall Static Pressures
		PT56 (20)	Low Pressure Turbine Discharge Total Pressures
		PS6REF	Afterburner Inlet Reference Pressures
		PS6 (3)	Afterburner Inlet Wall Static Pressures
		PS7 (4)	Exhaust Nozzle Wall Static Pressures

*Parameters Also Used in Flight Test

The health of the engine was checked several times during the propu sion research portion of the flight program. The fan corrected speed - compressor corrected speed rela ionship, fan inlet guide vane as a function of corrected fan speed, compressor inlet guide vane positio as a function of compressor corrected speed, exhaust nozzle area as a function of fan corrected speed, and exhaust gas temperature as a function of compressor corrected speed were compared with calibration value s acquired during a ground run (Reference 5). No significant changes were noted. The fact that no significant change occurred probably is because the engine was already significantly deteriorated prior to the start of the propulsion research program. At the time of the departed flight maneuvers, the right engine had approximately 1529 EOT and 1217 EFH while the left engine had approximately 1204 EOT and 936 EFH.

2.3 Aircraft Instrumentation

The aircraft instrumentation, which was used to provide the data from which the departed flight results were obtained, is going to be treated as three separate categories. These are inlet airflow and distortion instrumentation, aircraft aerodynamic position instrumentation, and aircraft attitude position instrumentation. The following paragraphs address each of these types of instrumentation.

2.3.1 Inlet Airflow and Distortion Instrumentation

The inlet airflow and distortion instrumentation was comprised of forty high-response and forty time-averaged (also known as steady-state) total pressures and eight high-response and eight time-averaged wall-static pressures all located at the Aerodynamic Interface Plane (AIP). Figure 2 provides a schematic layout of the AIP total-pressure instrumentation. The AIP was located approximately 4.0 inches forward of the engine bullet nose. This inlet distortion rake, which is described in Reference 6, provides both high-response and low-response (quasi-steady) total-pressure measurements at forty probes located on the centroids of equal areas for a five-ring, eight-rake array. It should be noted that the probe sensing configuration was designed to be very insensitive to flow angularity, an important criterion when measuring total pressure in distorted flows. Per Reference 6, this configuration allows the sensors to read true pressure levels at yaw angles over the range ±25 degrees and pitch angles from +15 to -25 degrees with positive angles being in the direction of the engine centerline. The flow blockage of the distortion rake structure at the AIP is 0.4 percent. The maximum blockage of the rake, which is less than eight percent, is located 1.5 inches downstream of the AIP.

2.3.2 Aircraft Aerodynamic Position Instrumentation

The aircraft aerodynamic position is specified by two parameters - aircraft angle of attack and aircraft angle of sideslip. The typical noseboom-mounted air data system was not installed during the HARV flight program because at high angle of attack, the noseboom had a significant effect on the forebody aerodynamics and thus, on the stability and control of the aircraft. Instead, specially designed, self-aligning air data probes (also called swivel probes) and NACA angle-of-attack and angle-of-sideslip vanes were mounted on each wing tip (Reference 7). Each swivel probe consisted of a combined pitot-static tube with four fins attached to the end of the probe to aerodynamically align it to the local flow. Hence, because these probes aligned themselves with the local flow, total pressure losses as a result of local angle-of-attack and -sideslip effects were effectively eliminated. The probes swiveled freely for local angles of attack between -15 degrees and +72 degrees and for local angles of sideslip between ±40 degrees. However, the swivel probe static-pressure measurements still were affected by the presence of the aircraft.

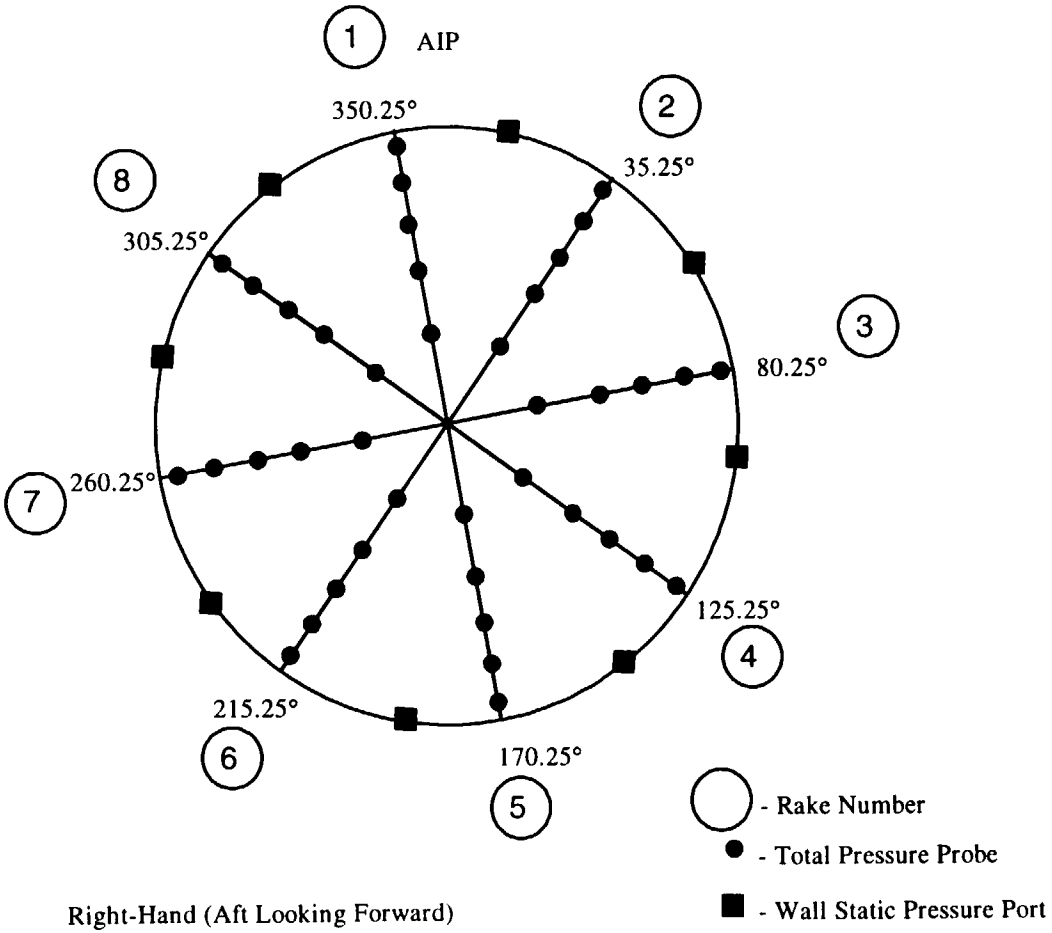

ANGULAR LOCATIONS OF WALL-STATIC PRESSURES		
BETWEEN RAKES	HIGH-RESPONSE	STEADY-STATE
1-2	12.25°	9.25°
2-3	58.75°	55.75°
3-4	97.50°	94.50°
4-5	144.0°	141.0°
5-6	189.0°	186.0°
6-7	234.0°	231.0°
7-8	283.0°	280.0°
8-1	323.0°	320.0°

Figure 2. AIP Pressure Sensing Locations.

Calibrations of the NACA angle-of-attack and angle-of-sideslip vanes provided accurate measurements from low to high angle of attack during steady aerodynamic conditions. This calibration accounted for aerodynamic effects such as local upwash and sidewash. The various flight test techniques that were used to establish the angle-of-attack and angle-of-sideslip calibrations are described in Reference 7. For the HARV inlet program, angle of attack was obtained from the left wing-tip vane, while angle of sideslip was obtained by averaging the left and right vanes. A total-temperature probe was mounted on the right wing tip without a pitot-static probe. Hence, the right angle-of-attack vane could not have Mach number corrections applied whereas the angle-of-sideslip vanes did not require Mach number corrections.

At high angles of attack, the wing-tip mounted flow angle vanes were subject to the effects of wing bending and torsional frequencies. The bending frequency mode of the wings was between 6 and 8 Hz, whereas the torsional mode frequency was 12 Hz. These frequencies influenced the measurement signal of the vanes. To compensate for these frequencies, a combination 12 Hz low-pass and 6-8 Hz notch filter was used to remove the frequency content from the angle-of-attack and angle-of-sideslip signals. To compensate for the time lag associated with the notch filter, a time skew of -0.14 seconds was applied to the filtered angle-of-attack and angle-of-sideslip signals.

2.3.3 Trajectory Reconstruction of Aircraft Attitude During Departures

The measurements of the angle-of-attack and angle-of-sideslip vanes together with their associated calibrations are accurate only during steady aerodynamic conditions. During rapid dynamic maneuvers such as aircraft departures, measurement hysteresis associated with angle-of-attack and angle-of-sideslip data results in unreliable and inaccurate measurements. An alternate approach described as "trajectory reconstruction" is employed. This approach uses data from the inertial navigation system (INS) to determine the aircraft orientation and to calculate angle-of-attack and angle-of-sideslip values.

To reconstruct the trajectory of an aircraft, the relationship between aerodynamic positions, aircraft body positions, and atmospheric winds must be defined. The angle of attack and angle of sideslip of an aircraft are defined using the aircraft body axes and the velocity vector. The velocity vector is the combination of the inertial velocity and the wind velocity. Therefore, angle of attack and angle of sideslip can be described as a function of pitch (angle between the longitudinal body axis and the horizon), roll (angle between the lateral body axis and the horizon), yaw (angle of movement about the vertical axis), the inertial velocity vector, and the wind velocity vector.

During steady aerodynamic conditions just before departure, the trajectory reconstruction methodology uses the wing-tip angle-of-attack and angle-of-sideslip measurements and the INS information to obtain a baseline average wind calculation. This average wind is then directly applied to the aircraft attitudes and INS velocity during a departure to calculate angle of attack and angle of sideslip for the departure.

2.4 Flight Test Data Acquisition System

All data during the test program were acquired using three PCM systems. The aircraft and engine data acquired using PCM1 and PCM2 were telemetered to a ground station for recording on magnetic tape in a digital format while the high-response data acquired using PCM3 were recorded on-board the aircraft on magnetic tape in a digital format. All PCM systems recorded an embedded time code which was taken from an on-board time code generator and was used in merging the three data streams during the data reduction sequence. The sample rates varied from 10 sps for a reference pressure to 2143 sps for the AIP high-response total pressures used for distortion calculations.

2.5 Flight Test Data Reduction

Each PCM data stream in raw counts was stored on NASA Dryden Flight Research Center computers. The embedded time code in each data stream was used to time tag each data sample. This allowed data from all three PCM systems to be merged into a single data set using the common time source. The raw count data were converted into engineering units using appropriate calibration curves. Then, a merged computer file was created for each flight test condition containing the parameters required for data analysis. This computer file was reduced further by applying the appropriate in-flight calibrations to the pressure transducers as explained below. The final reduced computer file was available to all members of the NASA/GE Aircraft Engines Propulsion Research Team.

2.5.1 Calibration

Although significant effort had been expended to assure that the AIP high-response transducers had minimum zero-shift and thermal-sensitivity characteristics, analysis of the in-flight AIP distortion rake data revealed significant differences between the mean pressure values obtained from the low-response pressure transducers and the high-response (Kulite) absolute-pressure transducers, even after accounting for the Kulite transducer temperature sensitivity. This possibility had been anticipated and procedures had been incorporated in the data reduction programs to handle this effect. These adjustments were termed "biases." There were two sets of biases. One set was for the low-response pressure transducers and was derived by applying equal pressure to both sides of the transducer. The second set was for the high-response pressure transducers and was determined from the difference between the means of the Kulite pressure transducer outputs and the means of the low-response transducers.

Typical magnitudes of the low-response transducers biases were very small, typically less than ± 0.02 psi. However, the Kulite biases could be as large as ±0.3 psi. To identify the bias levels to be applied to a given set of data, a short "calibration point" was acquired during straight and level flight prior to the start of a series of maneuver test conditions. During a given flight, five or more such calibration points were acquired. Each of these was associated with a single test or series of test conditions.

The distribution of the Kulite bias values was always similar, although the magnitudes could change. The reason for this has not been completely explained. Also, there were indications that the Kulite transducers tended to drift with time in flight (there was no evidence of such tendencies during hanger or ground checks). The longer in time that a test point was from a calibration point, the larger the difference in the mean signal level, and therefore, a greater question as to its accuracy. In-flight, the absolute value of the temperature used for Kulite compensation was not a big driver at the test conditions of interest - variations of ± 20 °F did not make a big difference (less than 0.05 psi) to the bias levels for a typical flight temperature condition.

The absence of a bias correction to the Kulite signals would result in significant differences in the indicated pressure values and consequently, the resulting engine-face pressure contours and distortion levels. Also, inlet pressure recovery was in error, but to a lesser extent.

A comparison of the engine face isobaric contours based on the time-averaged pressure values measured by the low-response system and those measured by the time high-response system, corrected only for temperature compensation effects, showed that there were a few similarities in the two patterns. The inclusion of the bias levels in the data reduction procedures forced the time-averaged Kulite pattern to mimic the low-response pressure-transducer pattern at the flight calibration condition.

2.5.2 Data Reduction and Analysis

Digital data files containing the aircraft, inlet, and engine measured parameters were produced by NASA Dryden Flight Research Center. The in-flight calibration bias had been applied to these data. The sampling rate was 2143 sps.

The initial step in the process of data reduction was to validate the data. This function was provided by the Quality Check Program (QCP). This program compared the raw data values to user-established limits and to relative change from the previous time-step values. Data substitution techniques were established for handling invalid or missing data.

The output from the QCP was fed into the HARV Analysis Program (HAP). This program filtered the data to the critical response time of the engine, and evaluated the AIP total-pressure time variant distortion descriptors in terms of GE Aircraft Engines and ARP 1420 (Reference 8) parameters, and isobaric-contour patterns. Also, the HAP provided mean and RMS levels for the inlet measurements, inlet airflow, and recovery values.

3.0 APPROACH

The flight-departure testing was conducted during a series of three flights (238-240) at the NASA Dryden Flight Research Center on June 6, 1994. The test responsibilities were shared by two pilots. Pre-flight rehearsals, using the NASA F-18 HARV flight simulator, were conducted to establish the pilot techniques for achieving the target levels of aircraft motion during departed flight. This allowed the pilots and the ground-station team to explore the most cost-effective and low-risk scenarios to meet the test objectives by recognizing the departure modes of the vehicle and practicing the necessary recovery actions. In the following paragraphs, the test techniques and the matrix of test data that were obtained are discussed.

3.1 Test Conditions and Test Technique

A total of twelve high-power departed-flight maneuvers were performed. These were flown at Mach numbers between 0.3 and 0.4 at an entry condition of 35 kft. The high yaw-rate departures were divided evenly between nose-left and nose-right maneuvers with increasing rates of change in yaw at departure recovery. The throttles for both engines were set at IRP at the start of the maneuvers and were reduced to idle power during the aircraft recovery phase.

The flight departure maneuvers were initiated by starting from a one "g" flight condition and pulling angle of attack to between 50 and 60 degrees and then inducing an either left or right entry into departure by moving the "stick" to the left or right at a rate and to a position that produced the desired yaw rate. After the rate was achieved, recovery of the aircraft from the departed flight condition was initiated by the pilot releasing the stick and allowing it naturally to come to the neutral position and at the same time moving the engine throttles to the idle power position.

During the departures, the aircraft would go into a nose down spin which sometimes included rapid rolls. These maneuvers were quite violent as characterized by the parameters shown in Table 2. The range information covers the extremes seen during all twelve maneuvers, not just the extremes of an individual flight.

Table 2. Ranges of parameters during departed flight maneuvers.

Parameter	Range
Heading Angle	265 to -970° and 315 to +935°
Pitch Angle	-92 to +48°
Roll Angle	-180 to +180°
Yaw Rate	-91 to +92 deg per sec
Pitch Rate	-49 to +47 deg per sec
Roll Rate	-91 to +52 deg per sec
Angle of Attack	34 to +100°
Angle of Sideslip	-36 to + 42°
Angle of Attack Rate	-35 to + 75 deg per sec
Angle of Sideslip Rate	-72 to + 62 deg per sec

It should be noted that the heading angle changes indicate more than three counter-clockwise (looking down on the aircraft) turns and almost two clockwise turns, respectively.

Interpretation of the propulsion and aircraft data obtained during the complex trajectory of the aircraft during a departed-flight maneuver was aided by the composite videos that were made from the ground-based-radar and visual-range cameras.

3.2 Test Matrix

The twelve departures that were obtained during the flight test program are described in Table 3. Engine stalls occurred during four of the departed flight conditions as noted Most of the stalls occurred on the right-hand engine. As previously noted, it was this inlet and engine that were heavily instrumented for propulsion research and allowed investigating the possible causes of the stalls.

Table 3. Departed maneuvers and engine stalls.

Flight/Test Point	Aircraft Direction	Recovery Yaw Rate (deg/sec)	Engine Response
239/34b	Nose Left	-41	Stalls (2) on Right Engine
238/35b	Nose Left	-52	Stall Free
238/36b	Nose Left	-64	Stall Free
239/37b	Nose Left	-67	Stall (1) on Right Engine
238/38b	Nose Left	-87	Stall Free
239/39b	Nose Left	-91	Stalls (9) on Right Engine and Stall (1) on Left Engine
238/40b	Nose Right	+45	Stall Free
240/41b	Nose Right	+57	Stall Free
238/42b	Nose Right	+64	Stall Free
240/43b	Nose Right	+71	Stall Free
238/44b	Nose Right	+81	Stall Free
240/45b	Nose Right	+91	Stalls (2) on Right Engine

4.0 ANALYSES AND DISCUSSION OF RESULTS

The twelve flight departures resulted in a significant amount of data. To present the data and results in the most effective manner, it was decided to choose one flight departure as an example. In the following paragraphs, data from a typical departed flight maneuver (Flight 240/Test Point 45b) are used for illustration of the data that were used for analysis, the types of analyses performed, and discussion of results. This right yaw-rate departure was performed to a maximum yaw rate of +91 degrees per second and two separate right-hand-engine stalls occurred. Where appropriate, summarized data from all departures are presented to support conclusions. Data for all the departed flight maneuvers previously itemized in Table 3, similar to the data shown for Flight 240/Test Point 45b in this section, are contained in Appendix B. It should be noted that the parameters which were acquired on PCM3 for Flight 239/Test Point 34b are time truncated due to a malfunction of the on-board recording system. Those data acquired by PCM1 and PCM2 were telemetered to the ground and were available for the full duration of the departure.

4.1 Aircraft Motion

Aircraft attitude and motion data were obtained from the INS and on-board rate-gyro measurements. Aircraft-attitude measurements describing pitch, roll, and heading are shown in Figure 3. The pitch angle describes the deviation of the longitudinal axis of the aircraft from the horizontal (approximately +50° to -80° range); the roll angle describes the deviation of the aircraft from the vertical position about the longitudinal axis (approximately +80° to -80° range); and the heading angle describes the orientation of the nose of the aircraft in the horizontal plane with north being zero degrees. The heading data indicate that the aircraft sustained about one and one-half rotations in the horizontal plane during the departure.

Aircraft-motion measurements describing rate-of-change of pitch, roll, and heading are shown in Figure 4. The derivative of the pitch, roll, and heading angles with respect to time provide the pitch rate (approximately -30 to +45 deg/sec range), the roll rate (approximately 0 to 70 deg/sec), and the yaw rate (approximately 0 to 90 deg/sec). Due to coupling between the axes, the derivatives of the pitch, roll, and heading angles with respect to time do not translate directly into pitch, roll, and yaw rates.

4.2 Aerodynamic Freestream Descriptors

The aircraft aerodynamic freestream descriptors, angle of attack (AOA) and sideslip (AOSS) and the associated rates of change, were obtained from a NASA trajectory reconstruction analysis procedure. Figure 5 shows inlet angle of attack ranging from approximately +20 to +90 degrees and angle of sideslip ranging from approximately +15 to -30 degrees. Figure 6 shows the rates of change of AOA and AOSS, respectively. Both parameters show an approximate -30 to +60 deg per sec range. Note that the rapid changes such as in the 9.5 to 10.5 second range are the result of the data processing techniques employed.

4.3 Engine Entry Flow Quality

Engine entry airflow quality was characterized by inlet performance and spatial total-pressure distortion descriptors as derived from the inlet-distortion-rake total-pressure measurements. These descriptors are

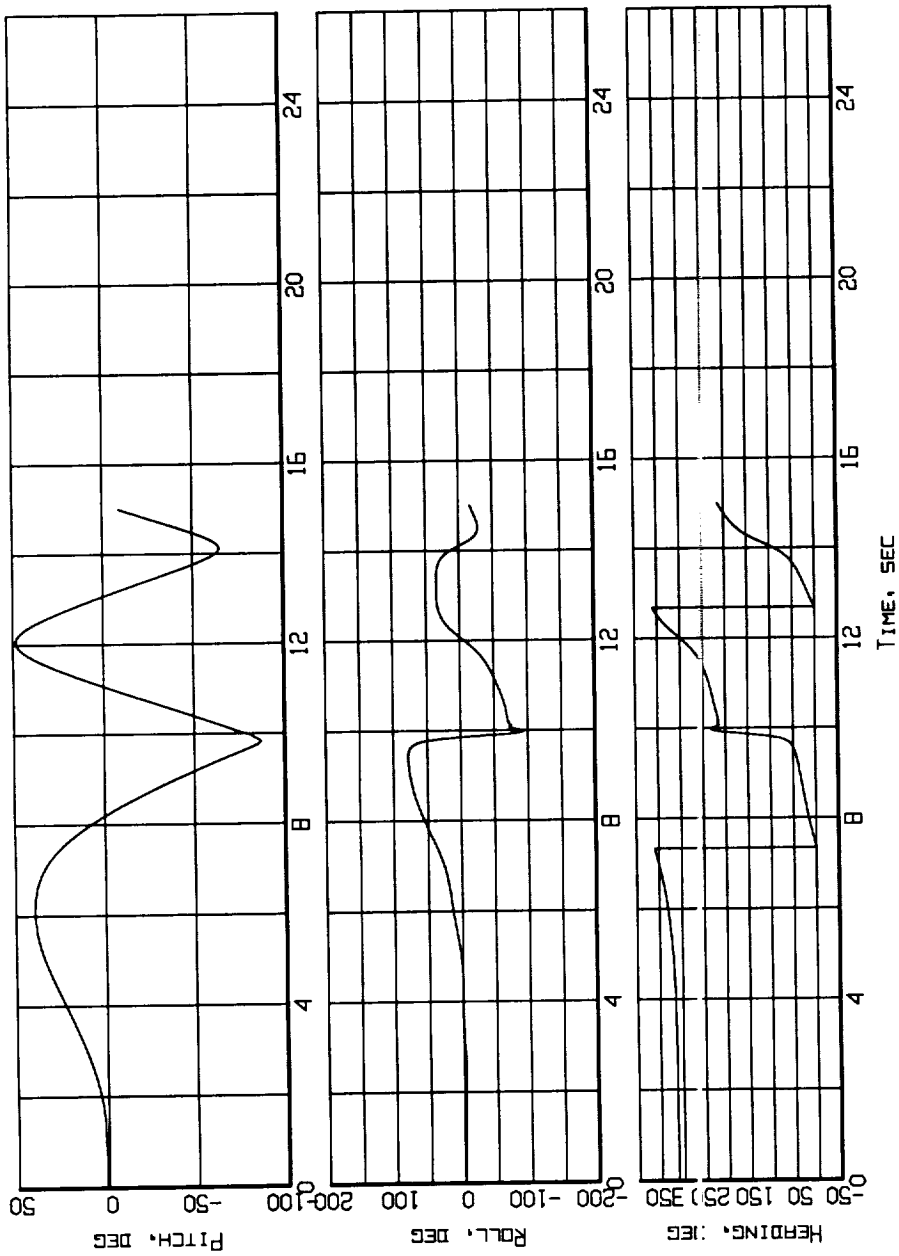

Figure 3. Aircraft attitude - Pitch, Roll, and Heading
(Flight 240, Test Point 45b).

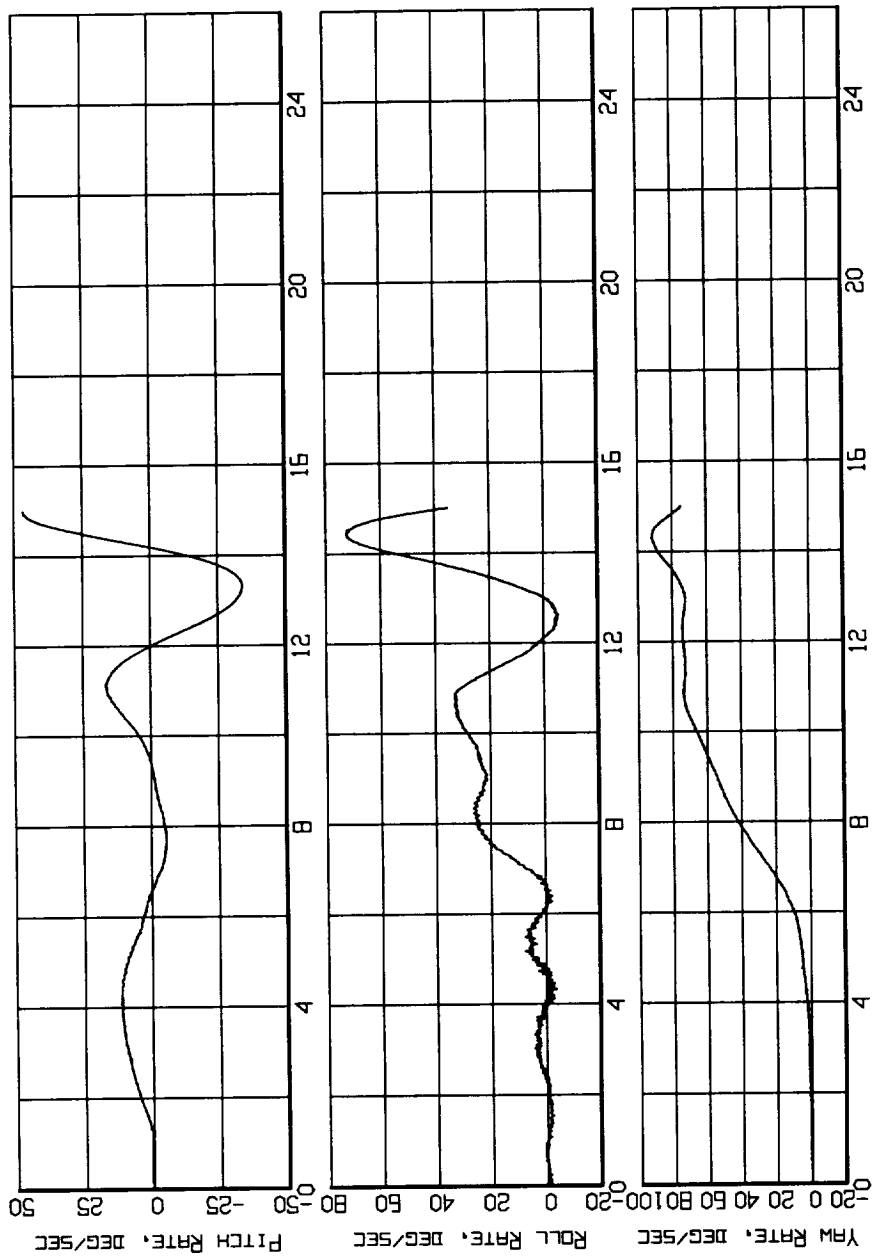

Figure 4. Aircraft Motion - Rate-of-Change of Pitch, Roll and Heading (Flight 240, Test Point 45b).

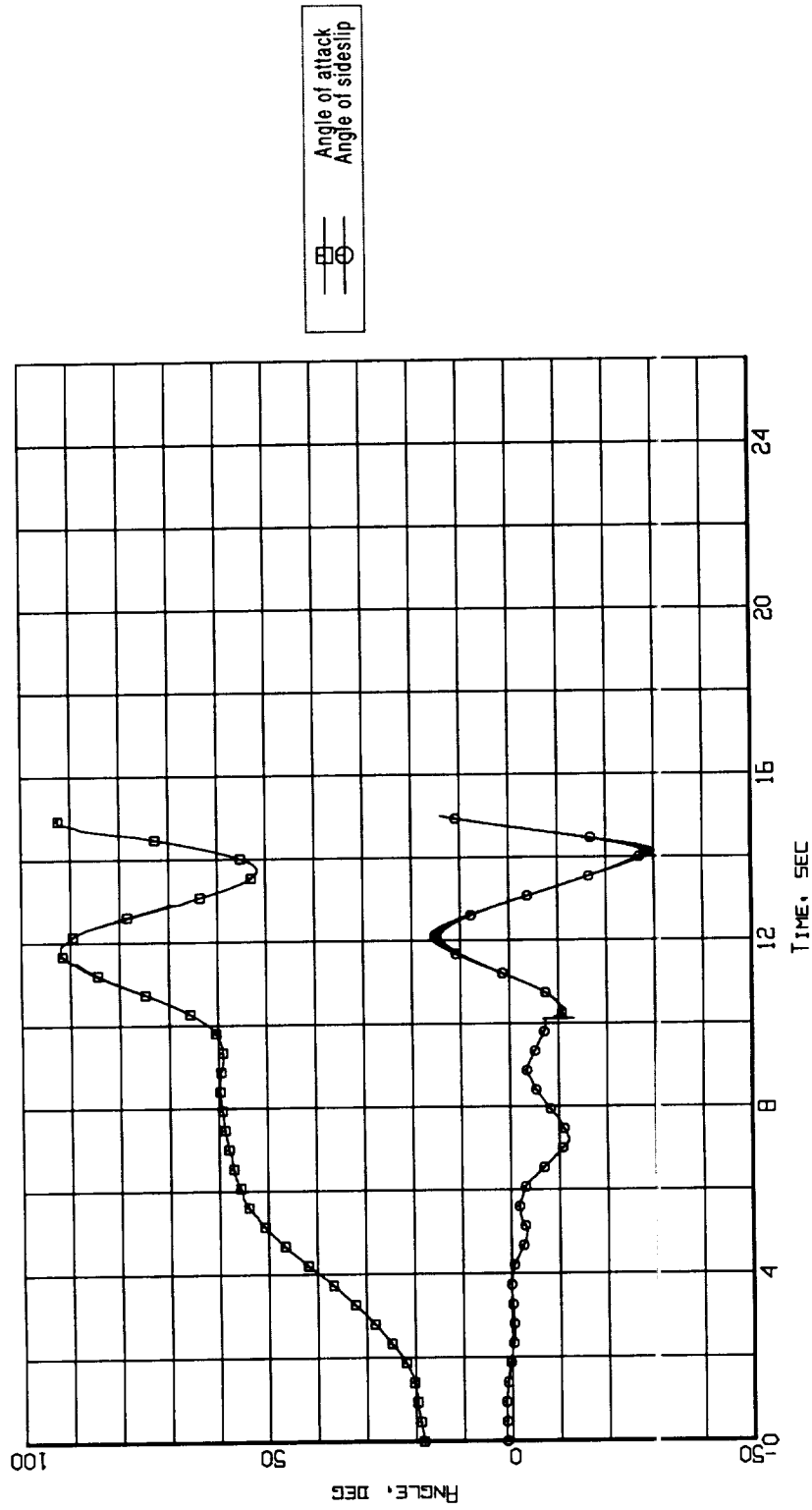

Figure 5. Aerodynamic flowstream descriptors - angle of attack and angle of sideslip (Flight 240, Test Point 45b).

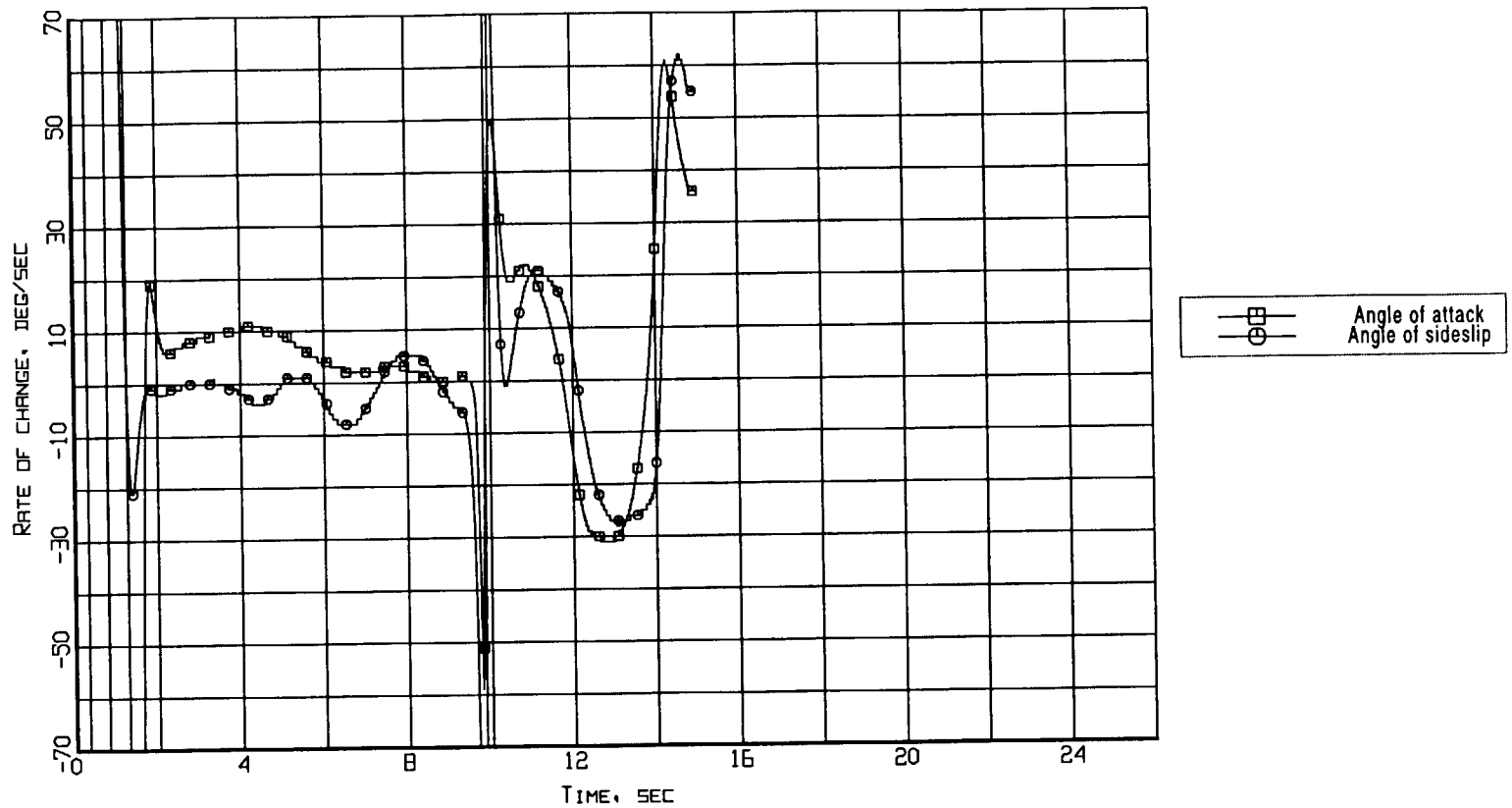

Figure 6. Aerodynamic flowstream descriptors - rate of change of angle of attack and angle of sideslip (Flight 240, Test Point 45b).

listed for reference and the definitions of the distortion descriptors are contained in Appendix A.

- Inlet Total-Pressure Recovery
- Circumferential Distortion Descriptor - DP/PC
- Radial Distortion Descriptors - DP/PR hub, DP/PR tip, and DP/PR max

Inlet pressure recovery is the time-averaged value of the AIP total-pressure measurements. The level of recovery affects the installed thrust of the engine. However, the rate of change of the spatial average of the total-pressure measurements can affect engine stability as can occur when inlet planar wave phenomena are present, for example, subsonic inlet purr or supersonic inlet buzz that depress the compression component stability limit line and can interact with operation of the engine/control. In the cases examined during the HARV flight test program, there were no instances where the engine behavior was affected by the presence of inlet planar waves.

The presence of time-varying spatial inlet total-pressure distortion at the engine face affects the stability limits of both the fan and the compressor of the engine. Both the magnitude and the combination of circumferential and radial total-pressure distortion levels are factors to be considered when assessing the potential implications of distortion on stable engine operation. The procedure to do this is commonly termed a distortion methodology. A distortion methodology is used to quantify the predicted changes in stability limit lines of the compression components resulting from the effects of inlet total-pressure distortion. The parameter used to quantify this change is the loss of stability pressure ratio (DPRS). The larger the level of DPRS, the greater the potential for engine stall. The inlet total-pressure data acquisition and processing techniques used during the HARV program were consistent with the procedures and distortion methodology specified by GE Aircraft Engines for the F404-GE-400 engine system.

Figure 7 shows the variations of the recovery and distortion parameters with time during the maneuver with the two stalls clearly evident at approximately 10.8 and 14.6 sec, respectively. The inlet recovery dropped from a value close to unity at the beginning of the event to nearly 0.3 at the time the first stall occurred. The effects of changes in inlet turbulence that are occurring are evident in the variation about the "mean" levels of the pressure recovery and distortion traces. The higher the turbulent content, the greater the variation from the "mean." Also, the increased losses described by the reduction in inlet recovery result in larger levels and more dynamic variations in the distortion descriptors. The maximum value of circumferential distortion rises to values of approximately 0.2 a number of times during the departed flight maneuver while the maximum radial distortion (tip) reaches values of approximately 0.1.

An examination of the peak time-variant circumferential and radial total-pressure distortion levels that occurred during all the departed flight maneuvers revealed:

- Peak circumferential distortion levels were ≤ 0.22 to 0.25. In eleven of the twelve cases, the maxima were greater than 0.2.
- The peak tip-radial-distortion levels were ≤ 0.12.
- For both the peak circumferential and tip-radial distortion levels, the departure recovery rate, direction, or length of data record were not a factors in the resulting maximum magnitude of the distortion levels.
- The peak hub-radial distortion levels were approximately ≤ 0.10.
- The occurrence of the stall events does not correlate with the magnitude of the distortion or the DPRS levels alone. Others factors appear to be involved.

Figure 8 shows a compilation of the peak time-variant circumferential and radial total-pressure distortion levels experienced during departed flight relative to the limits typically used as guidance in the design of F404-GE-400 engine-powered installations. The circumferential and tip-radial distortion levels significantly exceed those F404-GE-400 limits.

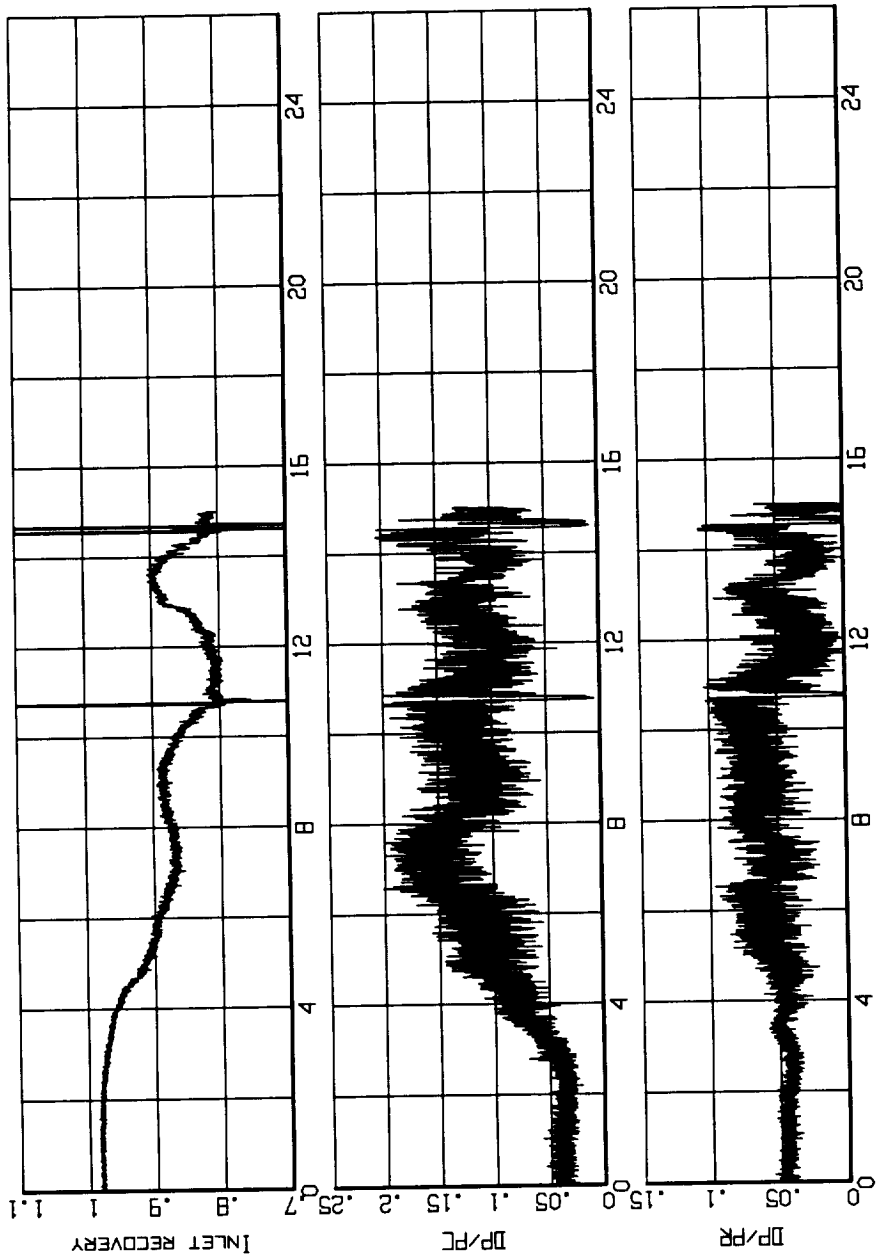

Figure 7. Time histories of inlet recovery and distortion descriptors (Flight 240, Test Point 45b).

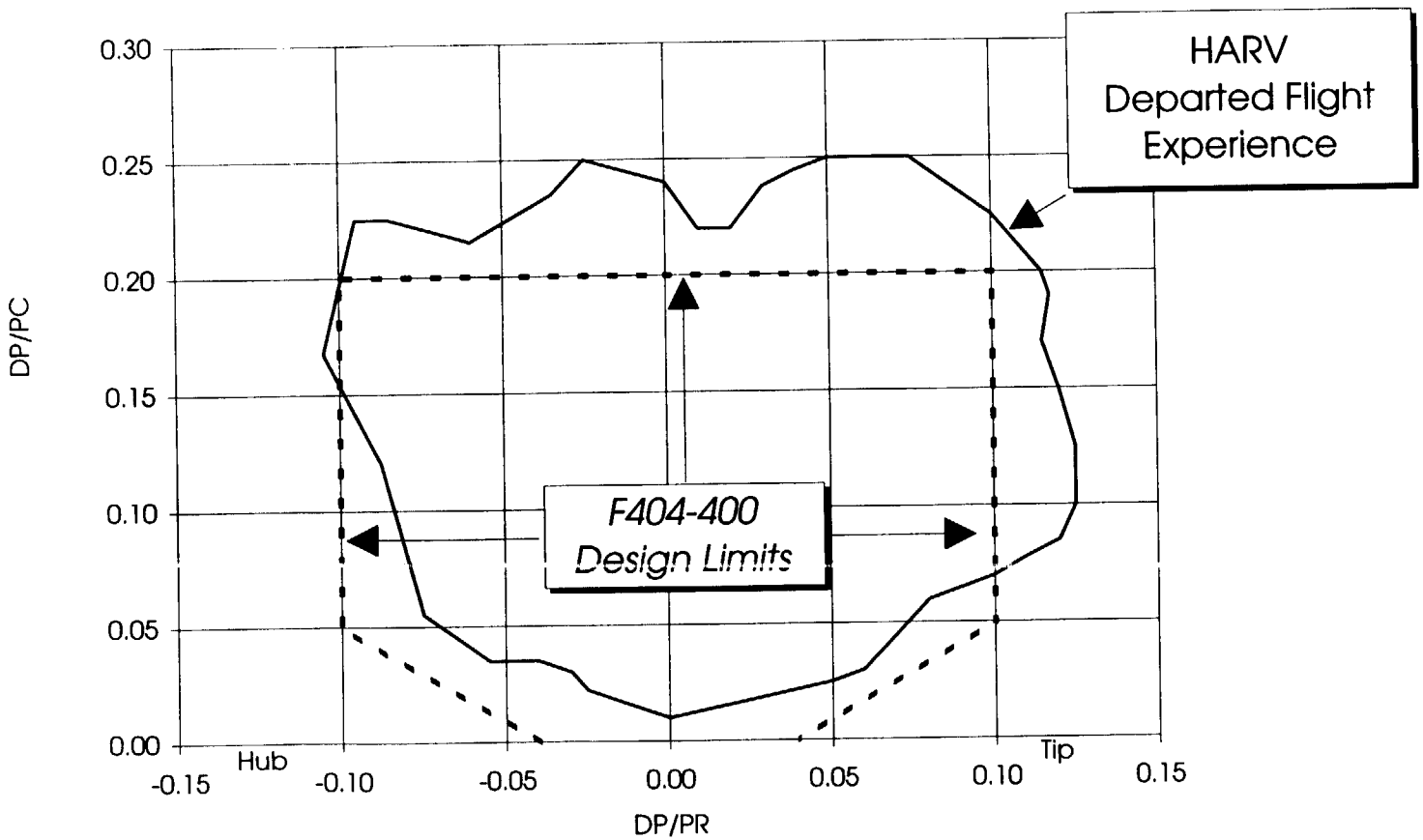

Figure 8. Bounds of time-variant circumferential and radial total-pressure distortion levels experienced during departed flight relative to the F404-GE-400 engine design guidance limits.

4.4 Engine Behavior During Maneuvers

The engine behavior during the maneuvers was described by the inlet and engine measurements. Based on examination of the inlet sensor measurements, there was no temperature ingestion (from the engine exhaust) prior to any of the stall events. However, during the maneuvers, there were small perturbations in the engine operating condition (not induced by the pilot) that could have had a destabilizing influence. These appeared to be associated with changes in the engine control and scheduling caused by the changing conditions at the inlet.

The stall-initiating engine compression component was identified by analysis of high-response inlet and engine pressure measurements. There were two compressor discharge pressures, two fan discharge wall-static pressures, and eight inlet duct/engine entry wall-static pressures. An example of the measured time-history pressure records is shown in Figure 9. A detailed examination of the relative phasing and the direction of the pressure perturbations during the time-history records gives the sequence and propagation of the instability. A simple analysis based on the fact that an increase in pressure from the pre-stall level indicates that the pressure wave associated with stall initiation is propagating forward from a location of higher pressure located downstream of the measurement station. Thus, one is able to identify the stall-initiating component. An analysis of the HARV departed flight stall events showed that, in all cases, the stalls initiated in the compressor.

4.5 Predicted Losses Of Compression Component Stability Pressure Ratio

Based on the levels of spatial inlet total-pressure distortion descriptors, the predicted loss of stability pressure ratio (DPRS) was calculated for the compression components using the F404-GE-400 distortion methodology. Values were assessed for the fan (DPRSF) and the compressor (DPRSH) components of the engine.

Figure 10 shows the time histories of the predicted losses of stability pressure ratio of the fan and the compressor resulting from the measured levels of time-varying spatial inlet total-pressure distortion. High levels of DPRS for the compressor were seen immediately before the stalls. However, there were also many instances where equally high DPRS levels occurred which did not initiate a stall.

4.6 Aircraft, Inlet Flow, and Engine Conditions Prior to and During Engine Stalls

The results of Paragraphs 4.4 and 4.5 presented three significant dilemmas to the propulsion system analysts. First, the stalls were not induced due to ingestion of hot gas such as might come from the engine exhaust. Second, if stalls were distortion induced, then based on component aerodynamic stability analyses and F/A-18 A/B/C/D flight experience, it would be expected that the stalls would have initiated in the fan rather than the compressor. Third, the compressor stalled when distortion levels were large, but not necessarily at maximum values as would be expected based on previous analyses and experience. These three findings caused the investigators to launch detailed studies of the aircraft, inlet flow, and engine conditions during the periods leading up to and during the stalls in an effort to determine the factors associated with stall initiation. The types of analyses undertaken and the associated results are presented in the following subparagraphs.

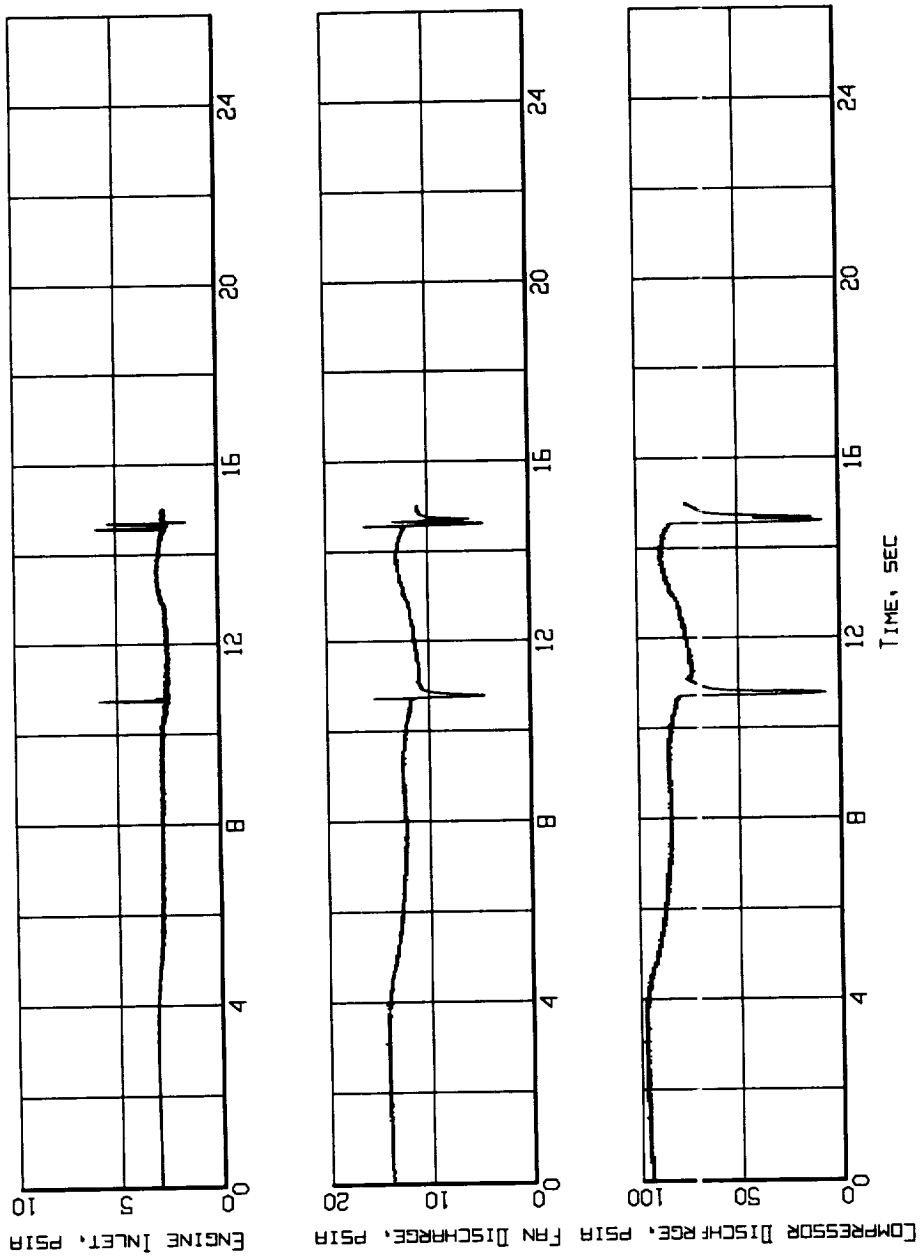

Figure 9. Measured inlet/engine entry and engine internal pressures time histories (Flight 240, Test Point 45b).

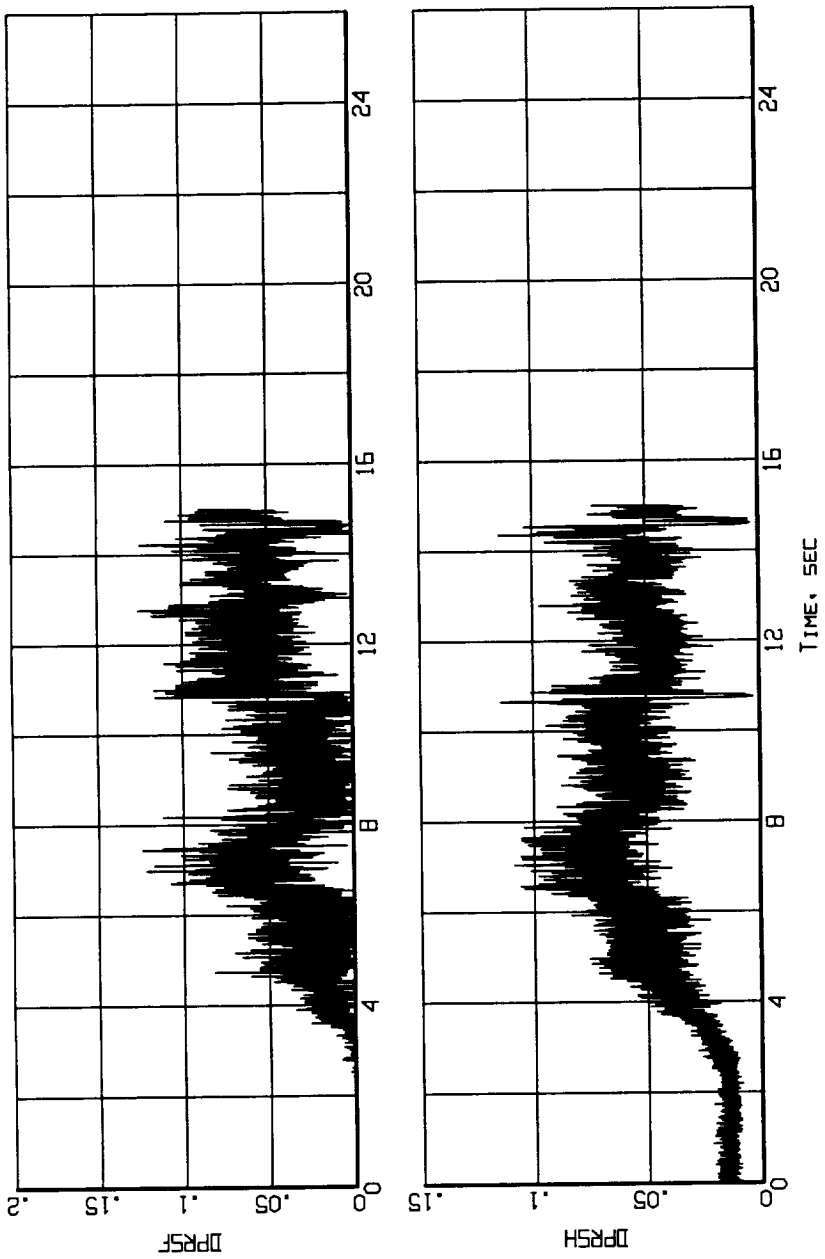

Figure 10. Time histories of the predicted loss of stability pressure ratio for the fan and the compressor (Flight 240, Test Point 45b).

4.6.1 Aircraft Attitude And Motion

In an effort to determine if an interrelationship existed between inlet flow descriptors and aircraft attitude and motion, the times at which the following events occurred were superposed on time traces of aircraft attitude and motion:

- The maximum of the inlet total-pressure circumferential (DP/PC) and radial (DP/PR hub, DP/PR tip) distortion descriptors,
- The maximum of the predicted loss in stability pressure ratio of the fan (DPRSF) and the compressor (DPRSH) resulting from the influence of spatial inlet total-pressure distortion environment, and
- Occurrence of engine instabilities.

Figures 11 and 12 show examples for the typical departure maneuver that is being used as an example. Note that only the maximum values of DP/PC, DPRSF, DPRSH, and the occurrence of the two stalls are denoted. Figure 11 shows the event markers superposed on the aircraft attitude time-histories. It is seen that aircraft attitude is not a factor in the stall events. Figure 12 shows the event markers superposed on the aircraft rate-of-attitude-change time histories. It is noted that the first stall occurred at local maxima in the pitch and roll rates while the second stall occurred at the maximum of all three rate parameters. Similar results were noted in the case of all the departure maneuvers during which stalls occurred. Thus, it appeared that the rate-of-change of the aircraft motion was a factor in the stall events.

After reviewing the body of data, it was decided that a parameter representing the combined rate-of-change of the aircraft motion might be a better correlating factor of the stall events. It is well known that rates of change of aircraft motion produce gyroscopic moments. The forces associated with these moments have the effect of causing the rotor to deviate from running concentrically within the casing and/or the engine mounts inducing mechanical distortion of the case. The net impact of these gyroscopic forces is to change the running clearances of the rotor airfoils and thereby affect the stability limit lines of the compression components. Because the gyroscopic moments are vector parameters and are related to the rates of change of pitch, roll, and yaw, it was decided to formulate a combined rate of change parameter (CROCP) defined as follows:

$$\text{CROCP} = [\,(\,\text{Pitch Rate}\,)^2 + (\,\text{Roll Rate}\,)^2 + (\,\text{Yaw Rate}\,)^2\,]^{0.5}$$

The occurrences of the stalls are superposed on the combined aircraft rate of attitude change time-history as illustrated in Figure 13. Examination of the figure shows that the stalls occurred on the curve of CROCP as a function of time at a point of relative maxima or at the maximum. Examination of this curve for the other departed flight stalls also showed the same type of general behavior. Thus, it was possible to conclude that high rates of change of aircraft motion played a part in the initiation of the stalls.

4.6.2 Aircraft Inlet Conditions

In order to be sure that the analyses were not leading the investigators to potentially unwarranted conclusions, an examination of the aircraft aerodynamic inlet conditions also was undertaken. The aircraft angle of attack (AOA) and the angle of sideslip (AOSS) and the respective rates-of-change with time were investigated in a manner similar to the parameters discussed in the preceding paragraphs, that is, the event markers were superposed on the AOA and AOSS time histories. Figure 14 provides an illustration of this type of presentation. There appeared to be no correlation of occurrence of stalls with maxima or minima in the AOA or AOSS parameters, that is, they occurred significantly ahead of a stall. In order to be considered

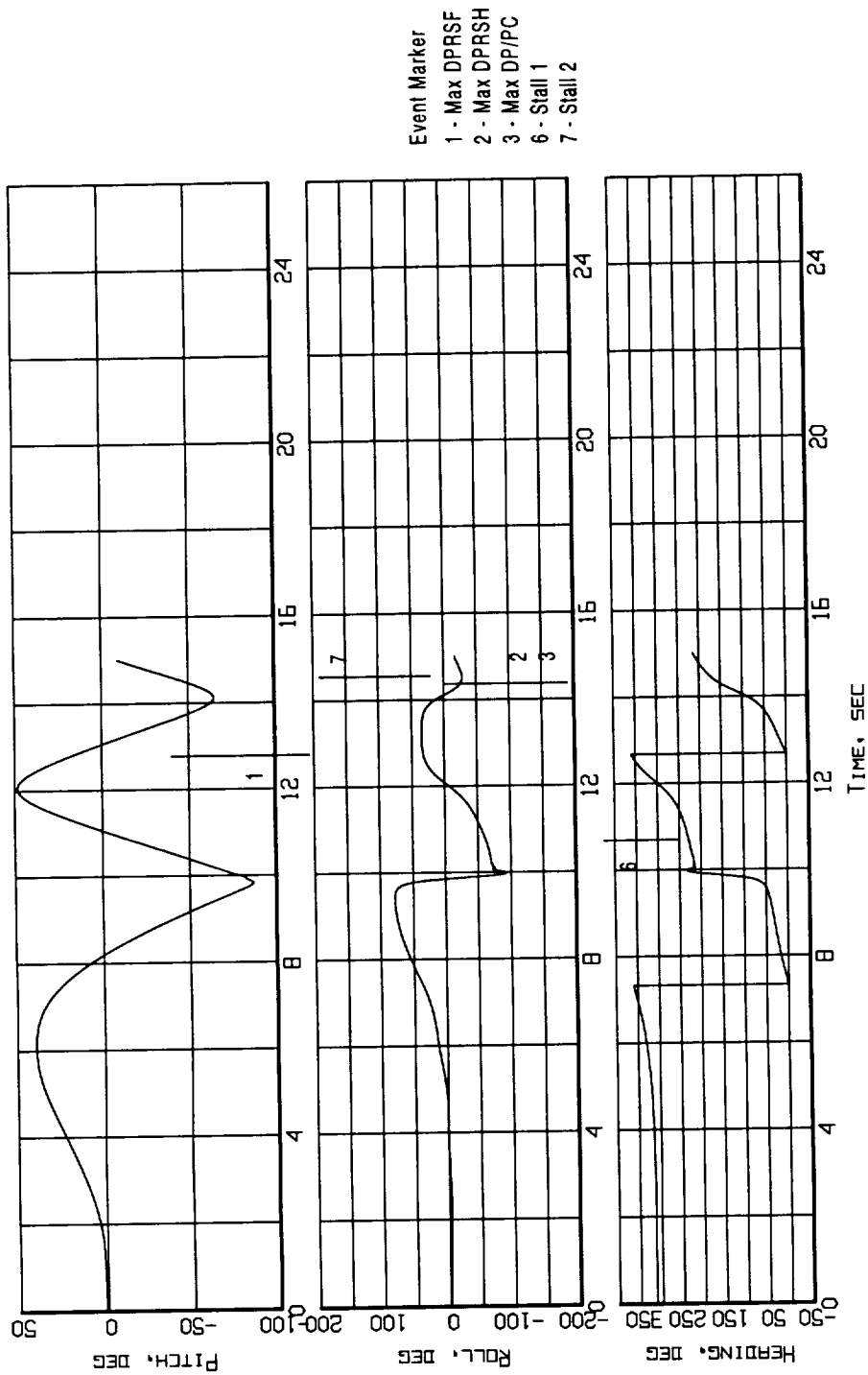

Figure 11. Event markers superposed on the aircraft attitude time histories (Flight 240, Test Point 45b).

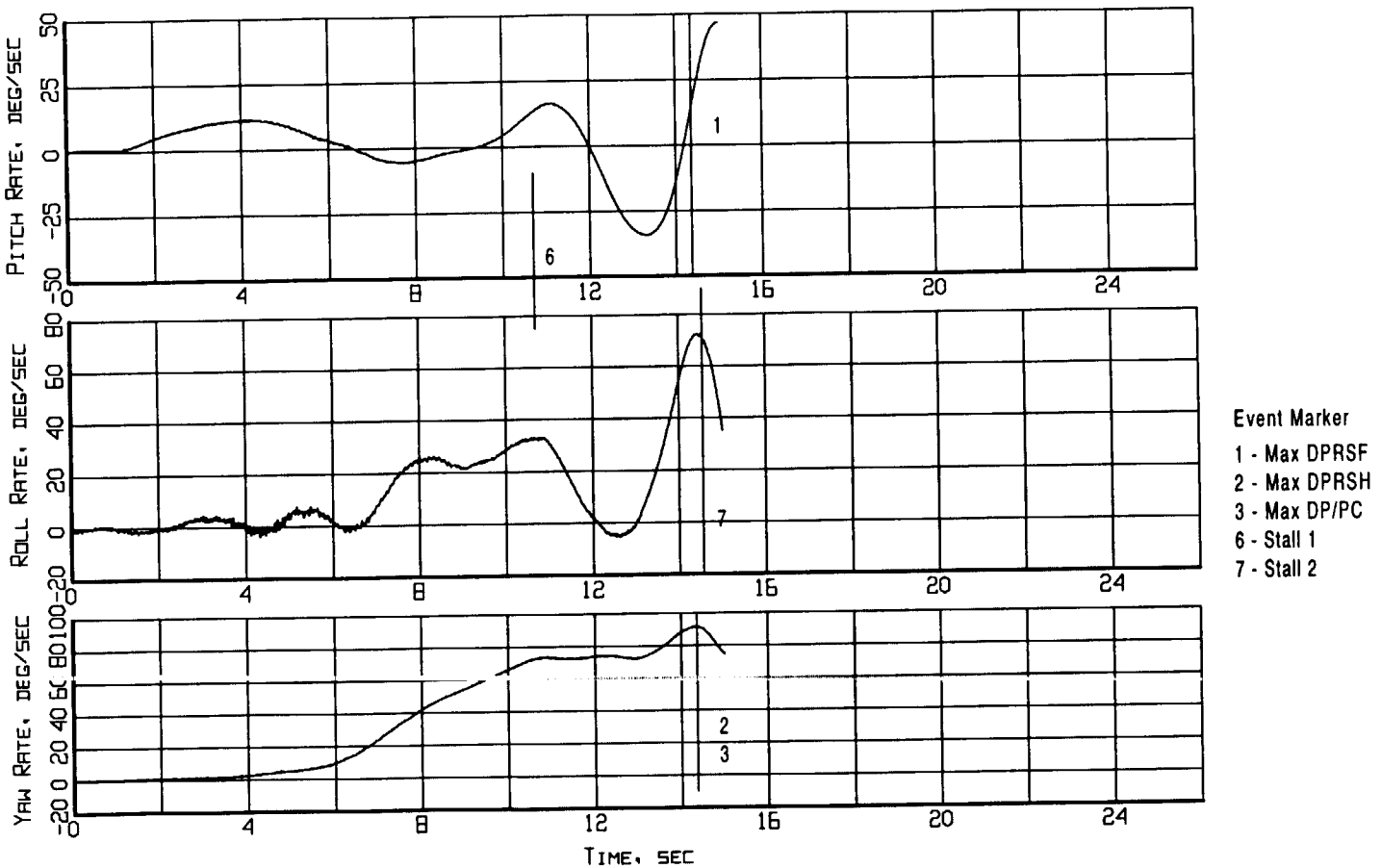

Figure 12. Event markers superposed on the aircraft motion time histories (Flight 240, Test Point 45b).

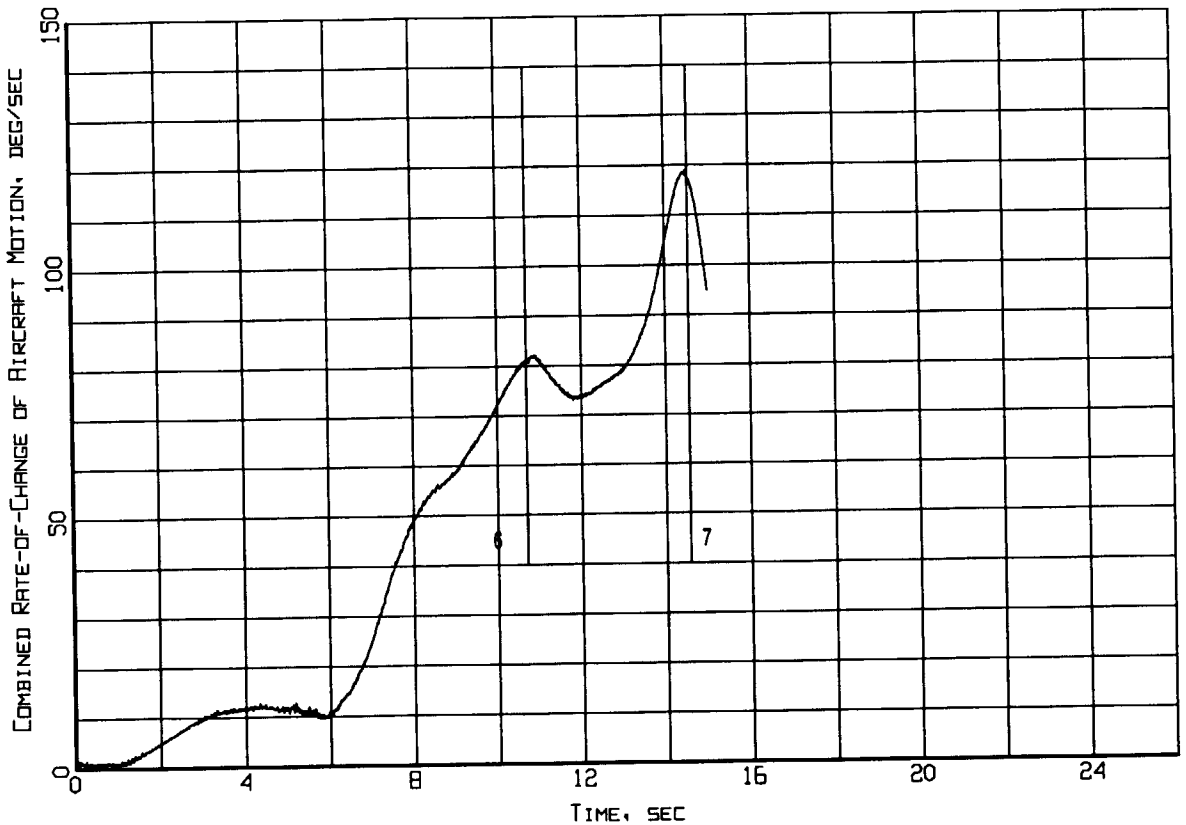

Figure 13. Event markers superposed on the combined of rate-of-change of aircraft motion time history (Flight 240, Test Point 45b).

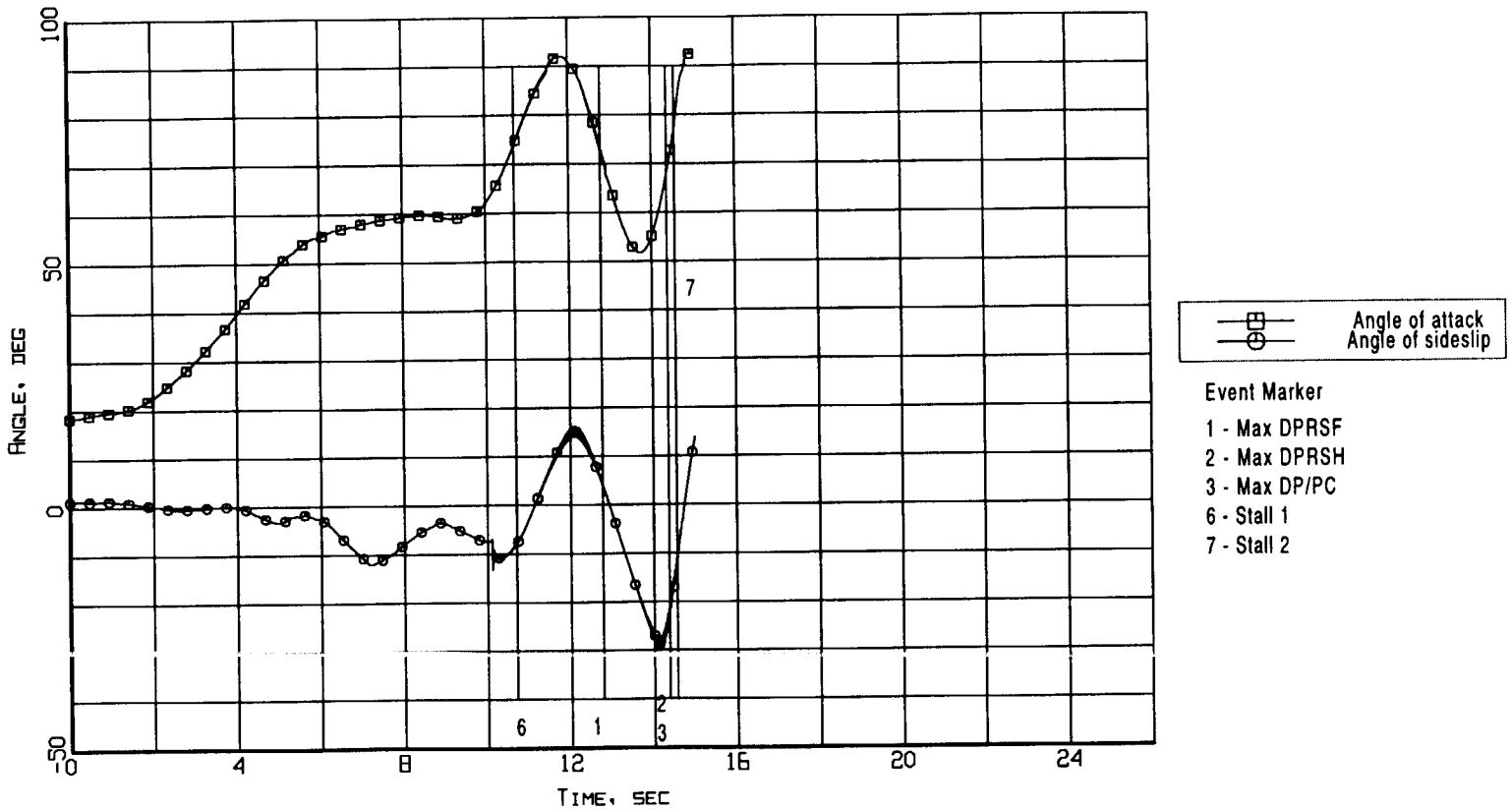

Figure 14. Event markers superposed on the angle-of-attack and angle-of-sideslip time histories (Flight 240, Test Point 45b).

as playing a role in a stall, they would have to occur approximately 5-10 milliseconds prior to the stall. Viewing plots from all the departed flights with stalls did show that stalls occurred at high angles of attack (>70 degrees) and a over a wide range of angles of sideslip. There was a possible dependence on sideslip angle. Stalls tended to occur at a lower negative AOSS (nose-right) for a given AOA. All events occurred at positive velocity. Superposing the event markers on the time rates of change plots as in Figure 15 again shows that the occurrence of these events is significantly ahead of the stall. Thus, the rate-of-change of the aerodynamic attitude was concluded to not be a factor in the stall events.

Figure 16 shows the event markers superposed on the aerodynamic flowstream (a combined AOA - AOSS plot) trajectory time history. Each successive square symbol along the trajectory represents an additional increment of time (one second) from the initiation of the maneuver. The pilot pulls the nose of the aircraft up with little sideslip until at approximately ten seconds and introduces sideslip to initiate the flight departure. During the next five seconds or so, the stalls and event markers are denoted. Note that there appears to be no correlation of the event markers with extrema of the trajectory other than for the maximum value of hub radial distortion (Max DP/PR hub) - the latter not being a consumer of compressor stability margin. Further, it is important to note that the change in the attitude of the aerodynamic flowstream with time was very slow when compared to the time scale (about 20 milliseconds) for aerodynamic disturbances to propagate from the inlet lip to the engine face.

4.7 Combined Effects of Inlet Distortion and Rate of Change of Aircraft Motion

The discussions of Paragraph 4.5 and 4.6.1 suggest that some combination of distortion and combined rate of change (clearances) effects could lead to the occurrence of compressor stalls in the F404-GE-400 engine. Assessing the combination of effects of time-variant inlet distortion (in terms of DPRSH) and aircraft motion can be accomplished by plotting the values of loss of compressor stability compressor ratio versus the value of the combined rate of change parameter throughout the maneuvers, at stall, and beyond. These results for all stall events as well as for many non-stall points from all the flight departure records are plotted in Figure 17.

It should be noted that the stall data fall into two classes - isolated and non-isolated. The isolated data are characterized by no stall occurring during the previous 2.4 seconds or more. The non-isolated stall data are characterized by the fact that a prior stall had occurred during the previous 2.4 seconds. In this latter case, it is believed that the engine did not have time to re-establish the thermal equilibrium characteristics associated with a normally operating engine.

Thus, of the fourteen stalls occurring on the right-hand engine, seven were isolated stalls and five were non-isolated stalls. For the remaining two stalls, the data were not available. This delineation of points is clearly shown in the Figure 17 data. The isolated stall data all tend to group at simultaneous high values of DPRSH and CROCP as might be expected while the non-isolated stalls tend to fall at lower combined values of these two parameters. Hence, based on these data, it appears that isolated stalls that occur in the F404-GE-400 engine installed in the F/A-18A aircraft during departed flight maneuvers can be attributed to the combined impact of inlet total-pressure distortion on the compressor and of compressor clearance changes resulting from eccentricity of the compressor rotor and/or distortion of the compressor casing.

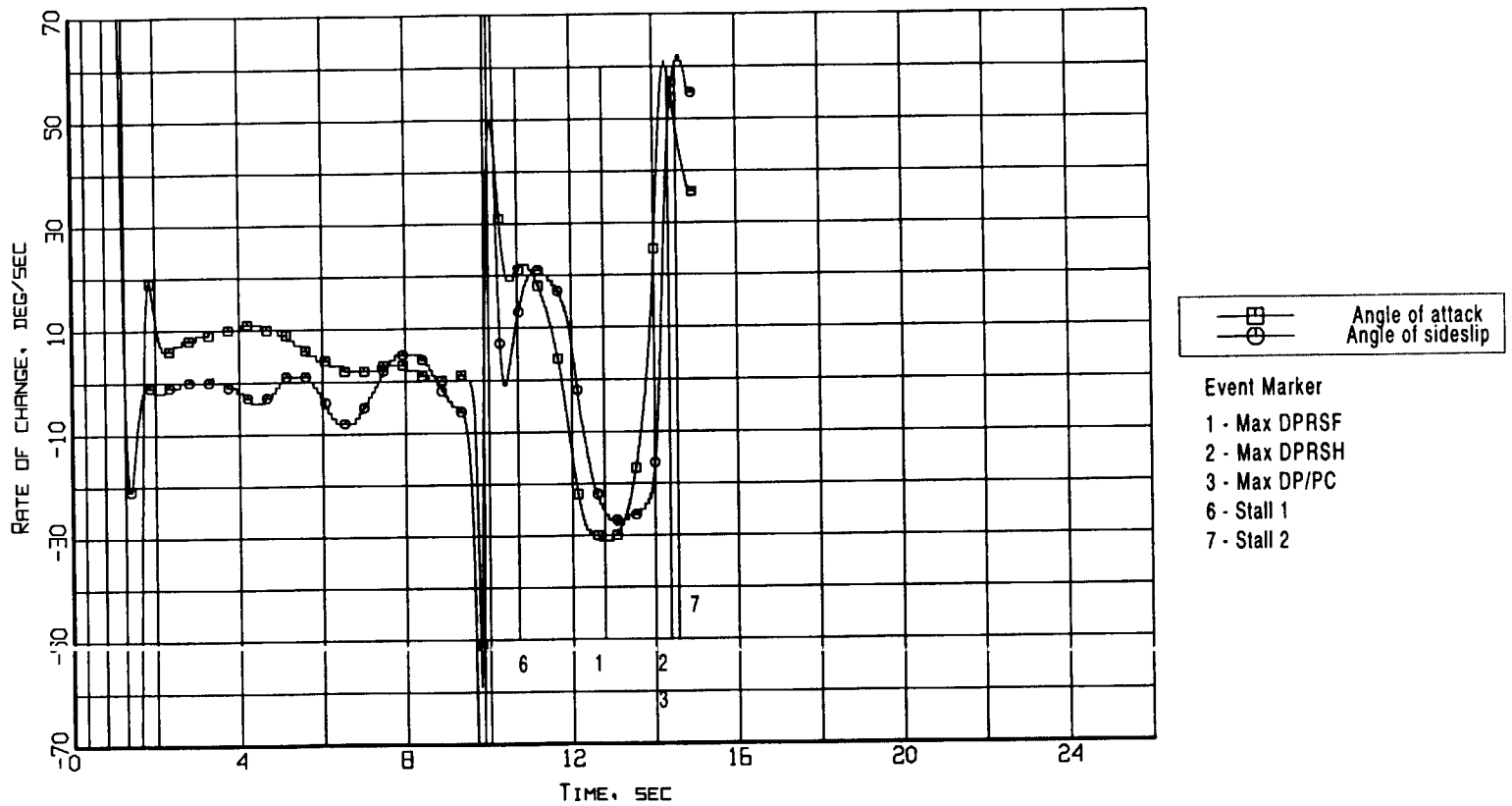

Figure 15. Event markers superposed on the rate-of-change of angle-of-attack and angle-of-sideslip time histories (Flight 240, Test Point 45b).

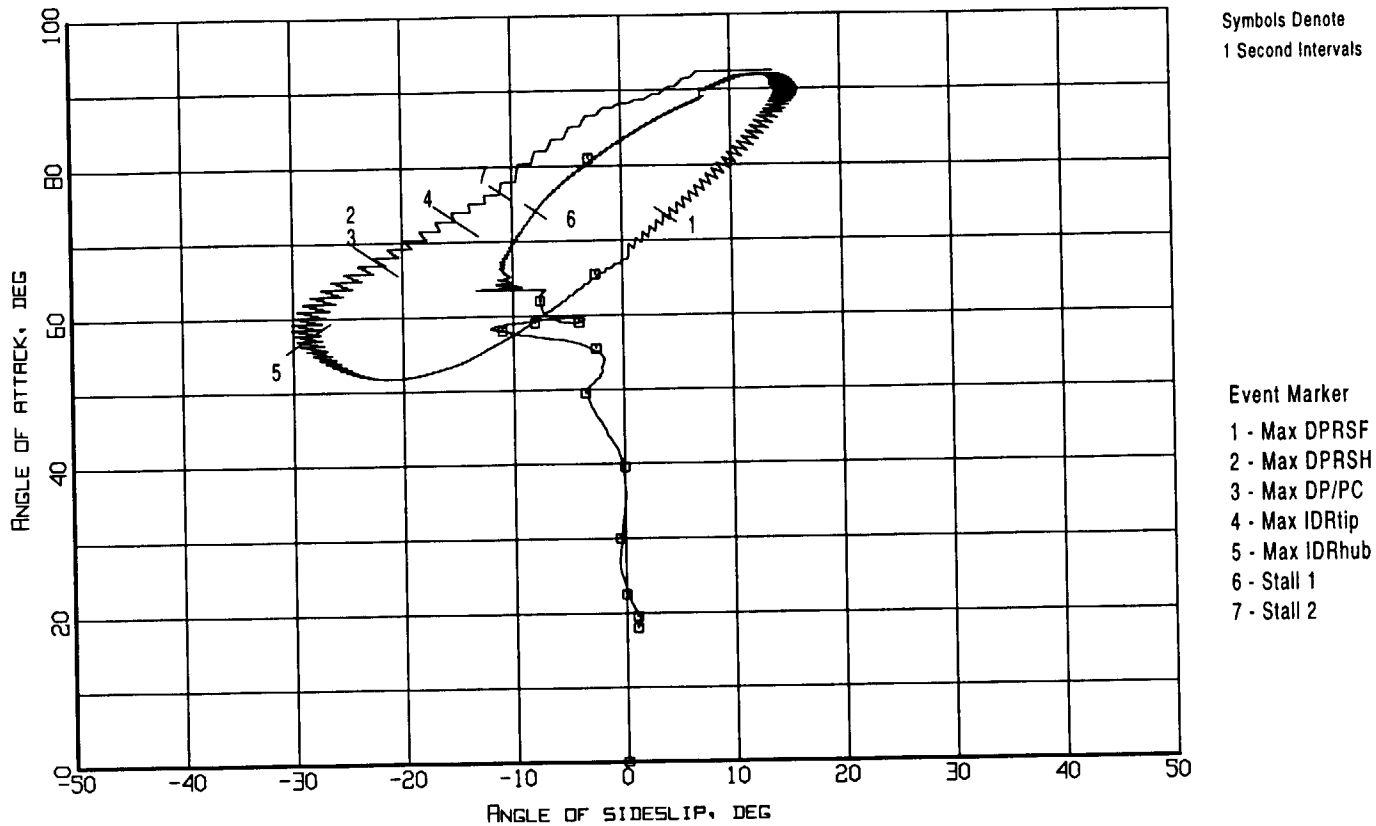

Figure 16. Event markers superposed on the aerodynamic flowstream descriptors trajectory (Flight 240, Test Point 45b).

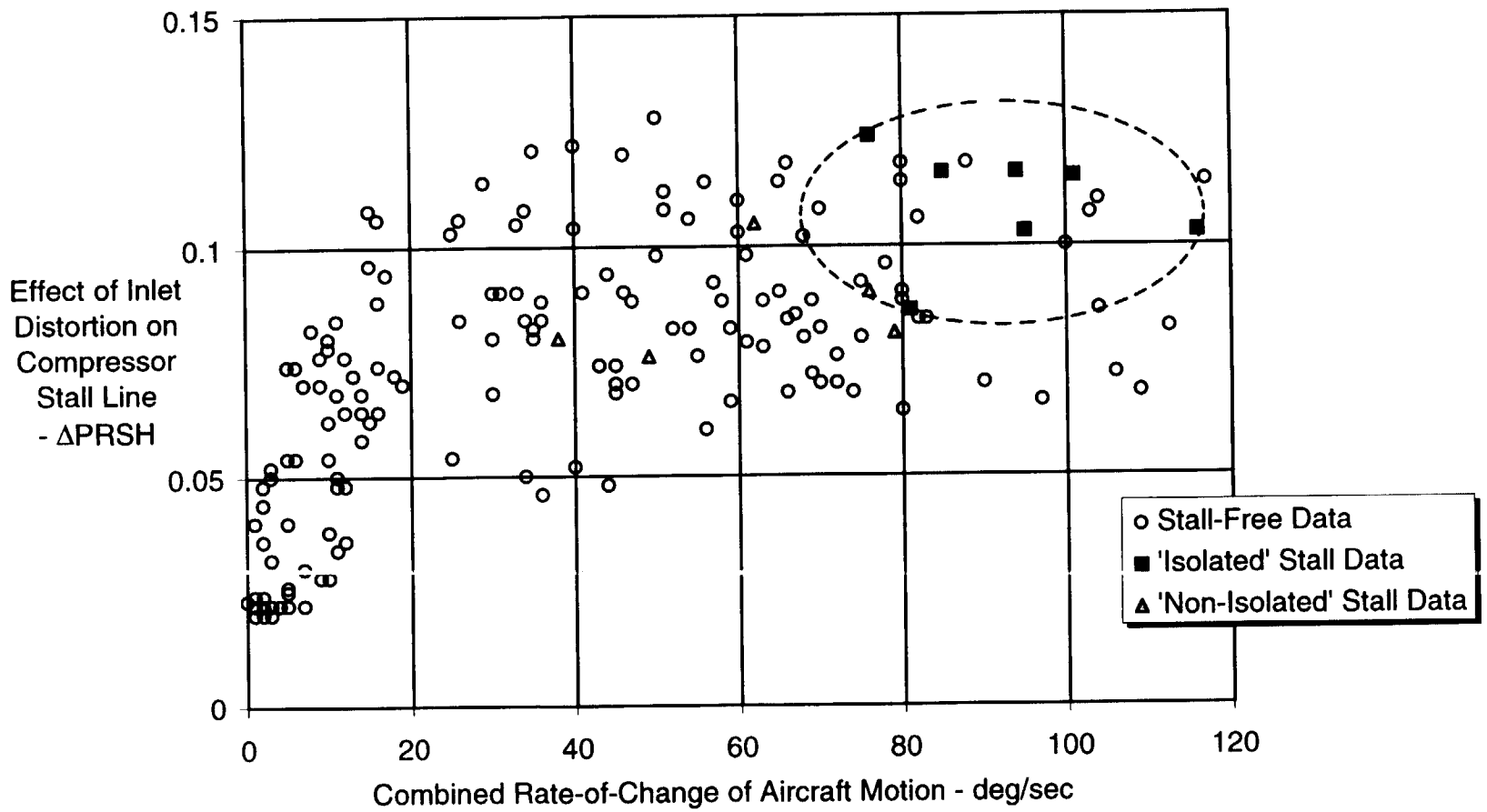

Figure 17. Correlation of stall and stall-free points with the loss of stability pressure ratio and combined rate of change parameter.

5.0 CONCLUSIONS AND RECOMMENDATIONS

The results obtained through the analysis of the aircraft and propulsion system data obtained during the departed flight maneuvers by the HARV aircraft provided significant insight to the inlet flow conditions entering the engine. In addition, new and unexpected findings were obtained which changed views about the causes of engine surge during departed flight maneuvers. In the discussion presented below, the specific findings will be enumerated and summarized.

- The objectives of the departed flight maneuver phase of the HARV inlet program were achieved. The departures were induced with nose-left and nose-right entries over a range of yaw rates. Typically, the greater the maximum yaw rate, the more violent the departed motion of the aircraft as parameterized by changes in pitch, heading, and roll angles and the associated time rates of change of these angles.

- During departed flight, the magnitude of the peak time-variant total-pressure distortion levels were well beyond those encountered in the normal operating regime for controlled flight. In fact, the peak time-variant circumferential total-pressure distortion levels at times exceeded by 25 percent the limits used as guidance for the F404-GE-400 engine installation.

- Examination of the engine inlet temperature confirmed that there was no evidence of ingestion of hot exhaust gas during the departed flight maneuvers, thus removing inlet total-temperature distortion as a potential source or contributor to the engine surges that occurred.

- All surges that occurred initiated in the compressor as determined by the examination of pressure waveforms obtained from high-response instrumentation at the fan discharge. Based on the F404-GE-400 distortion methodology, surges occurring due only to inlet maneuver distortion effects would have been expected to initiate in the fan. All of the surges recovered without pilot action.

- A surprising result was the finding that the surges did not occur when the time-variant circumferential and radial distortions combined in a manner to produce a maximum loss in stability pressure ratio. Rather, it was a combination of high loss of compressor stability pressure ratio due to distortion and the magnitude of the rate of change of aircraft motion. The latter was quantified by taking the root-sum-square of the pitch, yaw, and roll rates. These changes are related to the gyroscopic moments acting on the rotors of the engines and hence, producing transient changes in the rotor-to-casing compressor clearances.

During future departed flight maneuver investigations, it is recommended that provisions be made to include instrumentation, such as clearanceometers, to provide a direct measurement of clearance changes during maneuvers with high rates of change to the pitch, yaw, and roll angles and to configure data reduction programs to calculate the appropriate gyroscopic moments.

REFERENCES

1. Walsh, K. R., Yuhas, A. J., Williams, J. G., and Steenken, W. G., "Inlet Distortion for an F/A-18A Aircraft During Stabilized Maneuvers up to 60° Angle of Attack,' National Aeronautics and Space Administration Report TM-104329, April 1997.

2. Yuhas, A. J., Steenken, W. G., and Williams, J. G., and Walsh, K. R., "F/A-18A Inlet Flow Characteristics During Maneuvers with Rapidly Changing Angle of Attack," National Aeronautics and Space Administration Report TM-104327, June 1997.

3. Regenie, V., Gatlin, D., Kempel, R., and Matheny, N., "The F-18 High Alpha Research Vehicle: A High-Angle-of-Attack Testbed Aircraft," National Aeronautics and Space Administration Report TM 104253, September 1992.

4. Amin, N. F. and Hollweger, D. J., "F/A-18A Inlet/Engine Compatibility Flight Test Results," AIAA Paper No. AIAA-81-1393, July 1981.

5. Williams, J. G., Steenken, W. G., and Yuhas, A. J., "Estimating Engine Airflow in Gas-Turbine Powered Aircraft with Clean and Distorted Inlet Flows," National Aeronautics and Space Administration Contractor Report 198052, September 1996.

6. Yuhas, A. J., Ray, R. J., Burley, R. R., Steenken, W. G., Lechtenberg, L., and Thornton, D., "Design and Development of an F/A-18 Inlet Distortion Rake: A Cost and Time Saving Solution," American Institute of Aeronautics and Astronautics Paper No. AIAA-94-2132, June 1994.

7. Moes, T. R. and Whitmore, S. A., "A Preliminary Look at Techniques Used to Obtain Airdata from Flight at High Angles of Attack," National Aeronautics and Space Administration Report TM 101729, December 1990.

8. Society of Automotive Engineers, "Gas Turbine Engine Inlet Flow Distortion Guidelines," Aerospace Recommended Practice ARP 1420, March 1978.

APPENDIX A - INLET FLOW DESCRIPTOR DEFINITIONS

For a given pattern of 40 total-pressure measurements (8 rakes, 5 rings), the total-pressure distortion descriptors are defined as follows:

Maximum Circumferential Distortion Descriptor - DP/PC max

This circumferential ring pressure distortion index is based on the calculation of $DP/PC_{ring\ i}$, where the subscript "ring i" refers to any of the five pressure rings.

The rings are counted in ascending order, innermost to outermost.

$$DP/PC_{ring\ i} = \{[\ PAV_{ring\ i} - PMIN_{ring\ i}\ ] / PAV\} \quad \text{for rings } i=1,5$$

where:

1. $PAV_{ring\ i}$ = area-averaged total pressure of ring i
2. $PMIN_{ring\ i}$ = minimum total pressure in the largest low pressure region in ring i
3. PAV = area-averaged total pressure over the complete face

DP/PC max is defined as the largest of:

$$0.5 \cdot [DP/PC_{ring\ i} + DP/PC_{ring\ i+1}] \qquad \text{for } i=1,4 \qquad \text{(A1)}$$

Maximum Radial Distortion Descriptor - DP/PR max

Similar to DP/PC, DP/PR is calculated for each of the five rings as follows:

$$DP/PR_{ring\ i} = [\ PAV - PAV_{ring\ i}\ ] / PAV \quad \text{for rings } i=1,5 \qquad \text{(A2)}$$

where:

1. PAV = area-averaged total pressure over the complete face
2. $PAV_{ring\ i}$ = area-averaged total pressure of ring i

If a DP/PR_{ring} value is negative, it is assumed to be zero.

DP/PR max is defined as the larger of $DP/PR_{ring\ 1}$ or $DP/PR_{ring\ 5}$

If DP/PR max is located in ring 1, the distortion is hub radial.

If DP/PR max is located in ring 5, the distortion is tip radial.

APPENDIX B - DEPARTURE FLIGHT TIME HISTORIES

As stated at the beginning of Section 4, time history plots similar to those used in the text to describe the results and data for Flight 240, Test Point 45b are contained in this appendix for the remaining eleven departed maneuver cases.

Appendix B1 - Flight 239, Test Point 34b

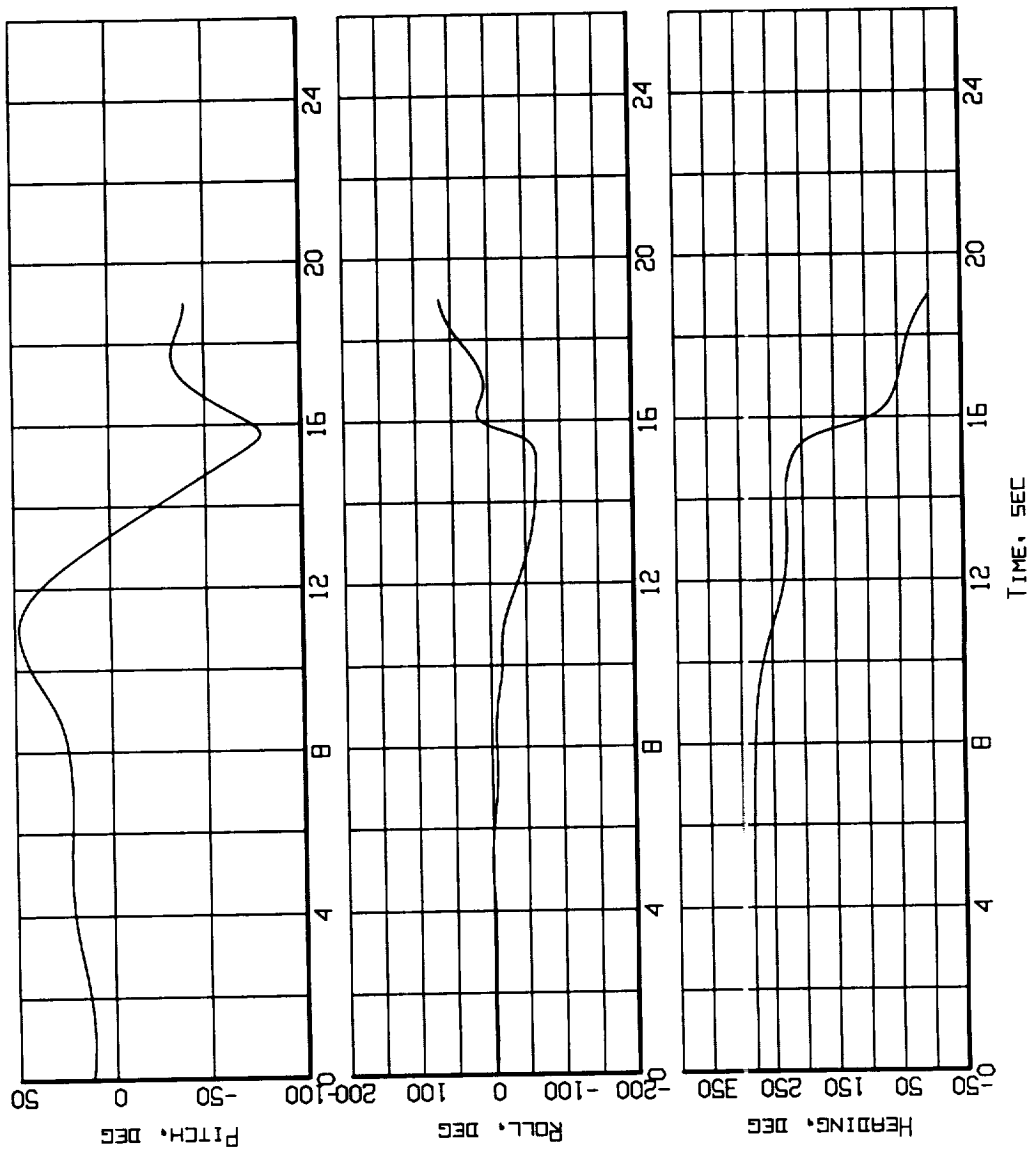

Figure B1-1. Aircraft attitude - Pitch, Roll, and Heading (Flight 239, Test Point 34b).

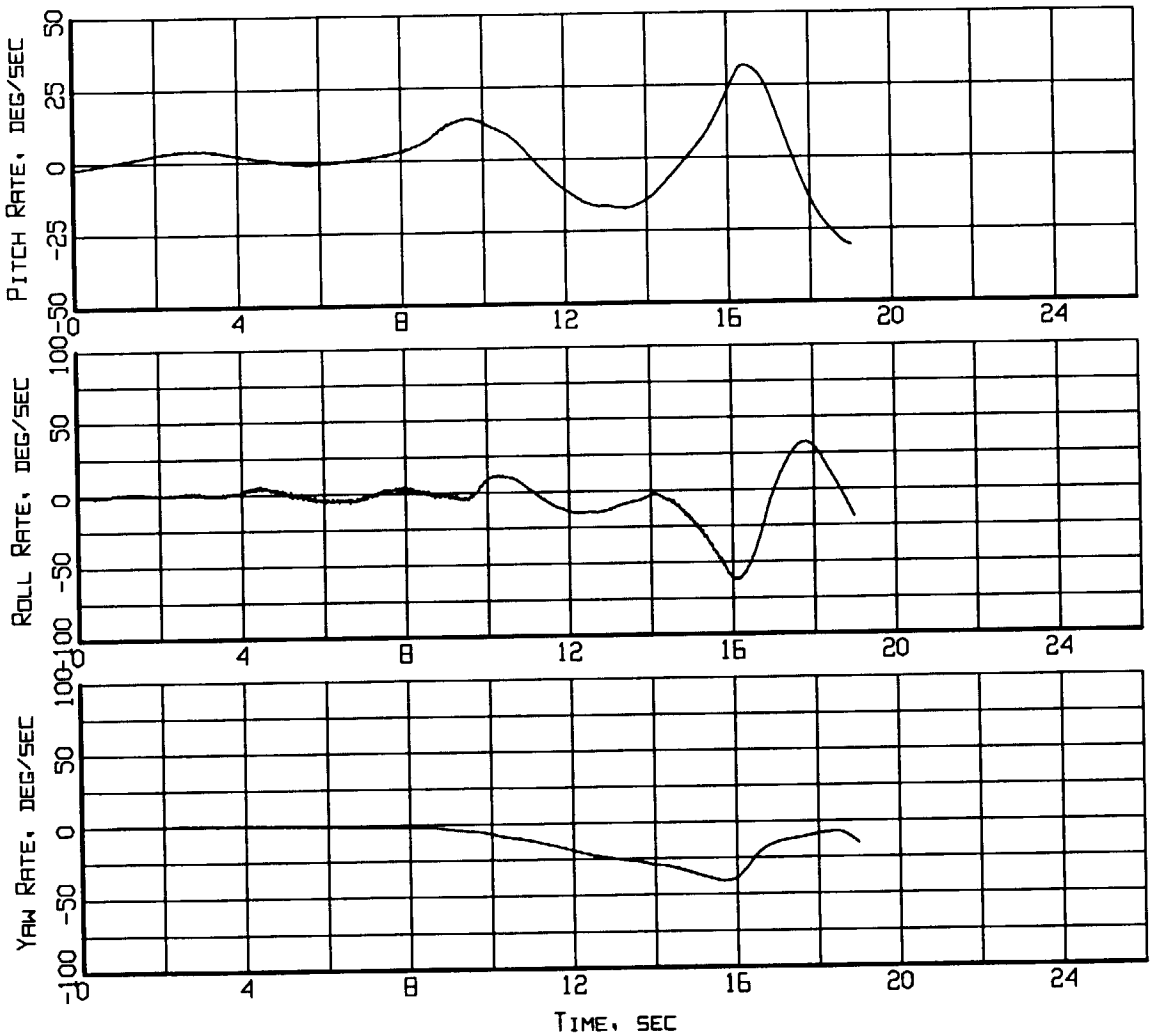

Figure B1-2. Aircraft Motion - Rate-of-Change of Pitch, Roll and Heading (Flight 239, Test Point 34b).

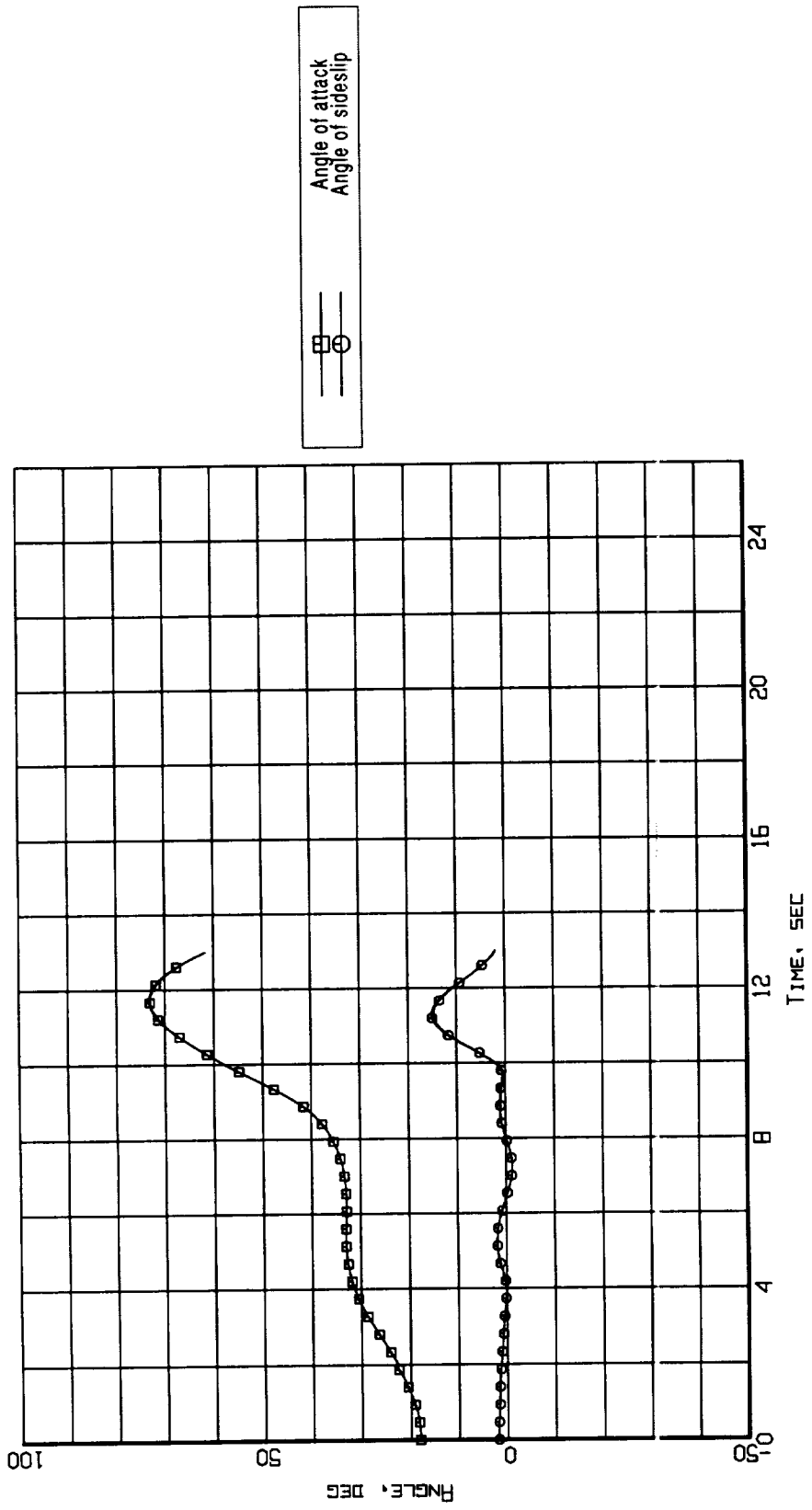

Figure B1-3. Aerodynamic flowstream descriptors - angle of attack and angle of sideslip (Flight 239, Test Point 34b).

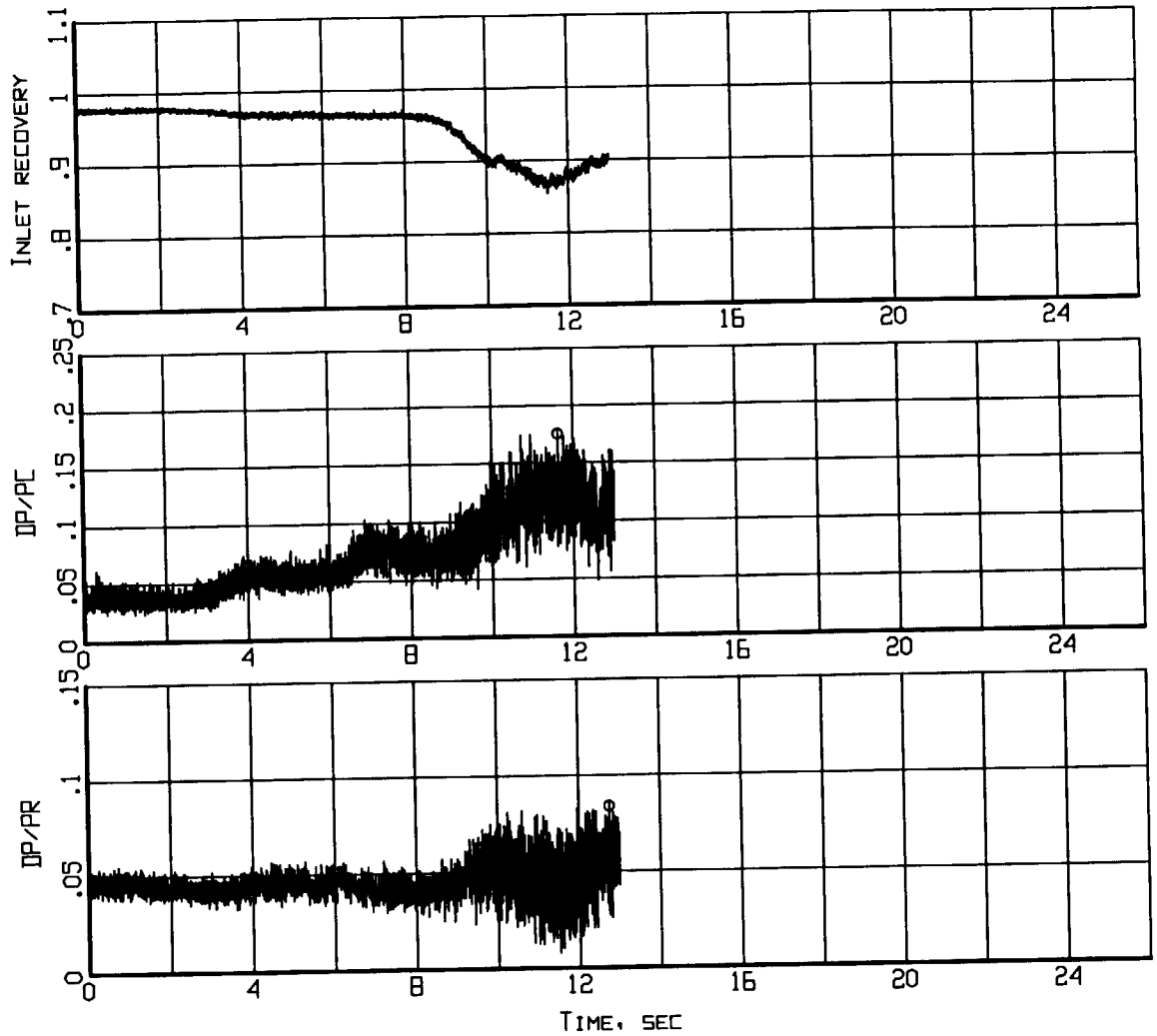

Symbols Denote
Max Points

Figure B1-5. Time histories of inlet recovery and distortion descriptors (Flight 239, Test Point 34b).

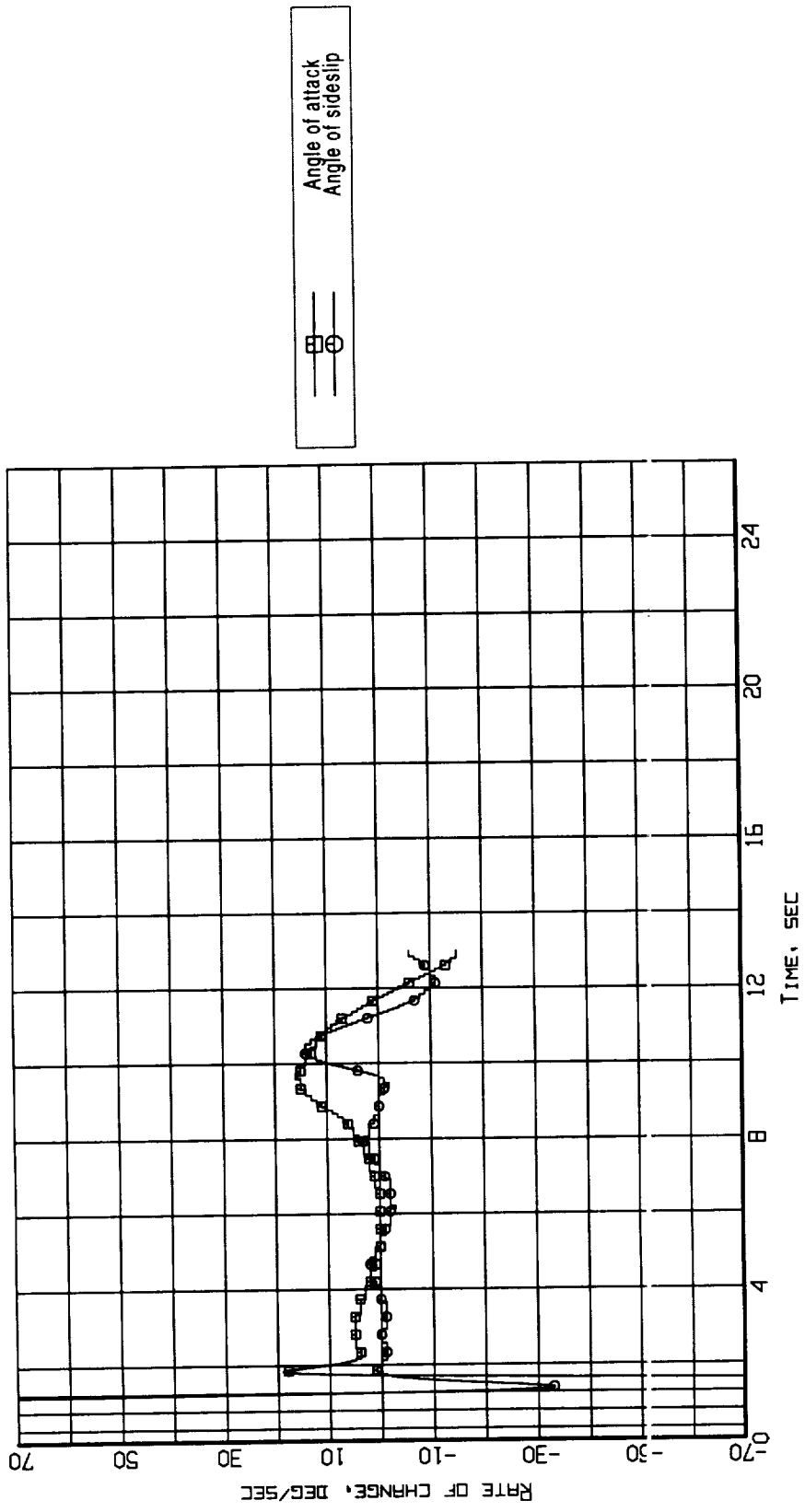

Figure B1-4. Aerodynamic flowstream descriptors - rate of change of angle of attack and angle of sideslip (Flight 239, Test Point 34b).

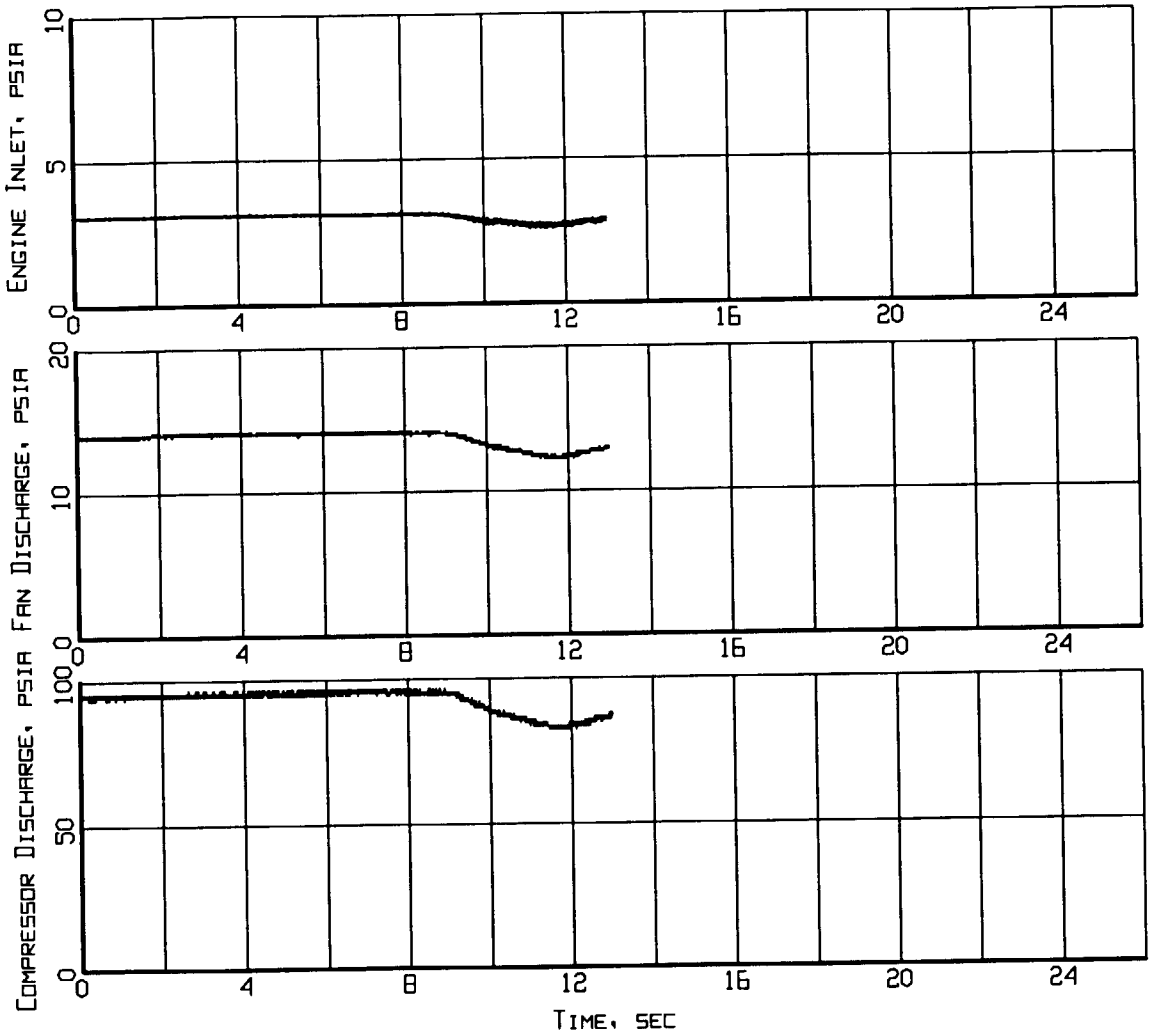

Figure B1-6. Measured inlet/engine entry and engine internal pressures time histories (Flight 239, Test Point 34b).

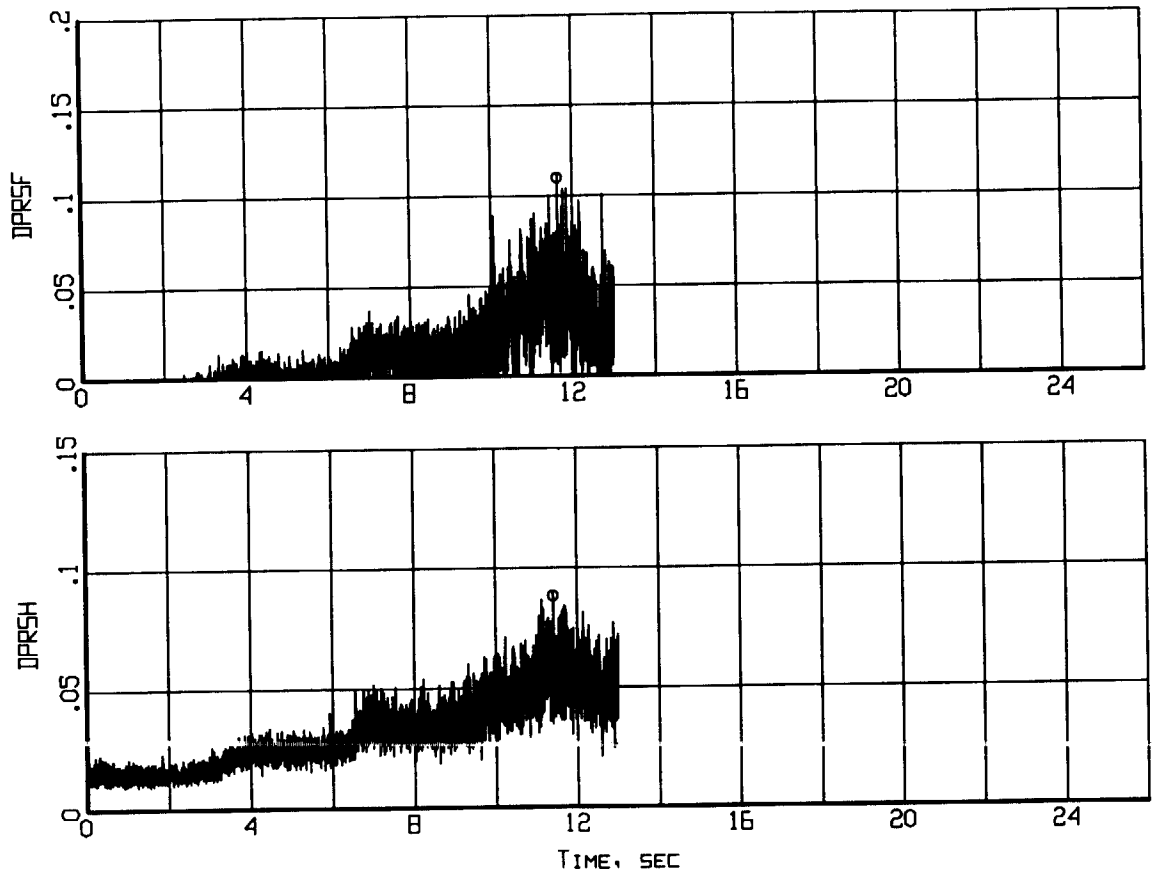

Symbols Denote
Max Points

Figure B1-7. Time histories of the predicted loss of stability pressure ratio for the fan and the compressor (Flight 239, Test Point 34b).

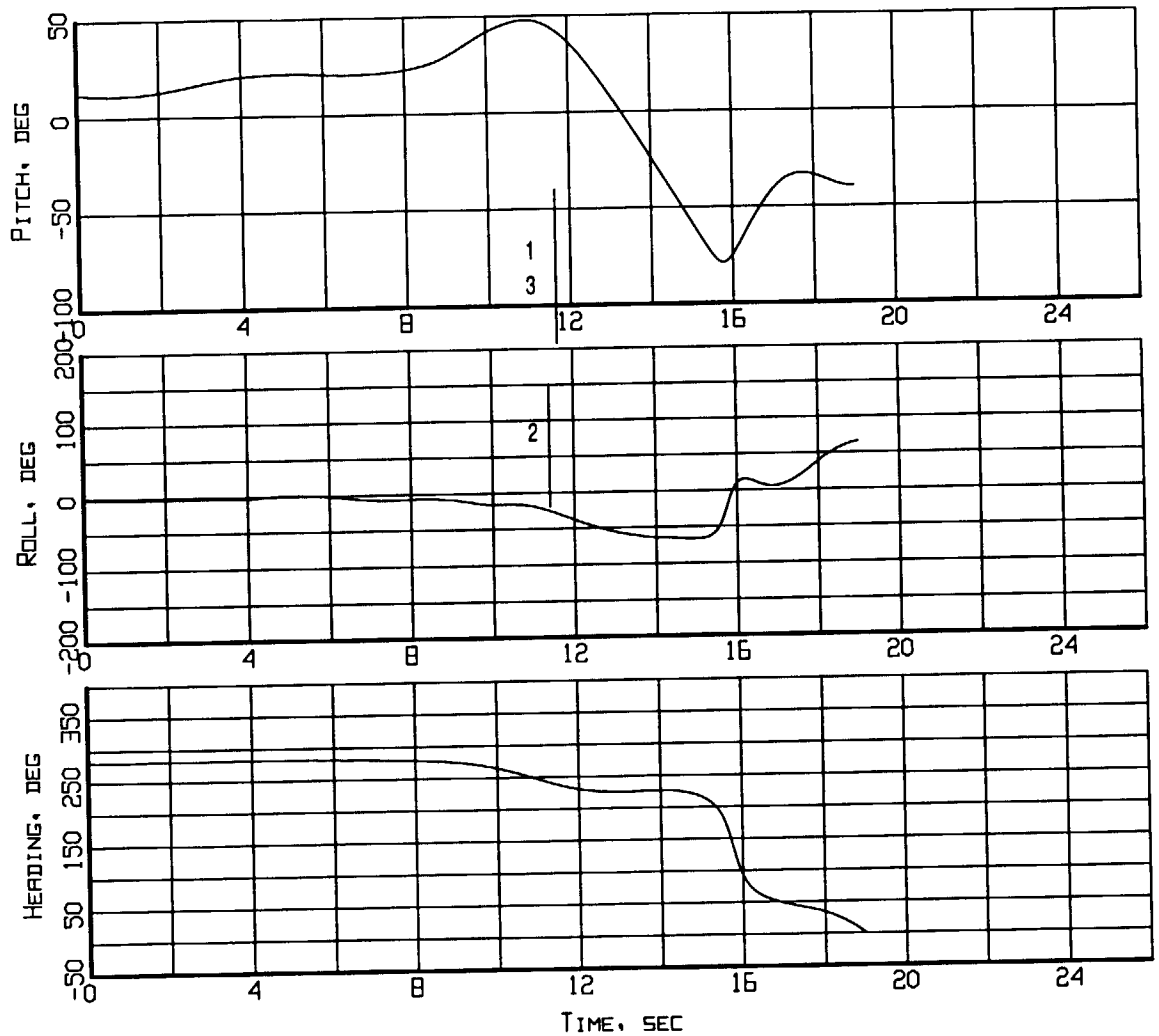

Event Marker

1 - Max DPRSF

2 - Max DPRSH

3 - Max DP/PC

Figure B1-8. Event markers superposed on the aircraft attitude time histories (Flight 239, Test Point 34b).

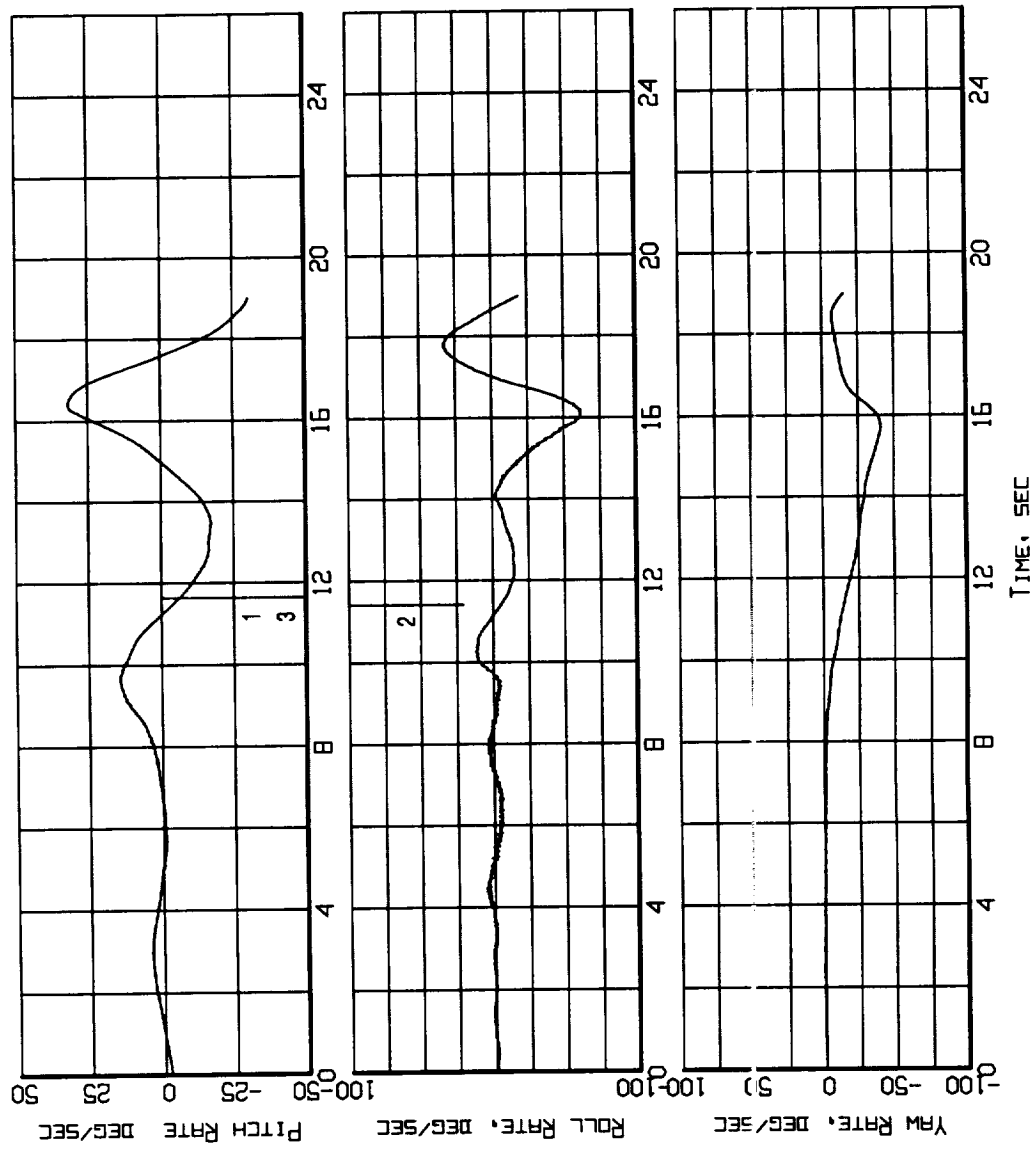

Figure B1-9. Event markers superposed on the aircraft motion time histories (Flight 239, Test Point 34b).

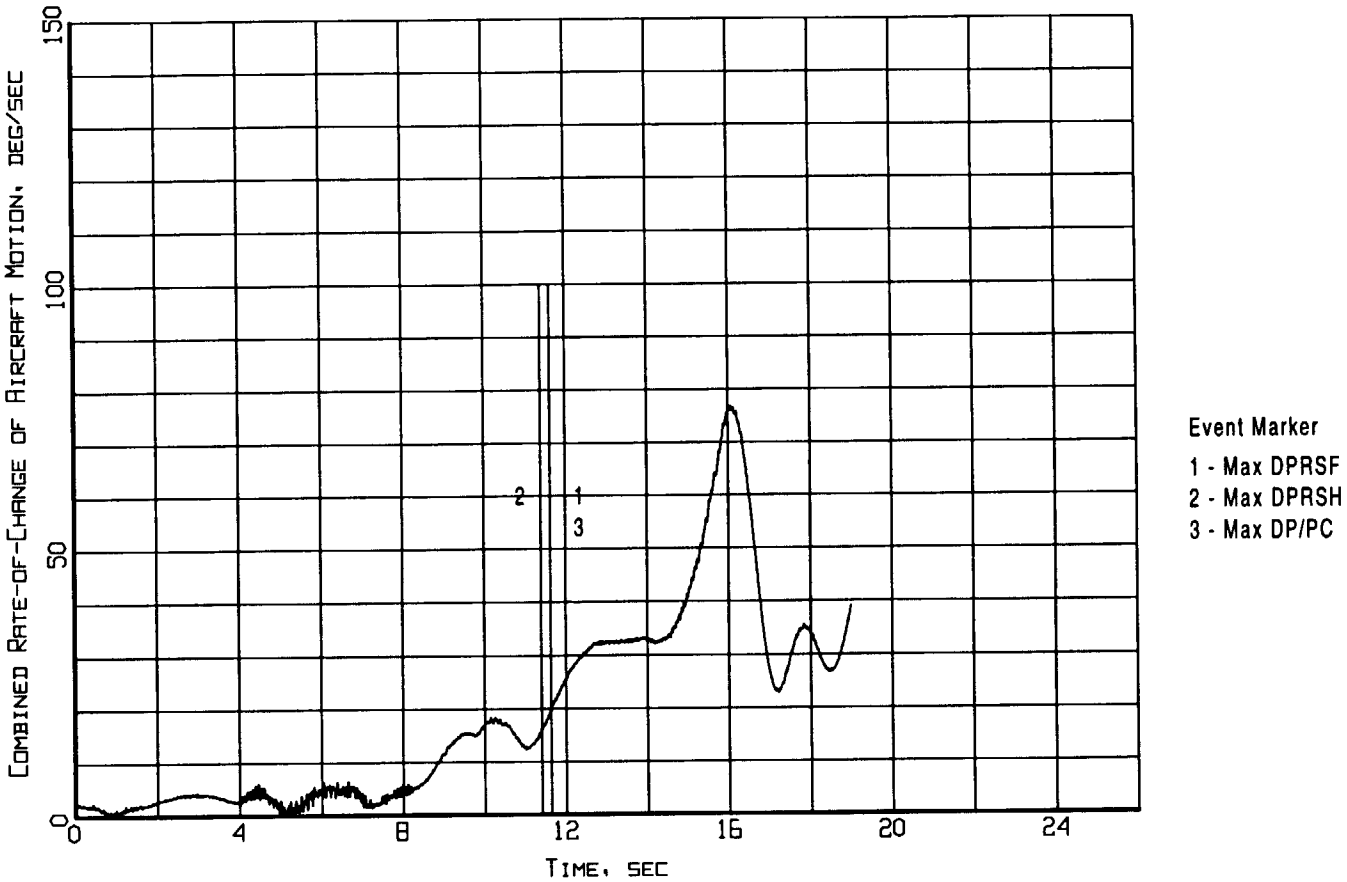

Figure B1-10. Event markers superposed on the combined of rate-of-change of aircraft motion time history (Flight 239, Test Point 34b).

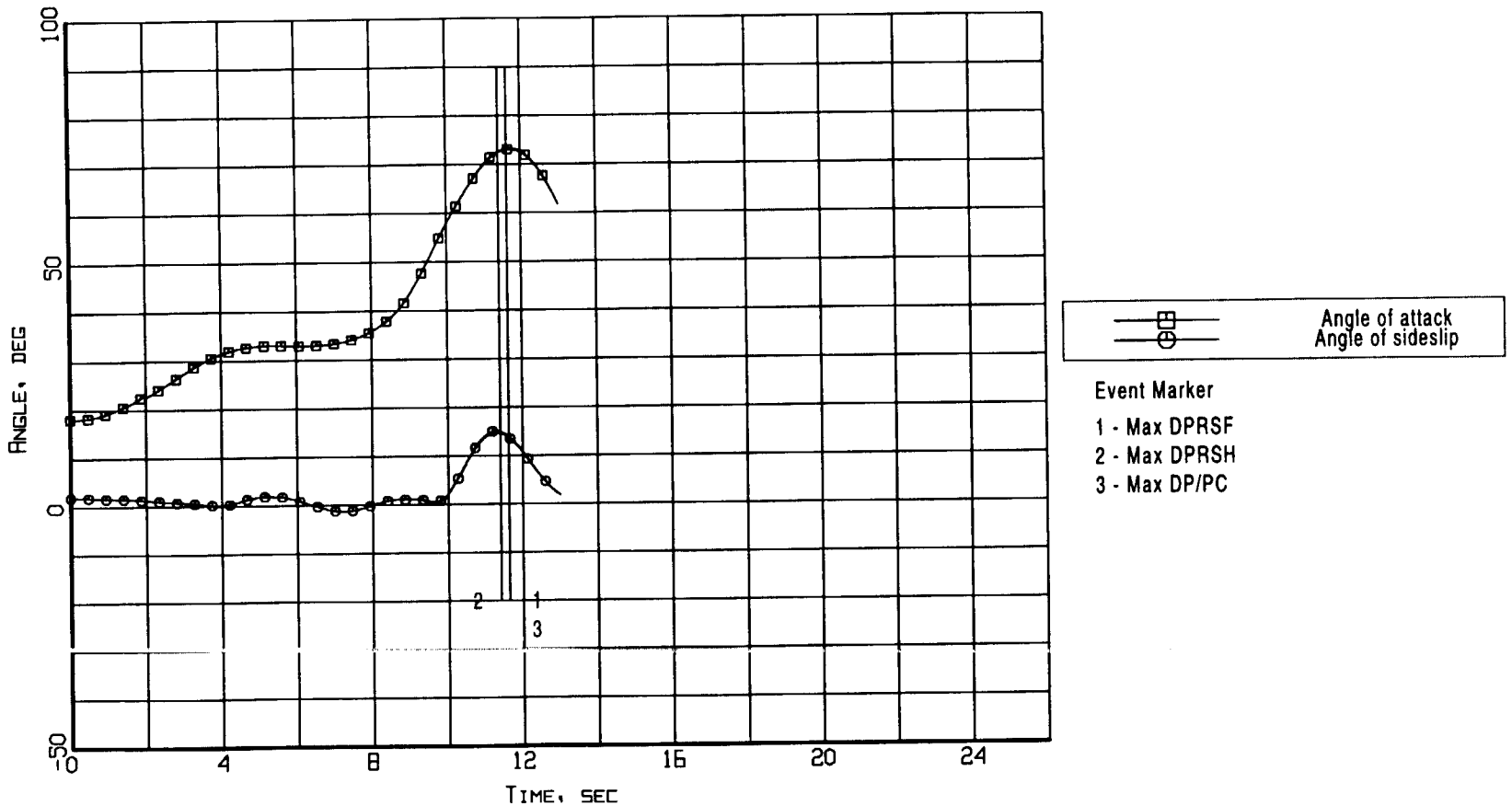

Figure B1-11. Event markers superposed on the aerodynamic flowstream descriptor time histories (Flight 239, Test Point 34b).

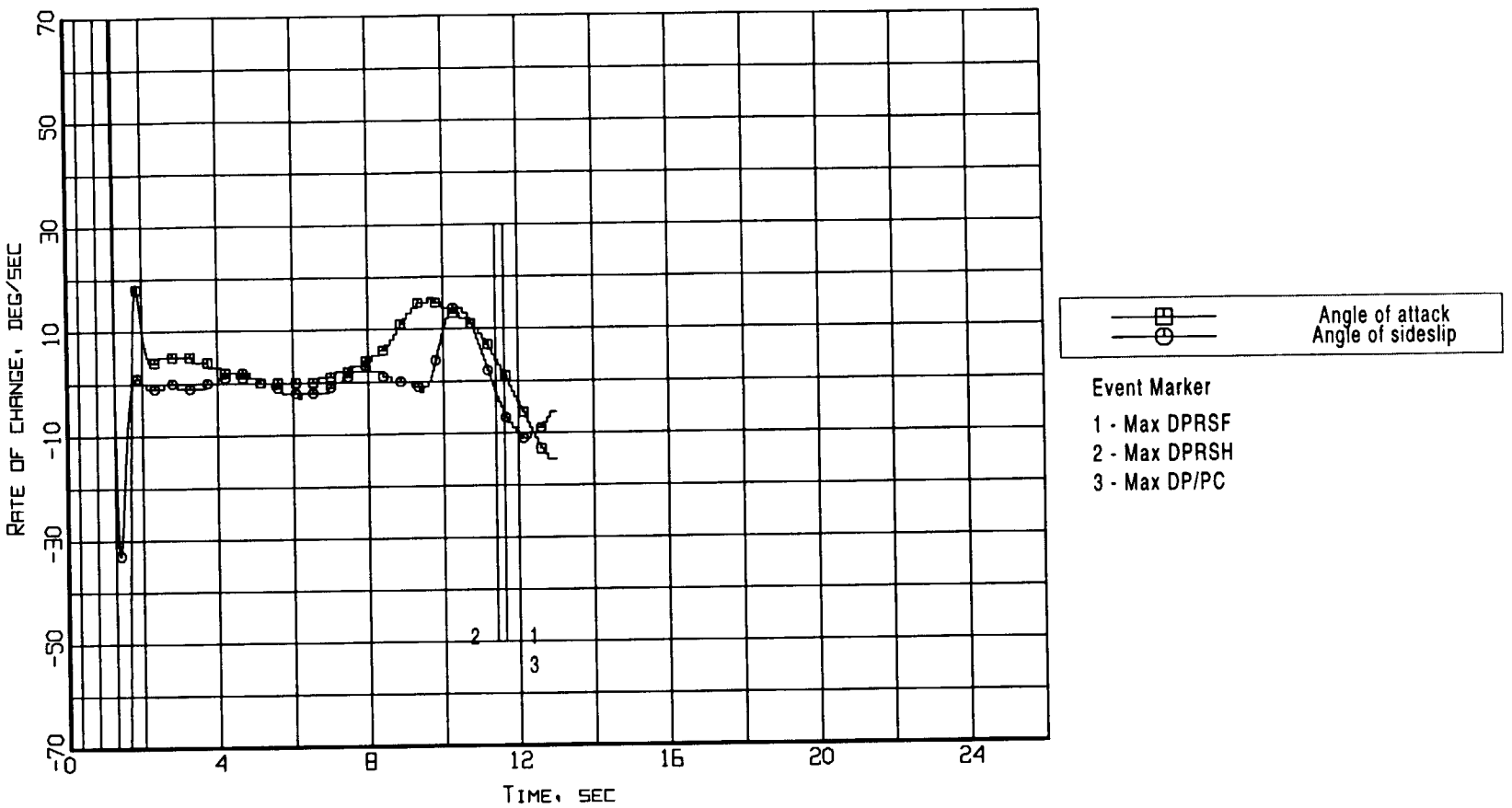

Figure B1-12. Event markers superposed on the aerodynamic flowstream descriptors rate-of-change time histories (Flight 239, Test Point 34b).

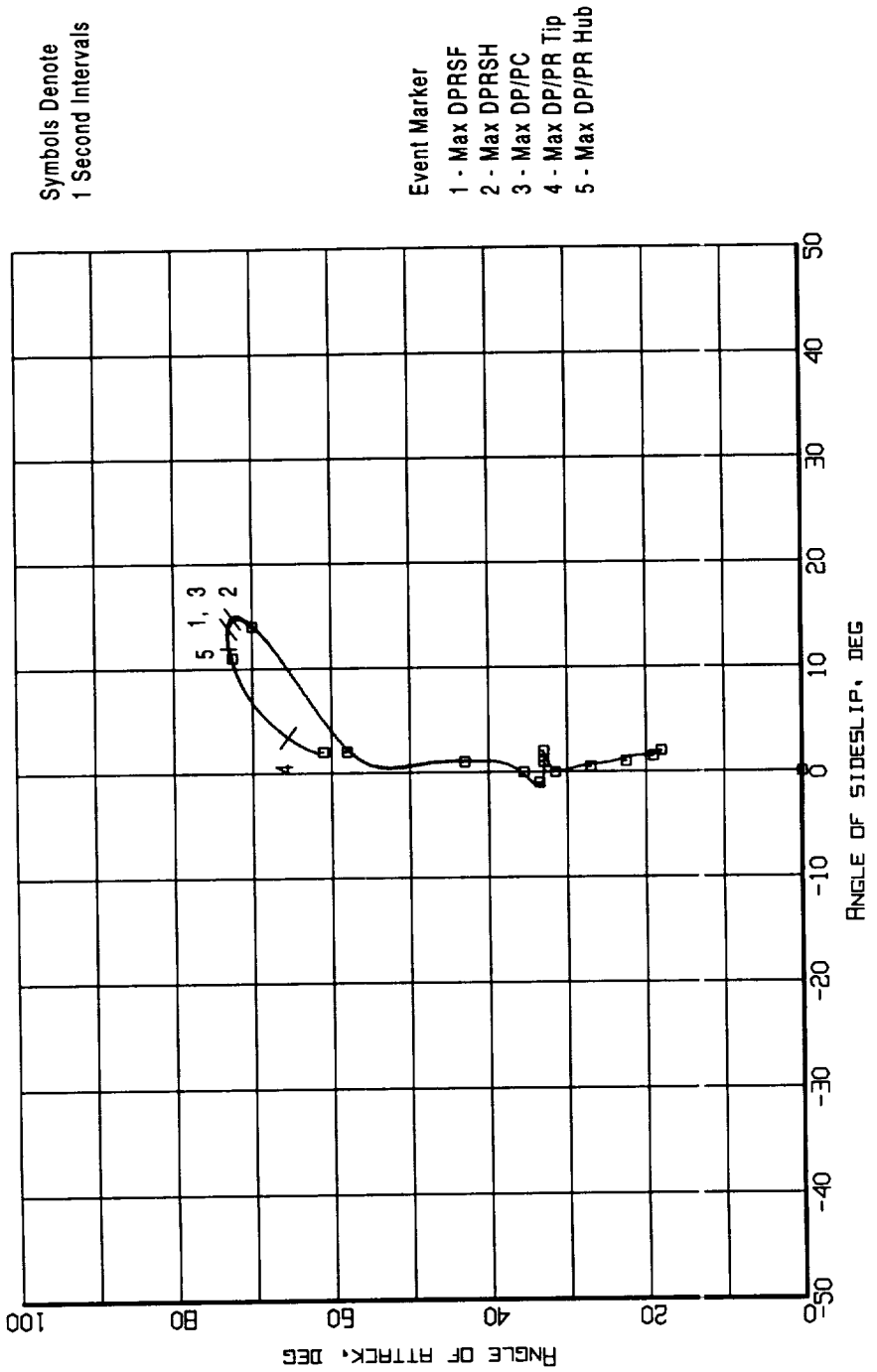

Figure B1-13. Event markers superposed on the aerodynamic flowstream descriptors trajectory (Flight 239, Test Point 34b).

Appendix B2 - Flight 238, Test Point 35b

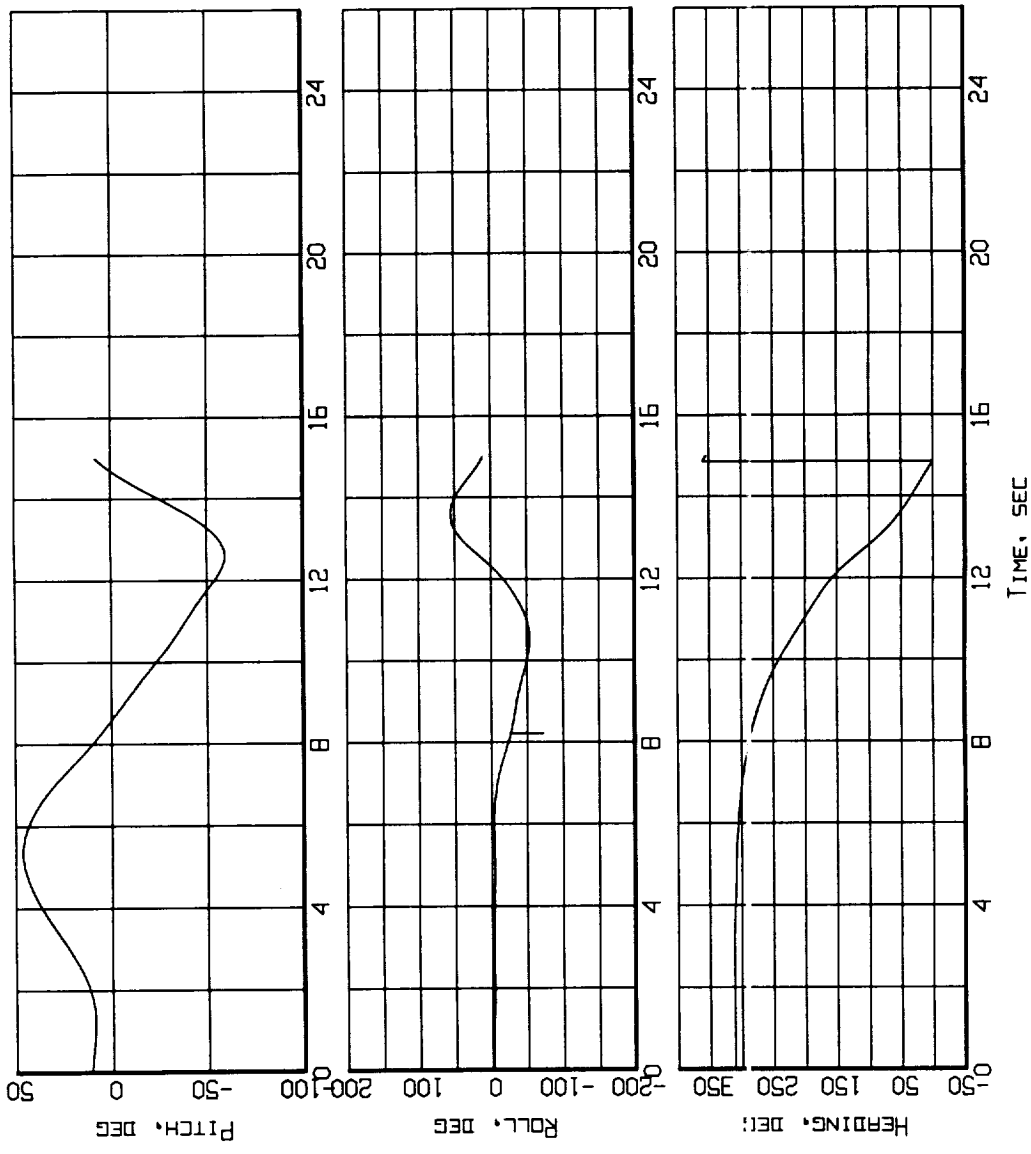

Figure B2-1. Aircraft attitude - Pitch, Roll, and Heading
(Flight 238, Test Point 35b).

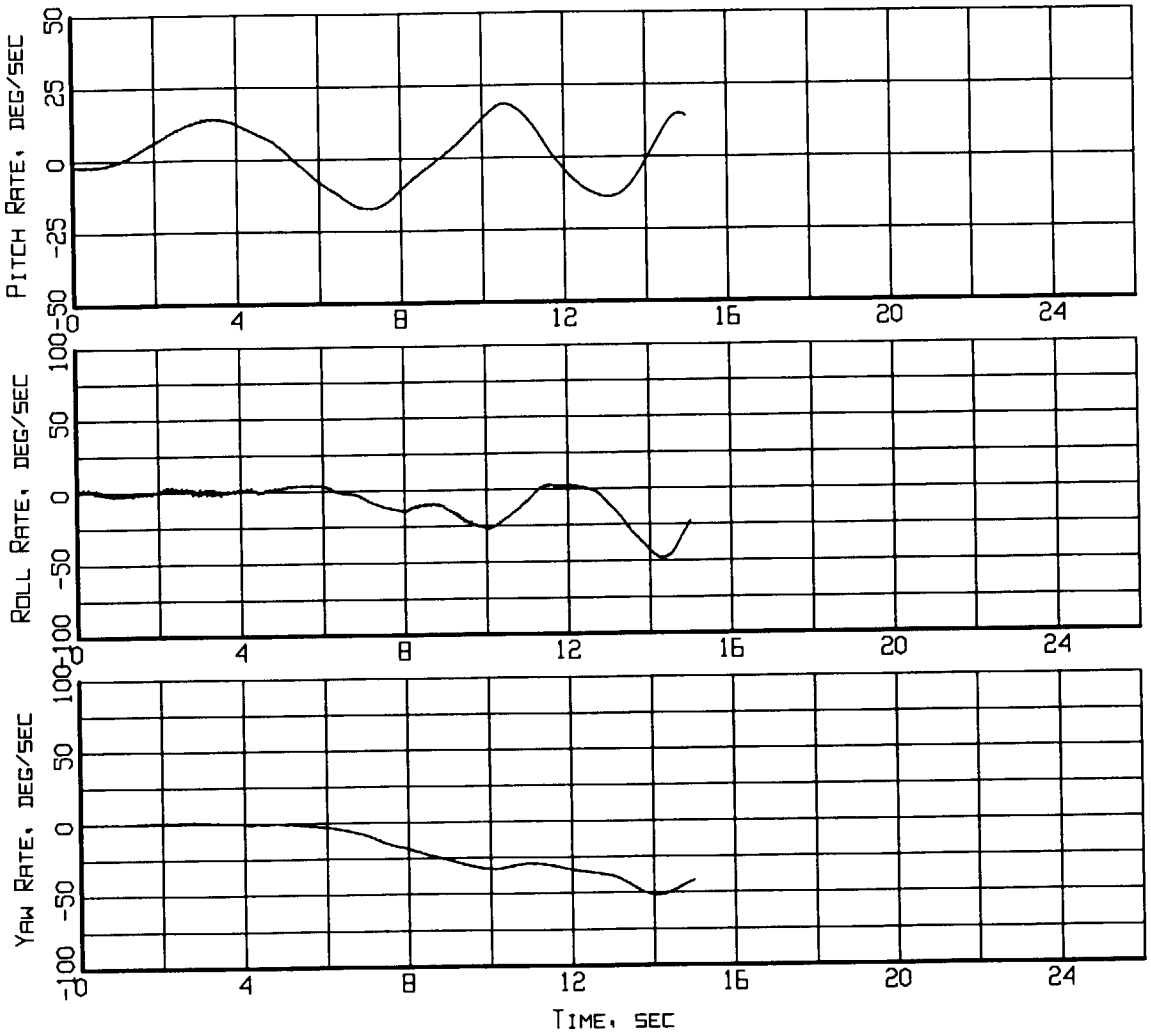

Figure B2-2. Aircraft Motion - Rate-of-Change of Pitch, Roll and Heading (Flight 238, Test Point 35b).

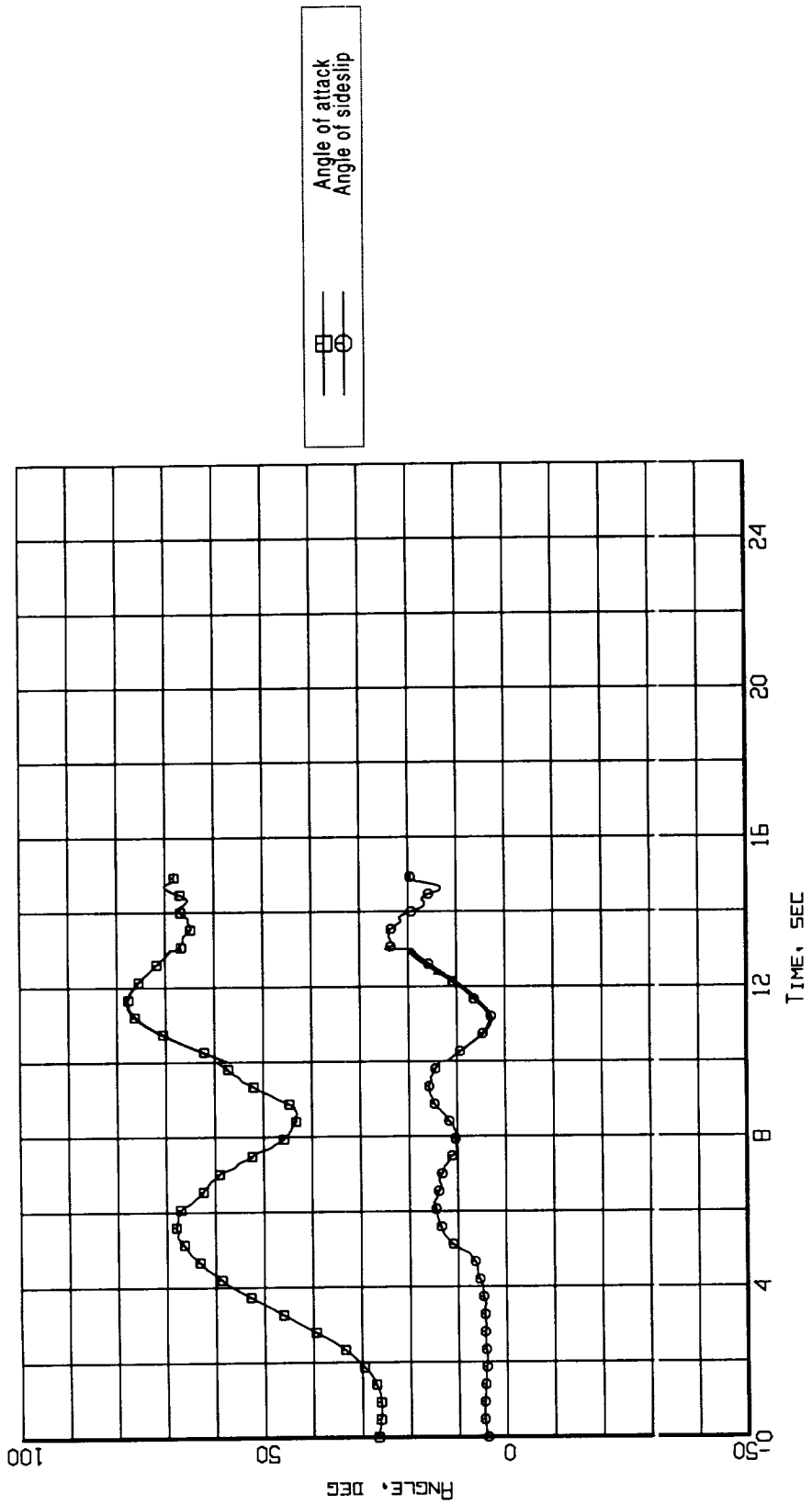

Figure B2-3. Aerodynamic flowstream descriptors - angle of attack and angle of sideslip (Flight 238, Test Point 35b).

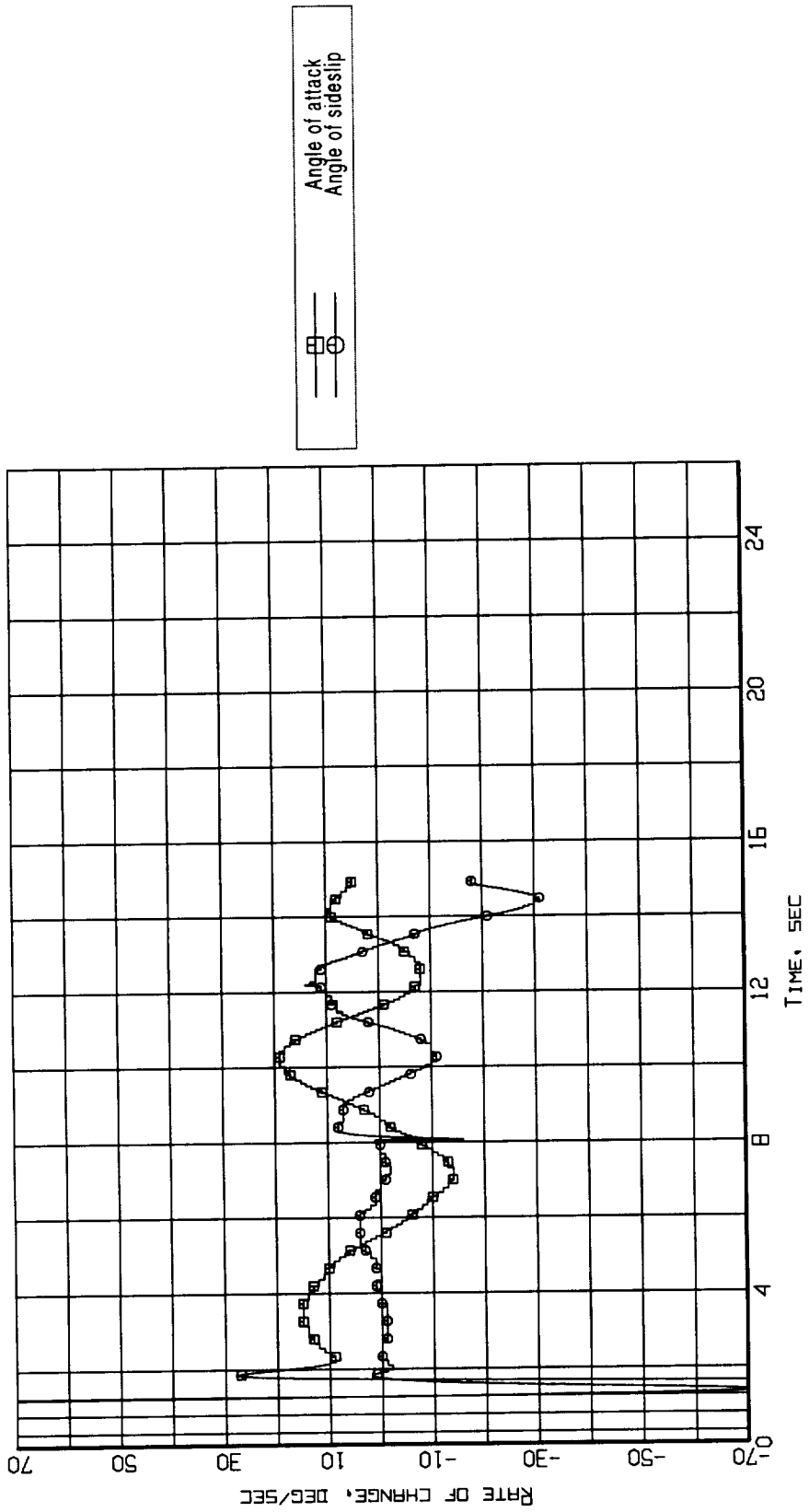

Figure B2-4. Aerodynamic flowstream descriptors - rate of change of angle of attack and angle of sideslip (Flight 238, Test Point 35b).

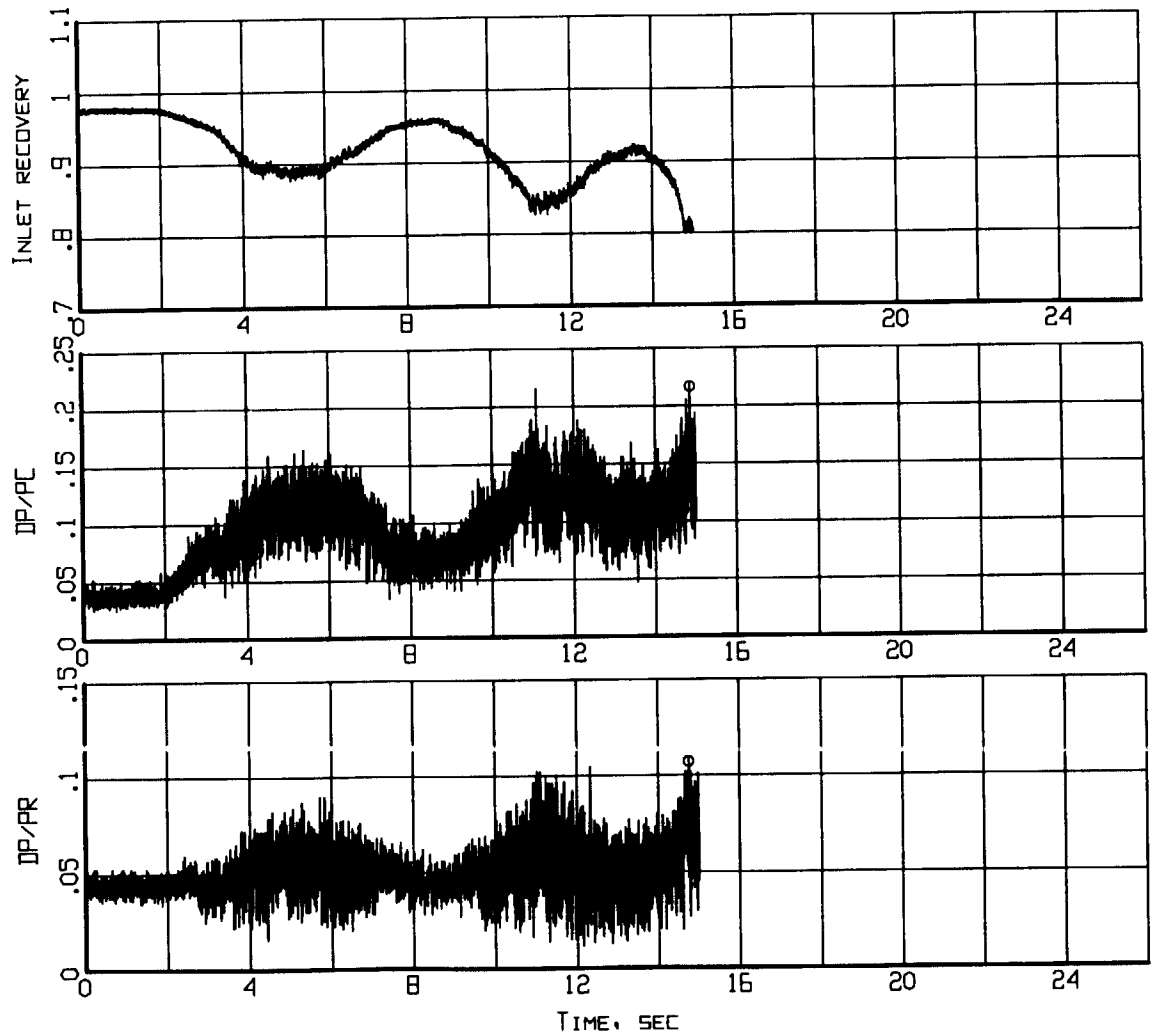

Figure B2-5. Time histories of inlet recovery and distortion descriptors (Flight 238, Test Point 35b).

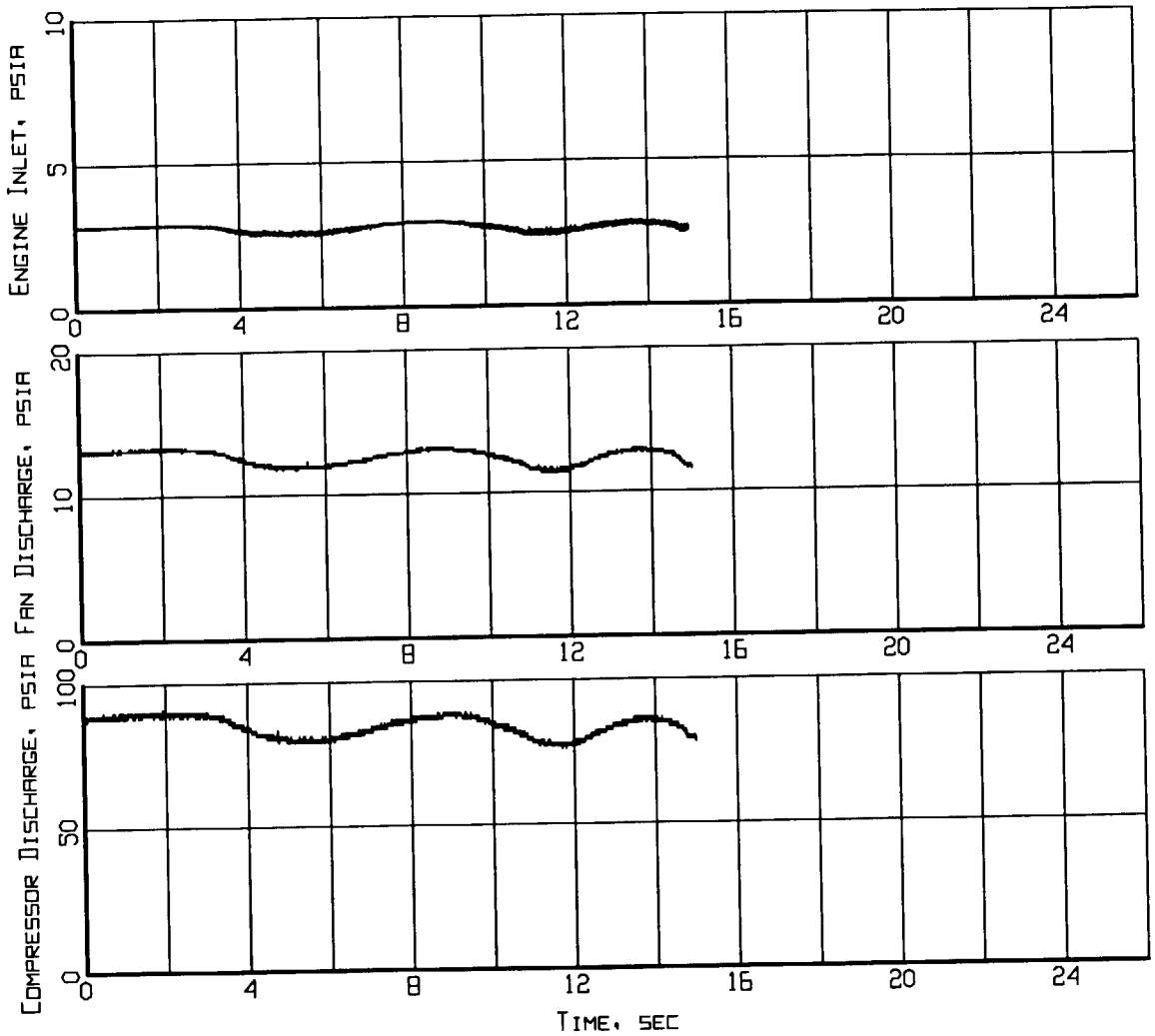

Figure B2-6. Measured inlet/engine entry and engine internal pressures time histories (Flight 238, Test Point 35b).

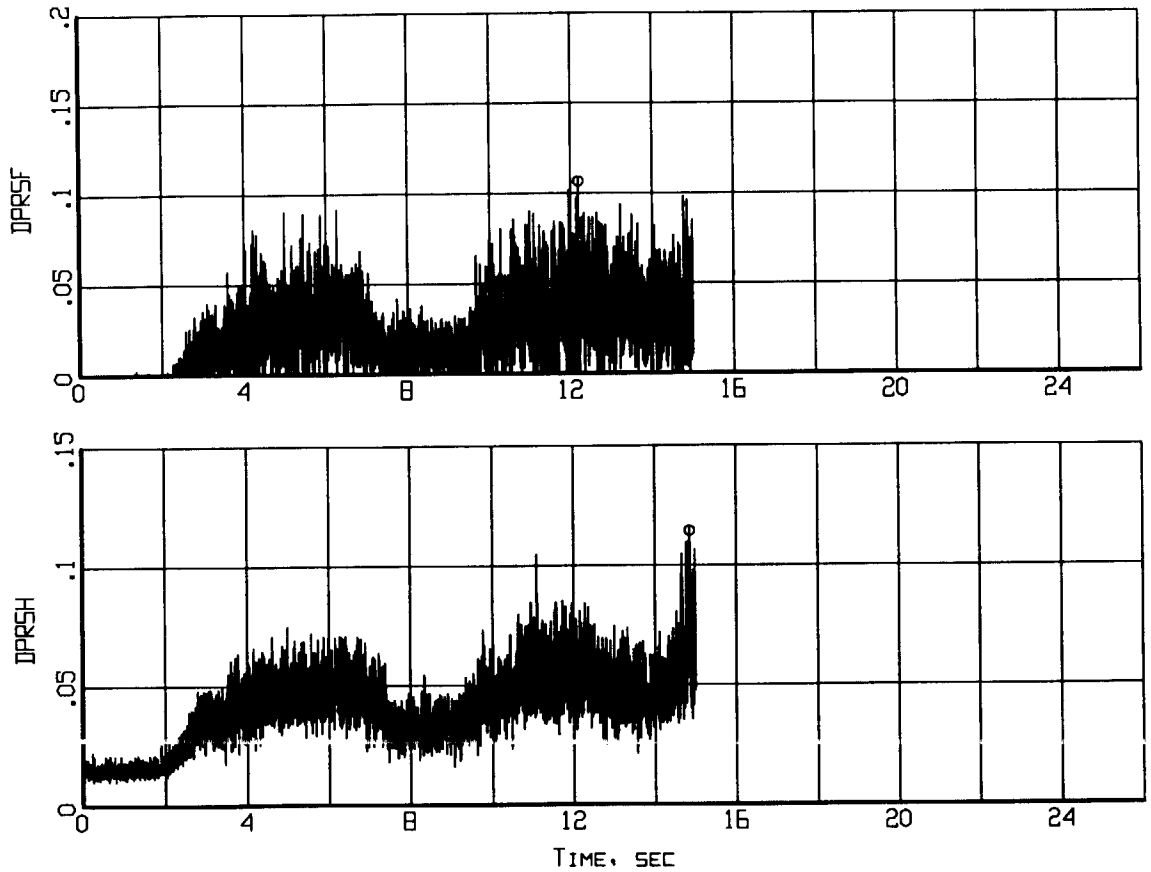

Symbols Denote
Max Points

Figure B2-7. Time histories of the predicted loss of stability pressure ratio for the fan and the compressor (Flight 238, Test Point 35b).

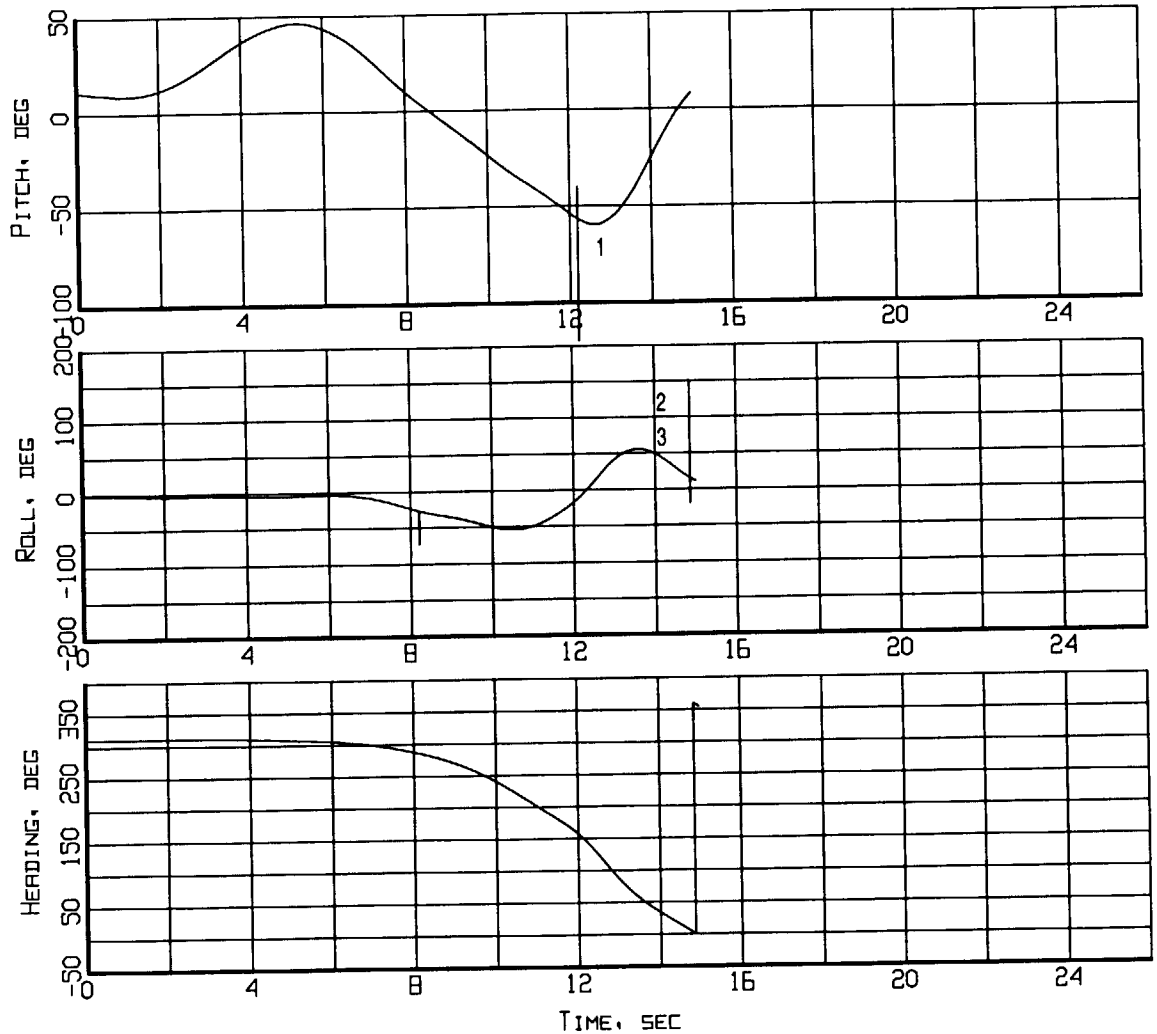

Event Marker

1 - Max DPRSF

2 - Max DPRSH

3 - Max DP/PC

Figure B2-8. Event markers superposed on the aircraft attitude time histories (Flight 238, Test Point 35b).

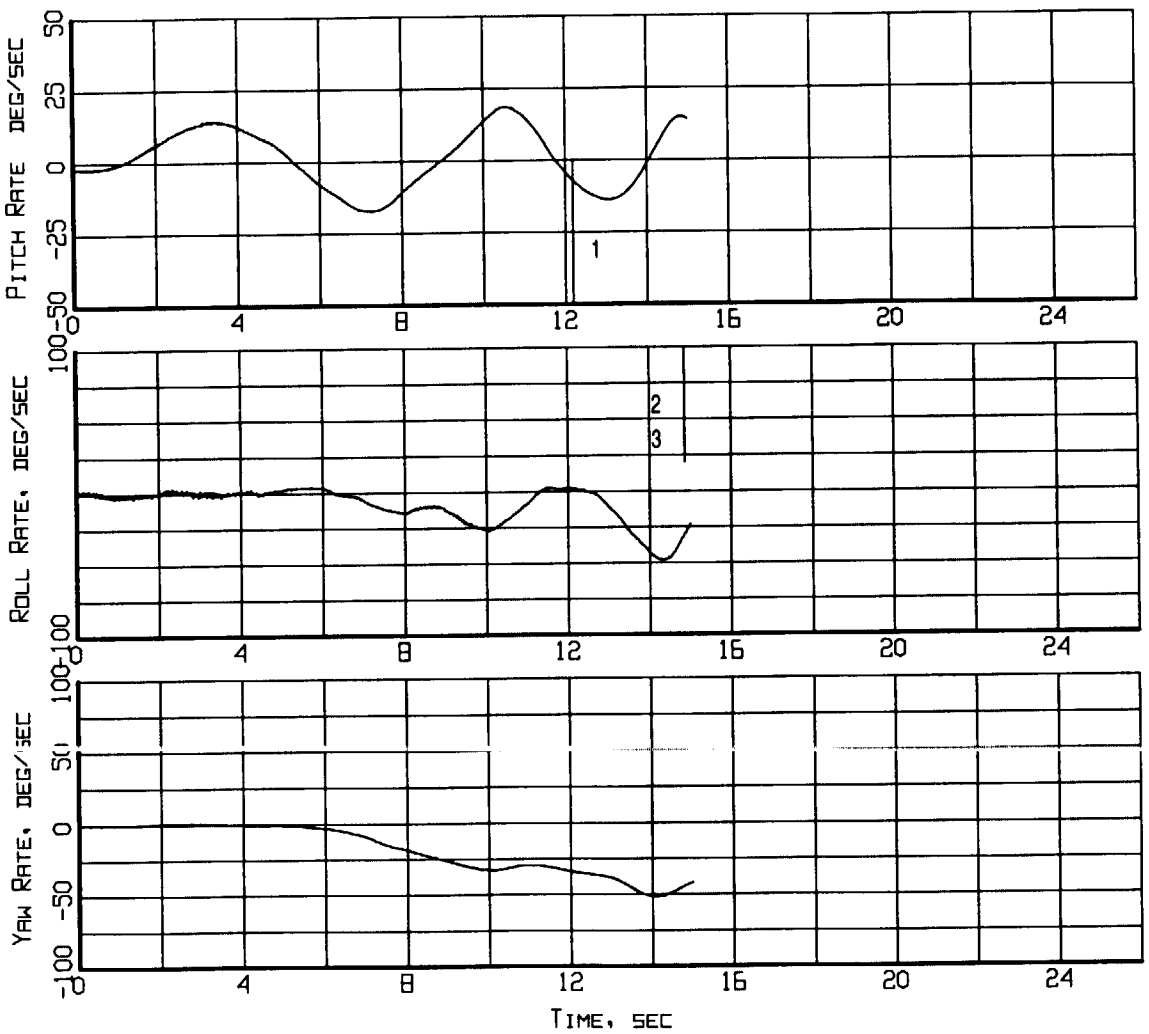

Event Marker

1 - Max DPRSF

2 - Max DPRSH

3 - Max DP/PC

Figure B2-9. Event markers superposed on the aircraft motion time histories (Flight 238, Test Point 35b).

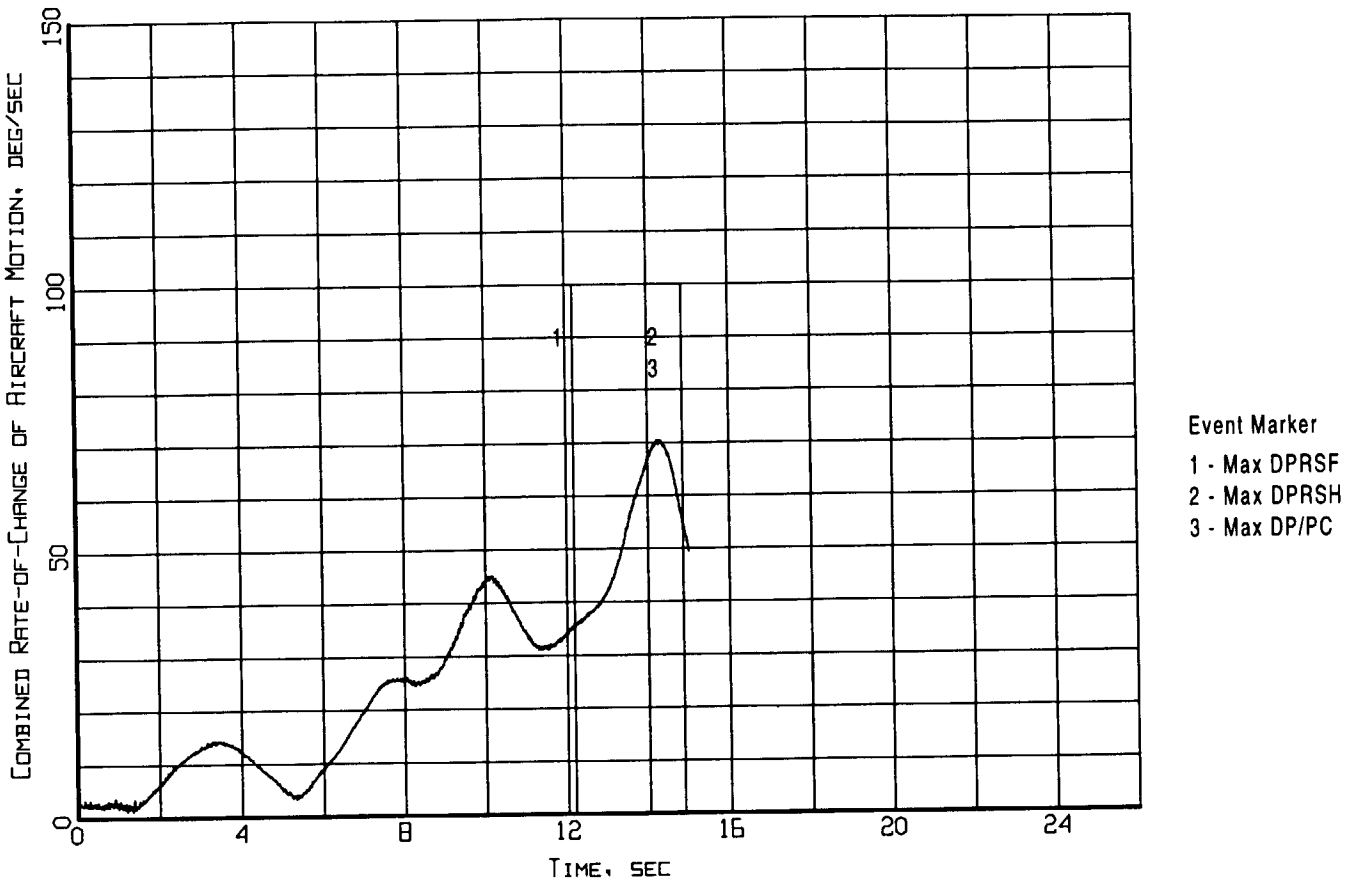

Figure B2-10. Event markers superposed on the combined of rate-of-change of aircraft motion time history (Flight 238, Test Point 35b).

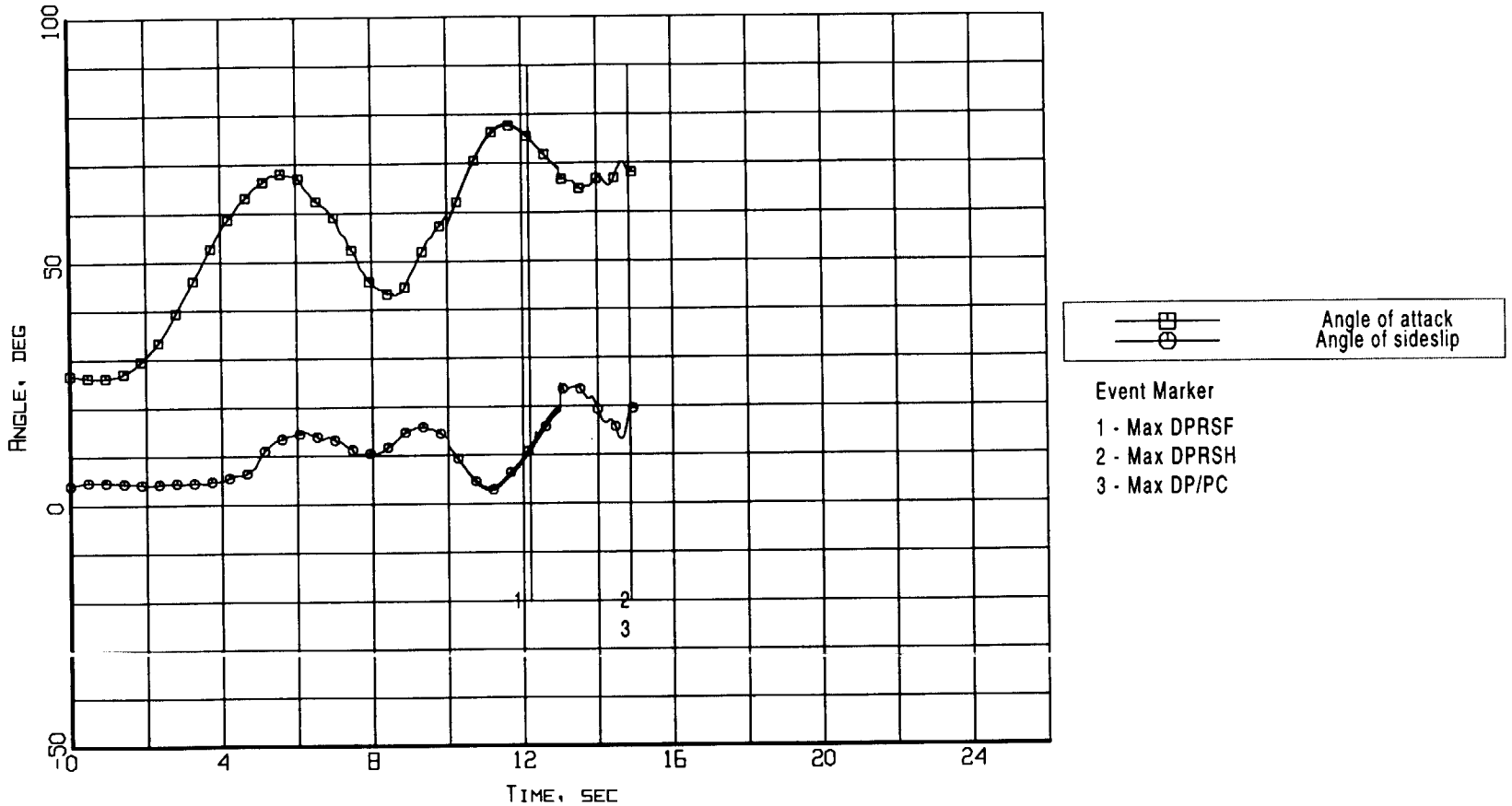

Figure B2-11. Event markers superposed on the aerodynamic flowstream descriptor time histories (Flight 238, Test Point 35b).

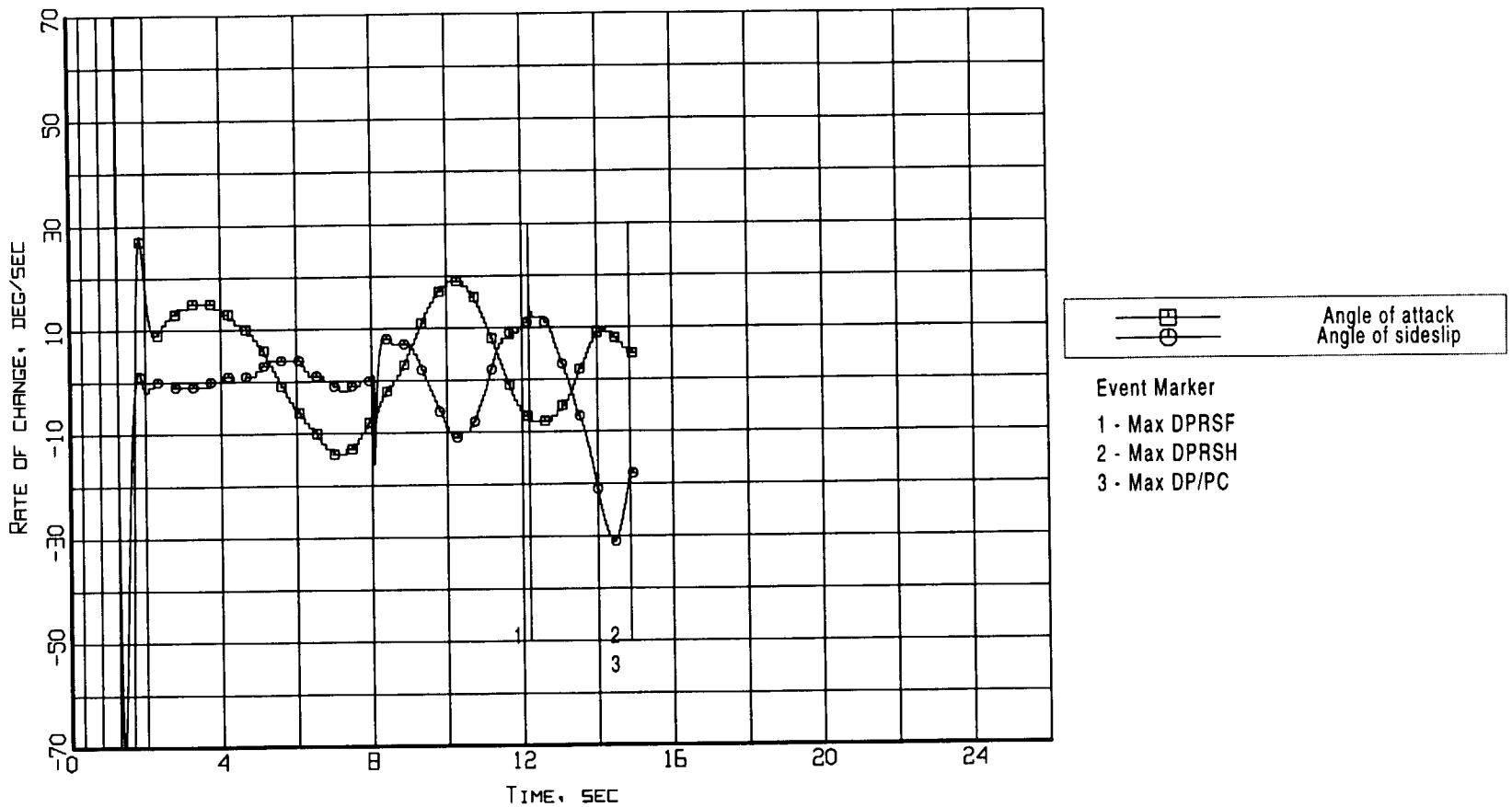

Figure B2-12. Event markers superposed on the aerodynamic flowstream descriptors rate-of-change time histories (Flight 238, Test Point 35b).

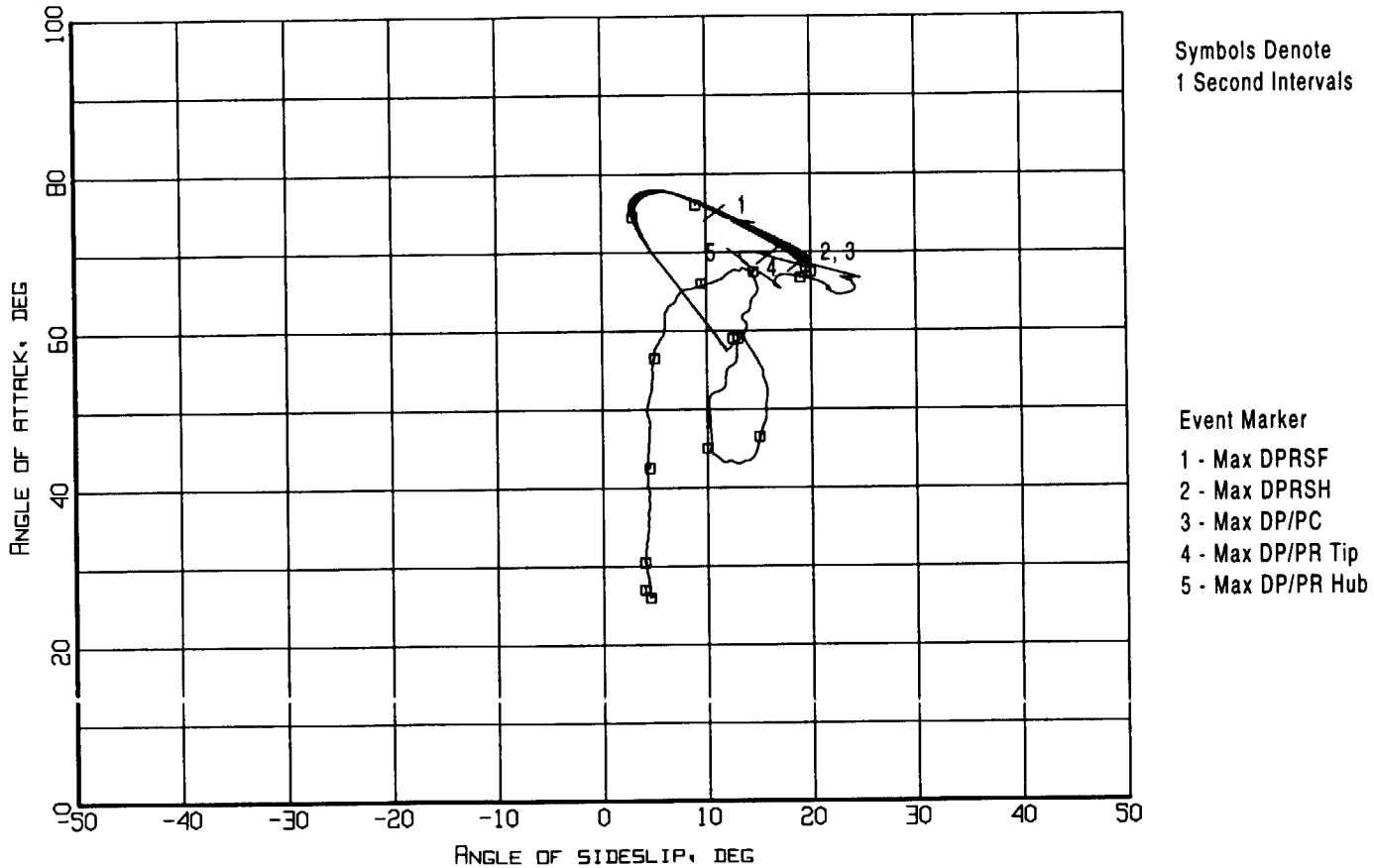

Figure B2-13. Event markers superposed on the aerodynamic flowstream descriptors trajectory (Flight 238, Test Point 35b).

Appendix B3 - Flight 238, Test Point 36b

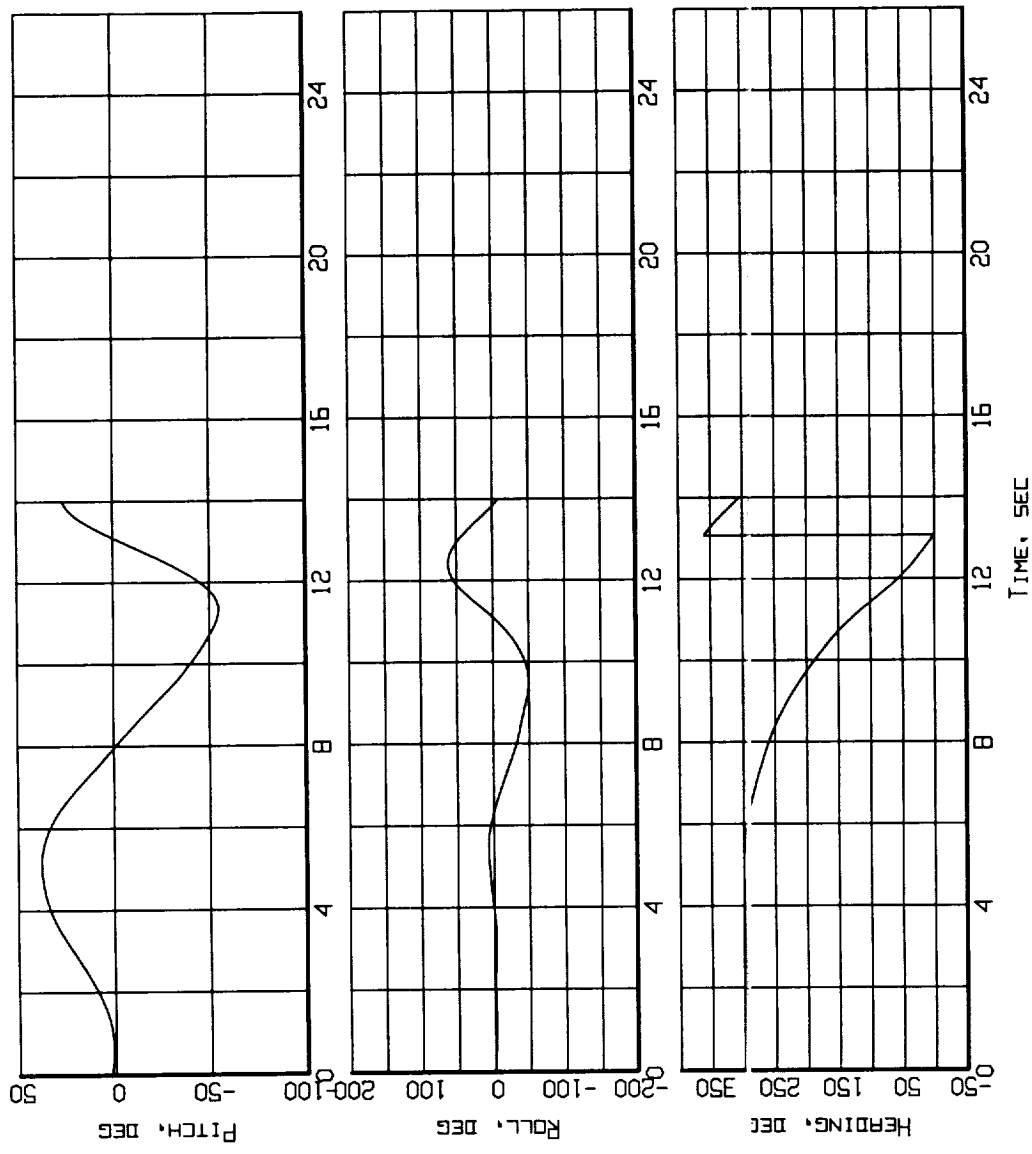

Figure B3-1. Aircraft attitude - Pitch, Roll, and Heading
(Flight 238, Test Point 36b).

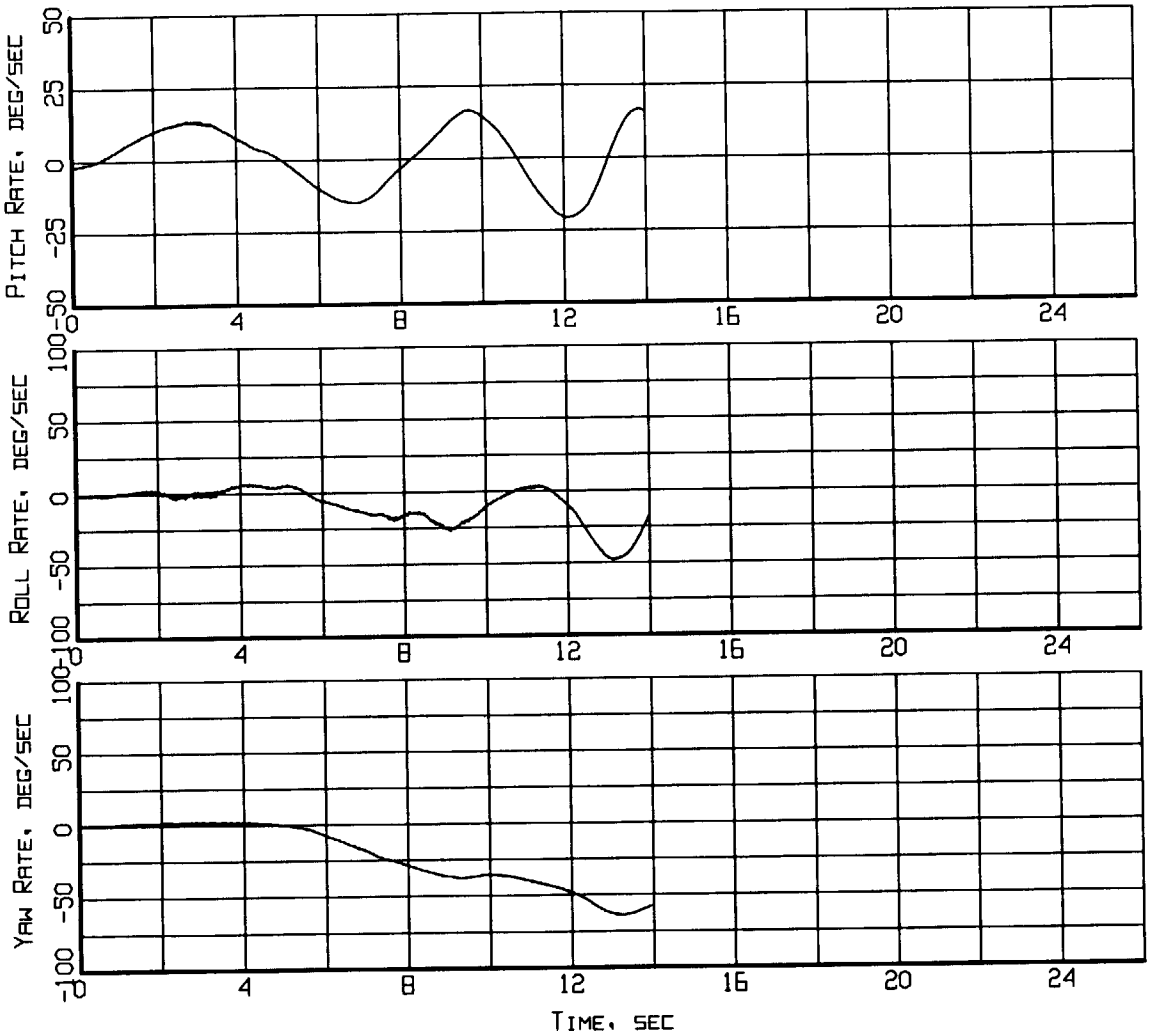

Figure B3-2. Aircraft Motion - Rate-of-Change of Pitch, Roll and Heading (Flight 238, Test Point 36b).

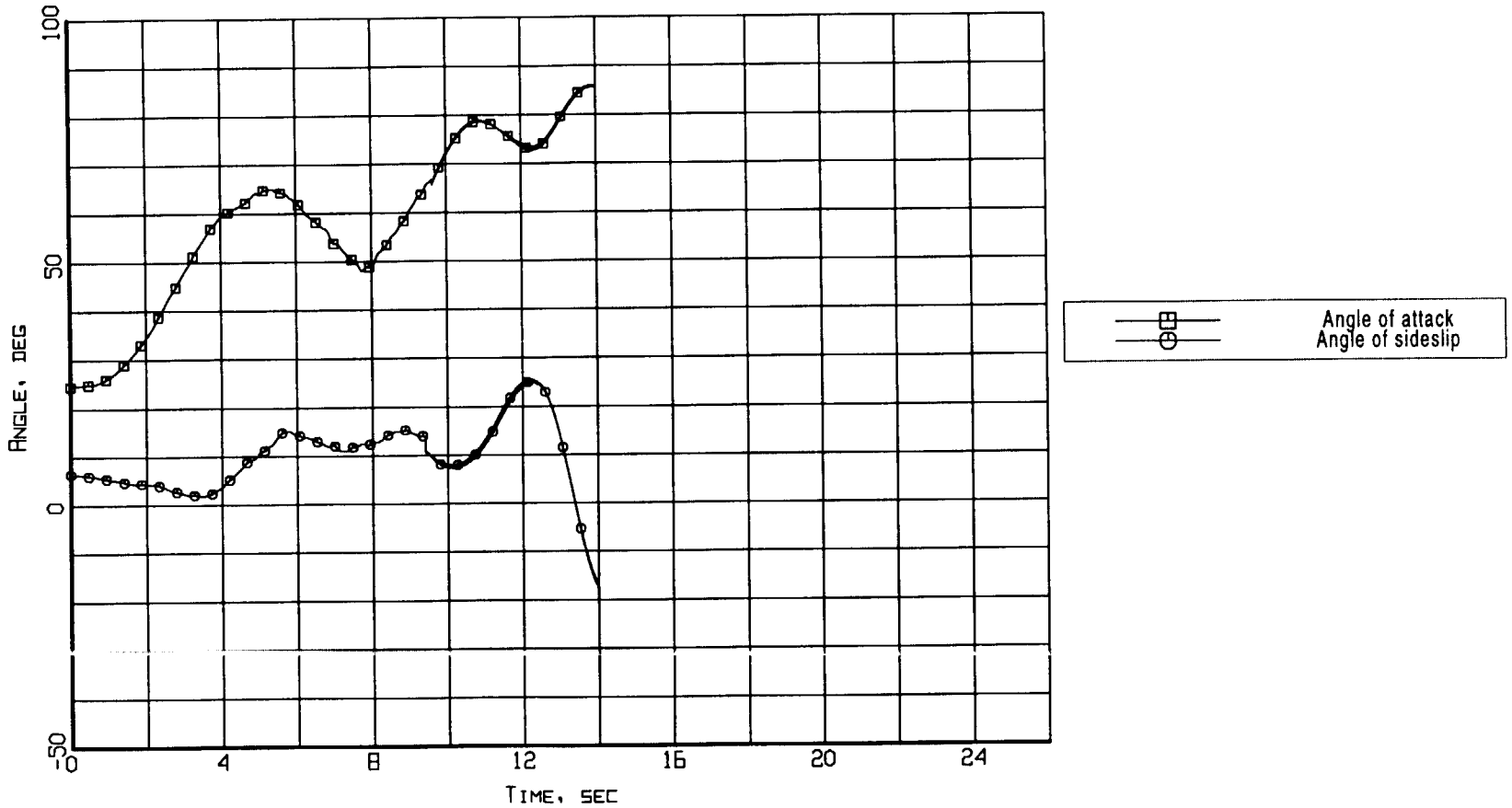

Figure B3-3. Aerodynamic flowstream descriptors - angle of attack and angle of sideslip (Flight 238, Test Point 36b).

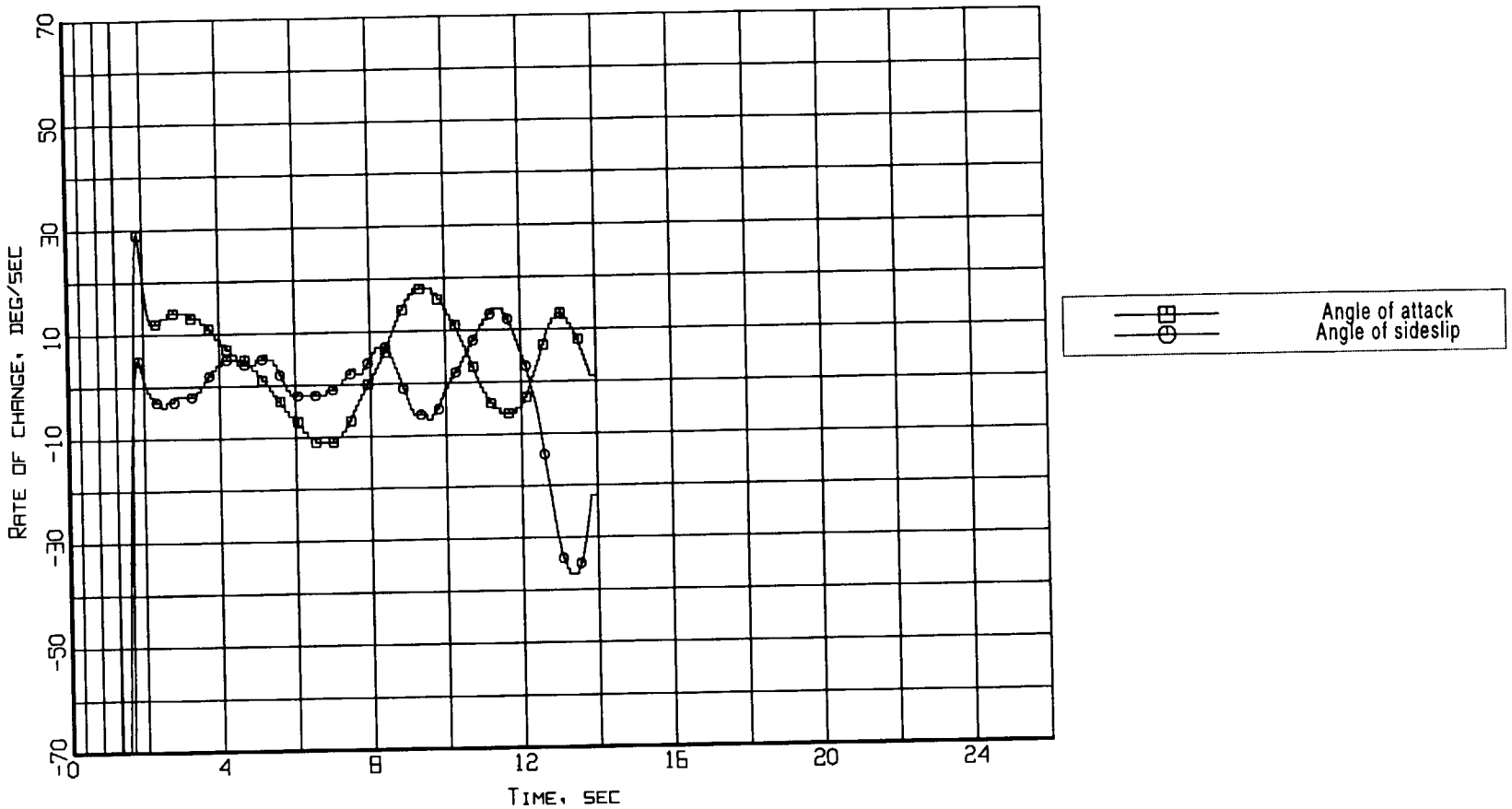

Figure B3-4. Aerodynamic flowstream descriptors - rate of change of angle of attack and angle of sideslip (Flight 238, Test Point 36b).

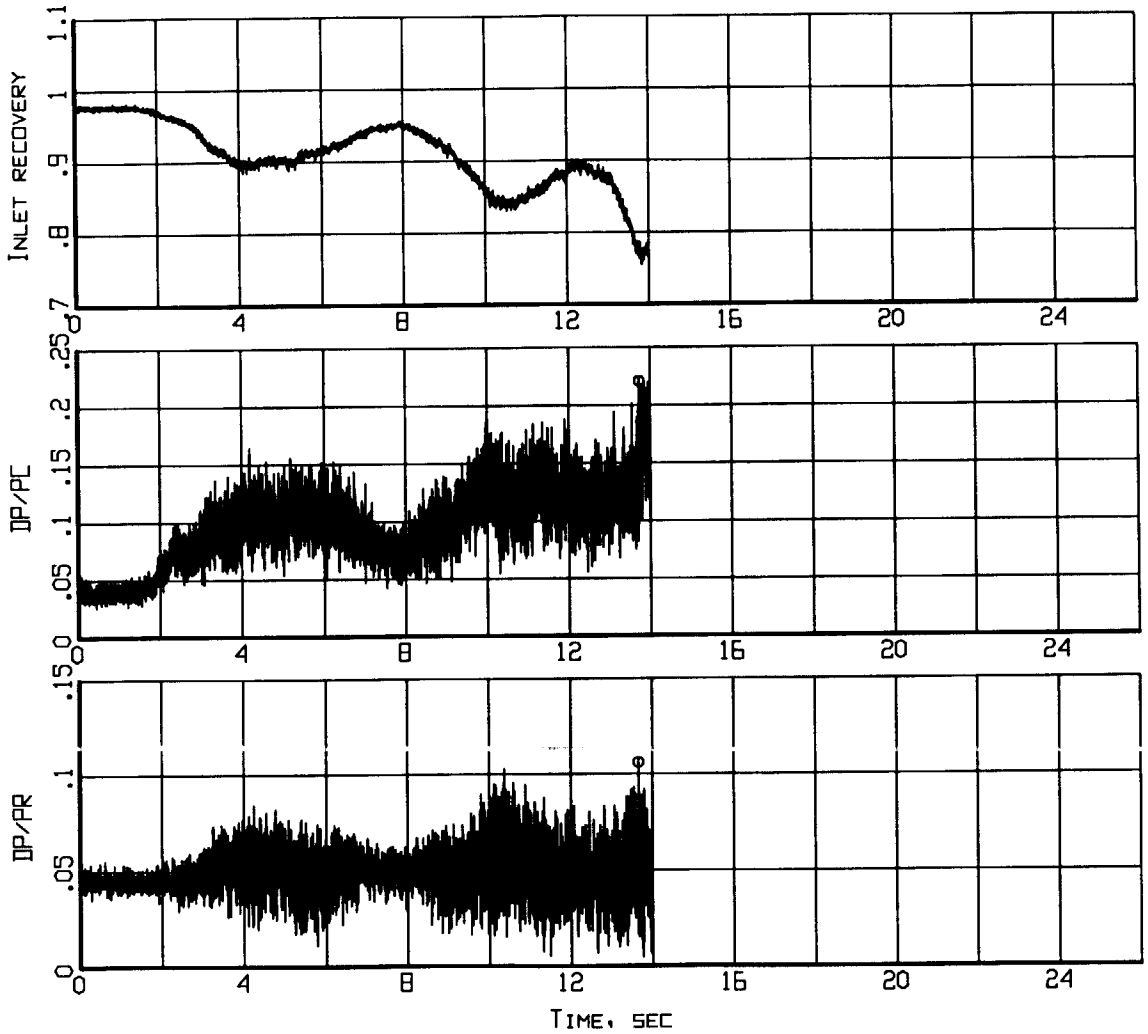

Figure B3-5. Time histories of inlet recovery and distortion descriptors (Flight 238, Test Point 36b).

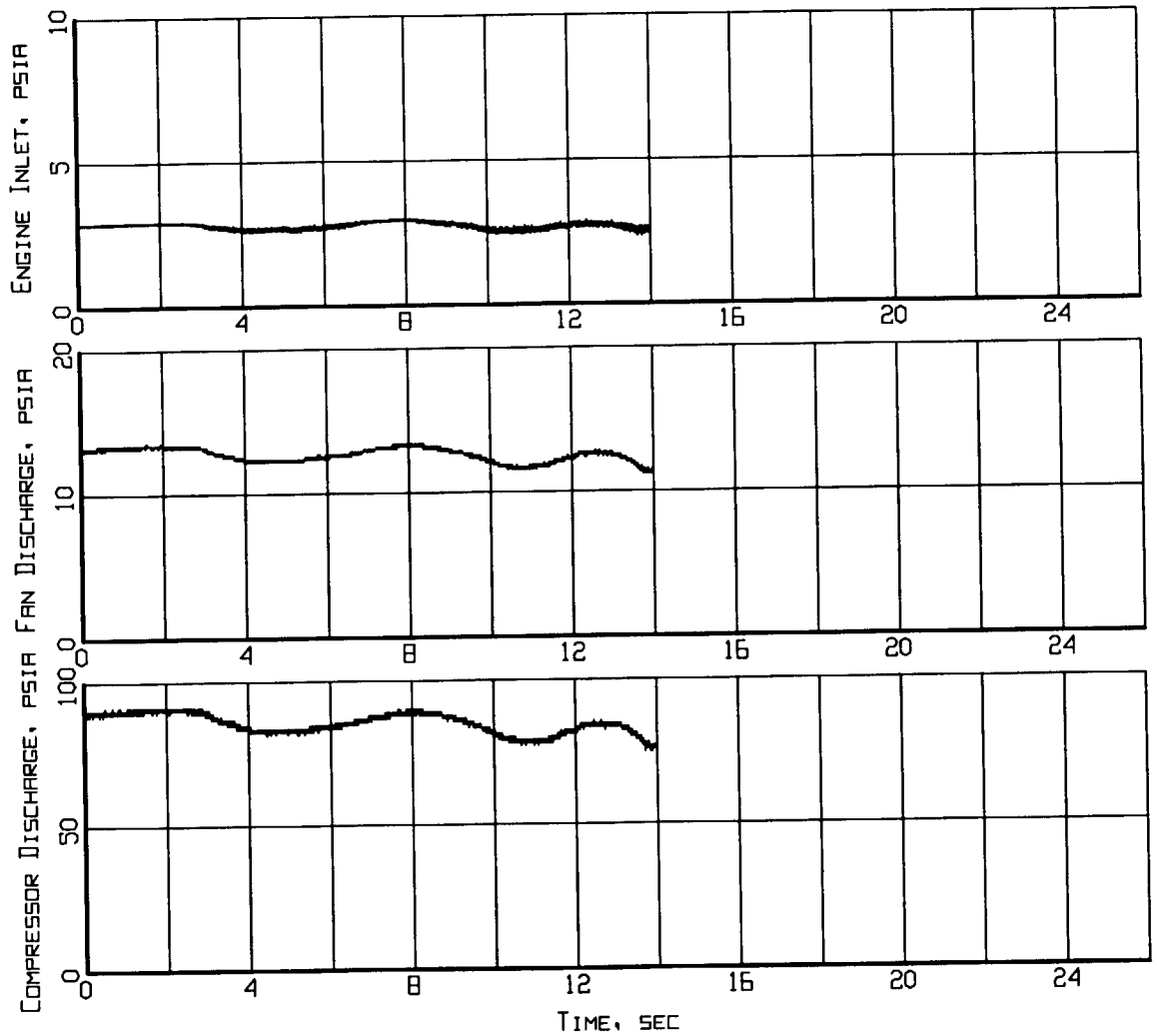

Figure B3-6. Measured inlet/engine entry and engine internal pressures time histories (Flight 238, Test Point 36b).

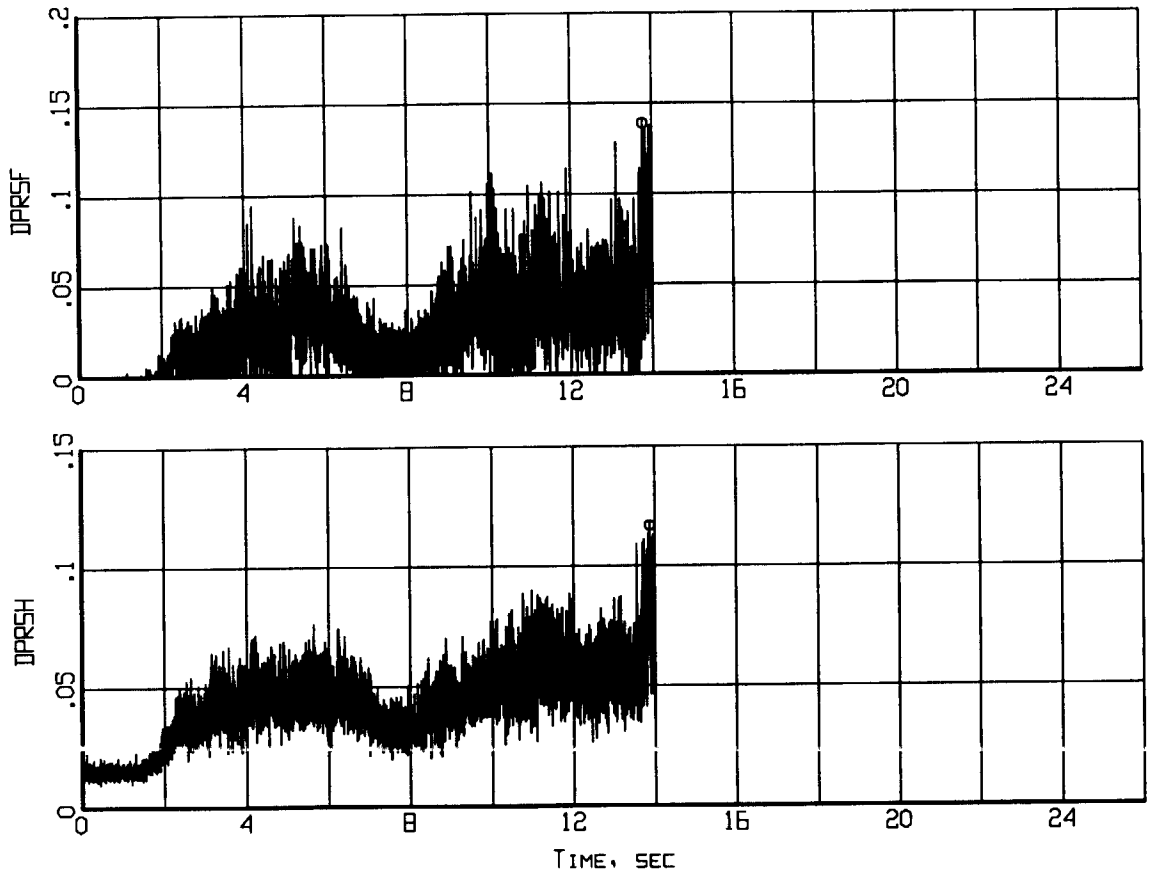

Figure B3-7. Time histories of the predicted loss of stability pressure ratio for the fan and the compressor (Flight 238, Test Point 36b).

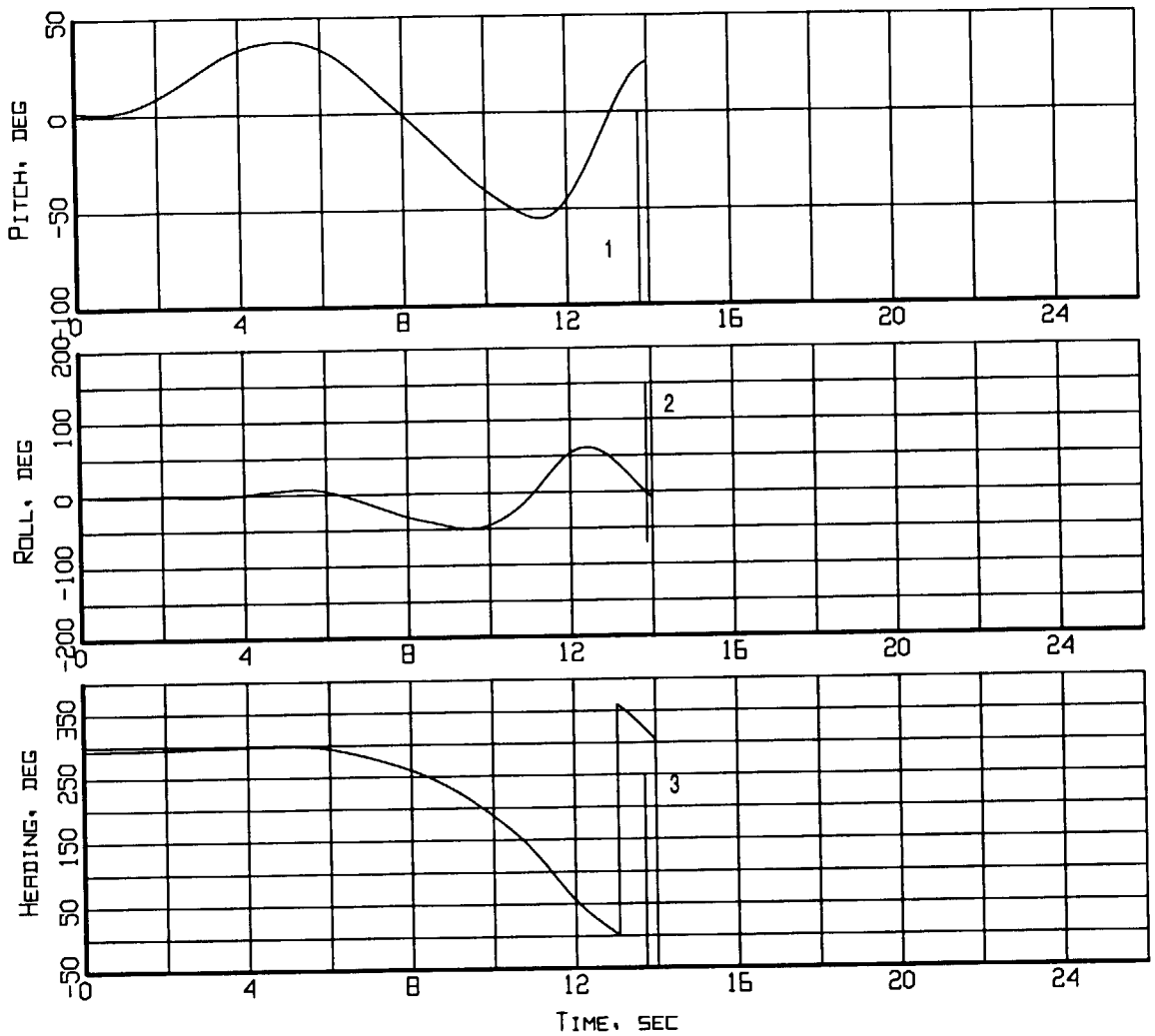

Event Marker

1 - Max DPRSF
2 - Max DPRSH
3 - Max DP/PC

Figure B3-8. Event markers superposed on the aircraft attitude time histories (Flight 238, Test Point 36b).

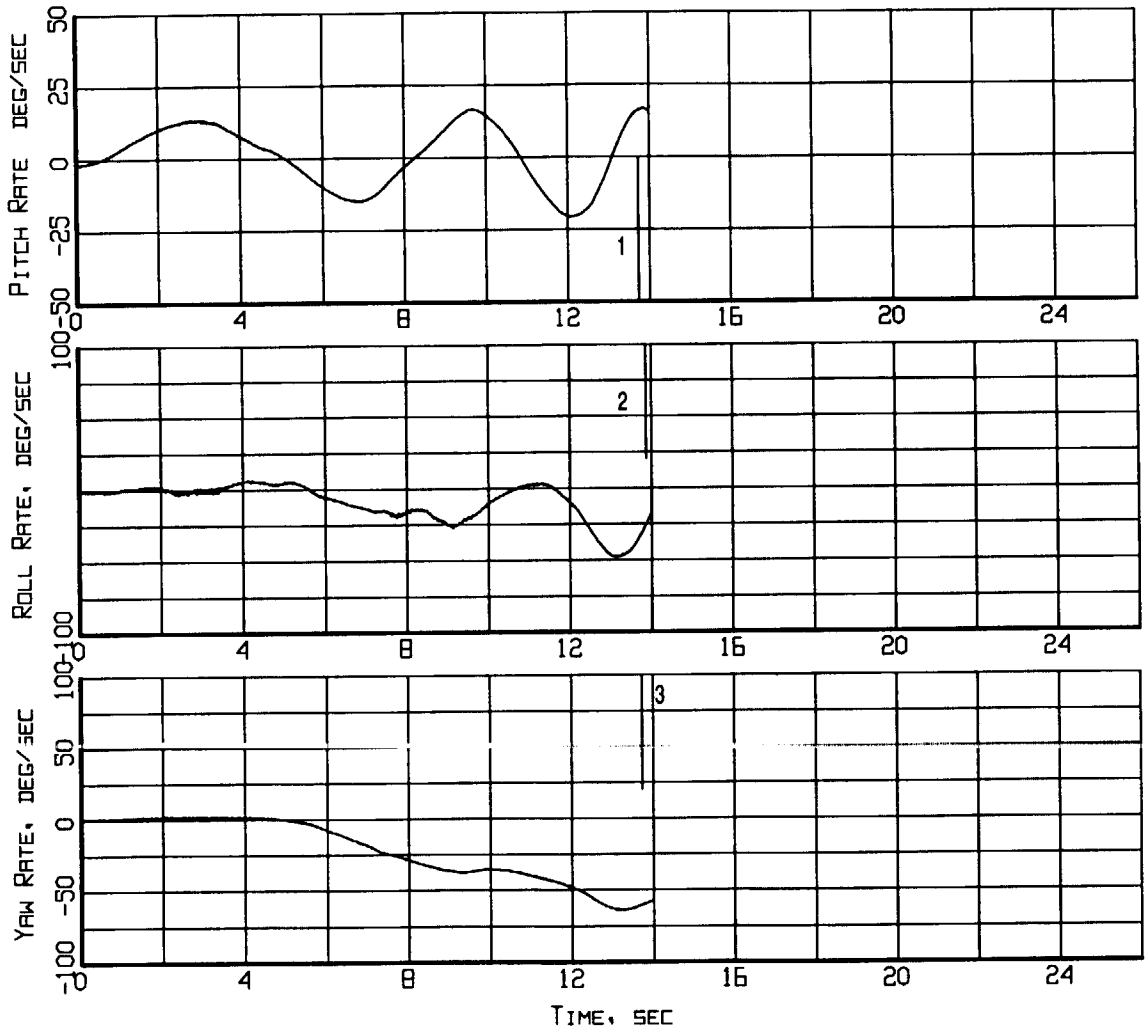

Event Marker

1 - Max DPRSF

2 - Max DPRSH

3 - Max DP/PC

Figure B3-9. Event markers superposed on the aircraft motion time histories (Flight 238, Test Point 36b).

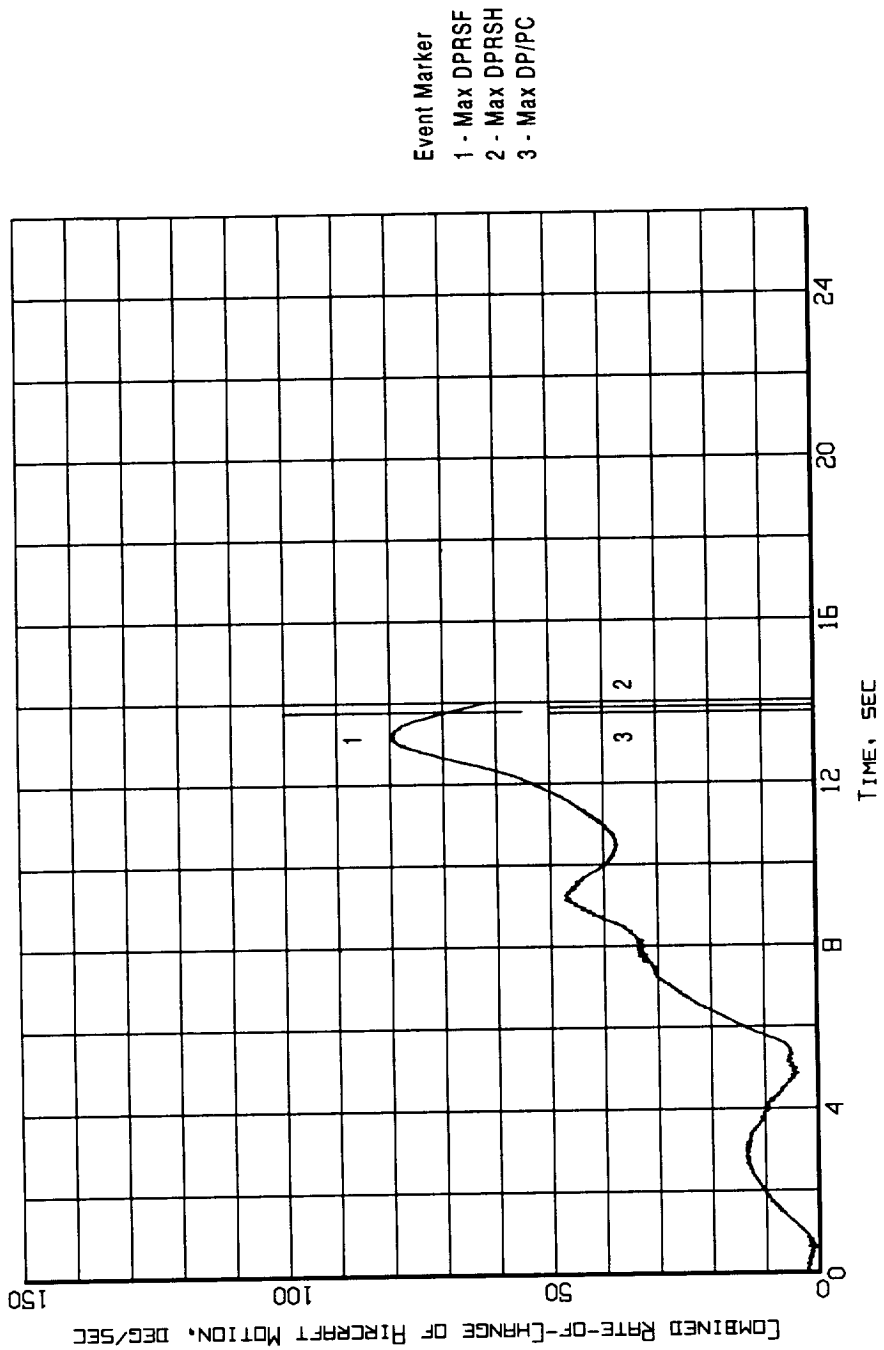

Figure B3-10. Event markers superposed on the combined of rate-of-change of aircraft motion time history (Flight 238, Test Point 36b).

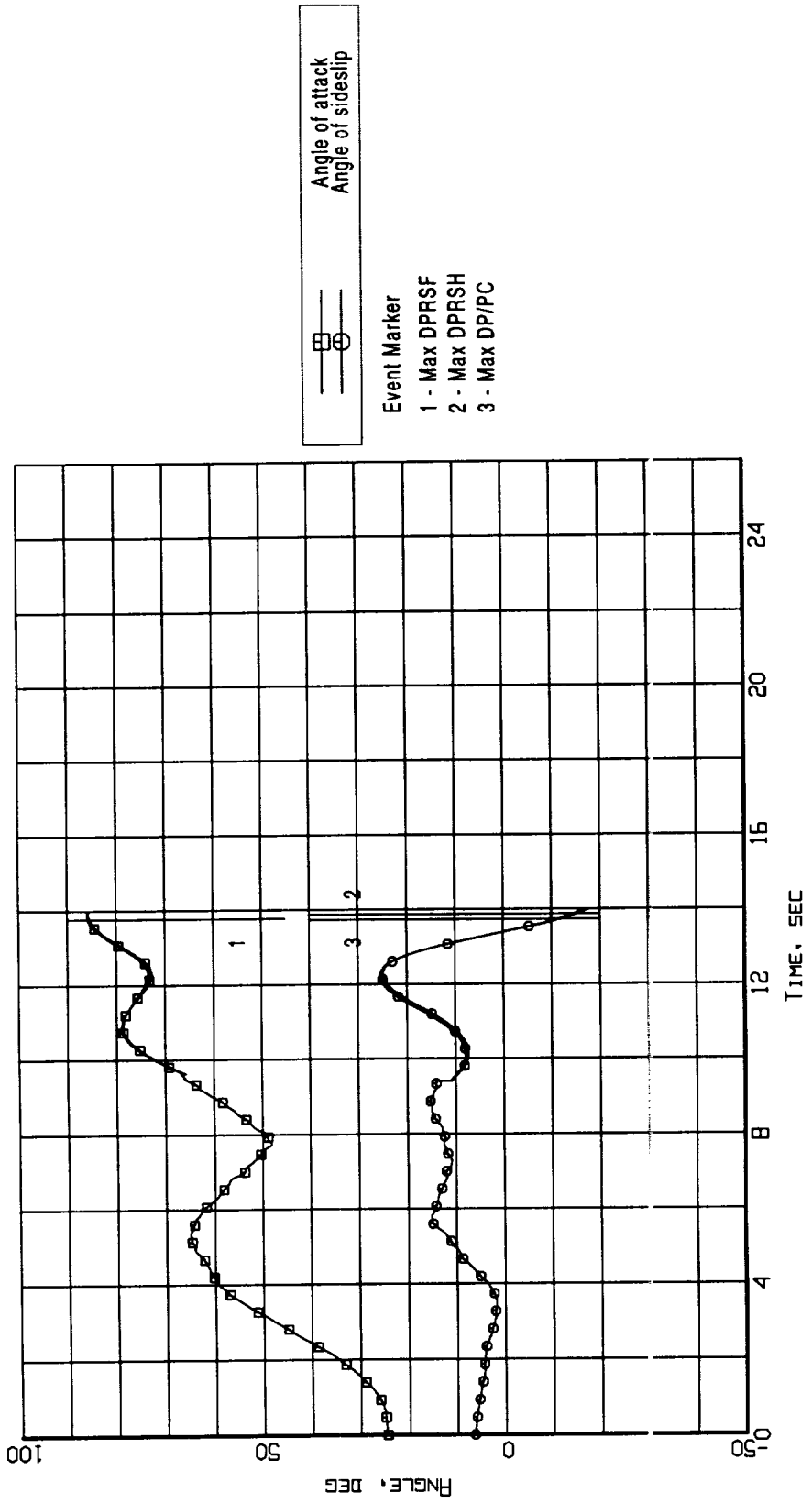

Figure B3-11. Event markers superposed on the aerodynamic flowstream descriptor time histories (Flight 238, Test Point 36b).

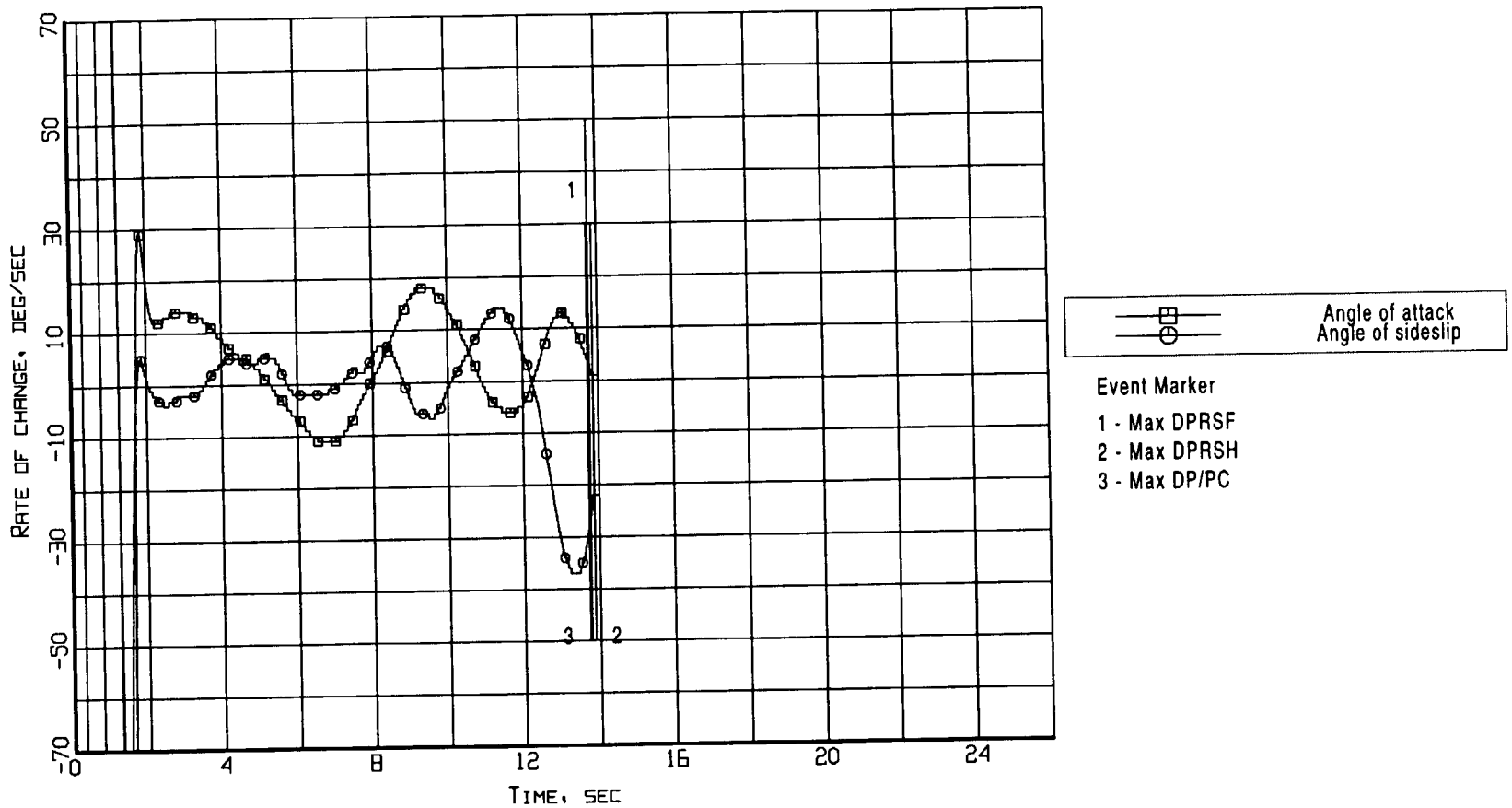

Figure B3-12. Event markers superposed on the aerodynamic flowstream descriptors rate-of-change time histories (Flight 238, Test Point 36b).

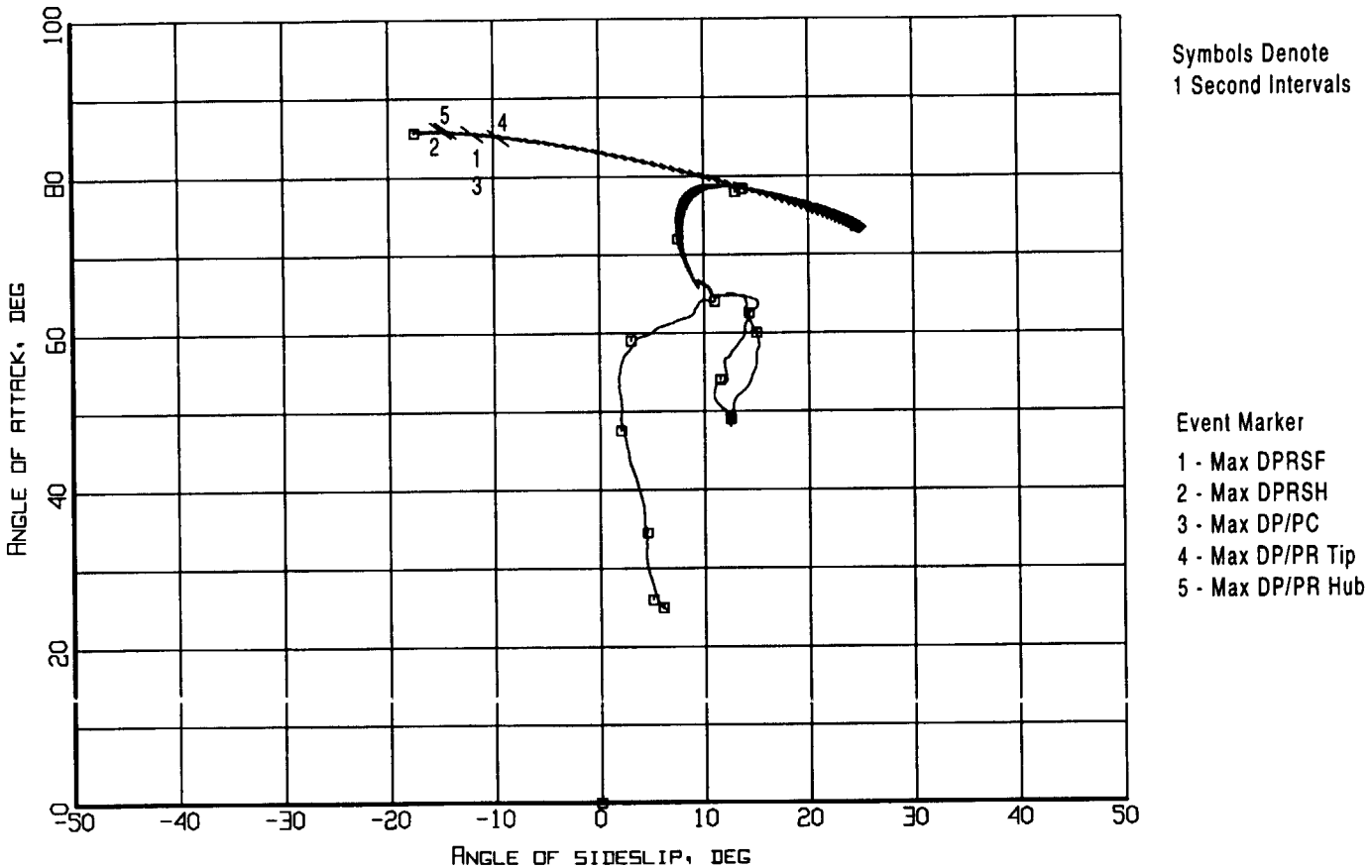

Figure B3-13. Event markers superposed on the aerodynamic flowstream descriptors trajectory (Flight 238, Test Point 36b).

Appendix B4 - Flight 239, Test Point 37b

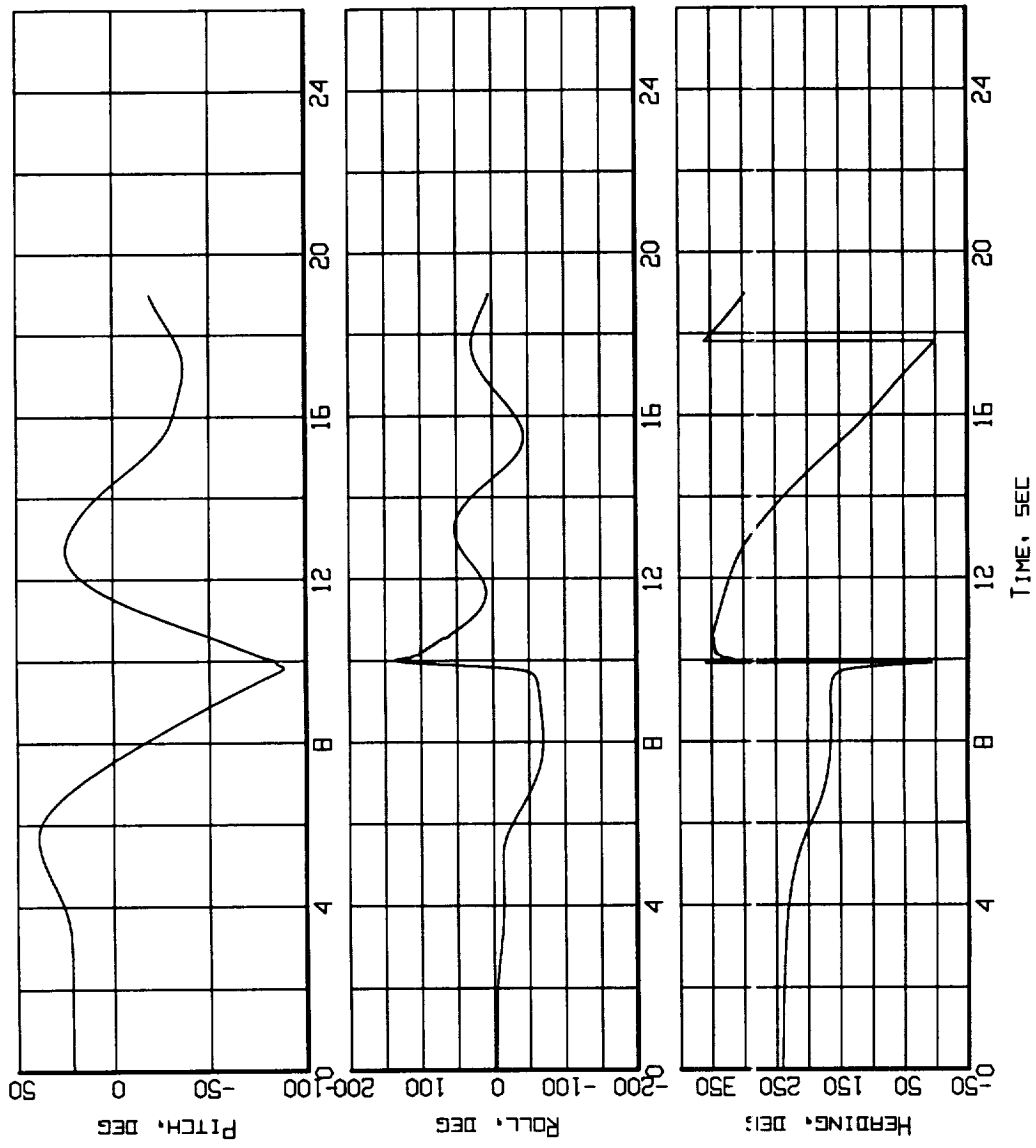

Figure B4-1. Aircraft attitude - Pitch, Roll, and Heading (Flight 239, Test Point 37b).

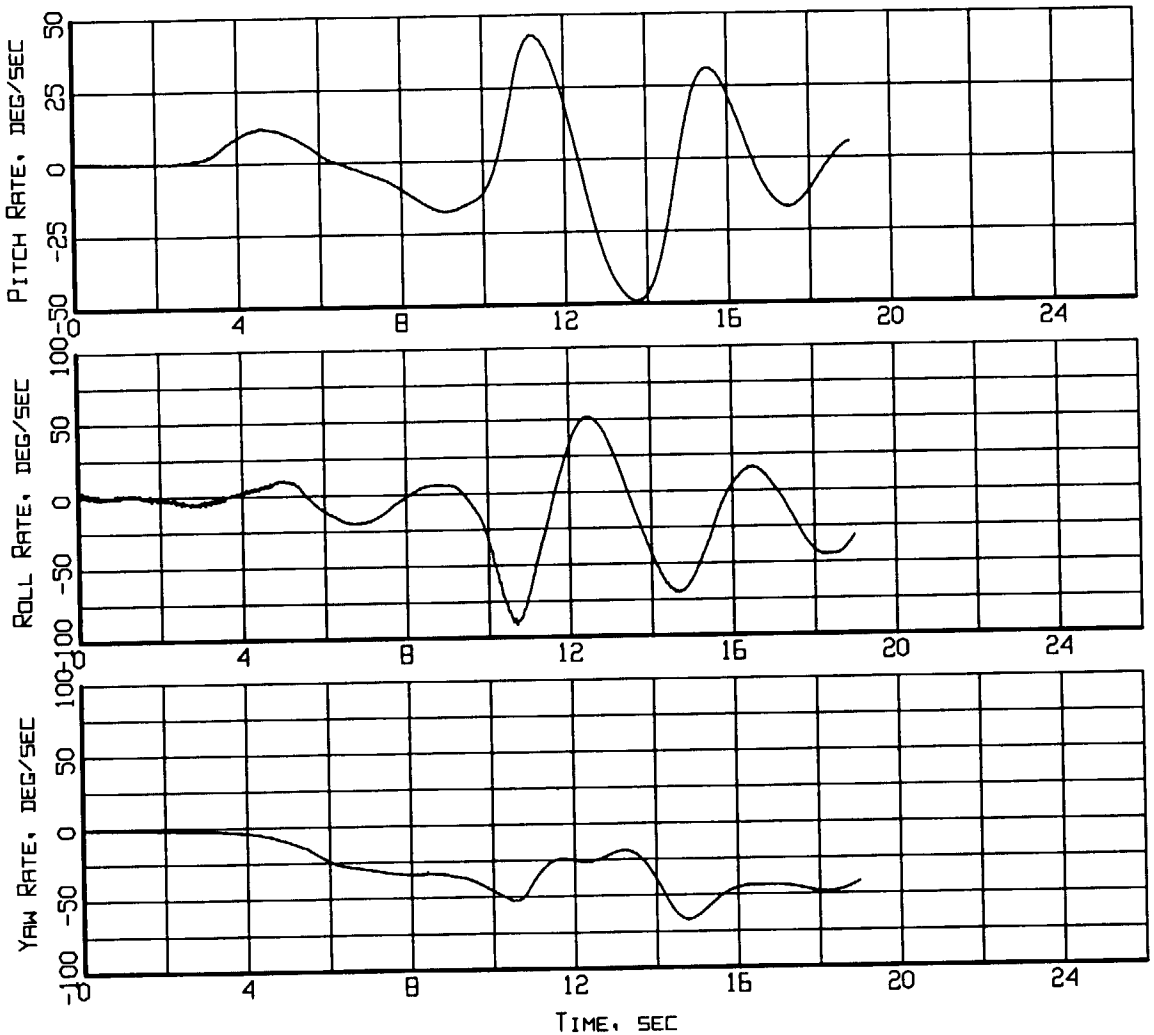

Figure B4-2. Aircraft Motion - Rate-of-Change of Pitch, Roll and Heading (Flight 239, Test Point 37b).

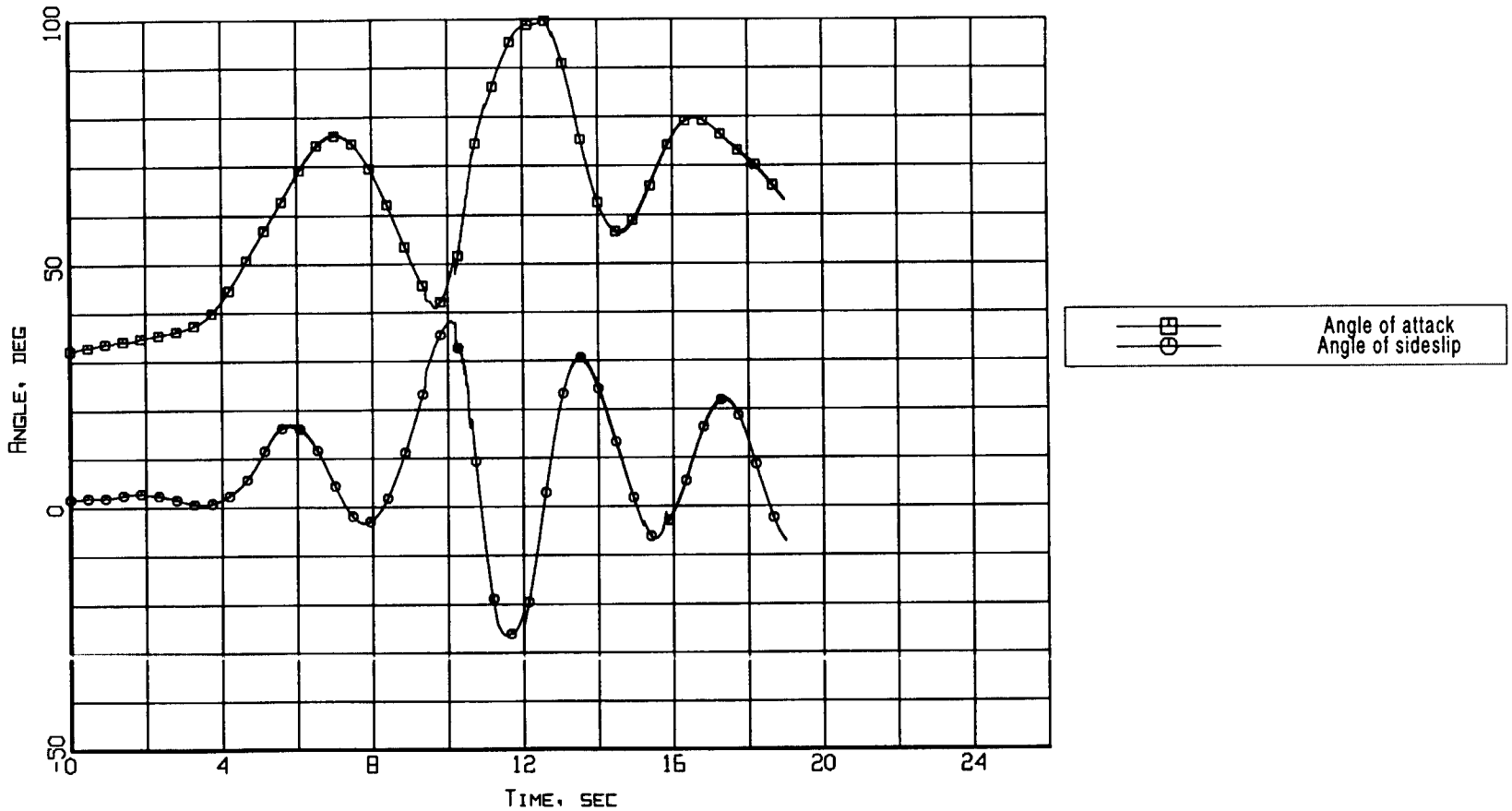

Figure B4-3. Aerodynamic flowstream descriptors - angle of attack and angle of sideslip (Flight 239, Test Point 37b).

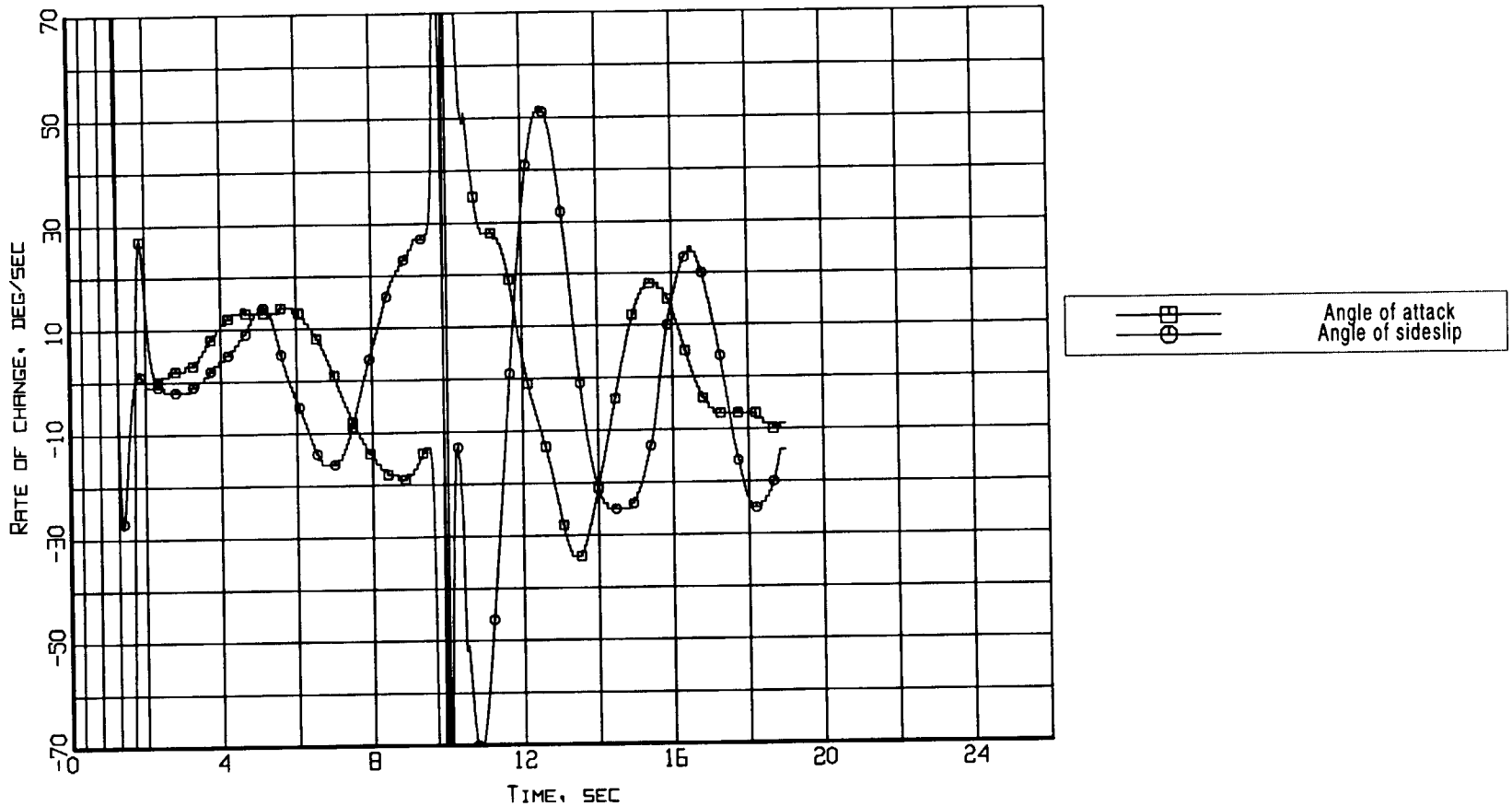

Figure B4-4. Aerodynamic flowstream descriptors - rate of change of angle of attack and angle of sideslip (Flight 239, Test Point 37b).

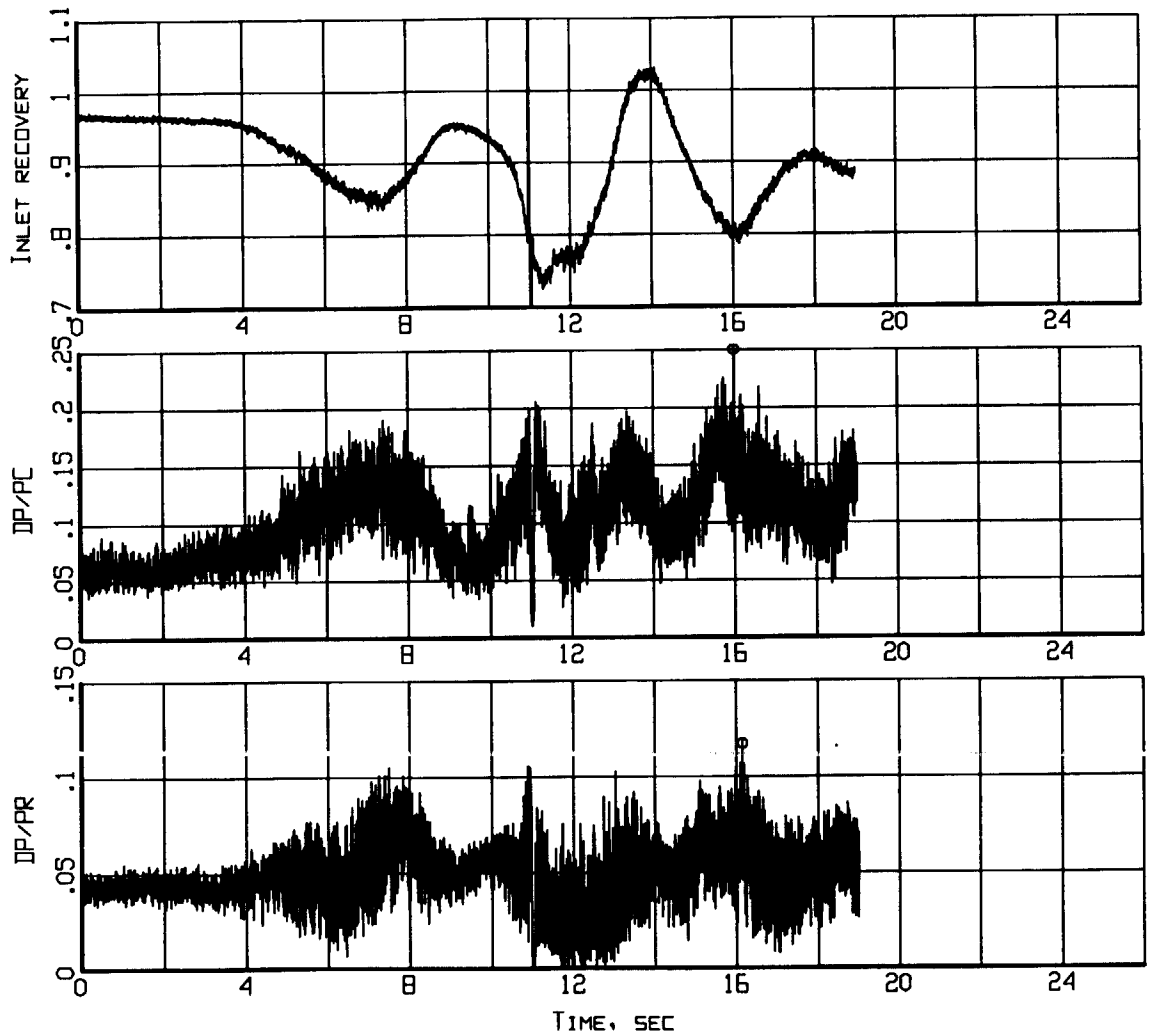

Symbols Denote
Max Points

Figure B4-5. Time histories of inlet recovery and distortion descriptors (Flight 239, Test Point 37b).

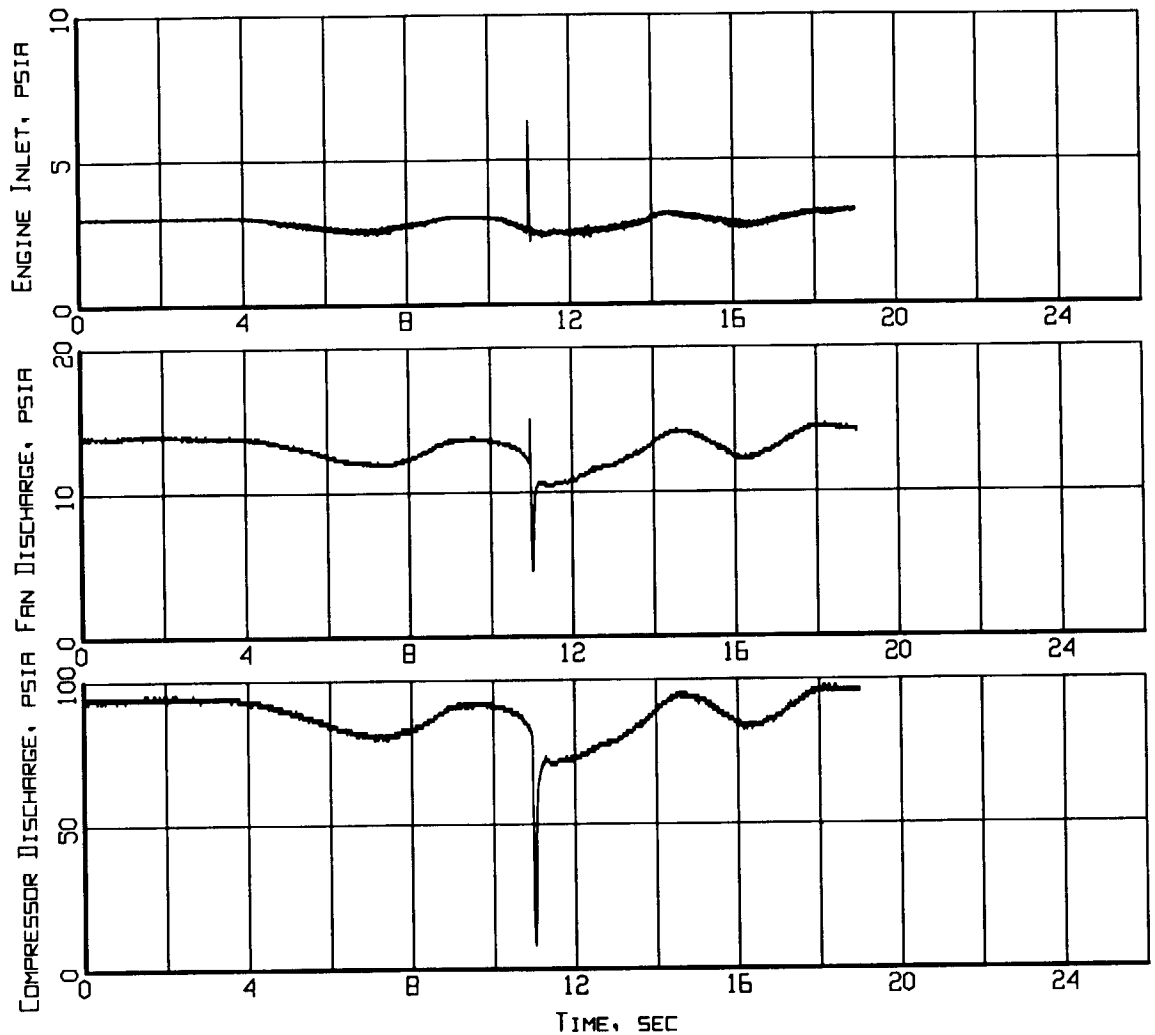

Figure B4-6. Measured inlet/engine entry and engine internal pressures time histories (Flight 239, Test Point 37b).

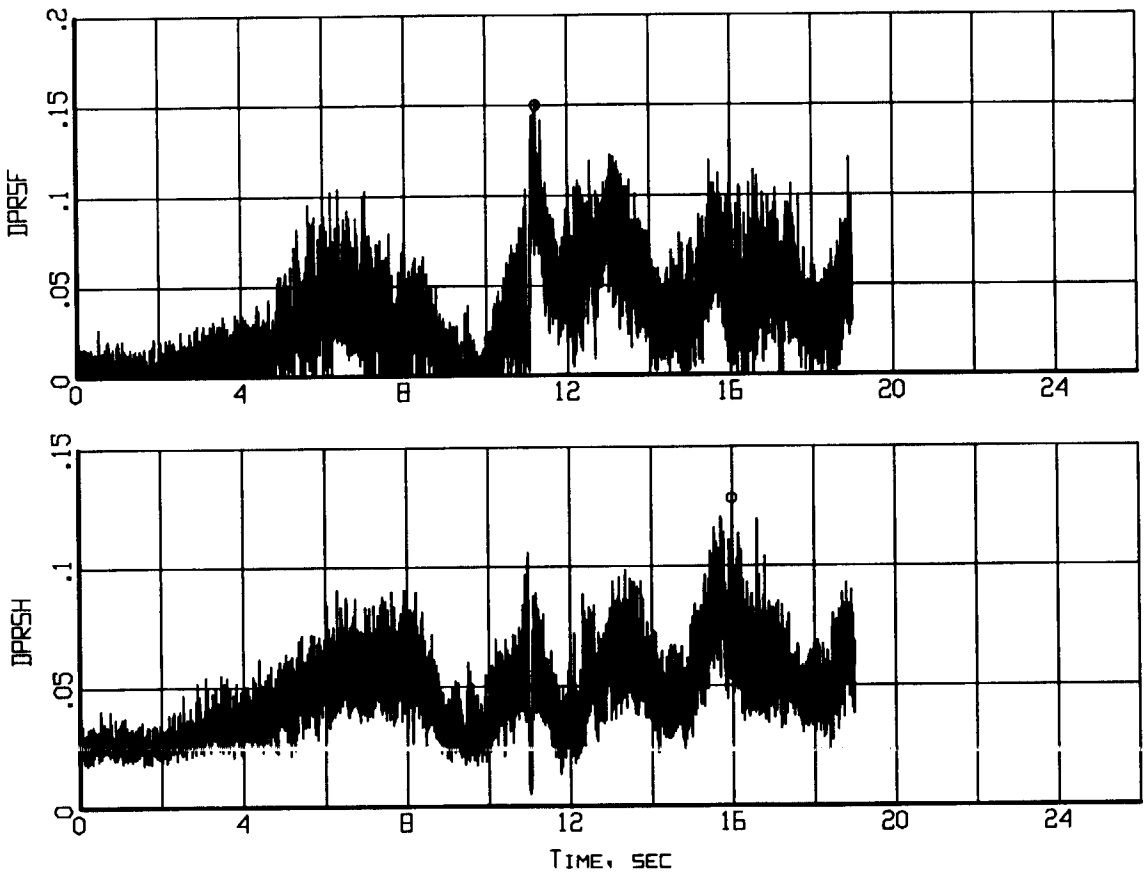

Symbols Denote
Max Points

Figure B4-7. Time histories of the predicted loss of stability pressure ratio for the fan and the compressor (Flight 239, Test Point 37b).

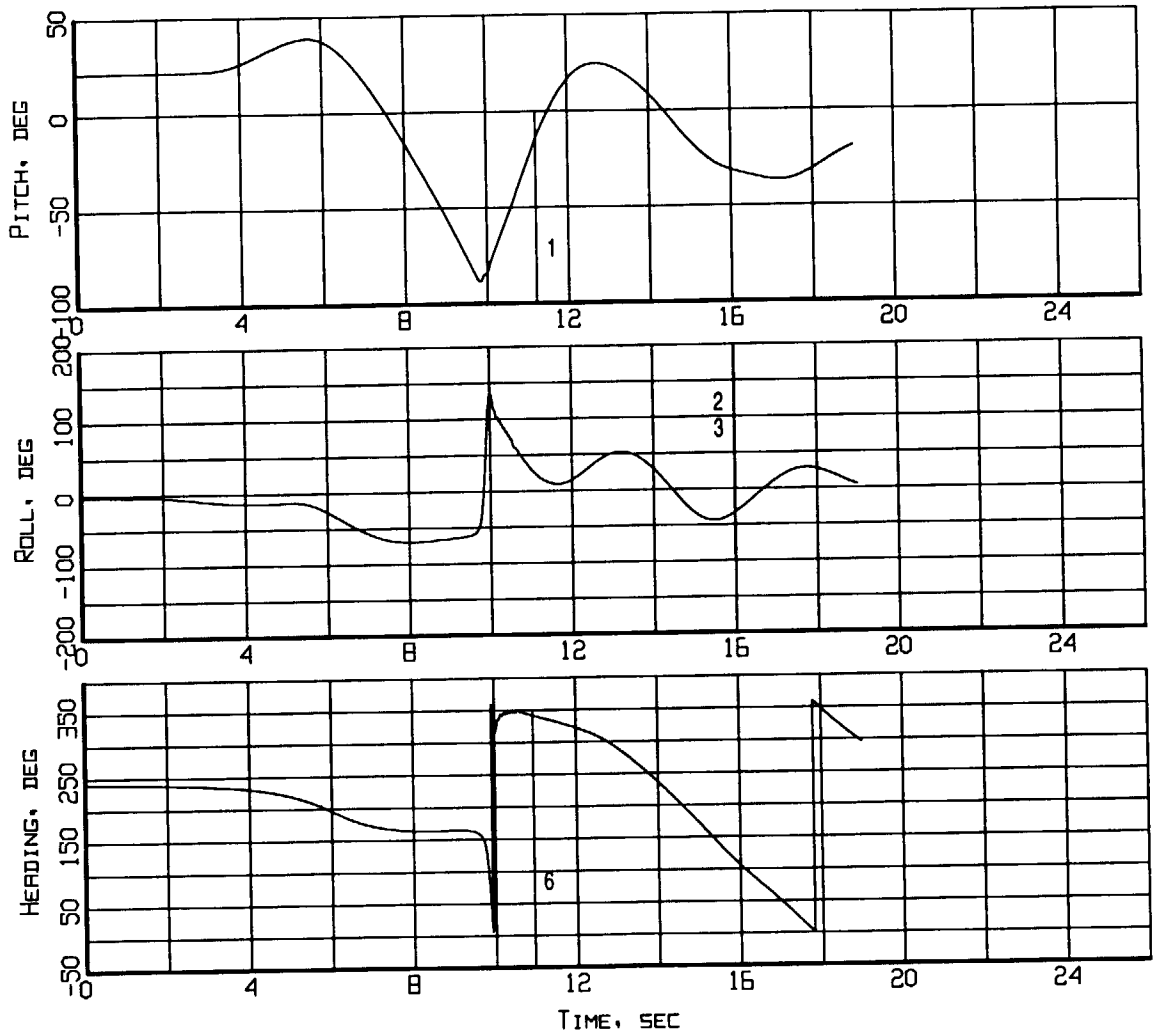

Event Marker

1 - Max DPRSF
2 - Max DPRSH
3 - Max DP/PC
6 - Stall 1

Figure B4-8. Event markers superposed on the aircraft attitude time histories (Flight 239, Test Point 37b).

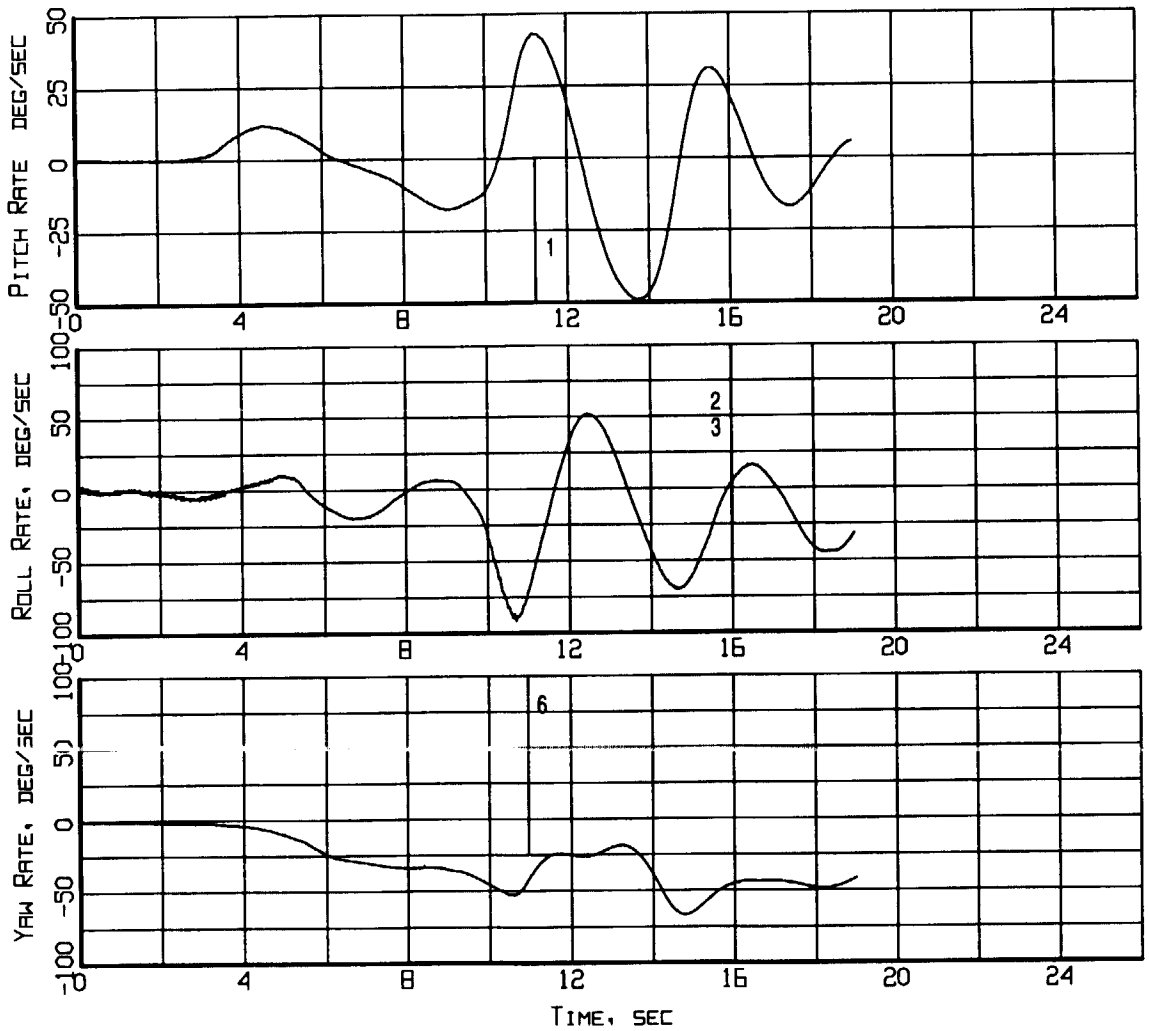

Event Marker

1 - Max DPRSF
2 - Max DPRSH
3 - Max DP/PC
6 - Stall 1

Figure B4-9. Event markers superposed on the aircraft motion time histories (Flight 239, Test Point 37b).

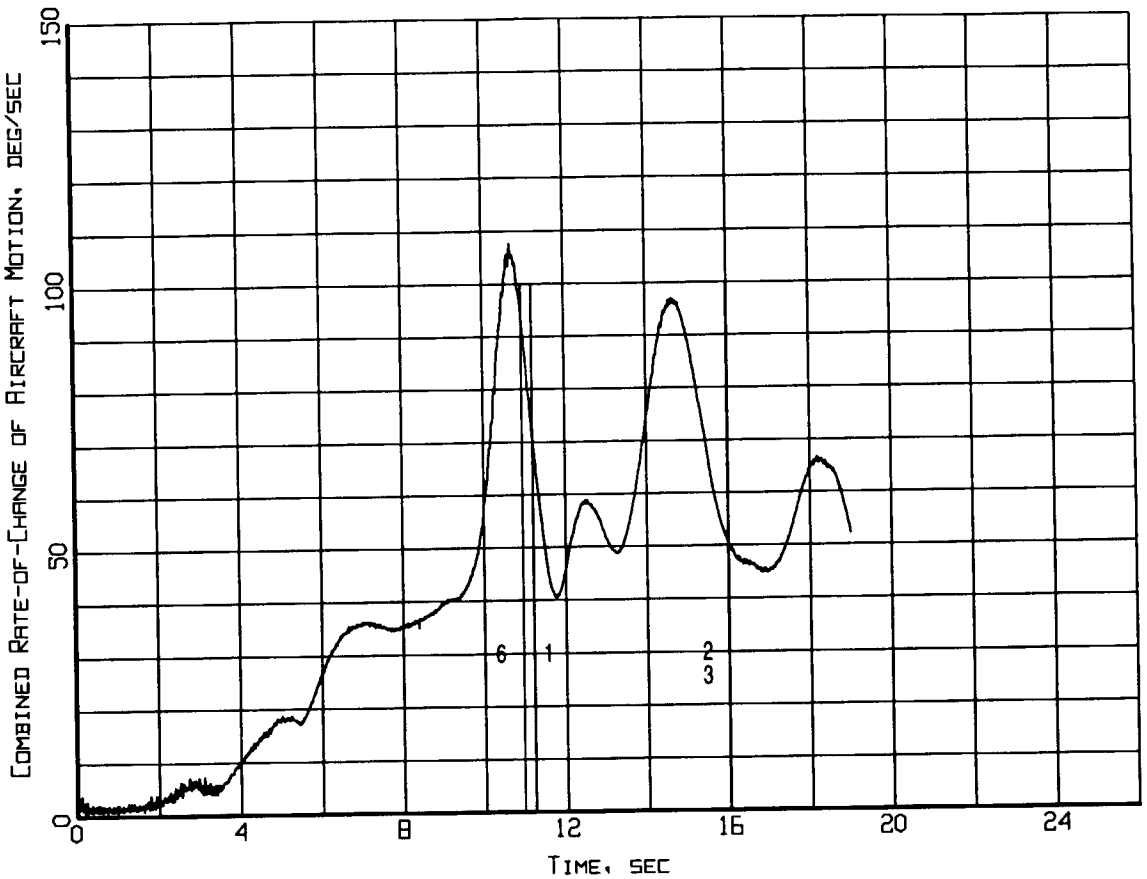

Figure B4-10. Event markers superposed on the combined of rate-of-change of aircraft motion time history (Flight 239, Test Point 37b).

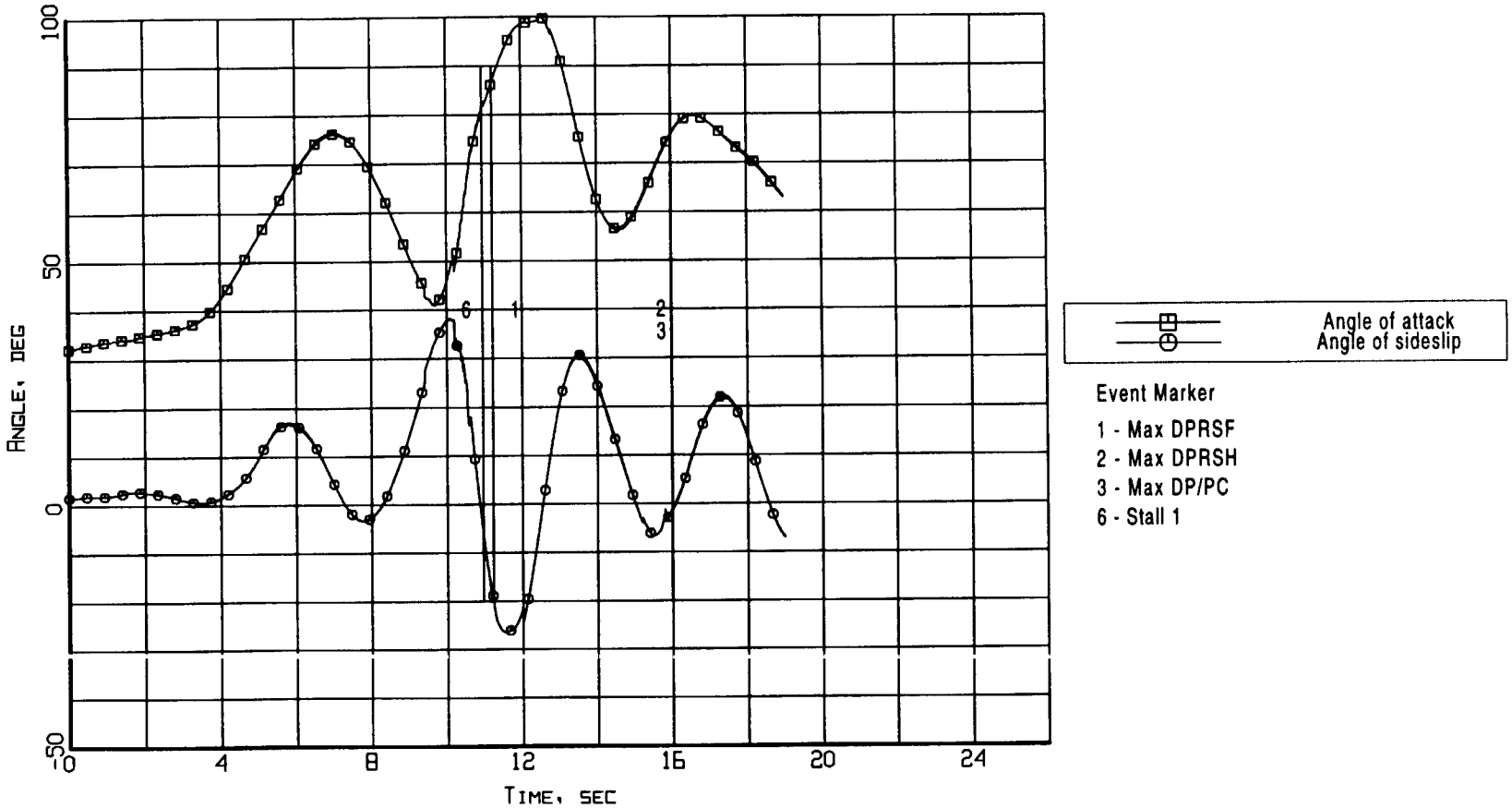

Figure B4-11. Event markers superposed on the aerodynamic flowstream descriptor time histories (Flight 239, Test Point 37b).

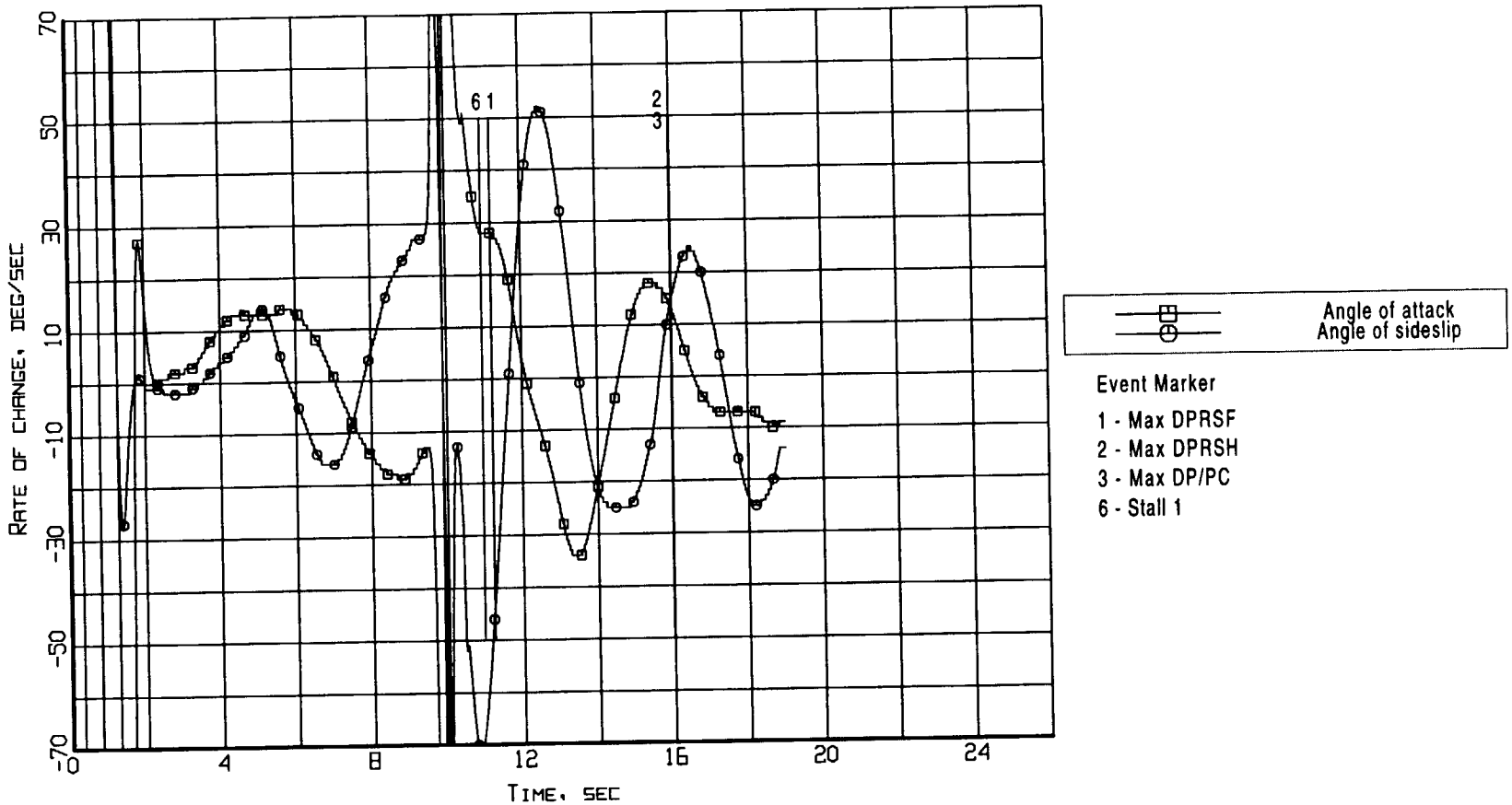

Figure B4-12. Event markers superposed on the aerodynamic flowstream descriptors rate-of-change time histories (Flight 239, Test Point 37b).

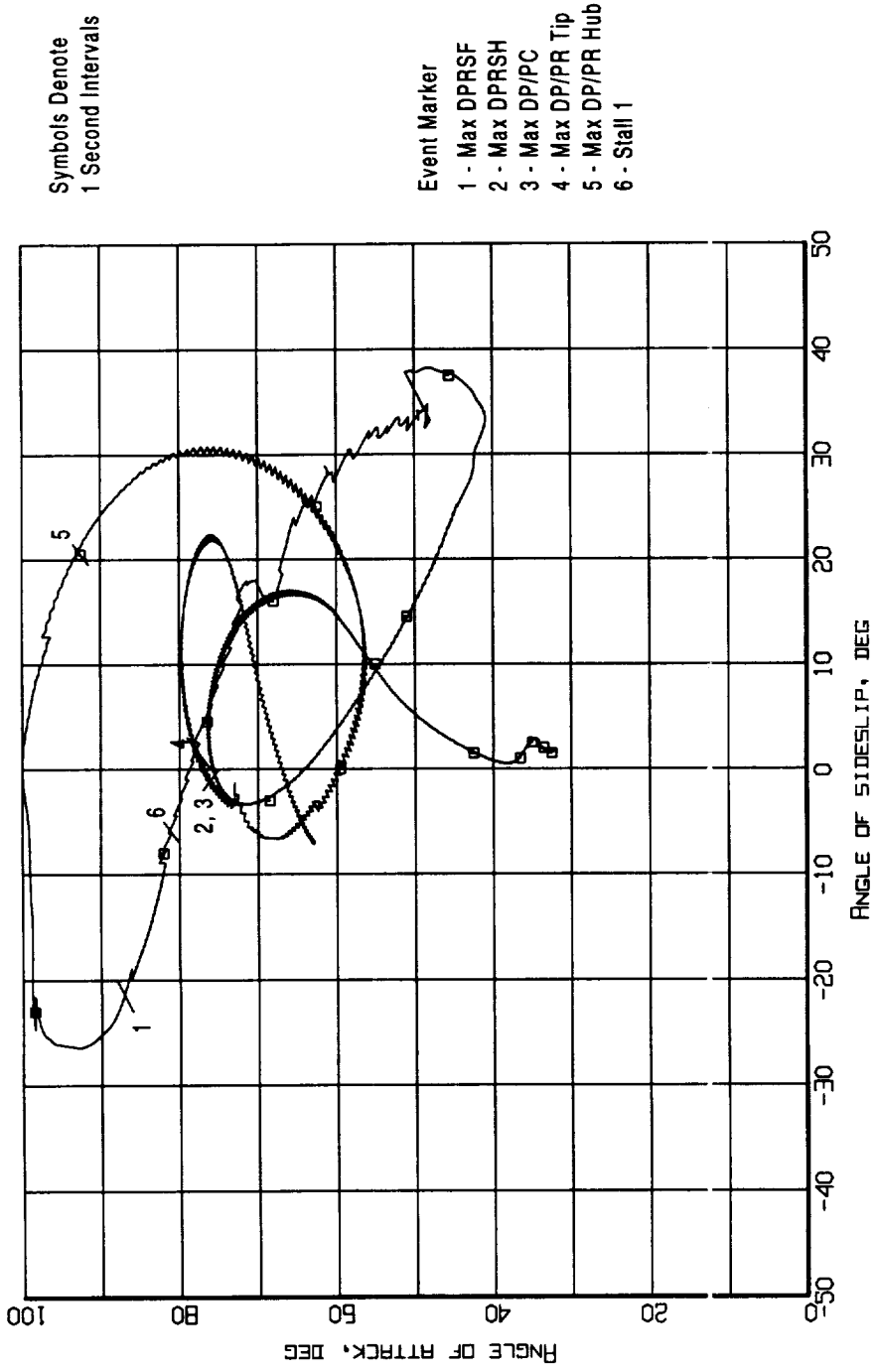

Figure B4-13. Event markers superposed on the aerodynamic flowstream descriptors trajectory (Flight 239, Test Point 37b).

Appendix B5 - Flight 238, Test Point 38b

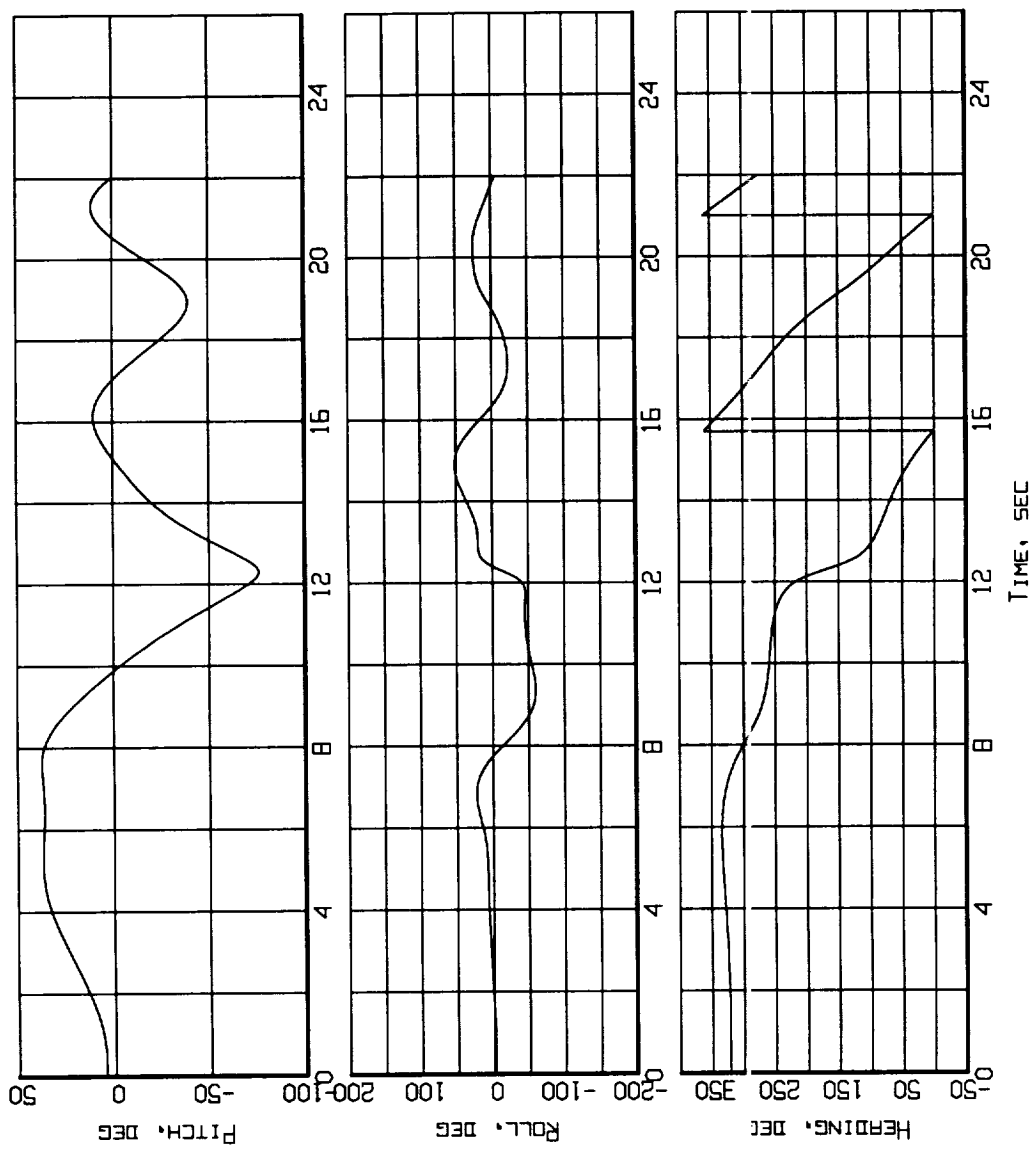

Figure B5-1. Aircraft attitude - Pitch, Roll, and Heading (Flight 238, Test Point 38b).

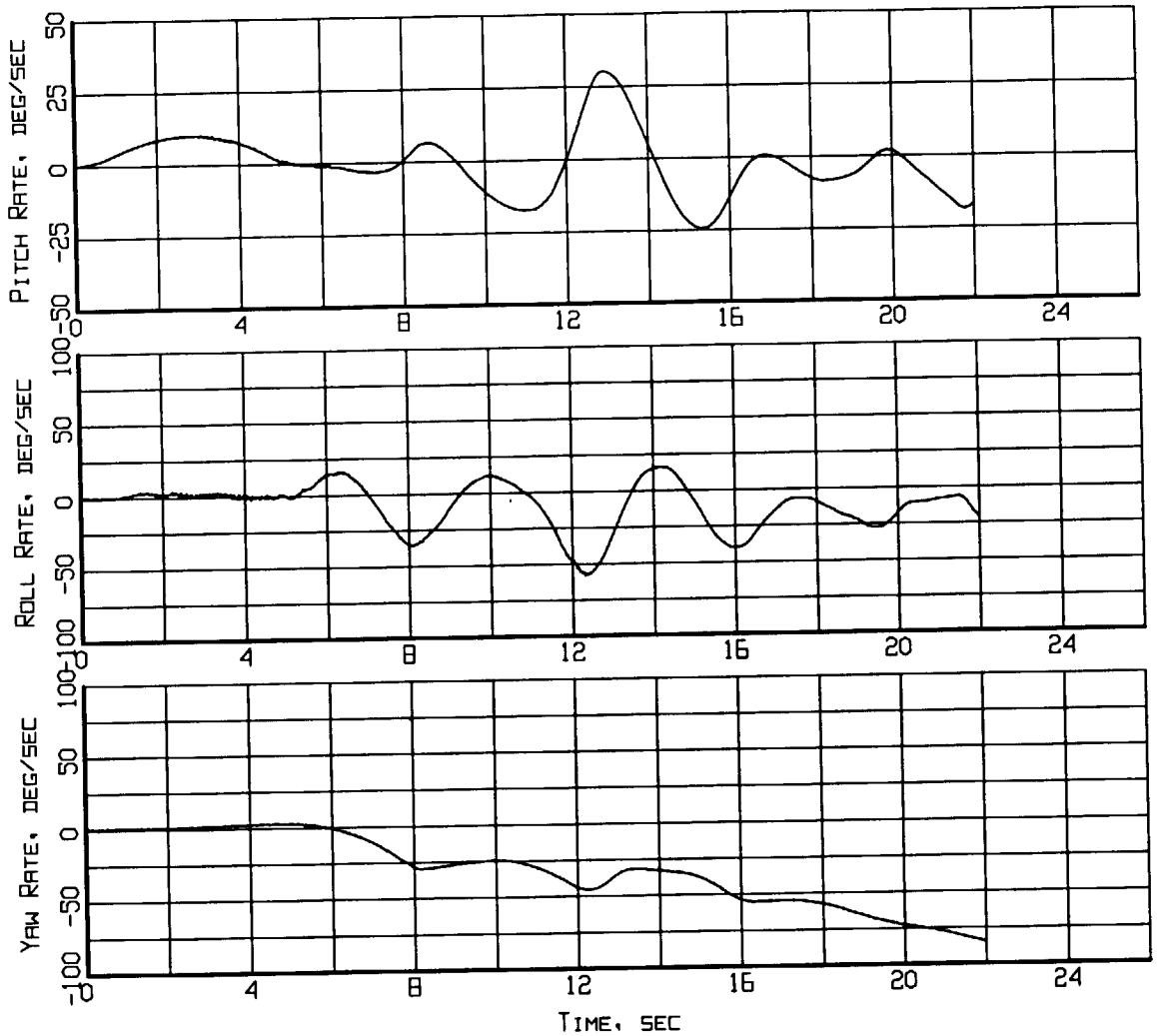

Figure B5-2. Aircraft Motion - Rate-of-Change of Pitch, Roll and Heading (Flight 238, Test Point 38b).

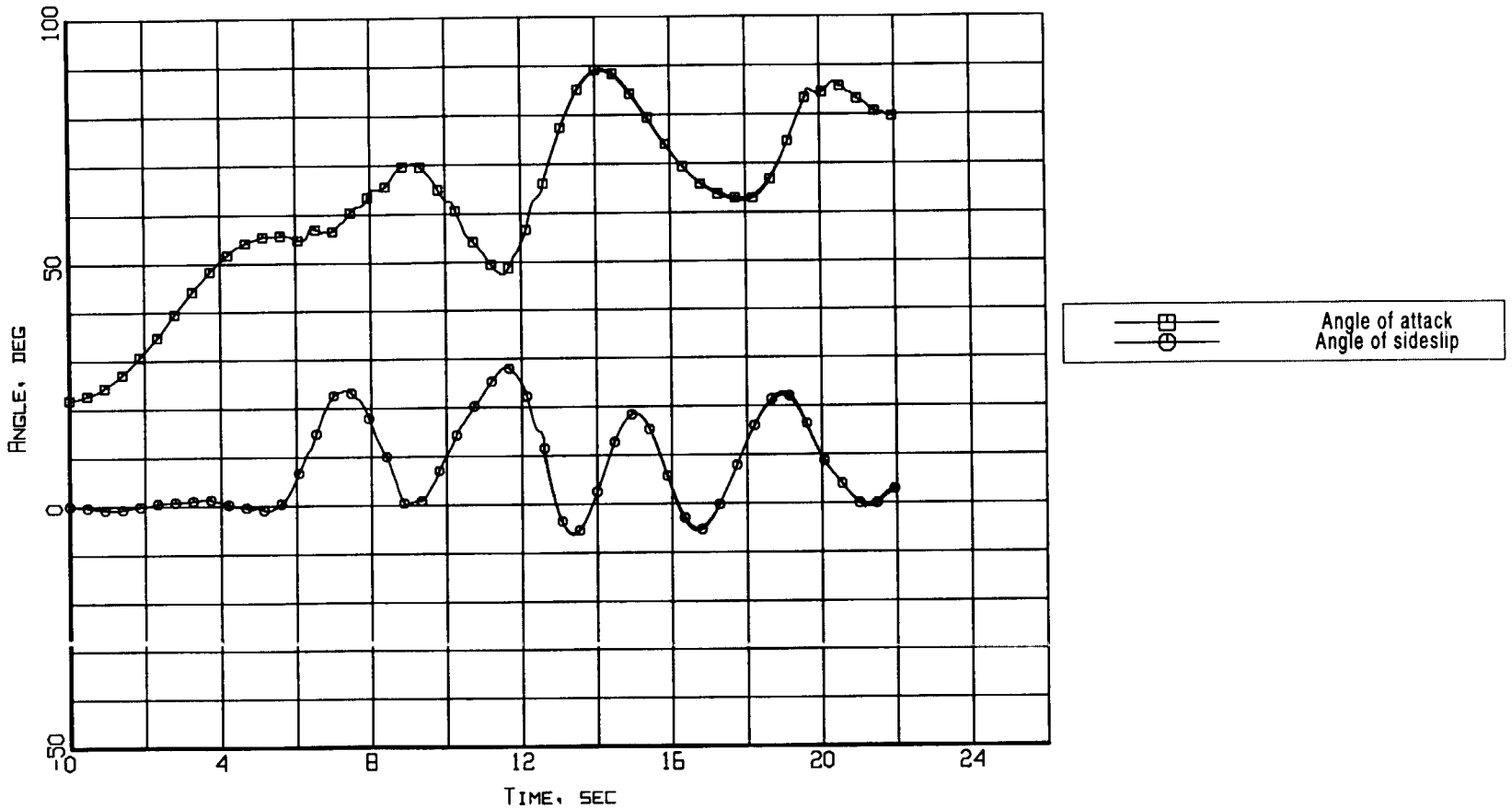

Figure B5-3. Aerodynamic flowstream descriptors - angle of attack and angle of sideslip (Flight 238, Test Point 38b).

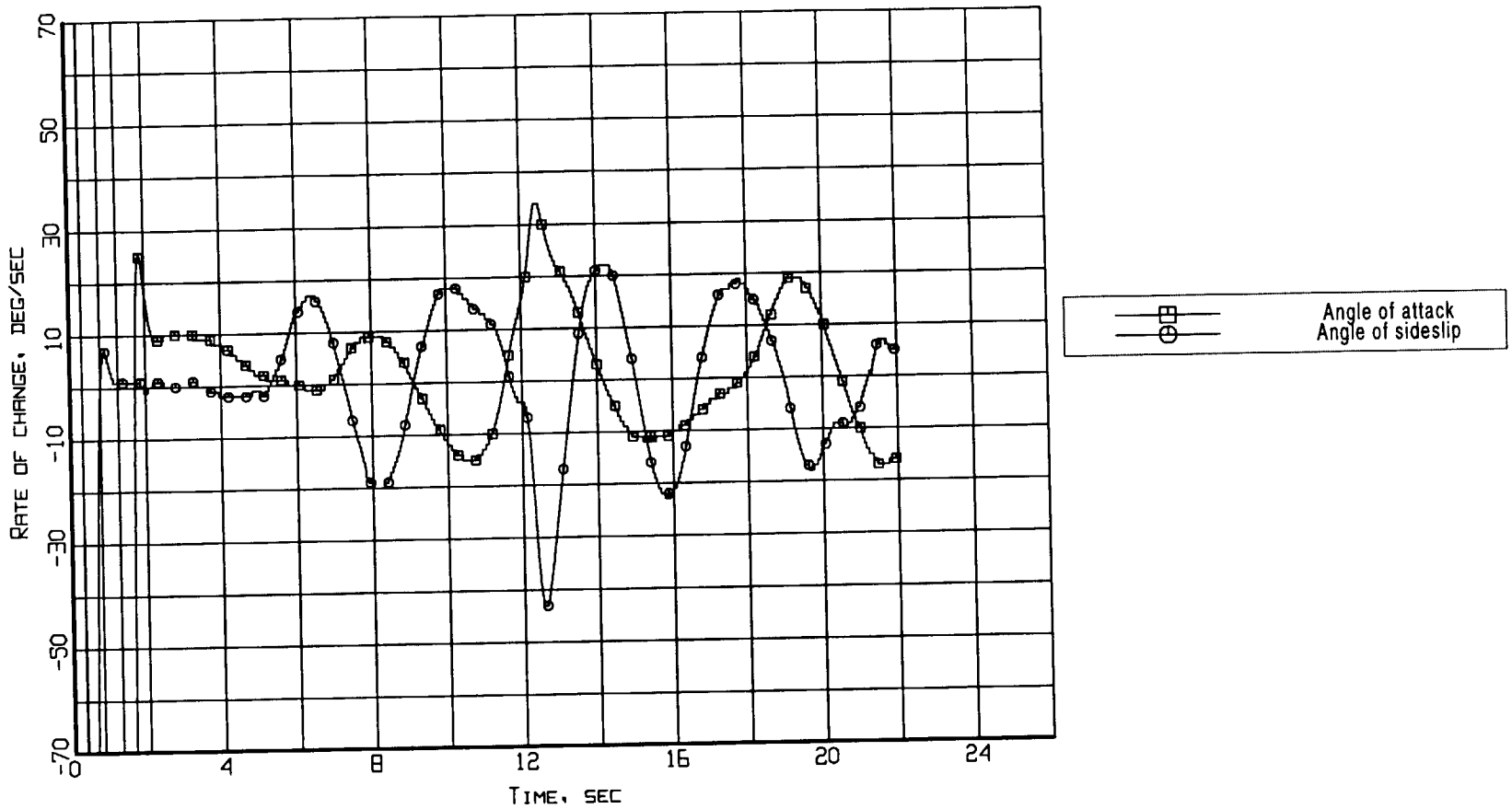

Figure B5-4. Aerodynamic flowstream descriptors - rate of change of angle of attack and angle of sideslip (Flight 238, Test Point 38b).

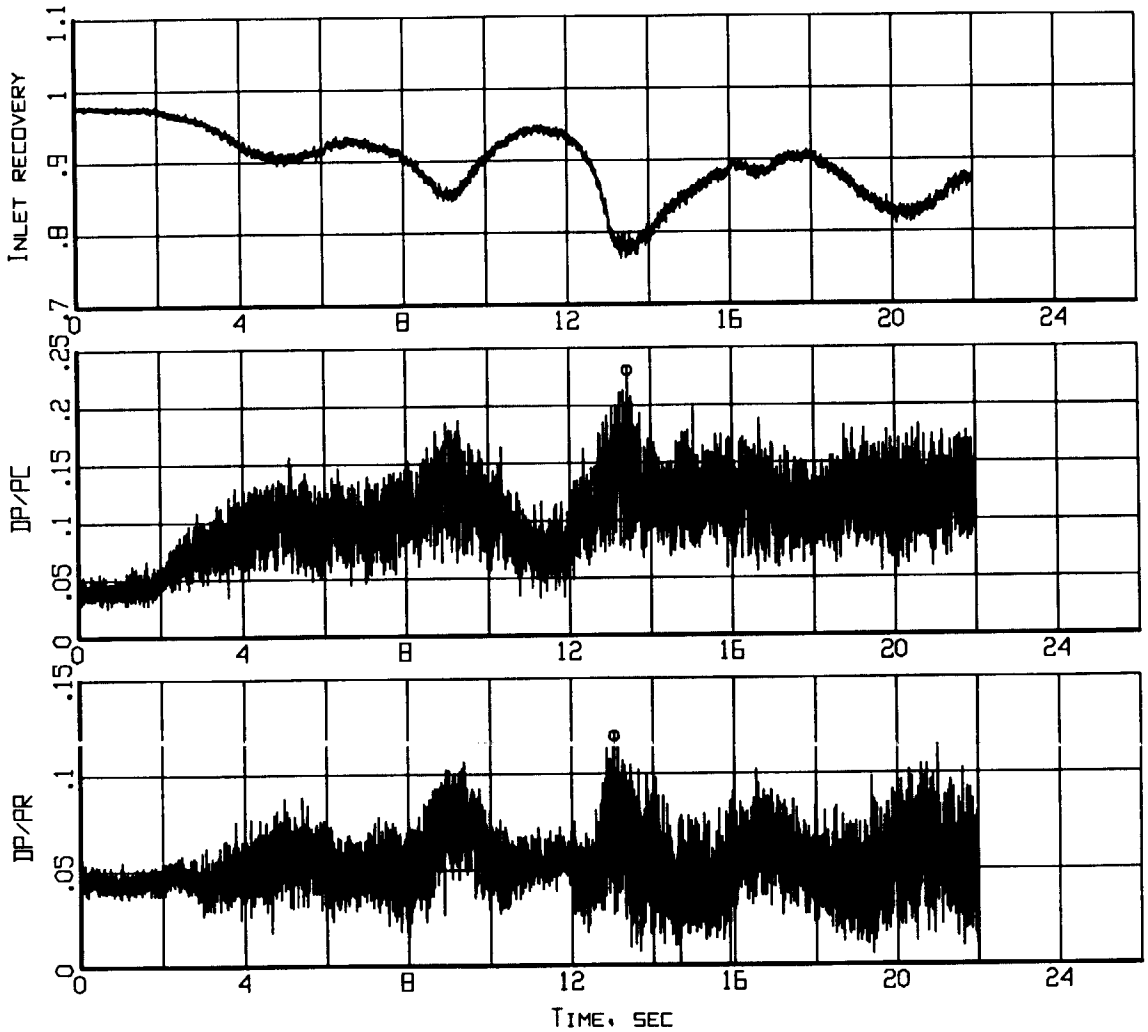

Figure B5-5. Time histories of inlet recovery and distortion descriptors (Flight 238, Test Point 38b).

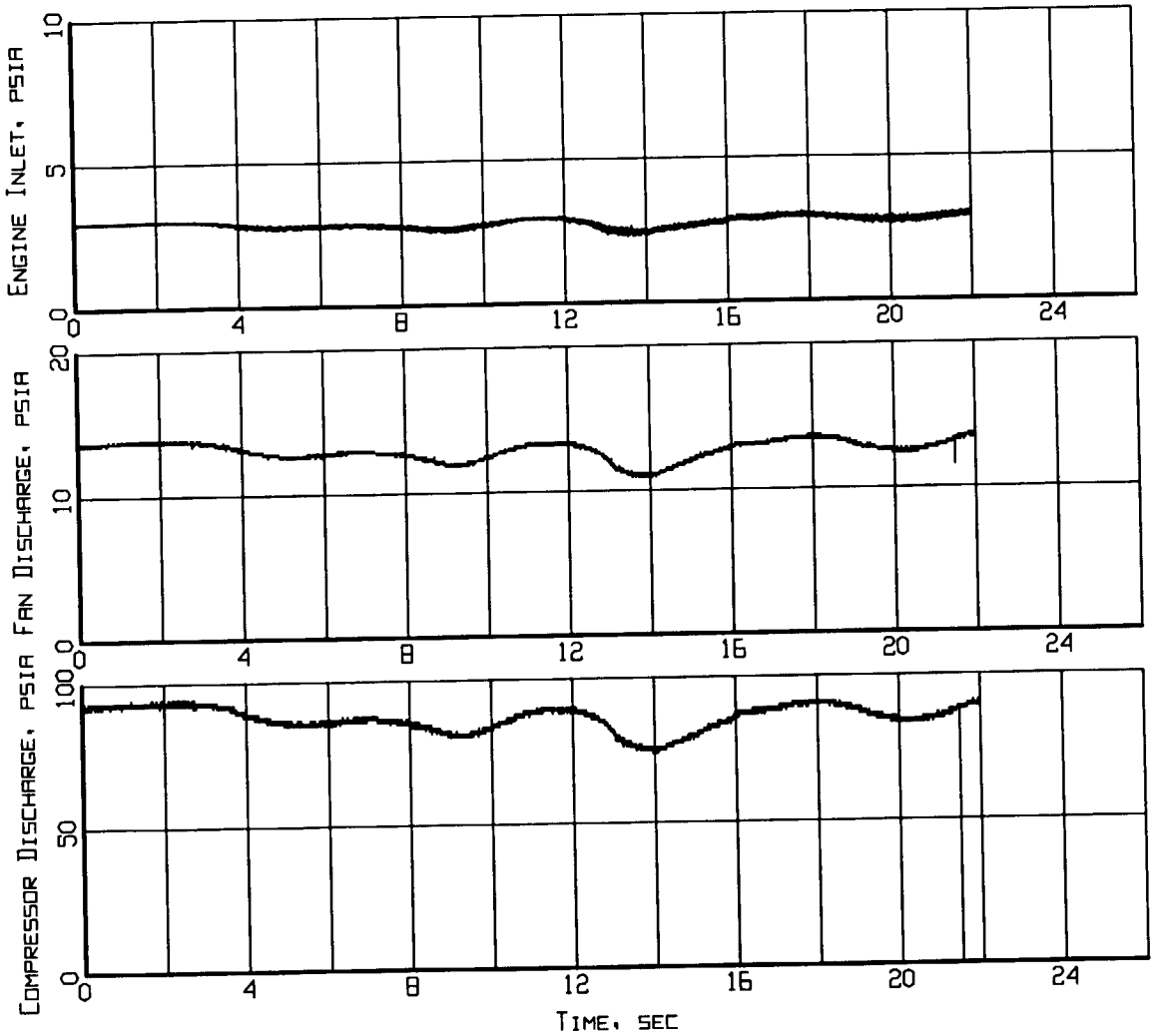

Figure B5-6. Measured inlet/engine entry and engine internal pressures time histories (Flight 238, Test Point 38b).

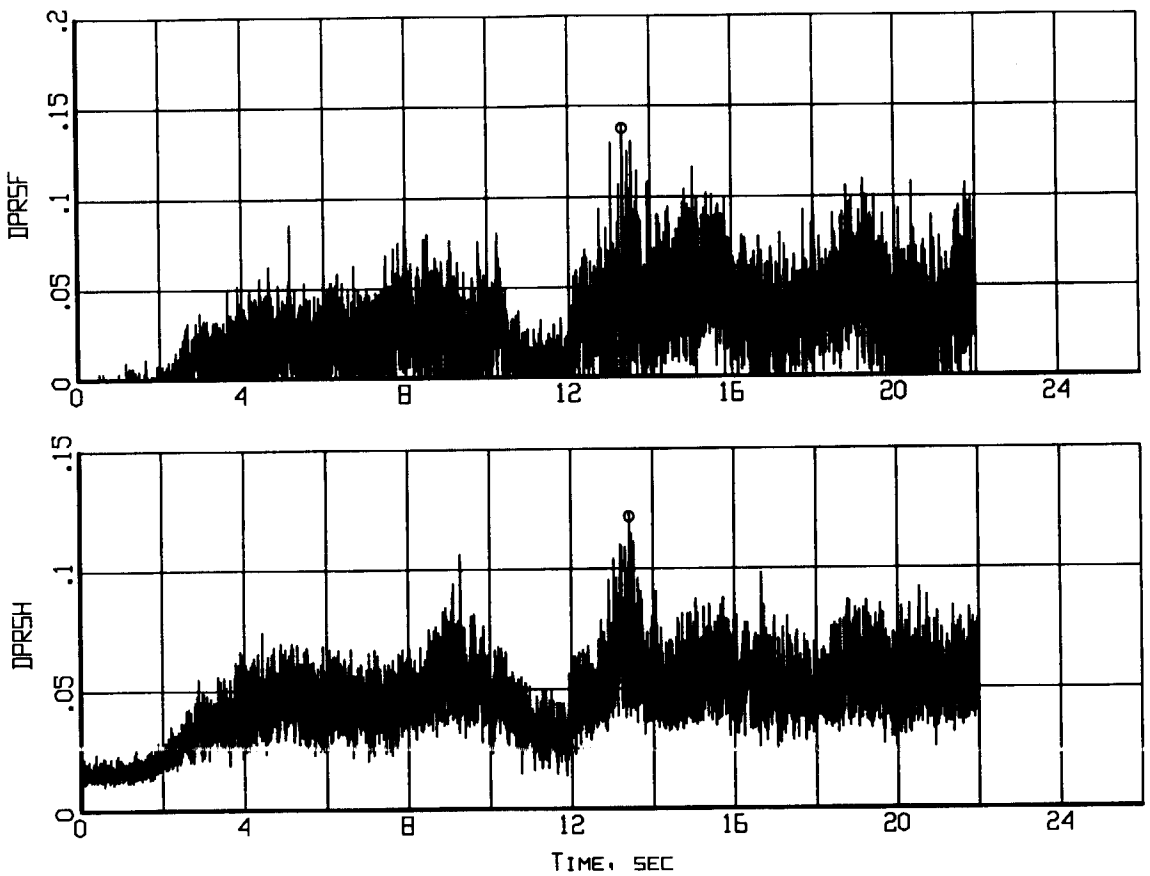

Symbols Denote
Max Points

Figure B5-7. Time histories of the predicted loss of stability pressure ratio for the fan and the compressor (Flight 238, Test Point 38b).

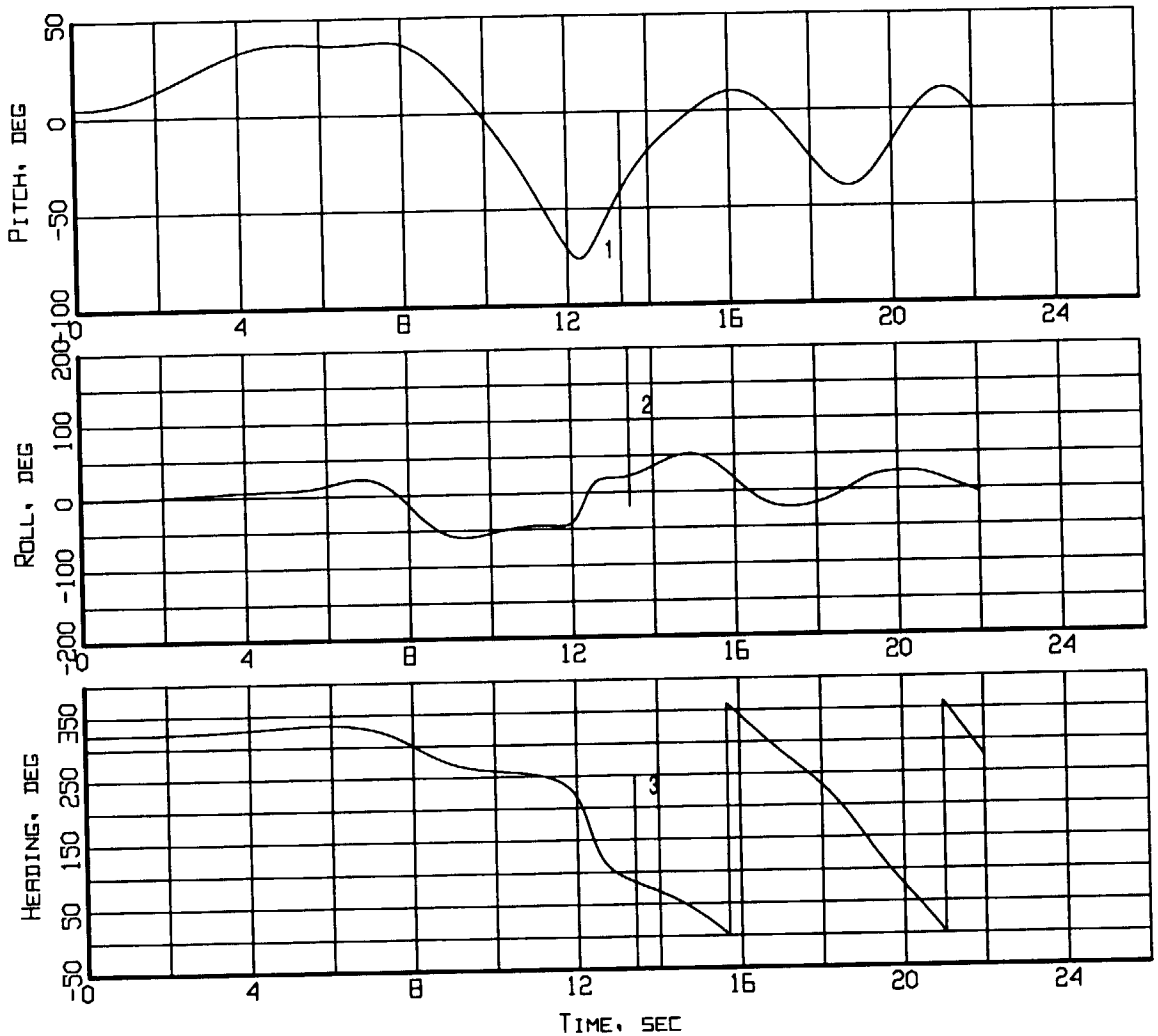

Event Marker

1 - Max DPRSF

2 - Max DPRSH

3 - Max DP/PC

Figure B5-8. Event markers superposed on the aircraft attitude time histories (Flight 238, Test Point 38b).

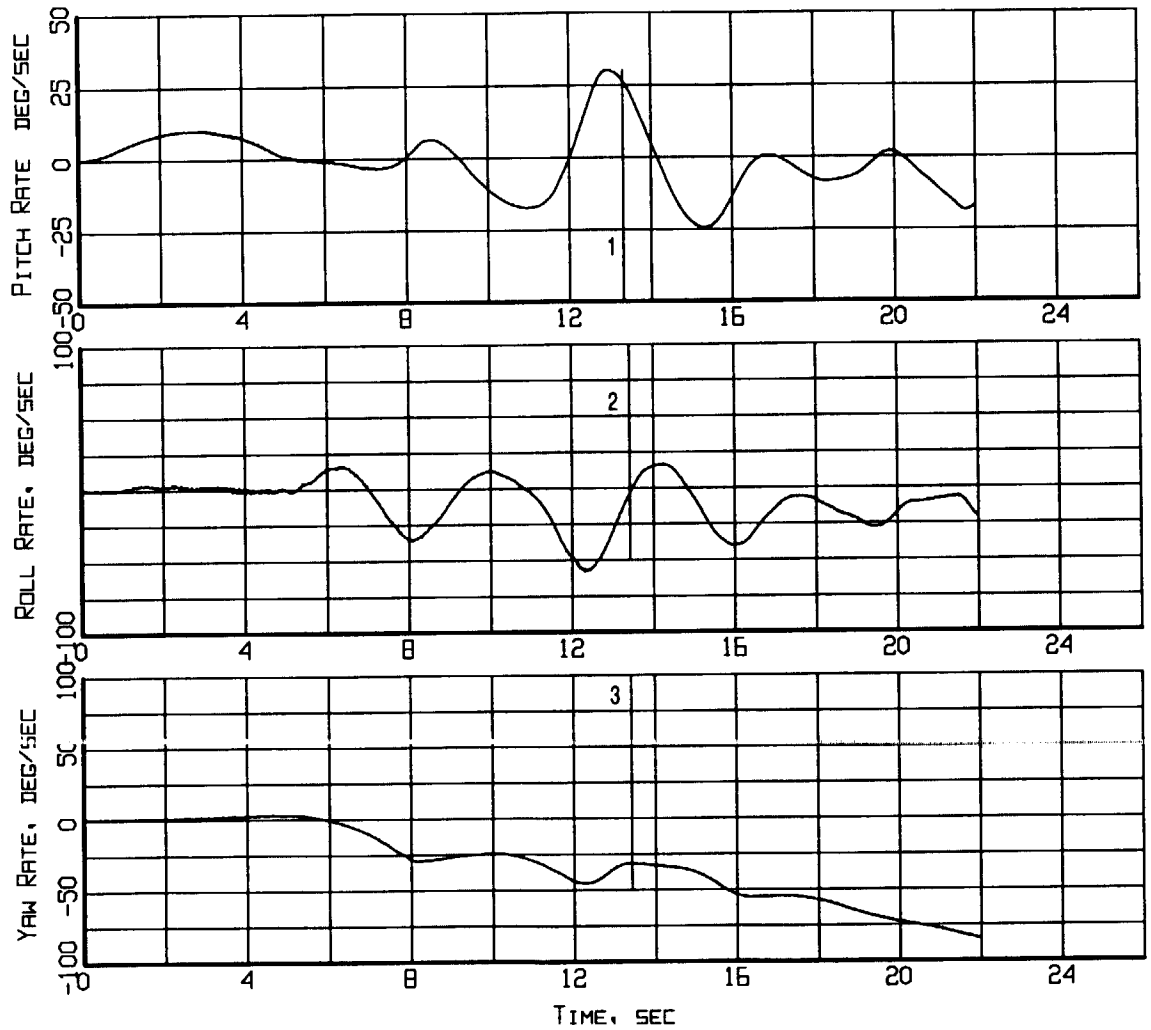

Event Marker

1 - Max DPRSF

2 - Max DPRSH

3 - Max DP/PC

Figure B5-9. Event markers superposed on the aircraft motion time histories (Flight 238, Test Point 38b).

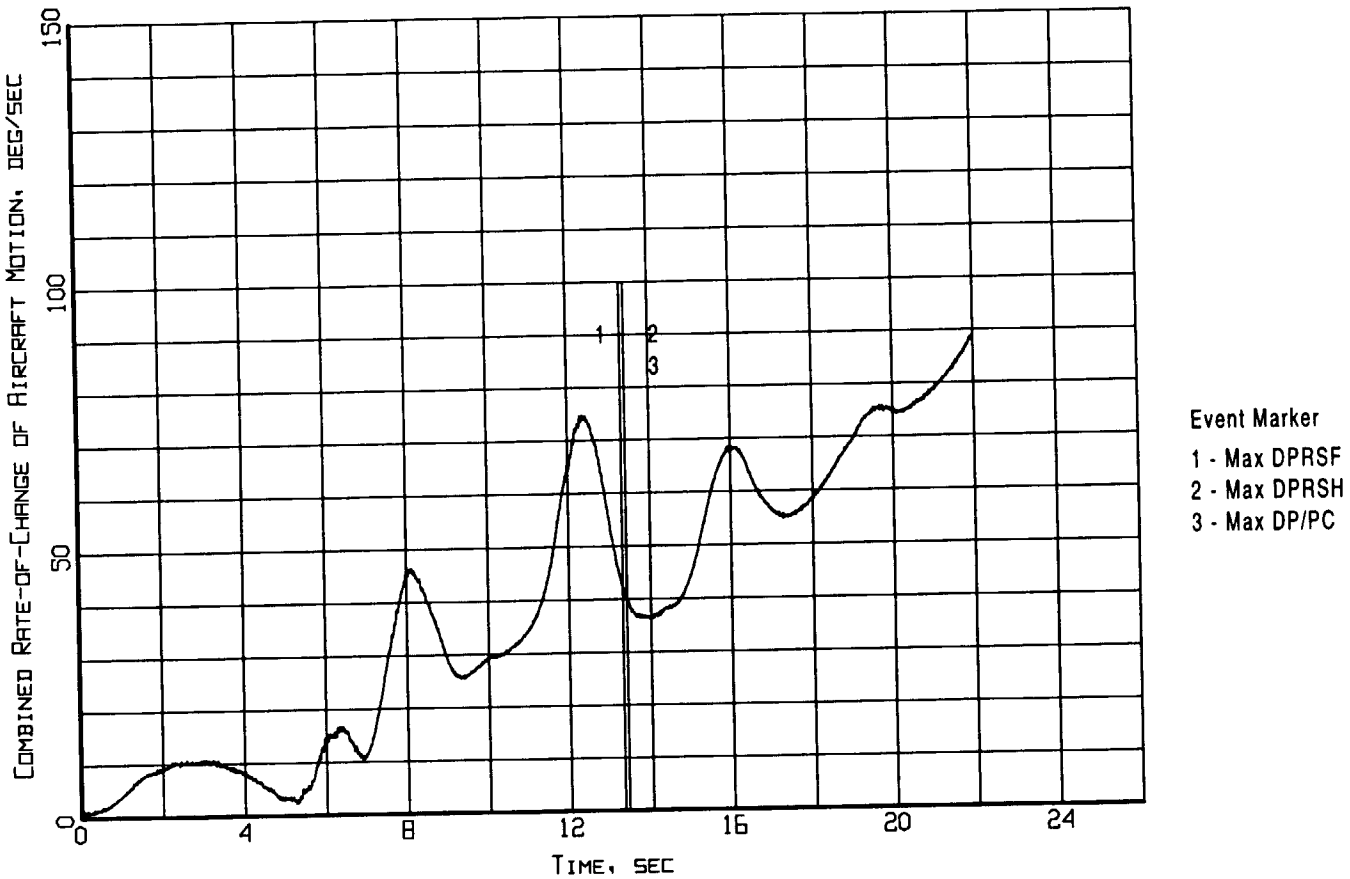

Figure B5-10. Event markers superposed on the combined of rate-of-change of aircraft motion time history (Flight 238, Test Point 38b).

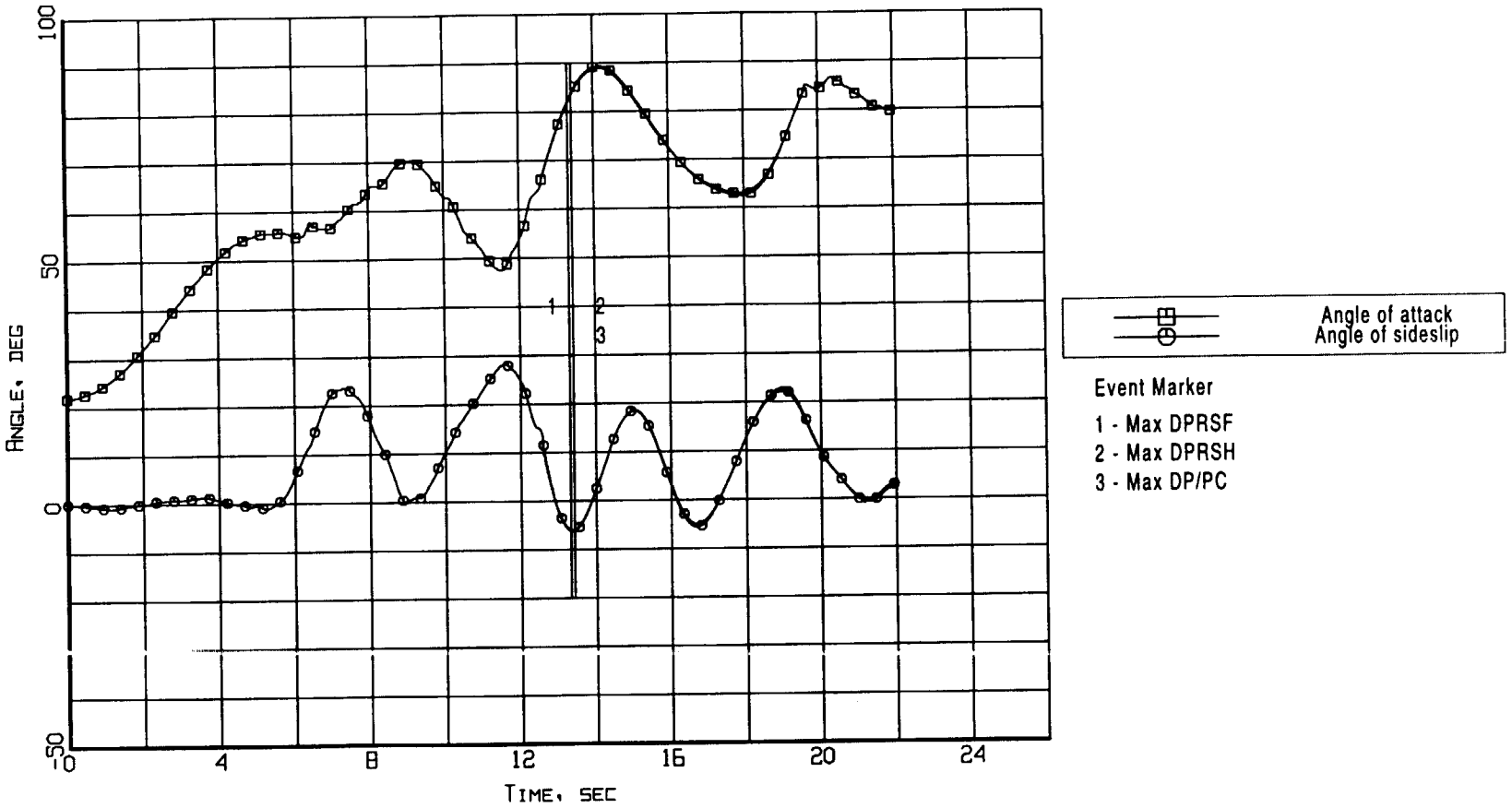

Figure B5-11. Event markers superposed on the aerodynamic flowstream descriptor time histories (Flight 238, Test Point 38b).

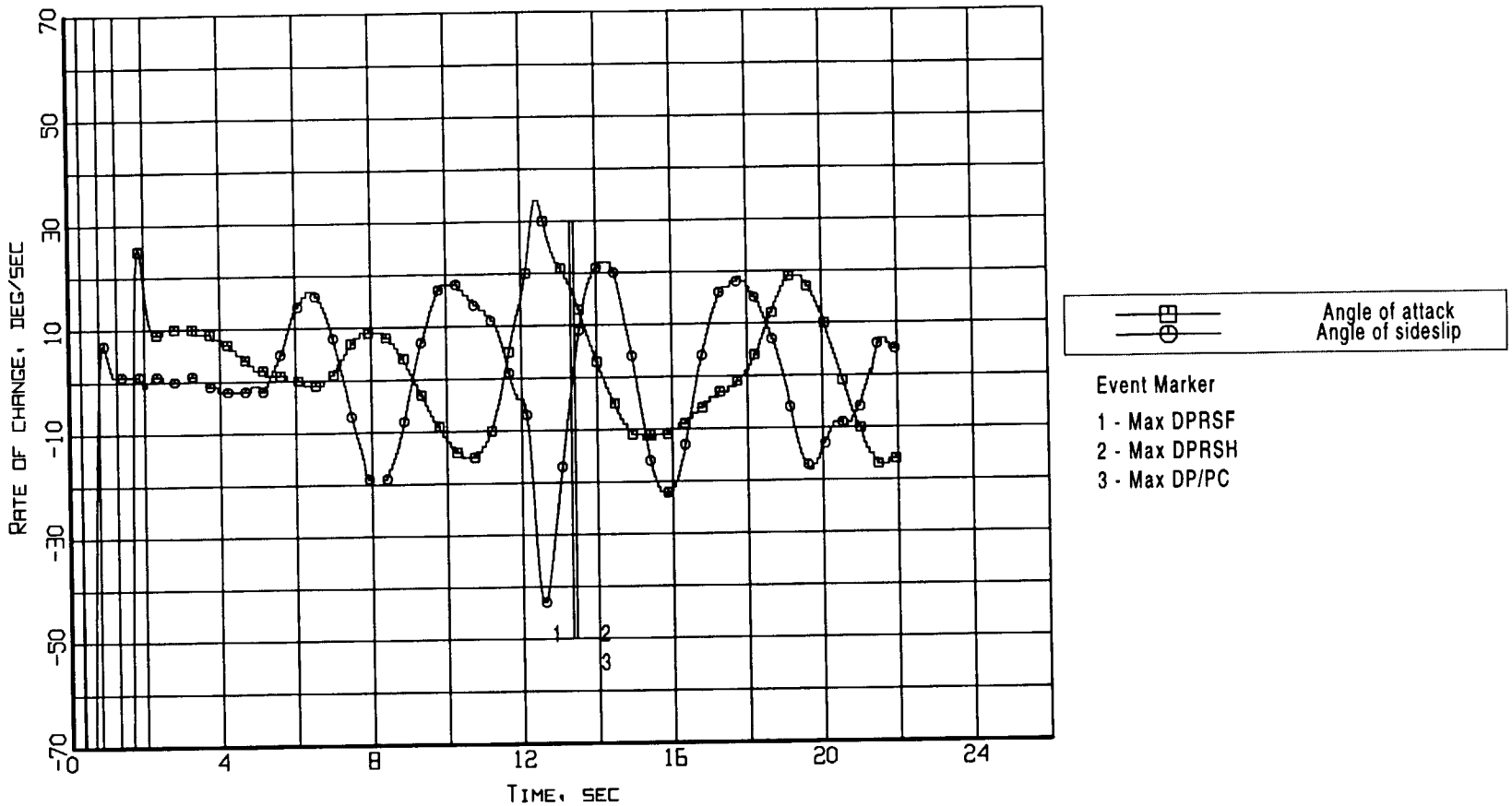

Figure B5-12. Event markers superposed on the aerodynamic flowstream descriptors rate-of-change time histories (Flight 238, Test Point 38b).

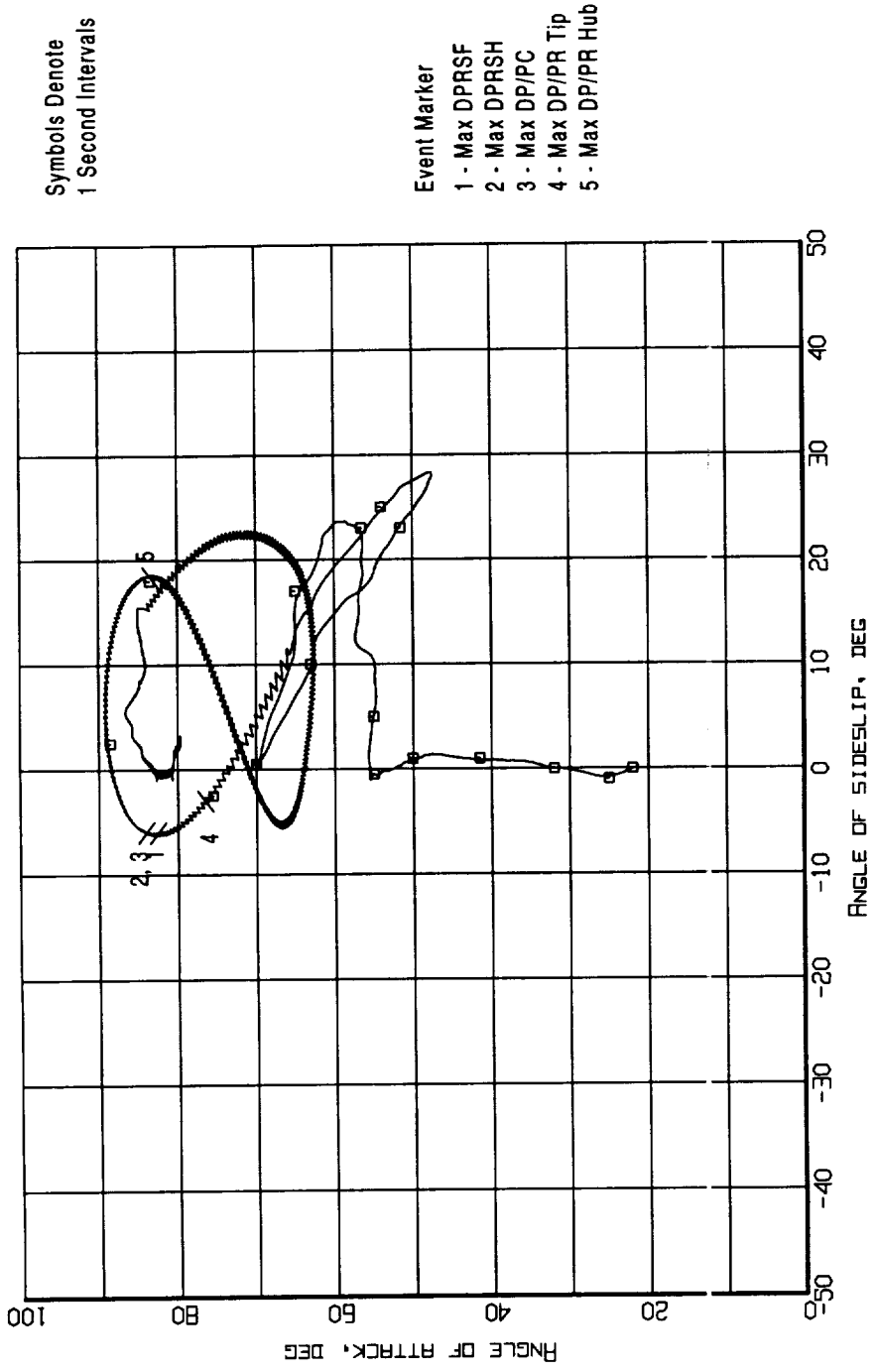

Figure B5-13. Event markers superposed on the aerodynamic flowstream descriptors trajectory (Flight 238, Test Point 38b).

Appendix B6 - Flight 239, Test Point 39b

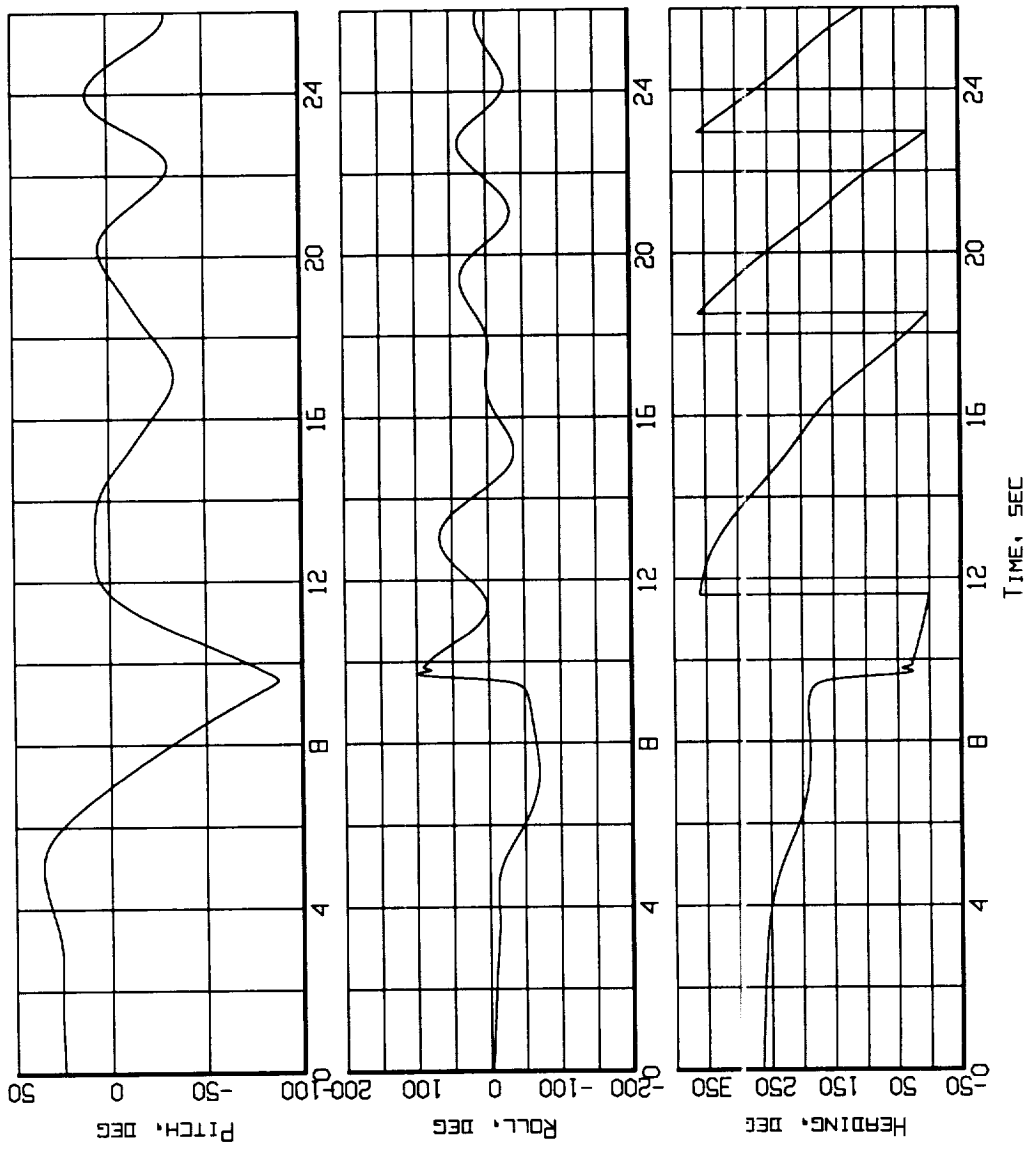

Figure B6-1. Aircraft attitude - Pitch, Roll, and Heading (Flight 239, Test Point 39b).

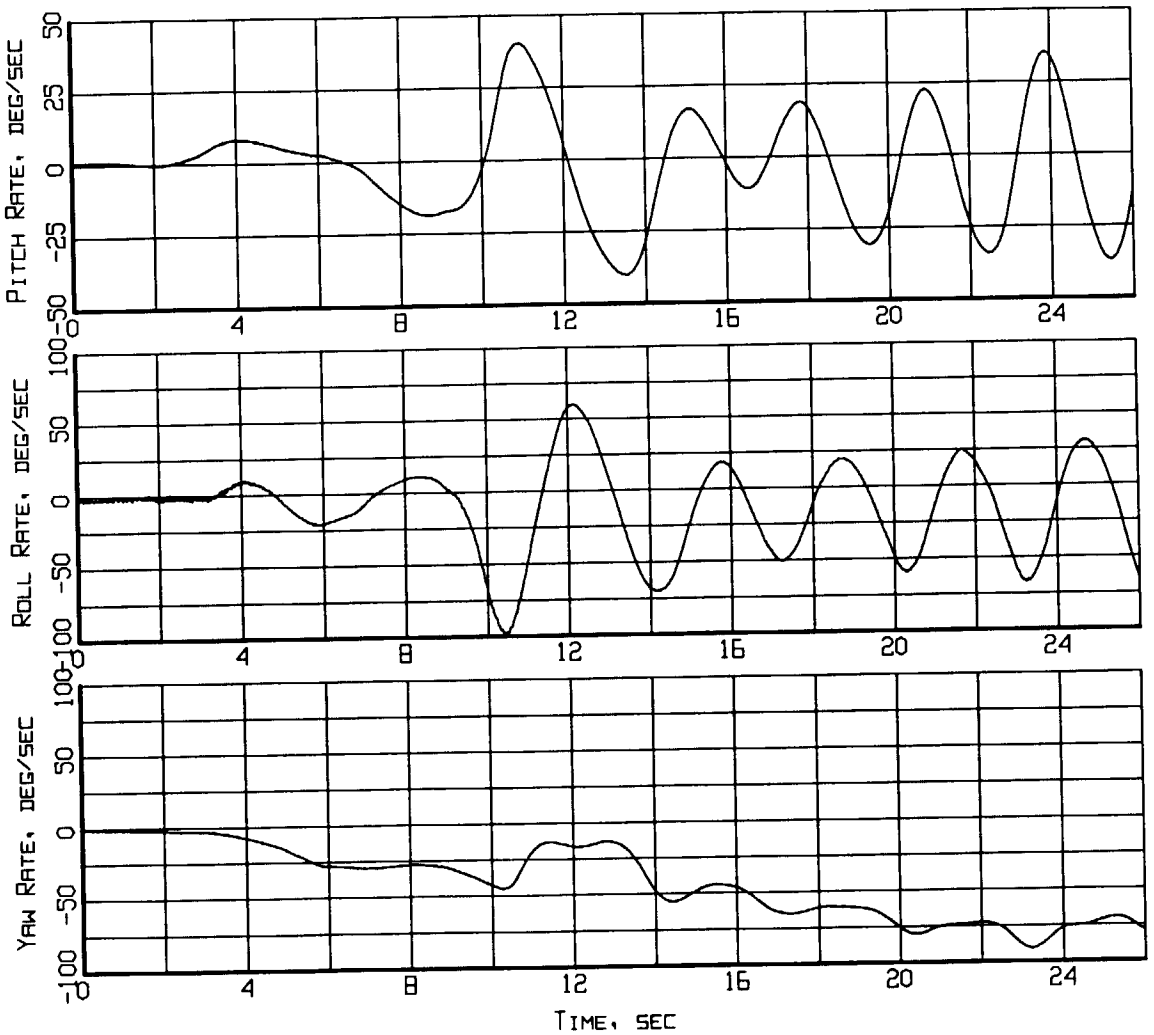

Figure B6-2. Aircraft Motion - Rate-of-Change of Pitch, Roll and Heading (Flight 239, Test Point 39b).

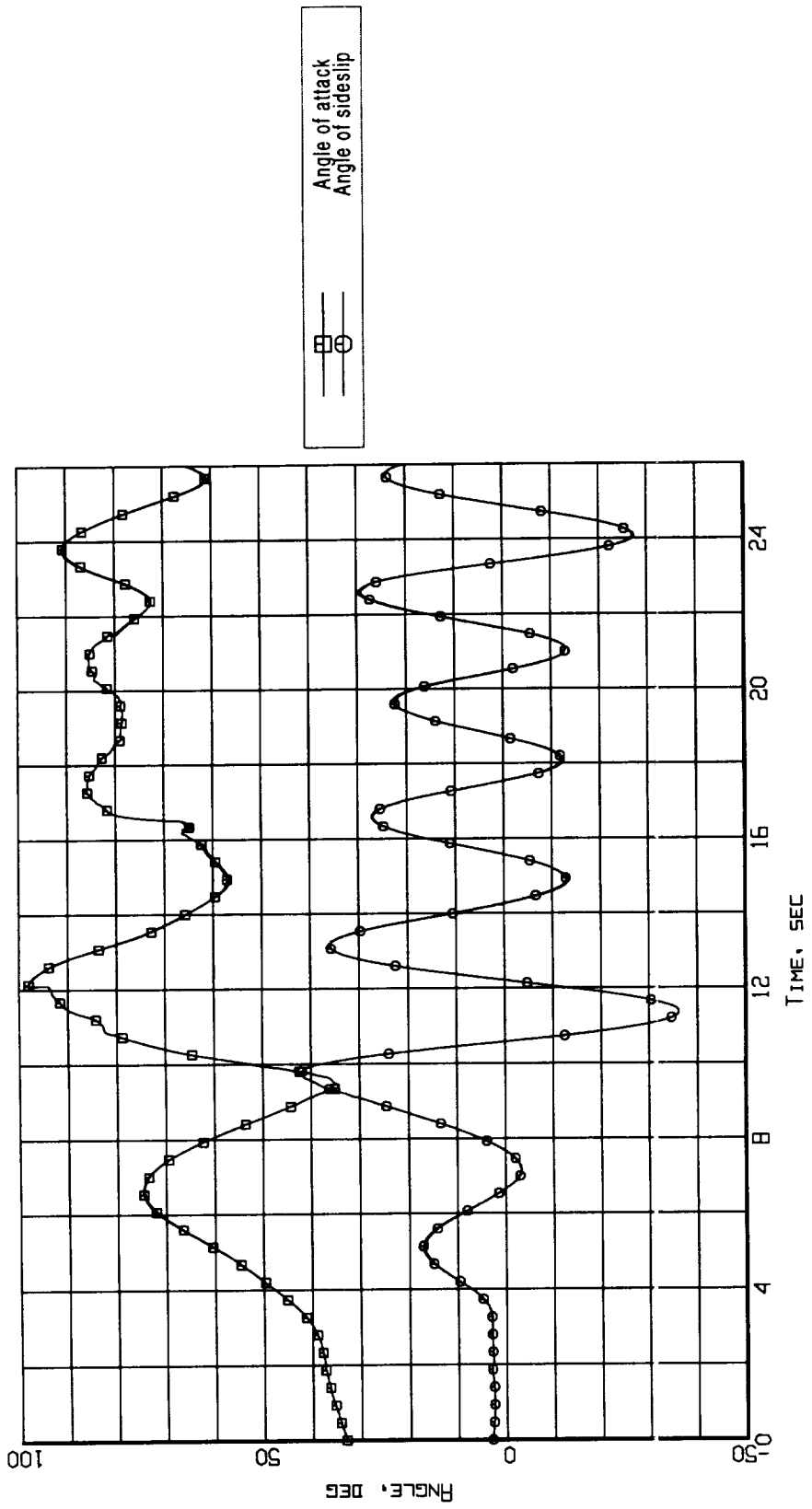

Figure B6-3. Aerodynamic flowstream descriptors - angle of attack and angle of sideslip (Flight 239, Test Point 39b).

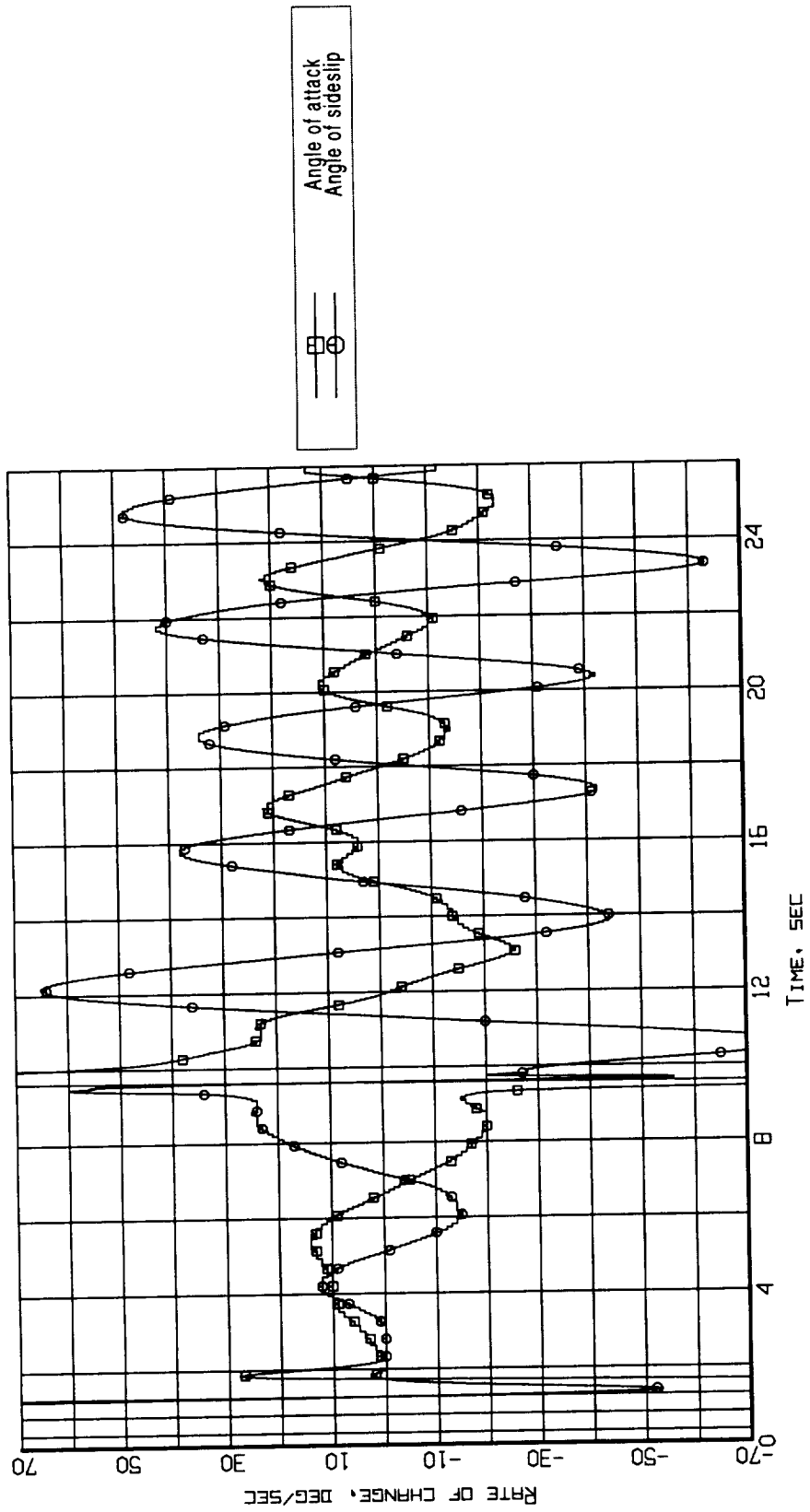

Figure B6-4. Aerodynamic flowstream descriptors - rate of change of angle of attack and angle of sideslip (Flight 239, Test Point 39b).

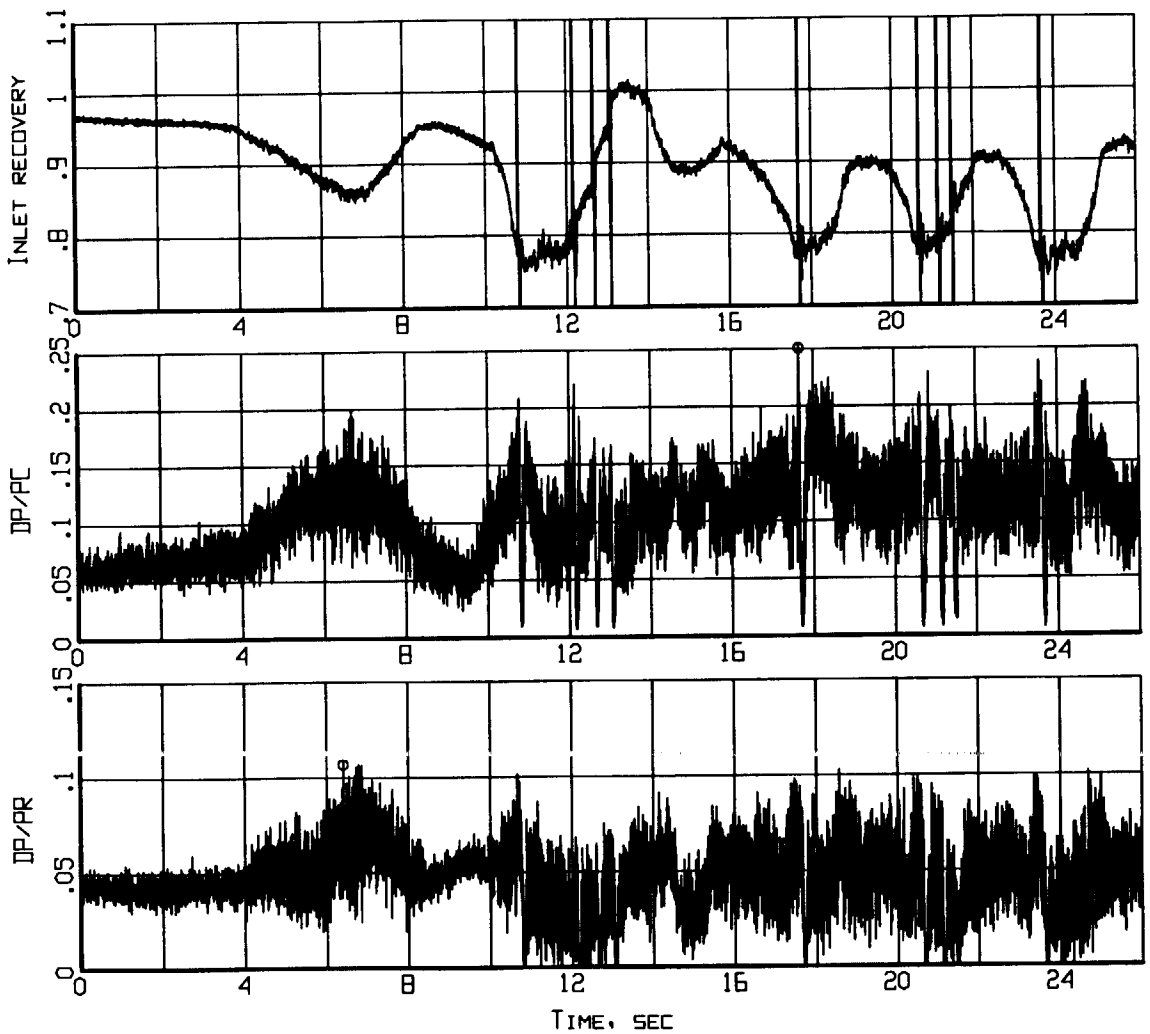

Figure B6-5. Time histories of inlet recovery and distortion descriptors (Flight 239, Test Point 39b).

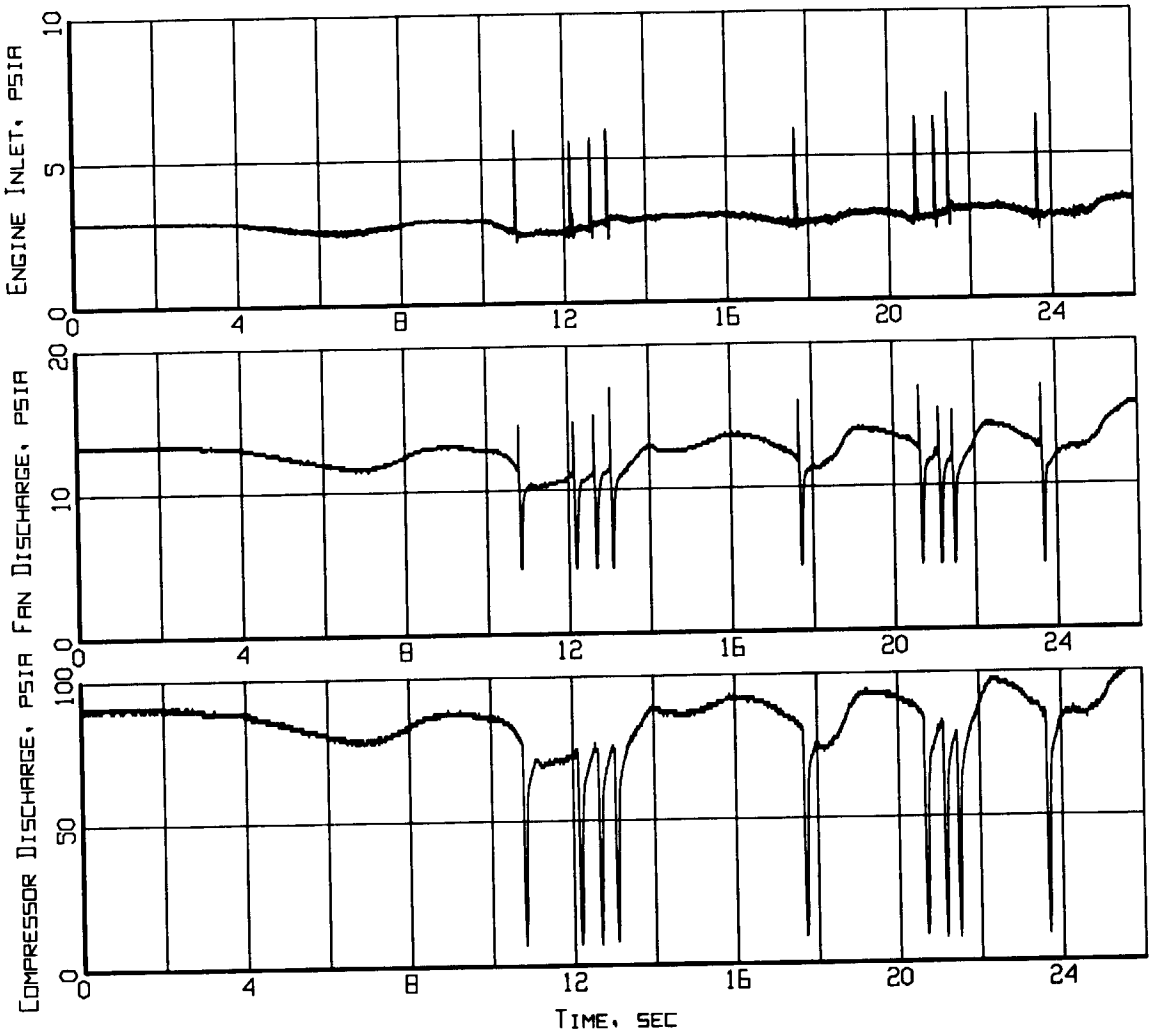

Figure B6-6. Measured inlet/engine entry and engine internal pressures time histories (Flight 239, Test Point 39b).

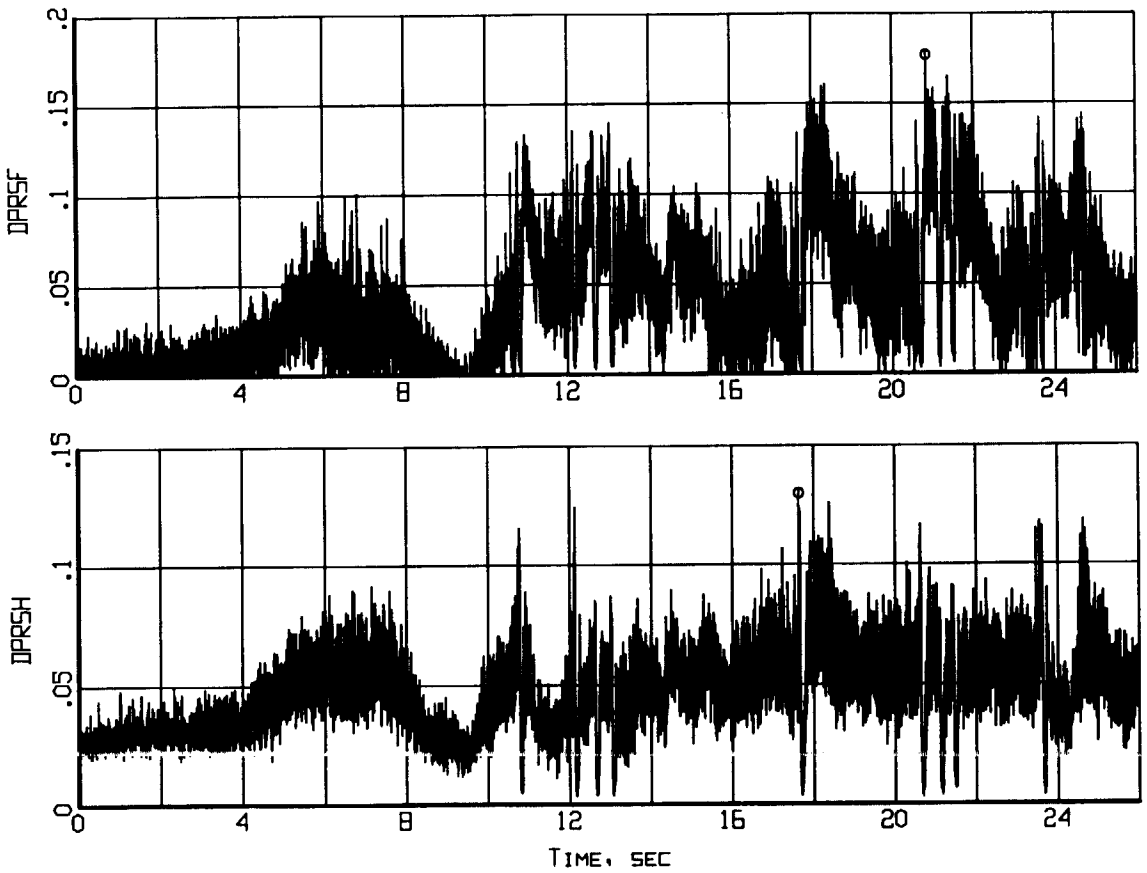

Symbols Denote
Max Points

Figure B6-7. Time histories of the predicted loss of stability pressure ratio for the fan and the compressor (Flight 239, Test Point 39b).

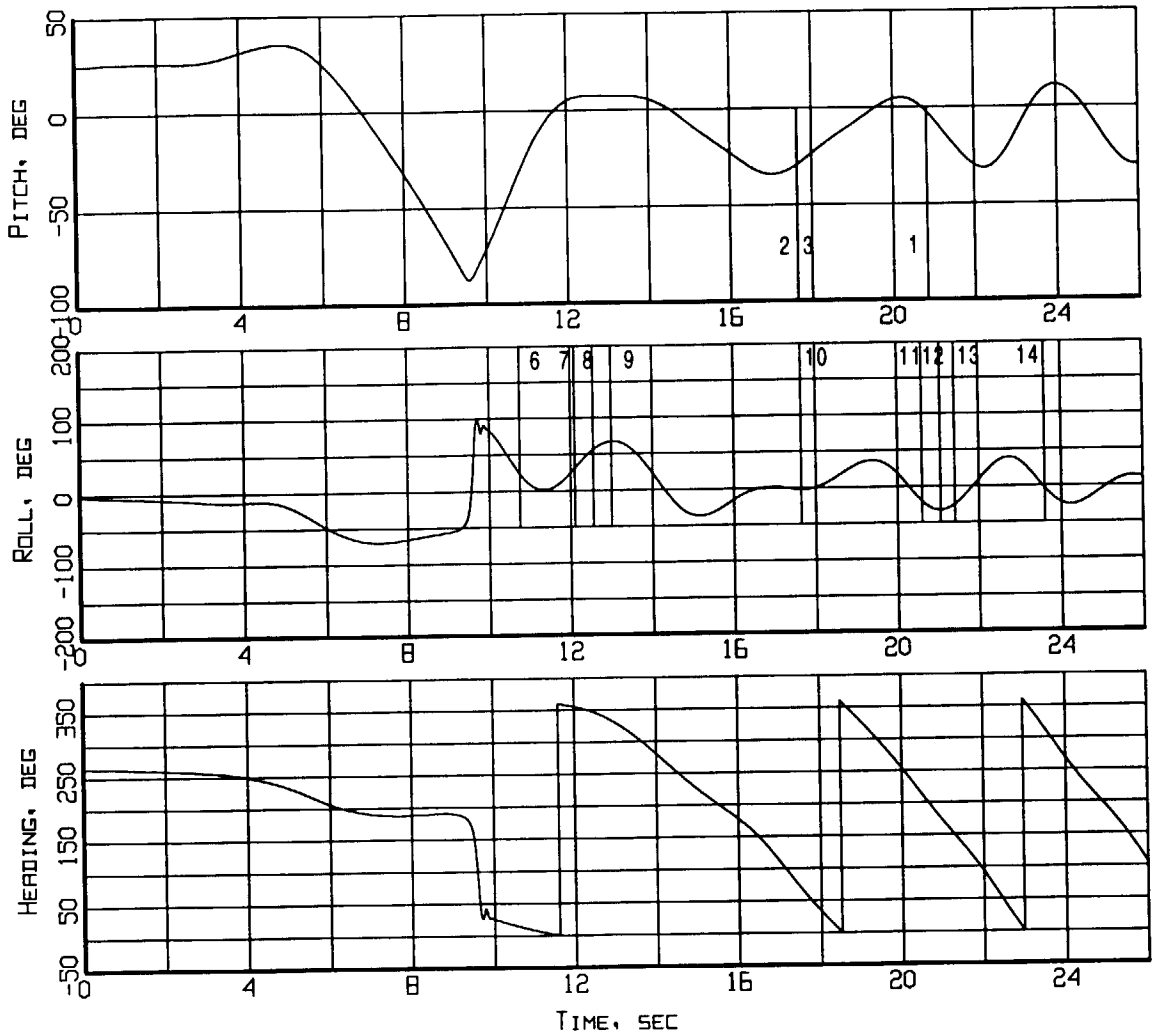

Event Marker

1 - Max DPRSF
2 - Max DPRSH
3 - Max DP/PC
6 - Stall 1
7 - Stall 2
8 - Stall 3
9 - Stall 4
10 - Stall 5
11 - Stall 6
12 - Stall 7
13 - Stall 8
14 - Stall 9

Figure B6-8. Event markers superposed on the aircraft attitude time histories (Flight 239, Test Point 39b).

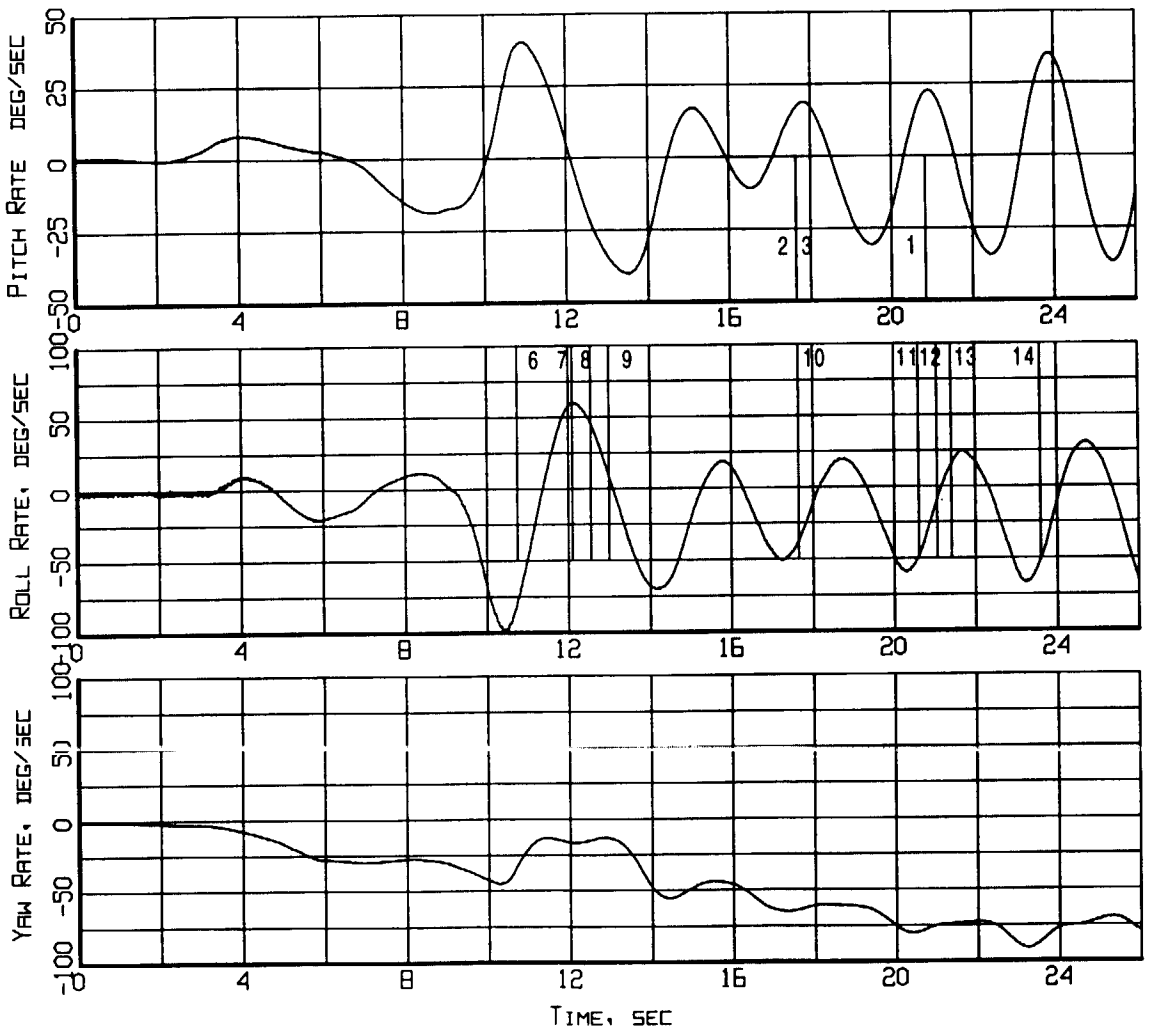

Event Marker

1 - Max DPRSF
2 - Max DPRSH
3 - Max DP/PC
6 - Stall 1
7 - Stall 2
8 - Stall 3
9 - Stall 4
10 - Stall 5
11 - Stall 6
12 - Stall 7
13 - Stall 8
14 - Stall 9

Figure B6-9. Event markers superposed on the aircraft motion time histories (Flight 239, Test Point 39b).

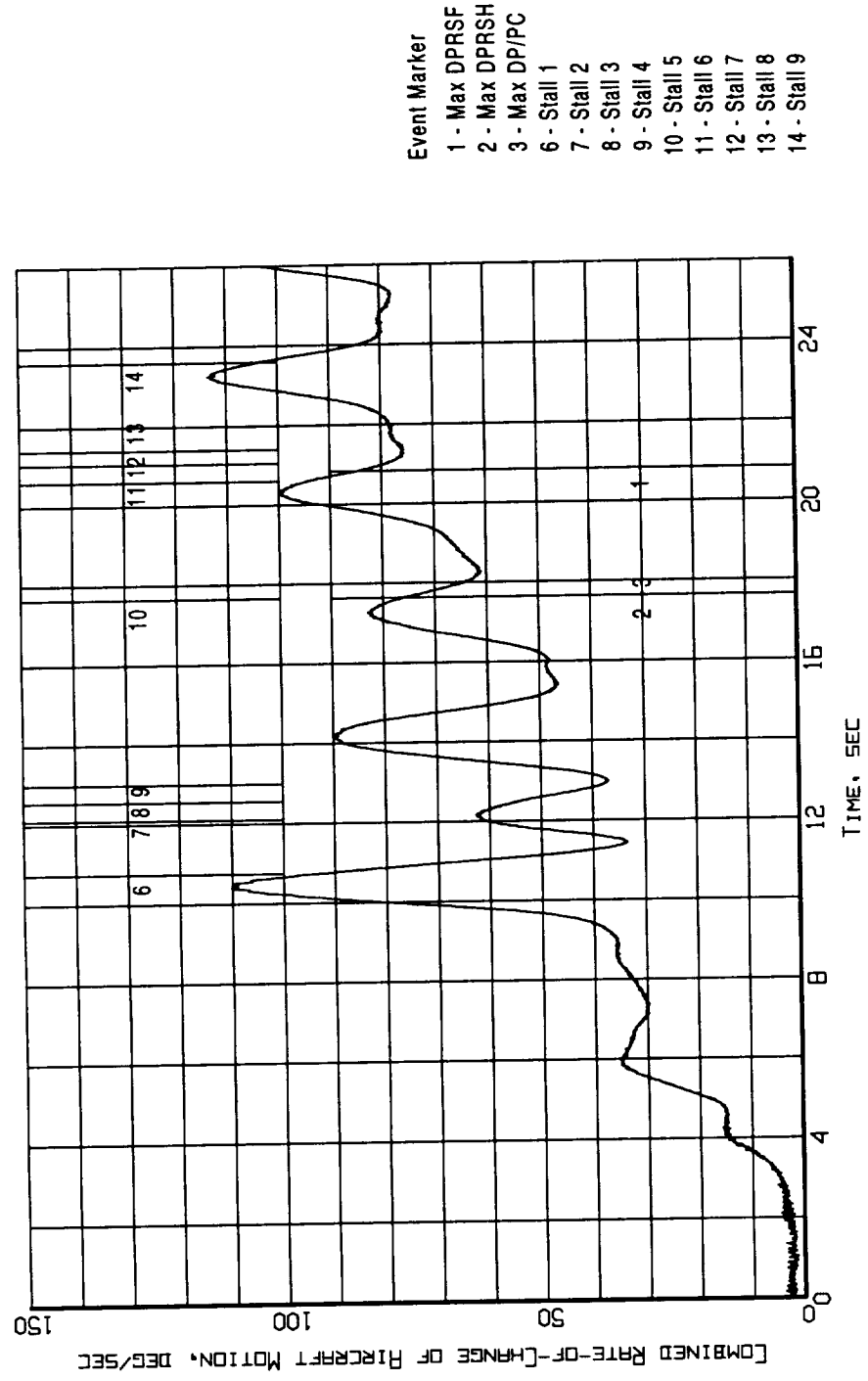

Figure B6-10. Event markers superposed on the combined of rate-of-change of aircraft motion time history (Flight 239, Test Point 39b).

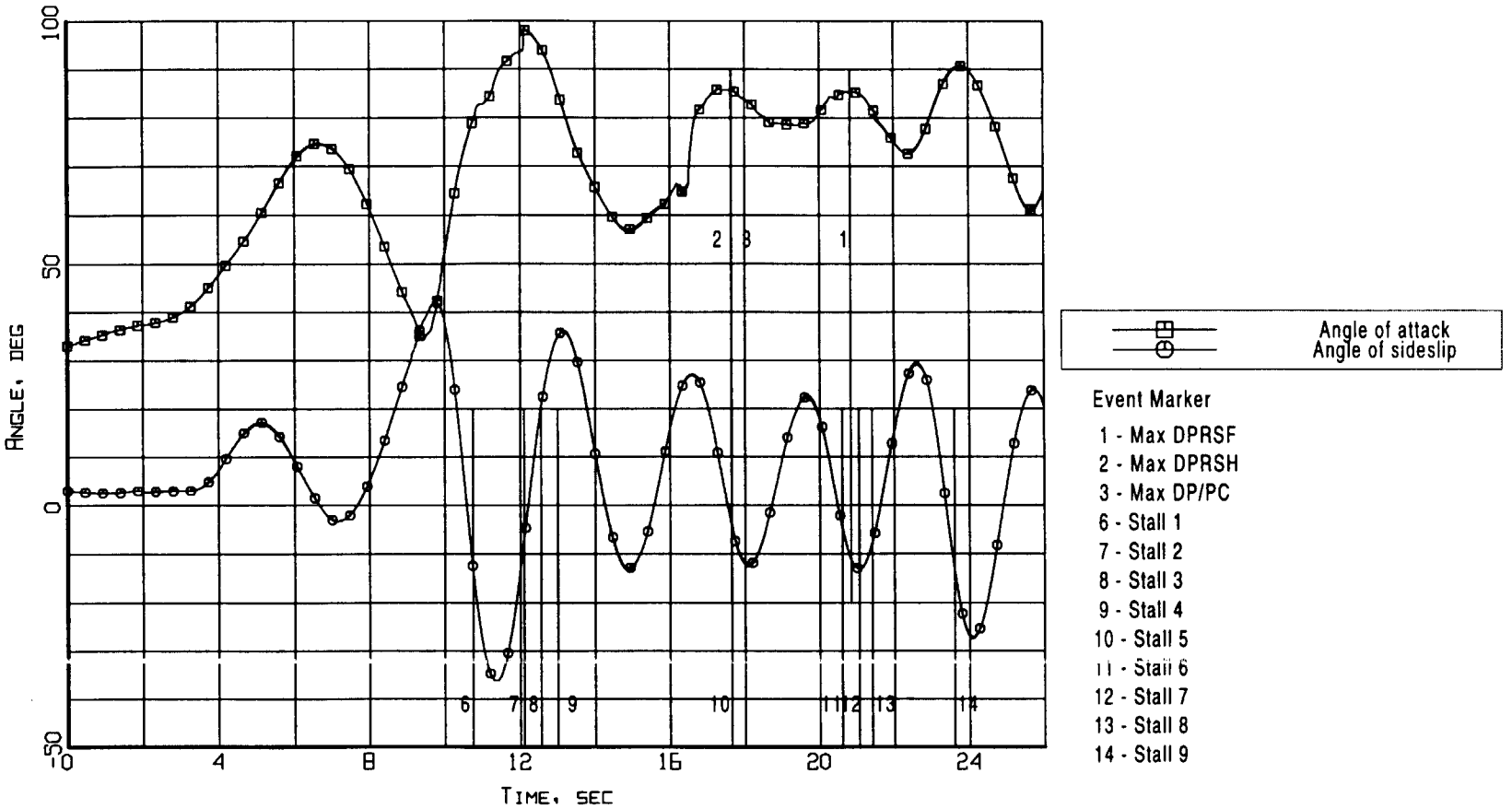

Figure B6-11. Event markers superposed on the aerodynamic flowstream descriptor time histories (Flight 239, Test Point 39b).

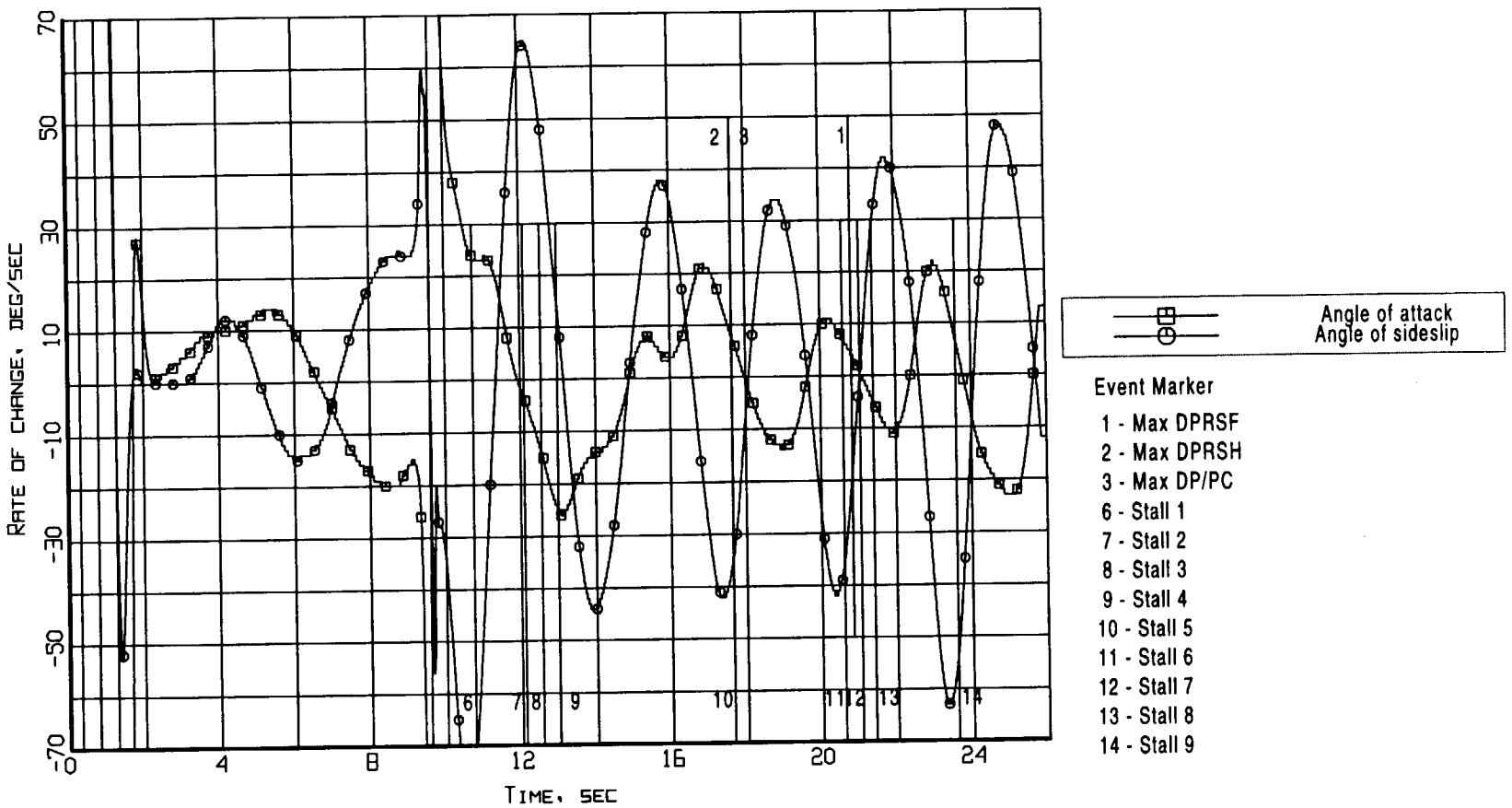

Figure B6-12. Event markers superposed on the aerodynamic flowstream descriptors rate-of-change time histories (Flight 239, Test Point 39b).

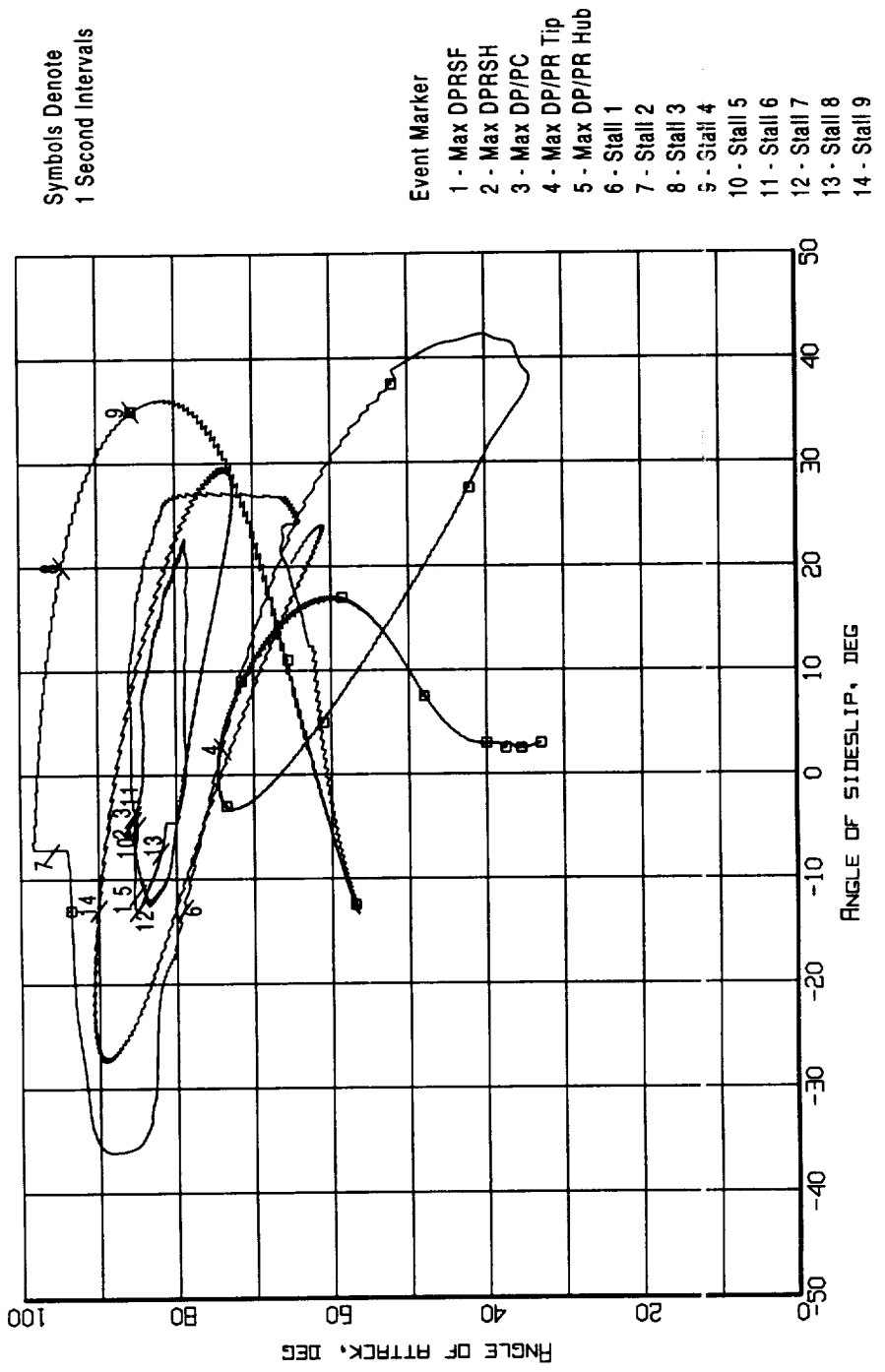

Figure B6-13. Event markers superposed on the aerodynamic flowstream descriptors trajectory (Flight 239, Test Point 39b).

Appendix B7 - Flight 238, Test Point 40b

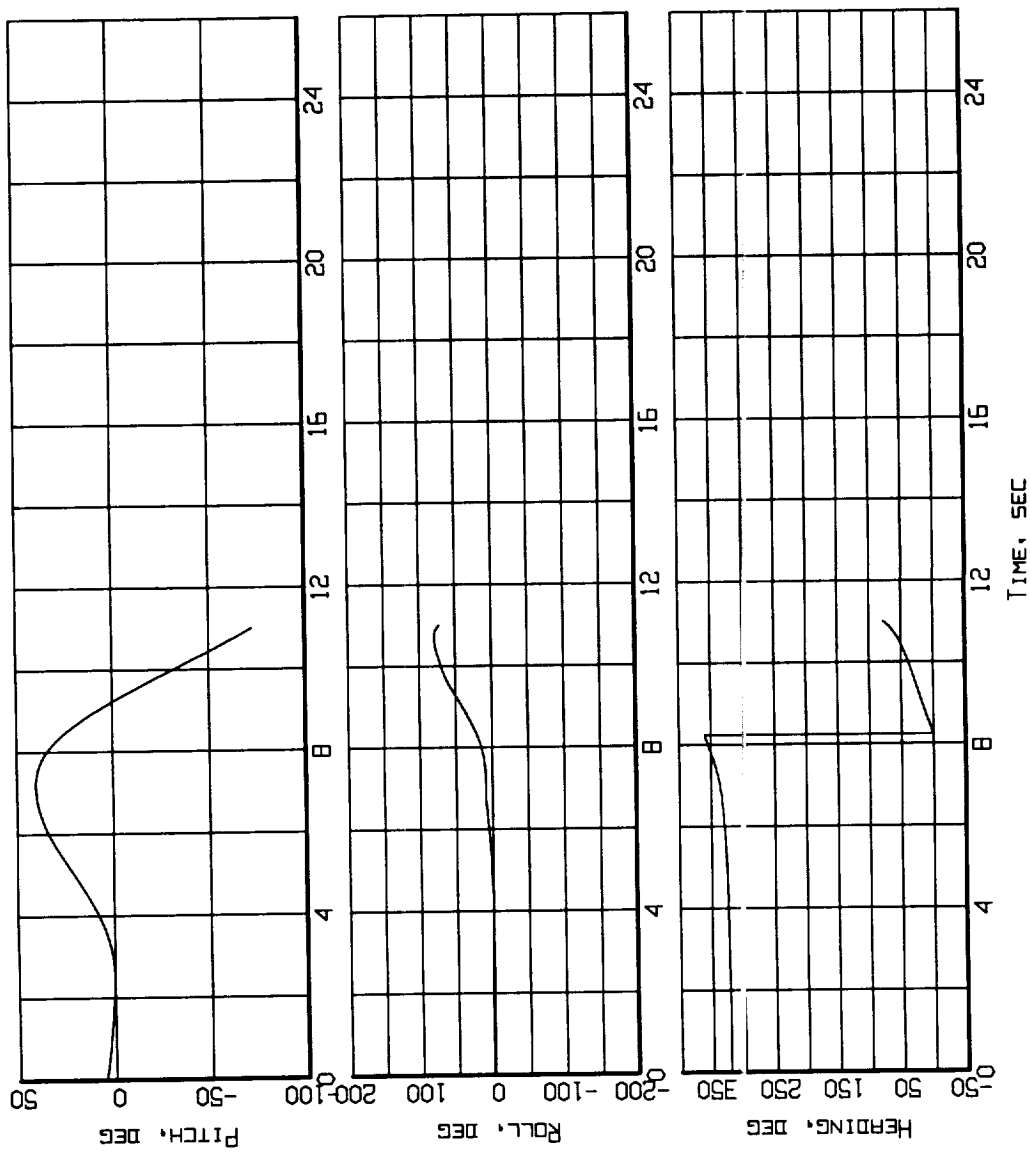

Figure B7-1. Aircraft attitude - Pitch, Roll, and Heading (Flight 238, Test Point 40b).

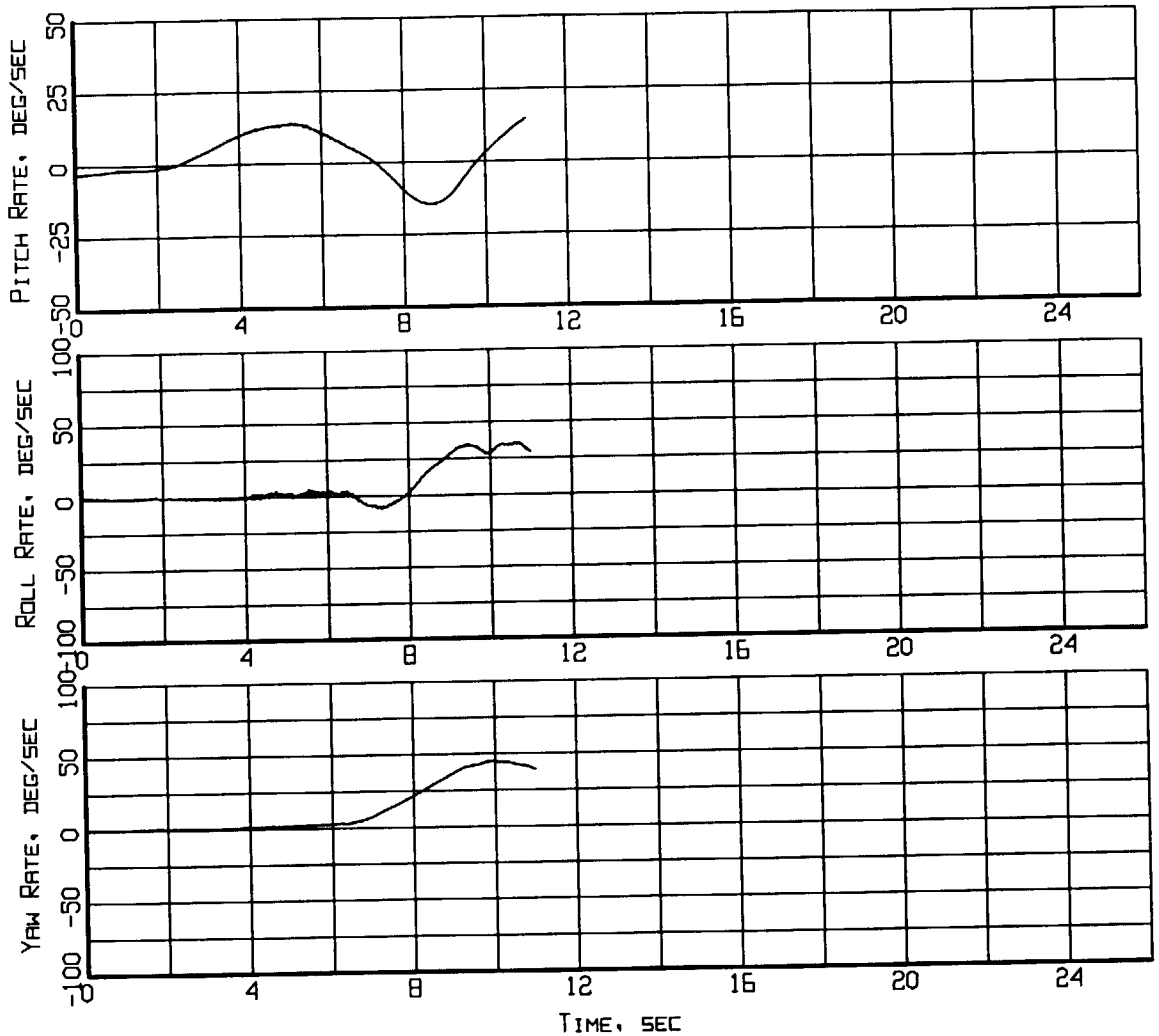

Figure B7-2. Aircraft Motion - Rate-of-Change of Pitch, Roll and Heading (Flight 238, Test Point 40b).

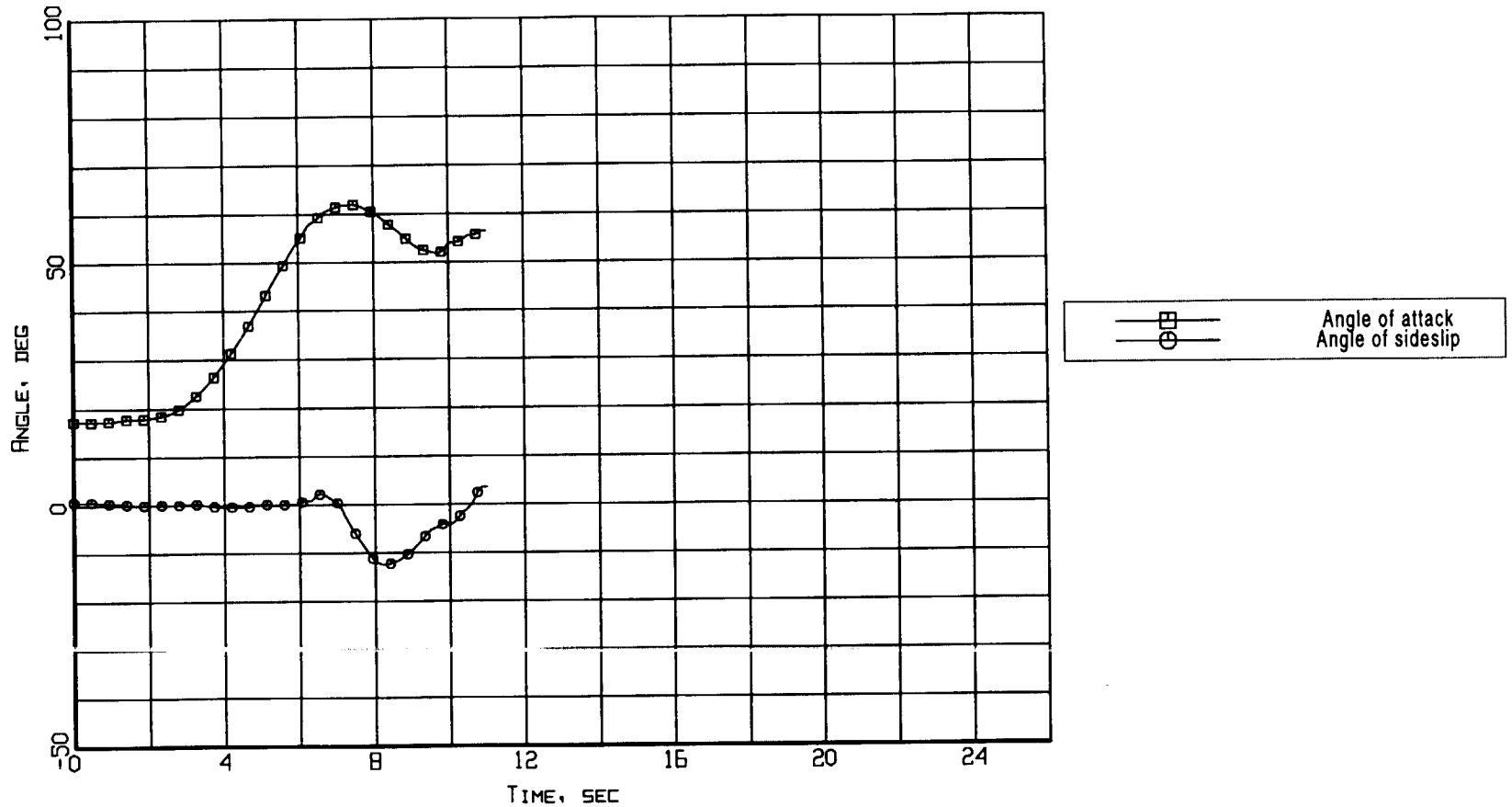

Figure B7-3. Aerodynamic flowstream descriptors - angle of attack and angle of sideslip (Flight 238, Test Point 40b).

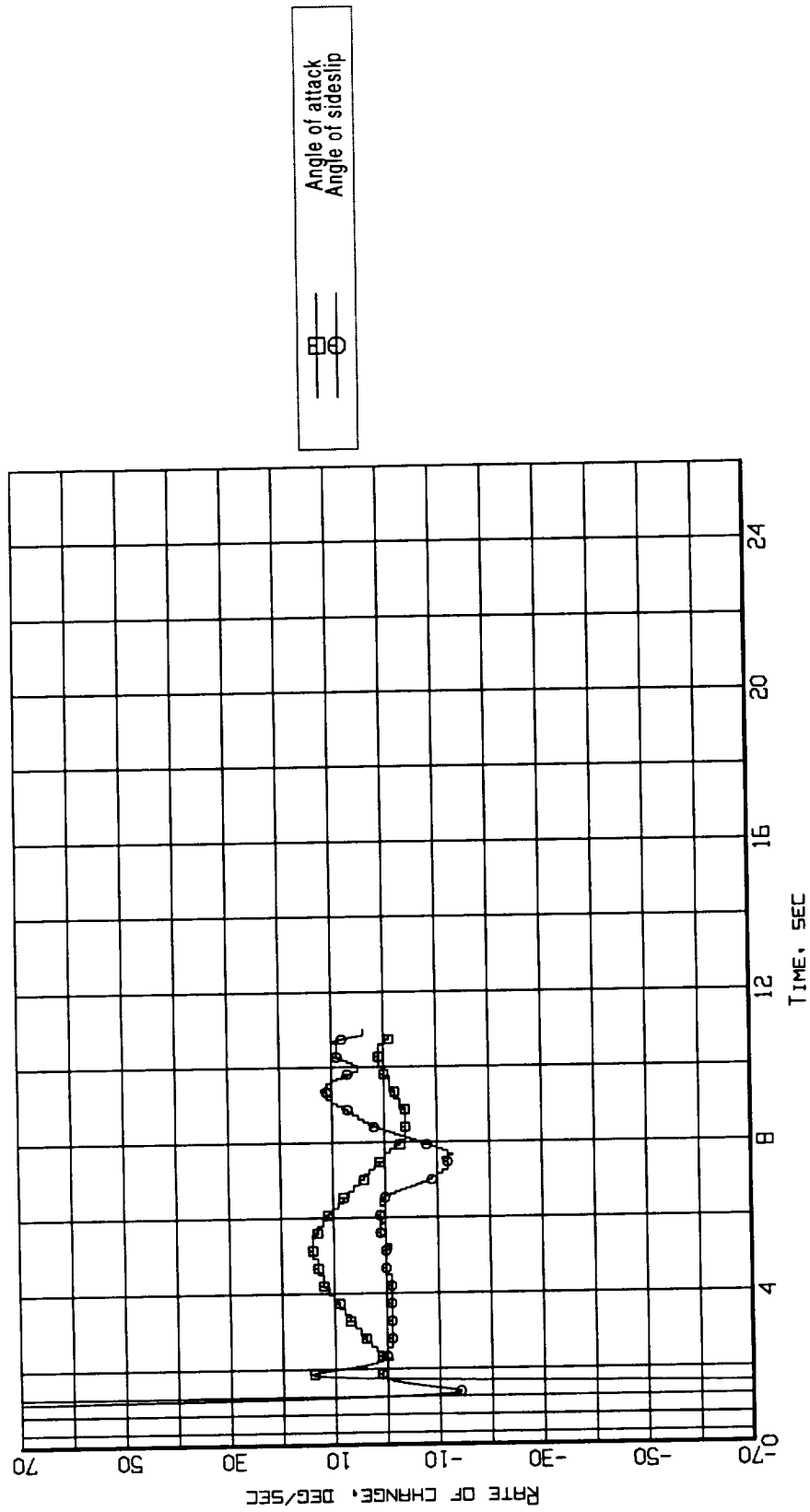

Figure B7-4. Aerodynamic flowstream descriptors - rate of change of angle of attack and angle of sideslip (Flight 238, Test Point 40b).

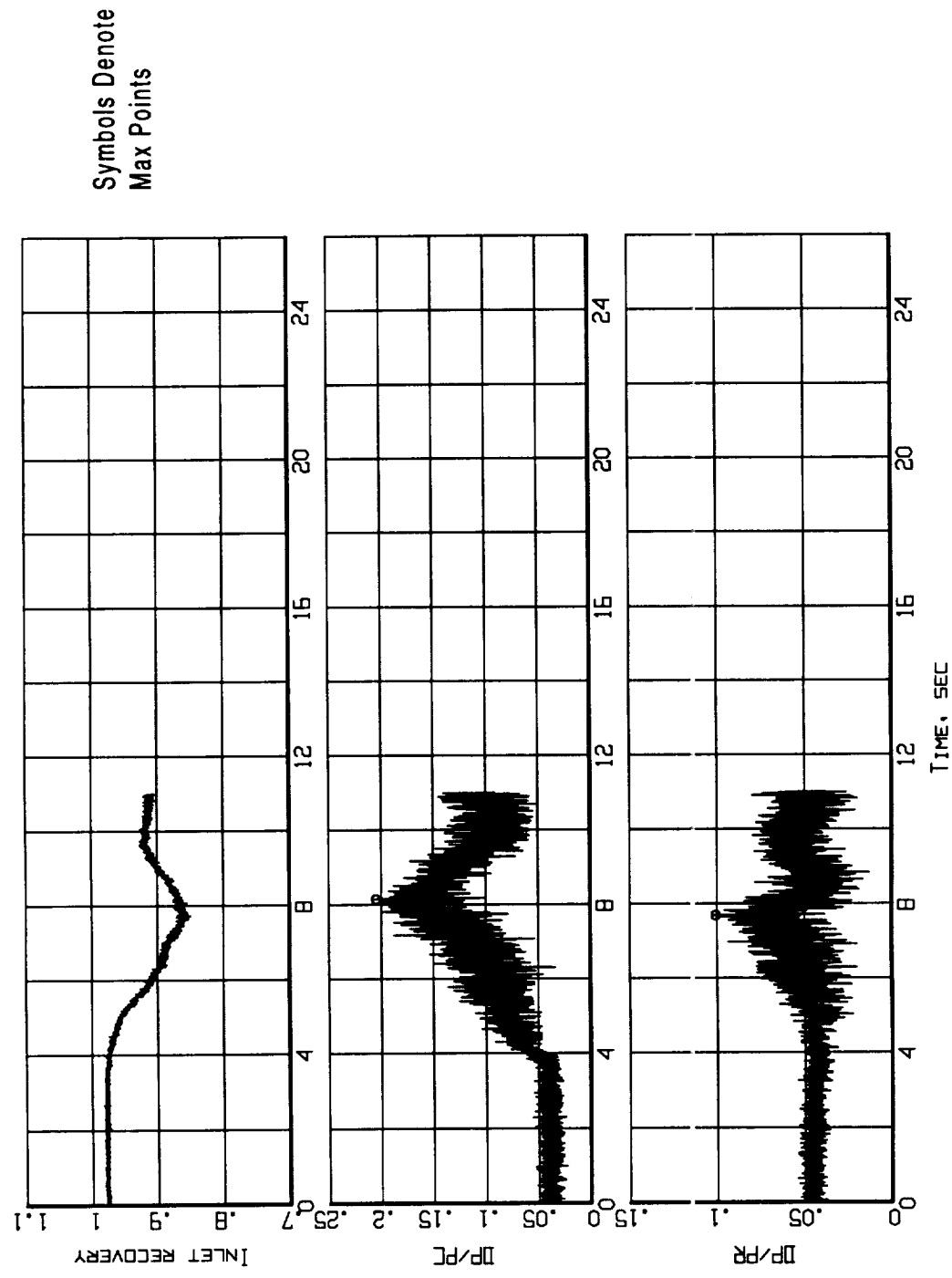

Figure B7-5. Time histories of inlet recovery and distortion descriptors (Flight 238, Test Point 40b).

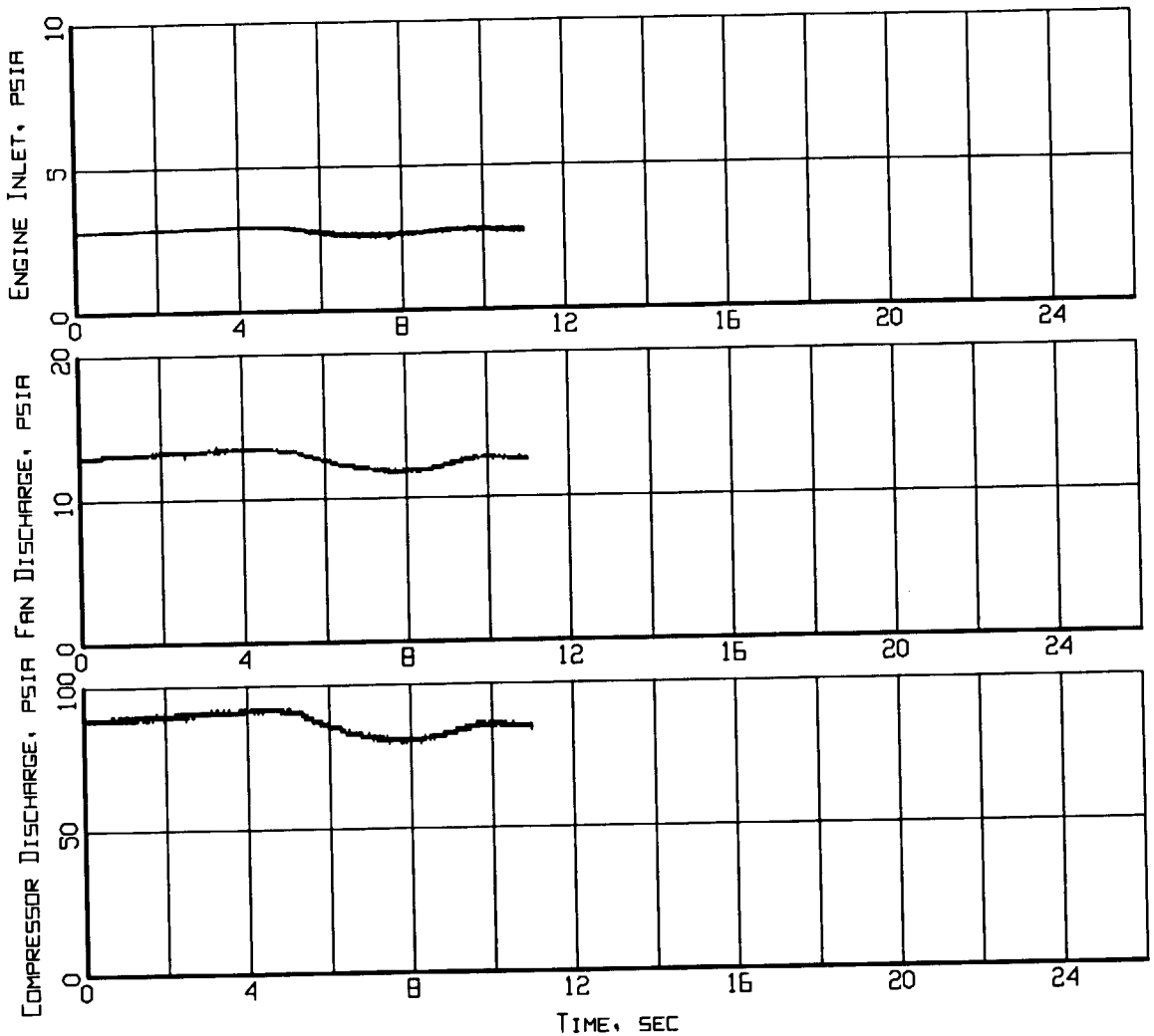

Figure B7-6. Measured inlet/engine entry and engine internal pressures time histories (Flight 238, Test Point 40b).

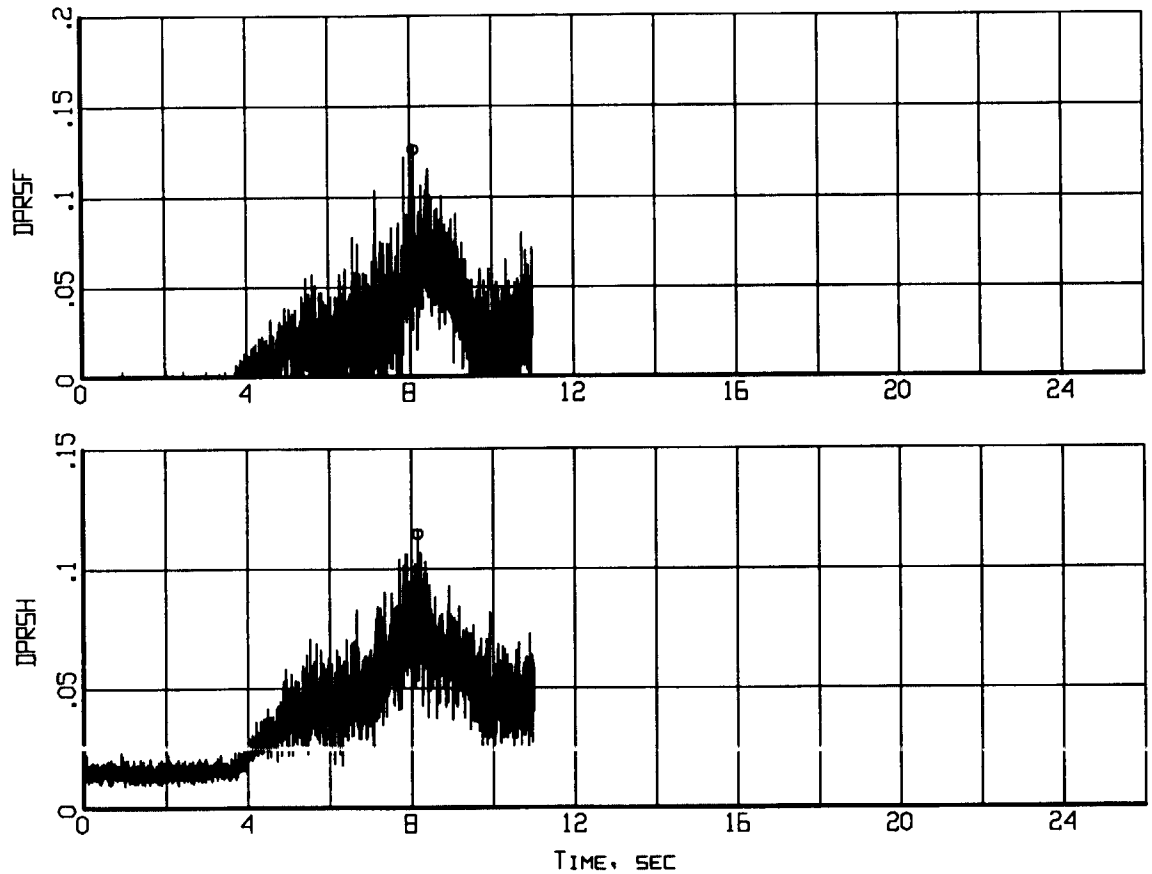

Symbols Denote
Max Points

Figure B7-7. Time histories of the predicted loss of stability pressure ratio for the fan and the compressor (Flight 238, Test Point 40b).

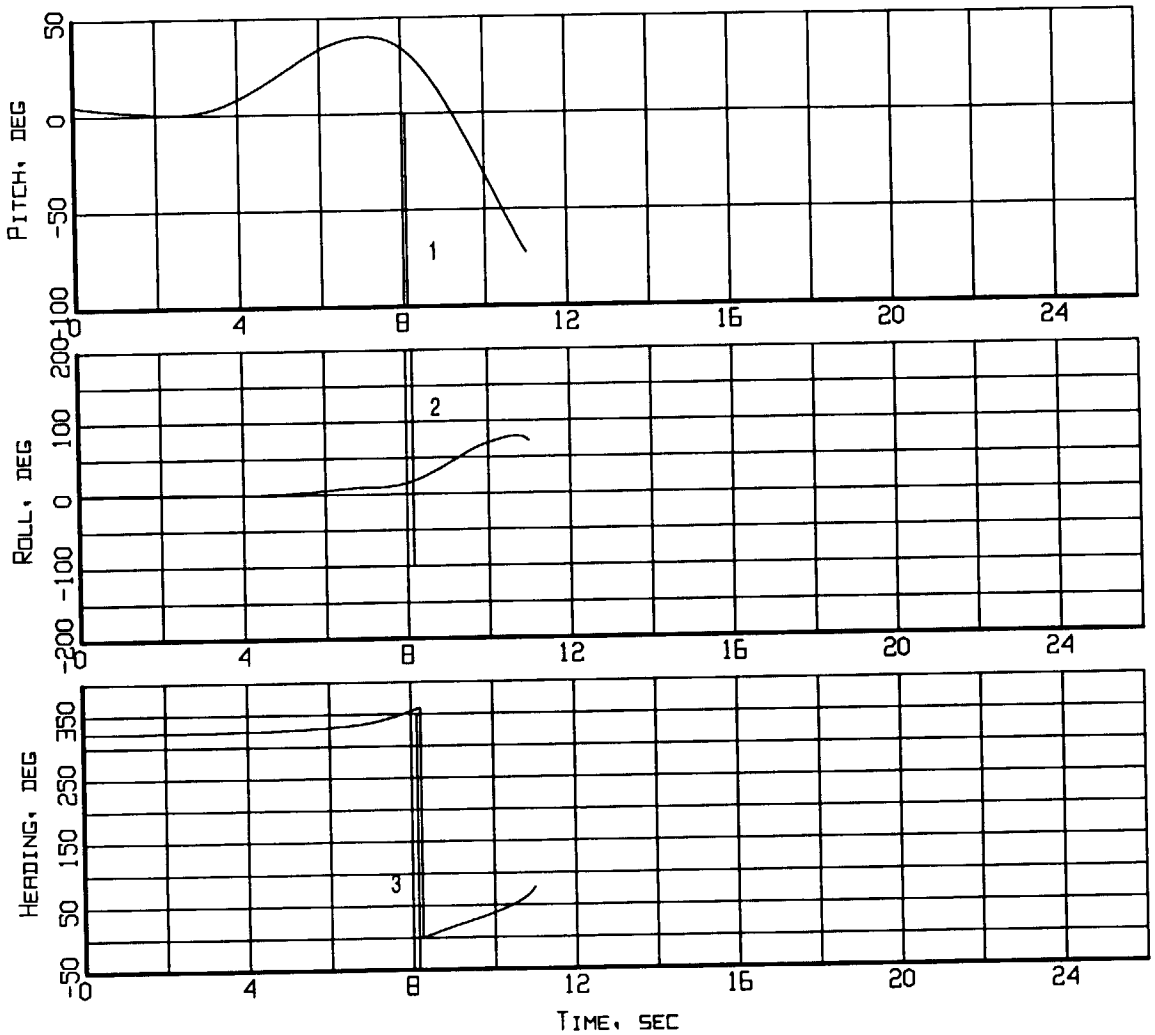

Event Marker

1 - Max DPRSF

2 - Max DPRSH

3 - Max DP/PC

Figure B7-8. Event markers superposed on the aircraft attitude time histories (Flight 238, Test Point 40b).

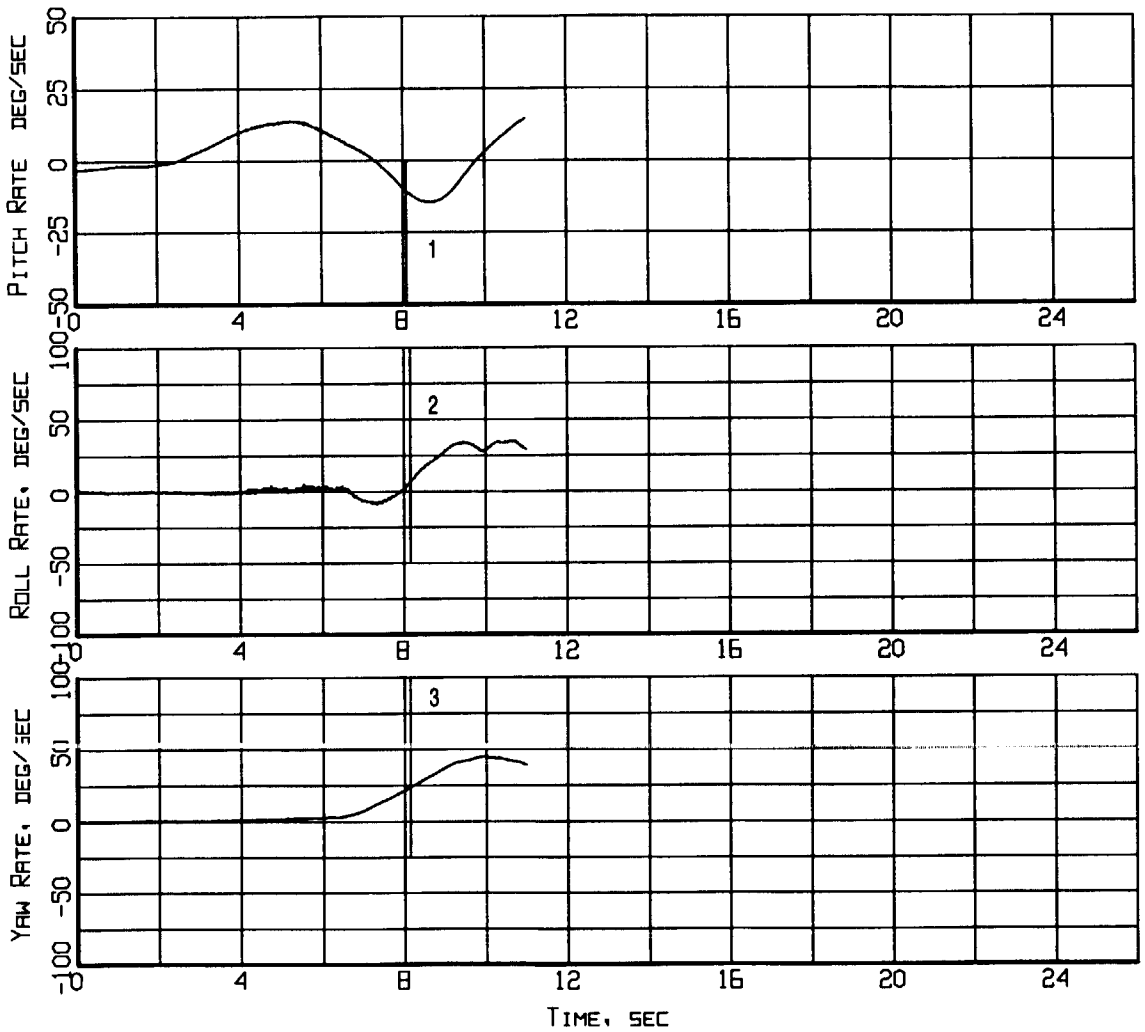

Event Marker

1 - Max DPRSF

2 - Max DPRSH

3 - Max DP/PC

Figure B7-9. Event markers superposed on the aircraft motion time histories (Flight 238, Test Point 40b).

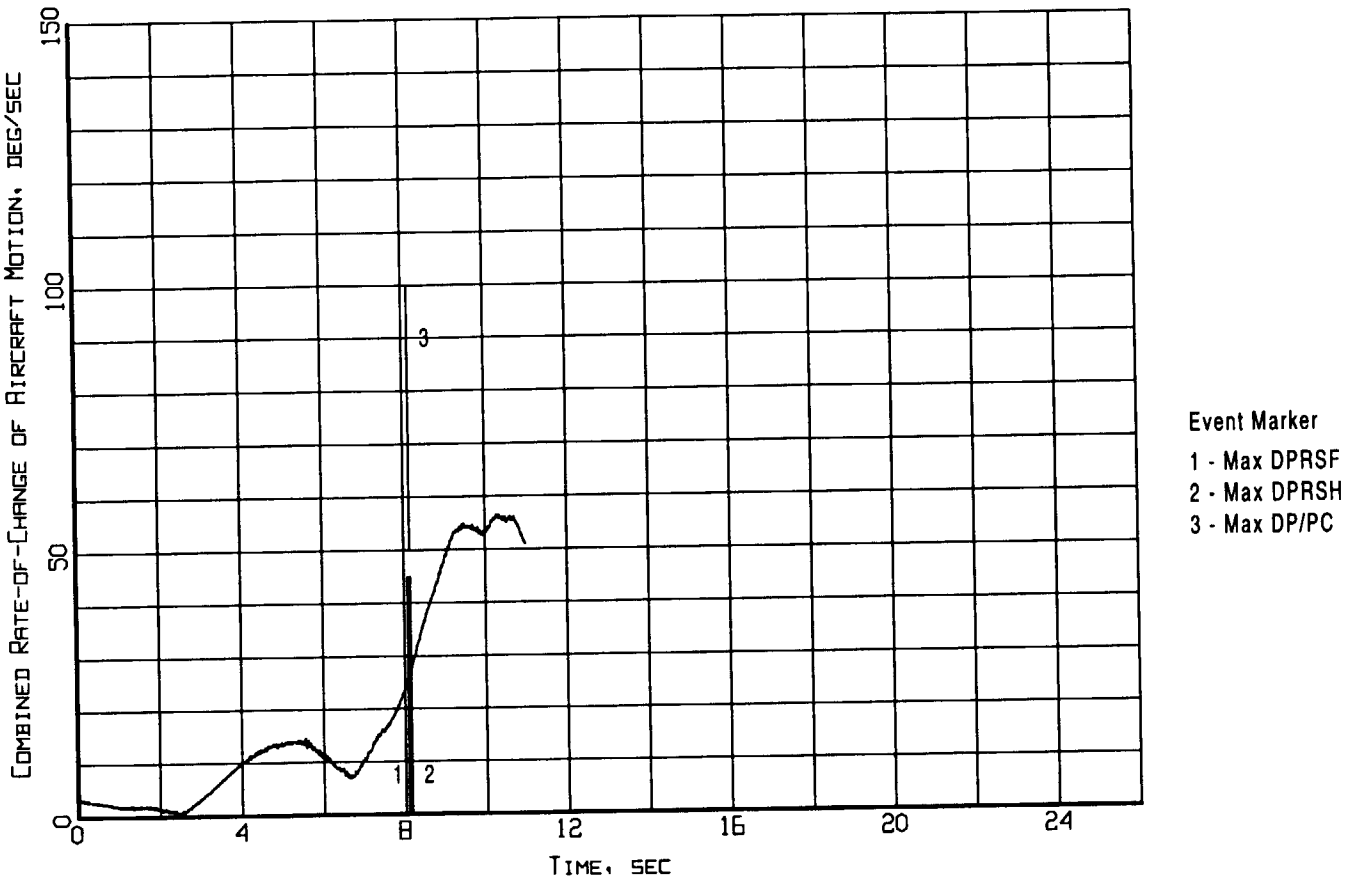

Figure B7-10. Event markers superposed on the combined of rate-of-change of aircraft motion time history (Flight 238, Test Point 40b).

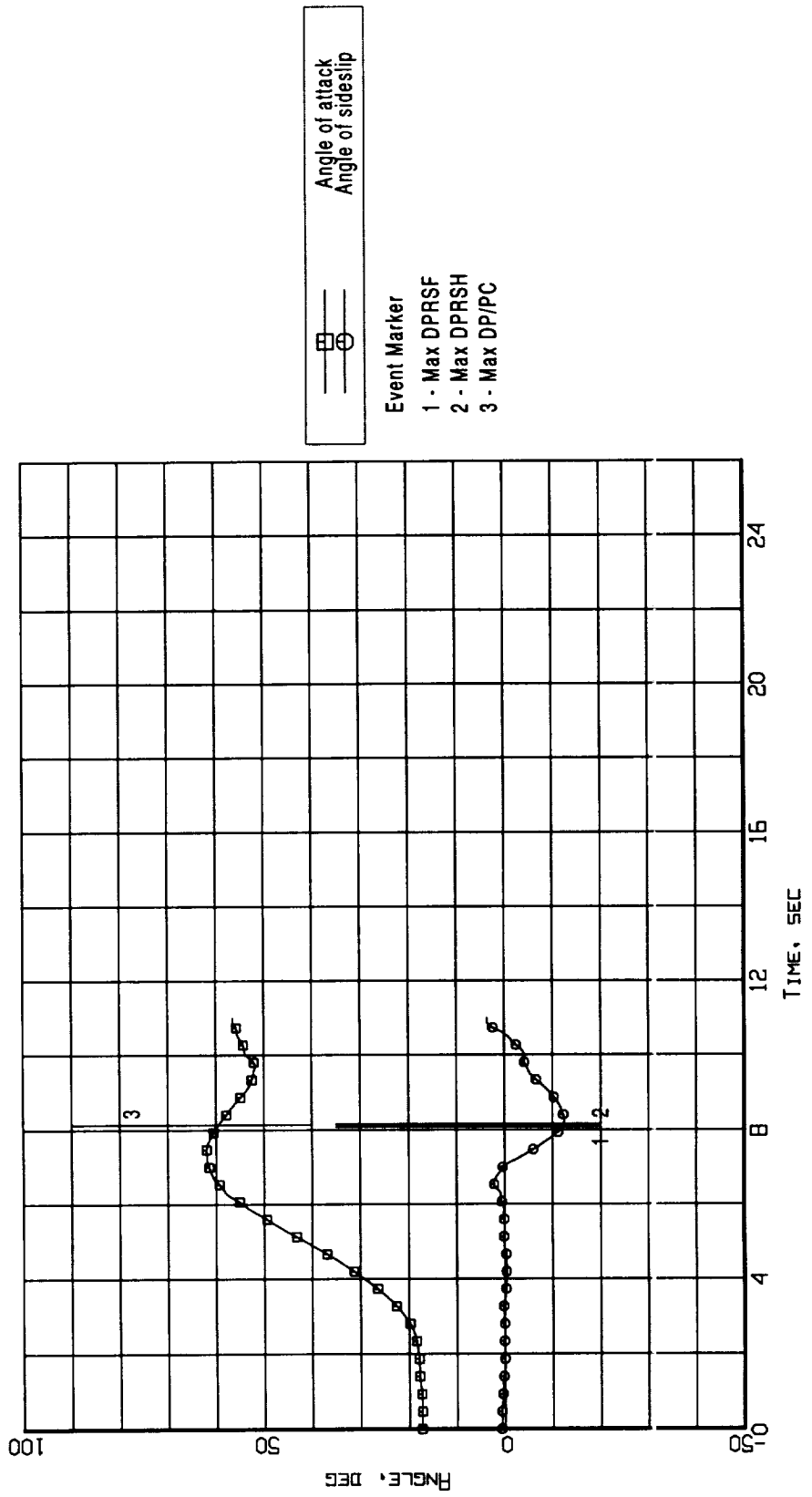

Figure B7-11. Event markers superposed on the aerodynamic flowstream descriptor time histories (Flight 238, Test Point 40b).

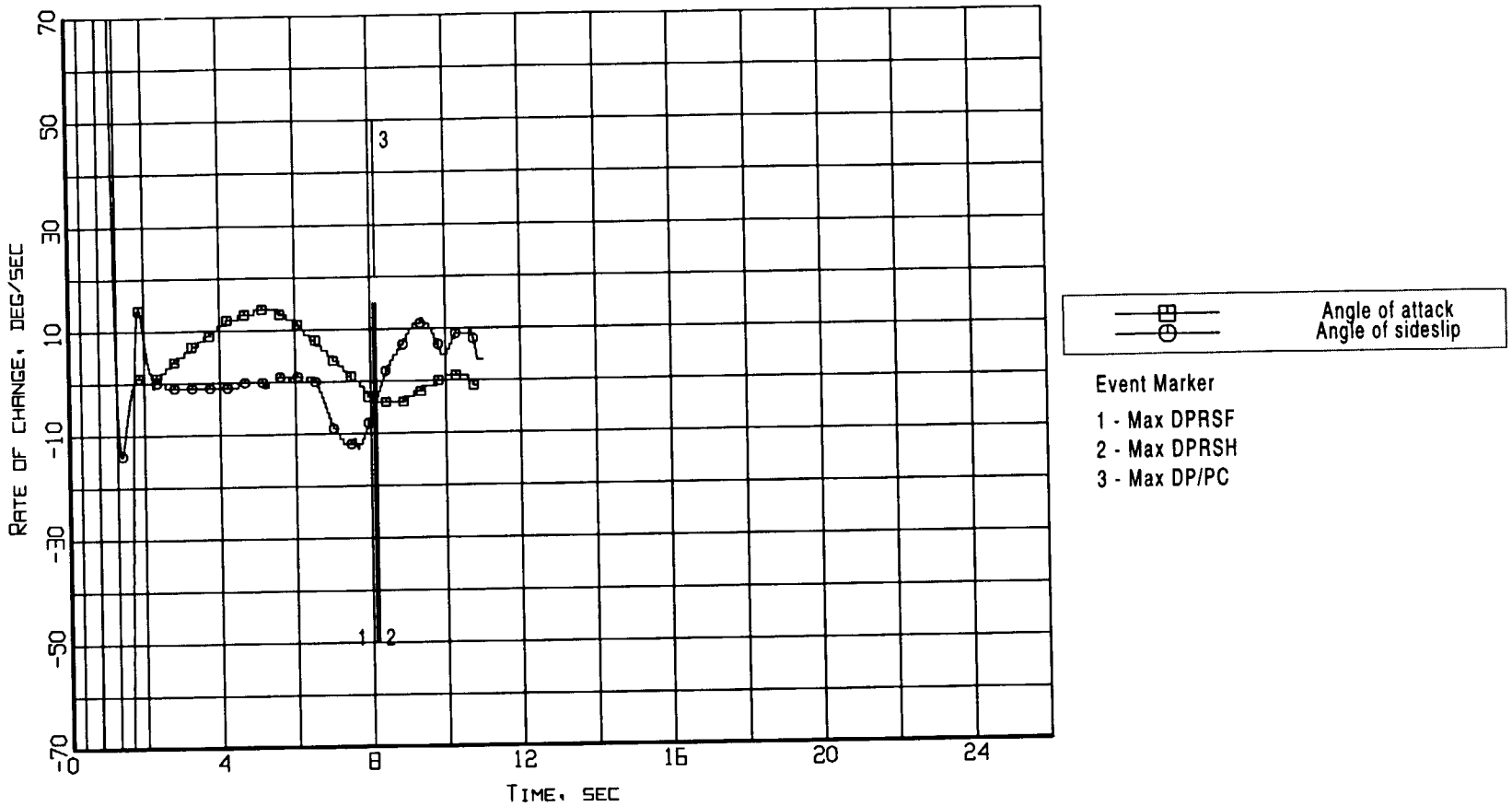

Figure B7-12. Event markers superposed on the aerodynamic flowstream descriptors rate-of-change time histories (Flight 238, Test Point 40b).

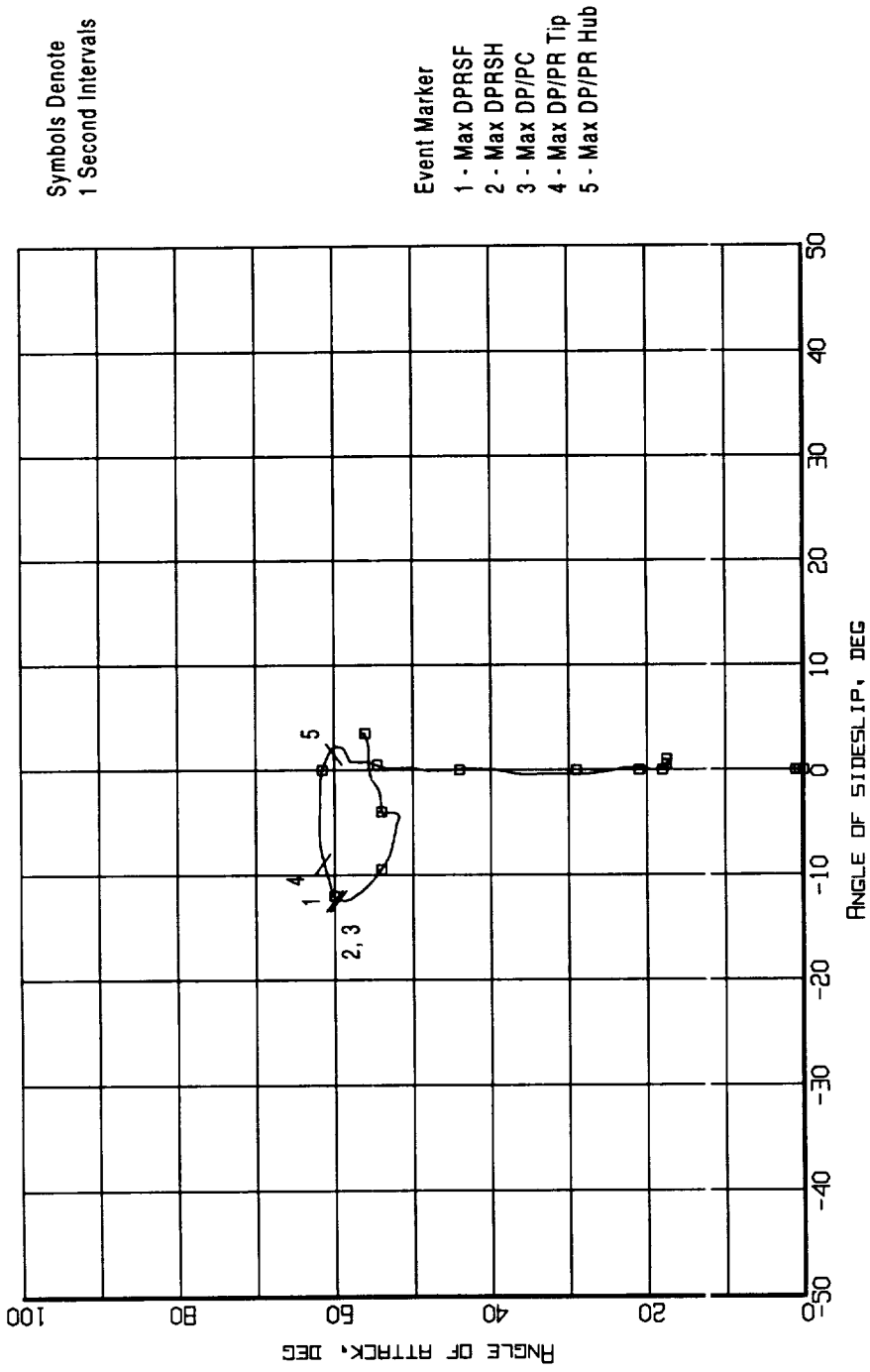

Figure B7-13. Event markers superposed on the aerodynamic flowstream descriptors trajectory (Flight 238, Test Point 40b).

Appendix B8 - Flight 240, Test Point 41b

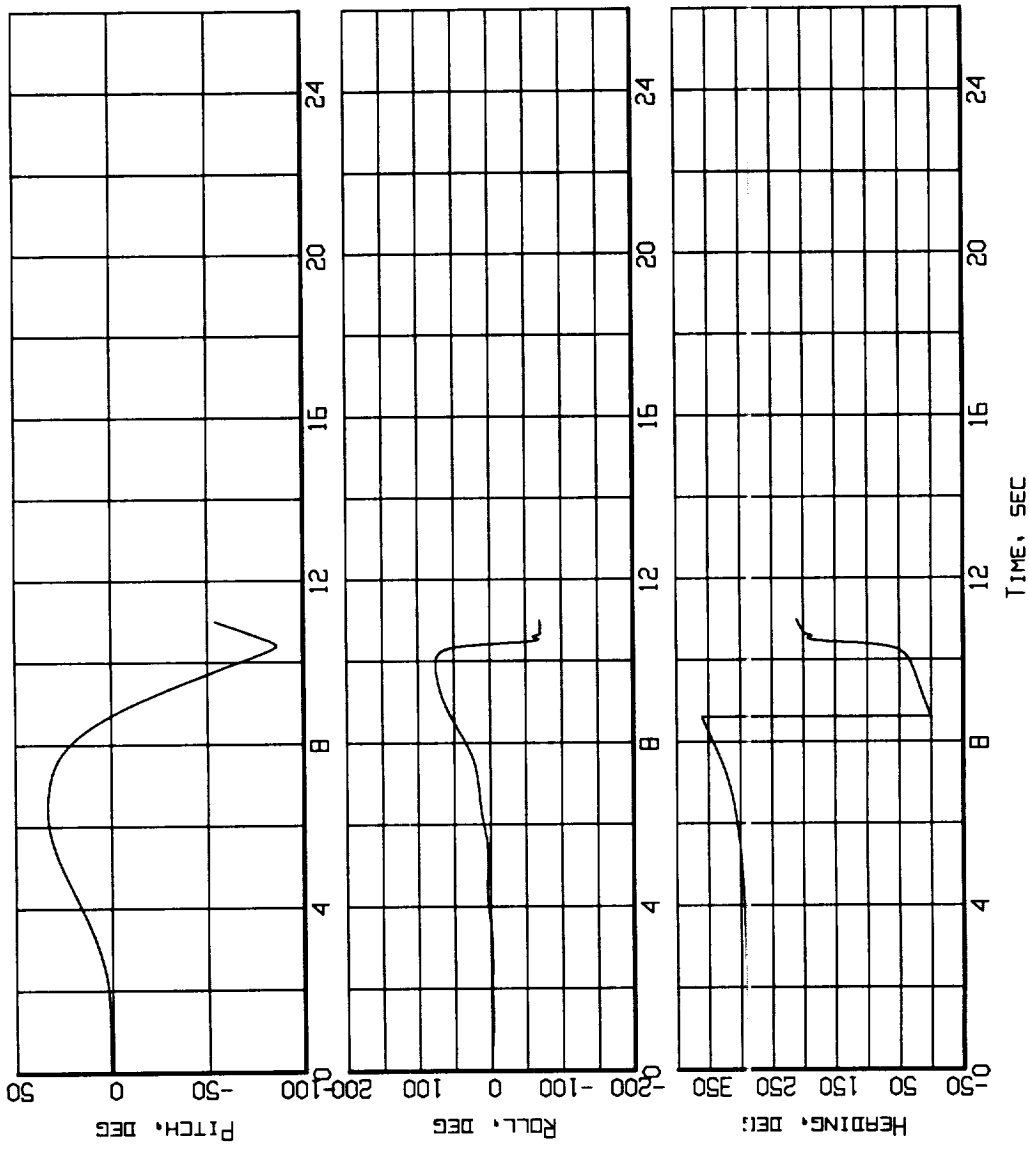

Figure B8-1. Aircraft attitude - Pitch, Roll, and Heading (Flight 240, Test Point 41b).

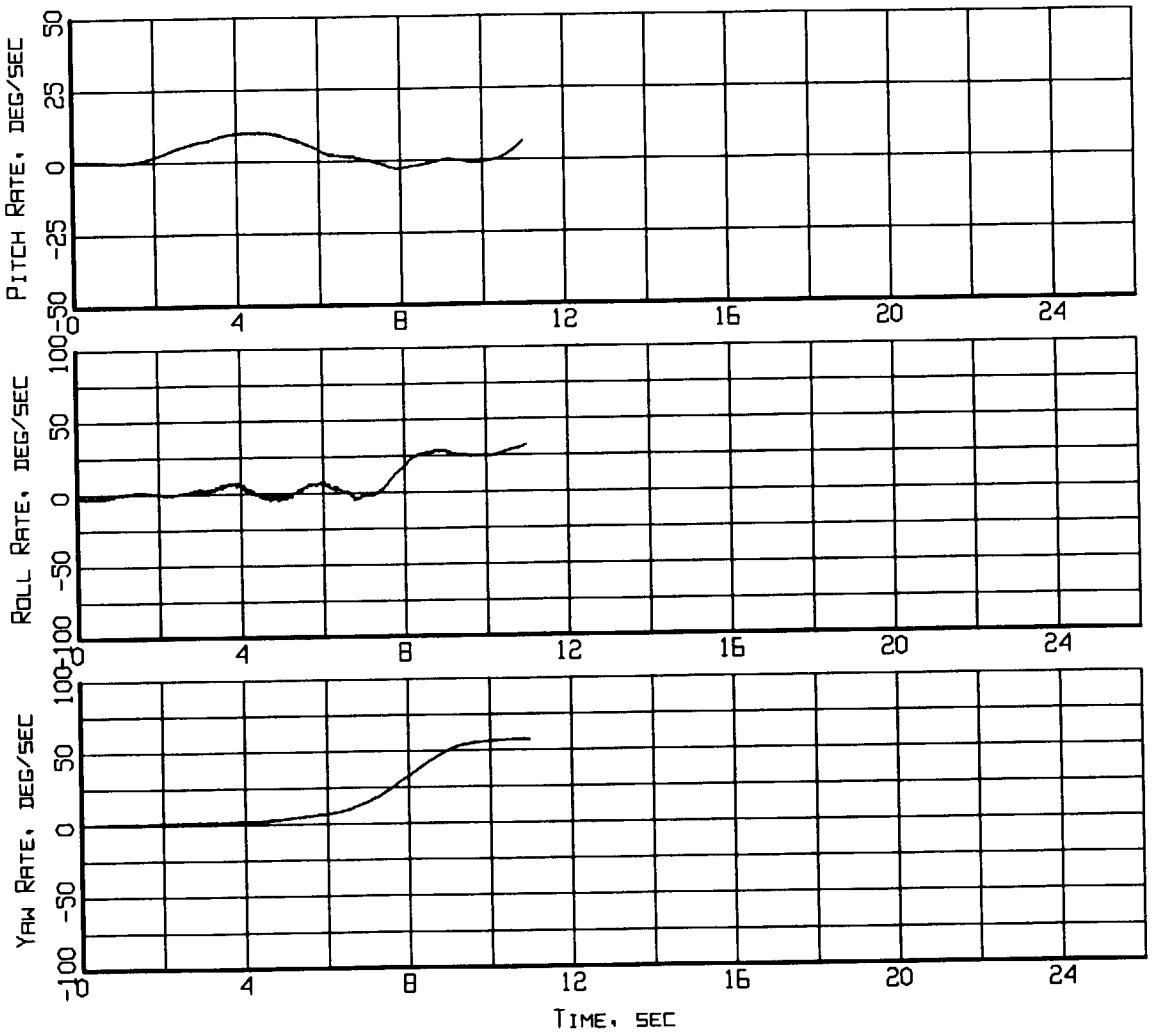

Figure B8-2. Aircraft Motion - Rate-of-Change of Pitch, Roll and Heading (Flight 240, Test Point 41b).

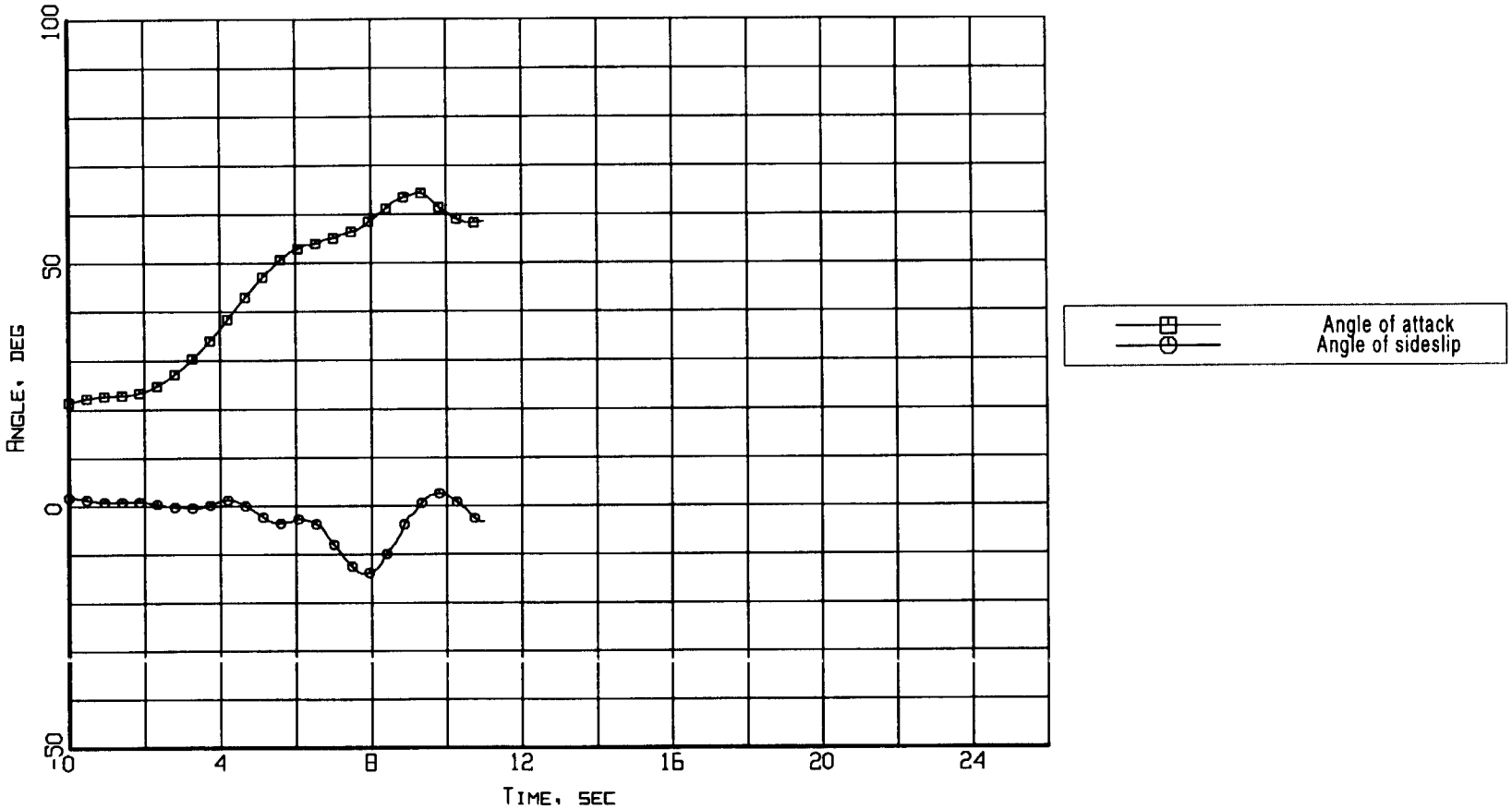

Figure B8-3. Aerodynamic flowstream descriptors - angle of attack and angle of sideslip (Flight 240, Test Point 41b).

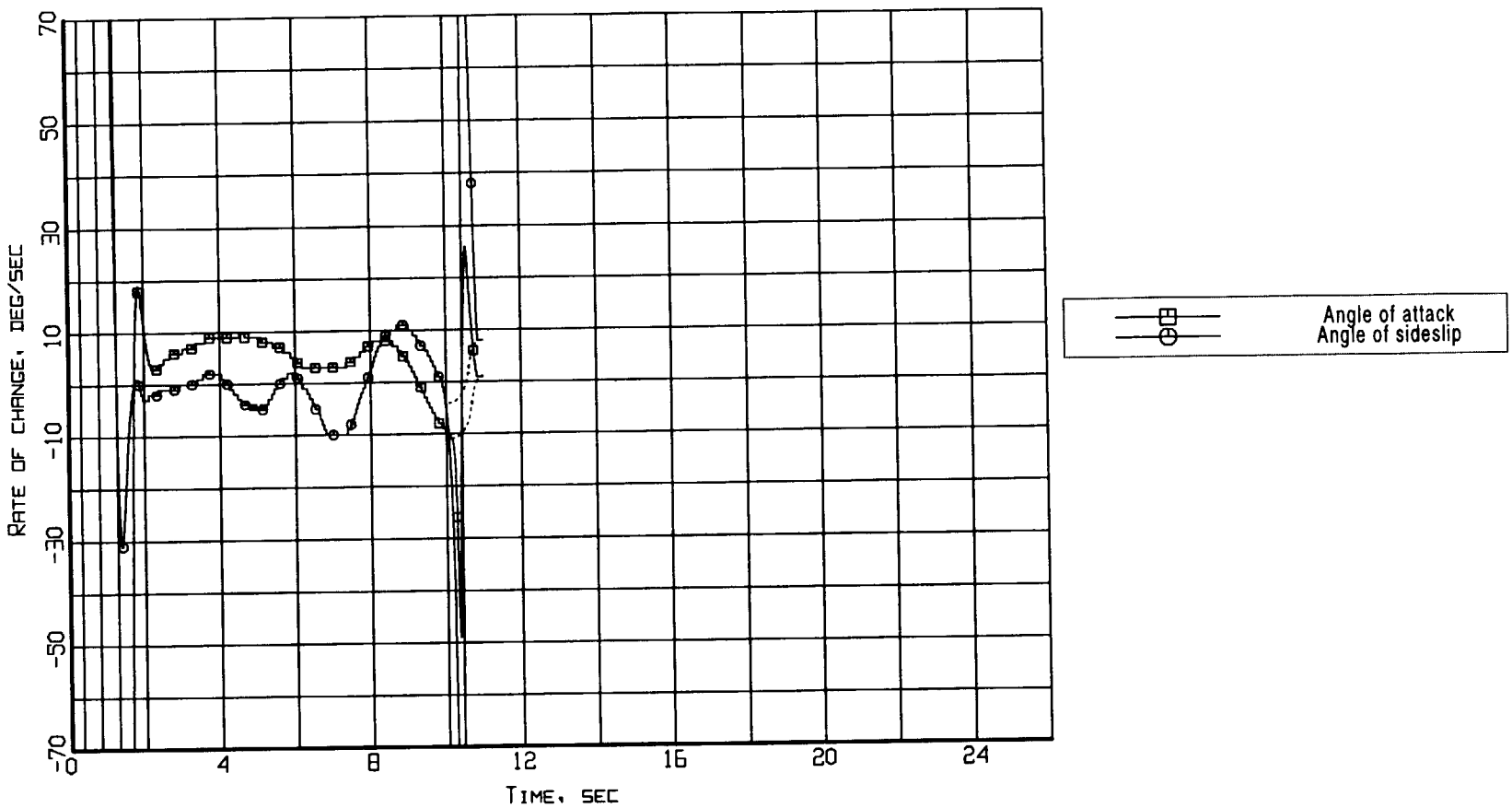

Figure B8-4. Aerodynamic flowstream descriptors - rate of change of angle of attack and angle of sideslip (Flight 240, Test Point 41b).

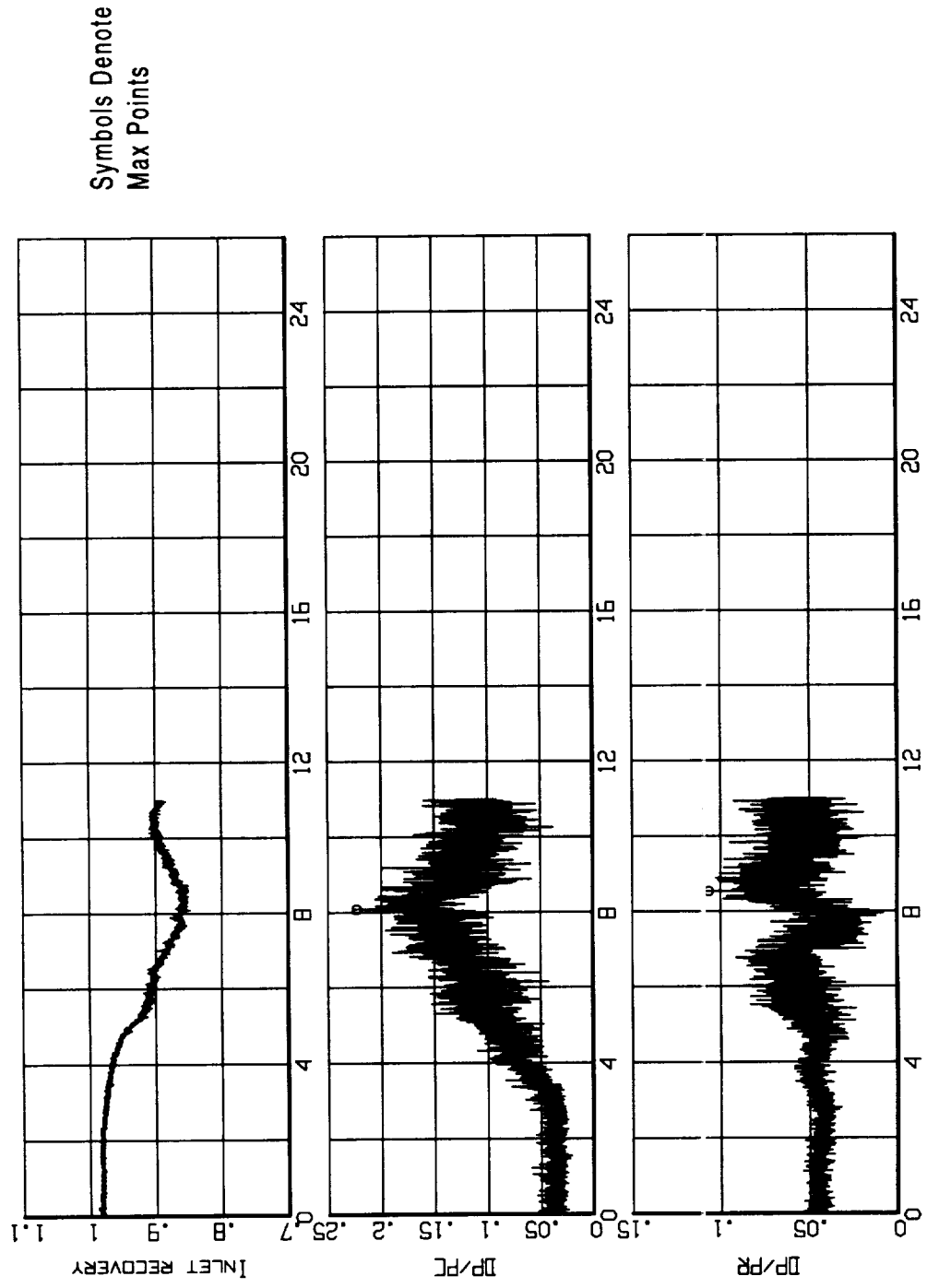

Figure B8-5. Time histories of inlet recovery and distortion descriptors (Flight 240, Test Point 41b).

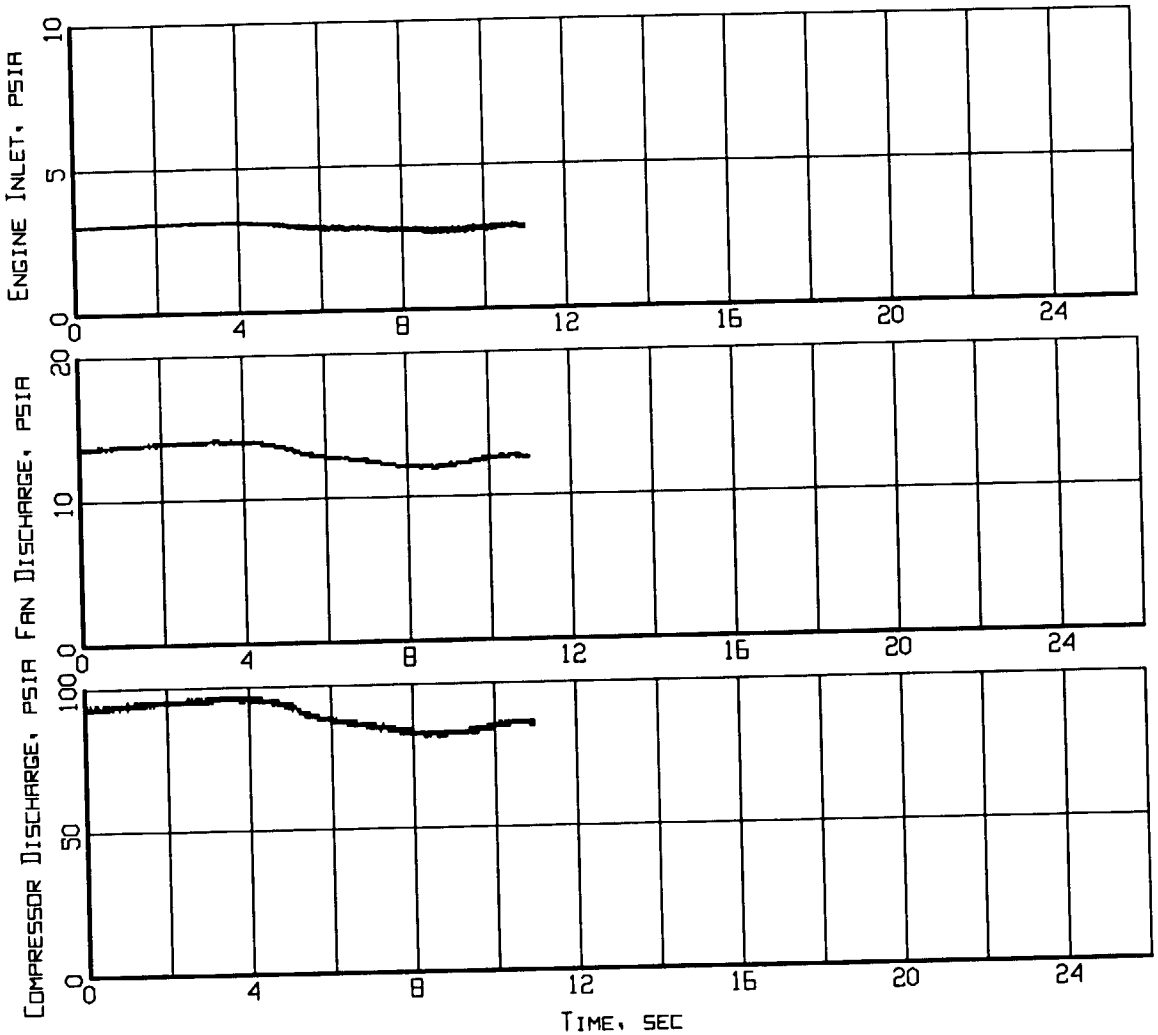

Figure B8-6. Measured inlet/engine entry and engine internal pressures time histories (Flight 240, Test Point 41b).

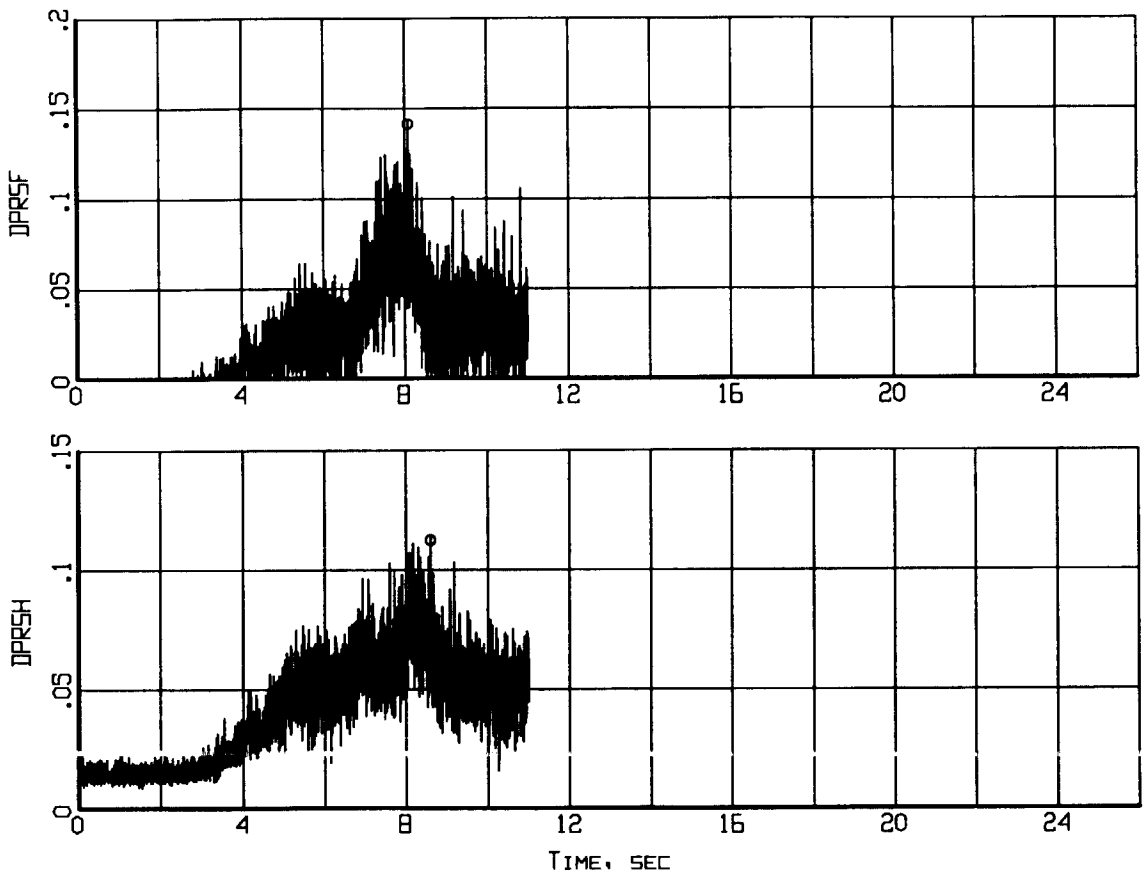

Symbols Denote
Max Points

Figure B8-7. Time histories of the predicted loss of stability pressure ratio for the fan and the compressor (Flight 240, Test Point 41b).

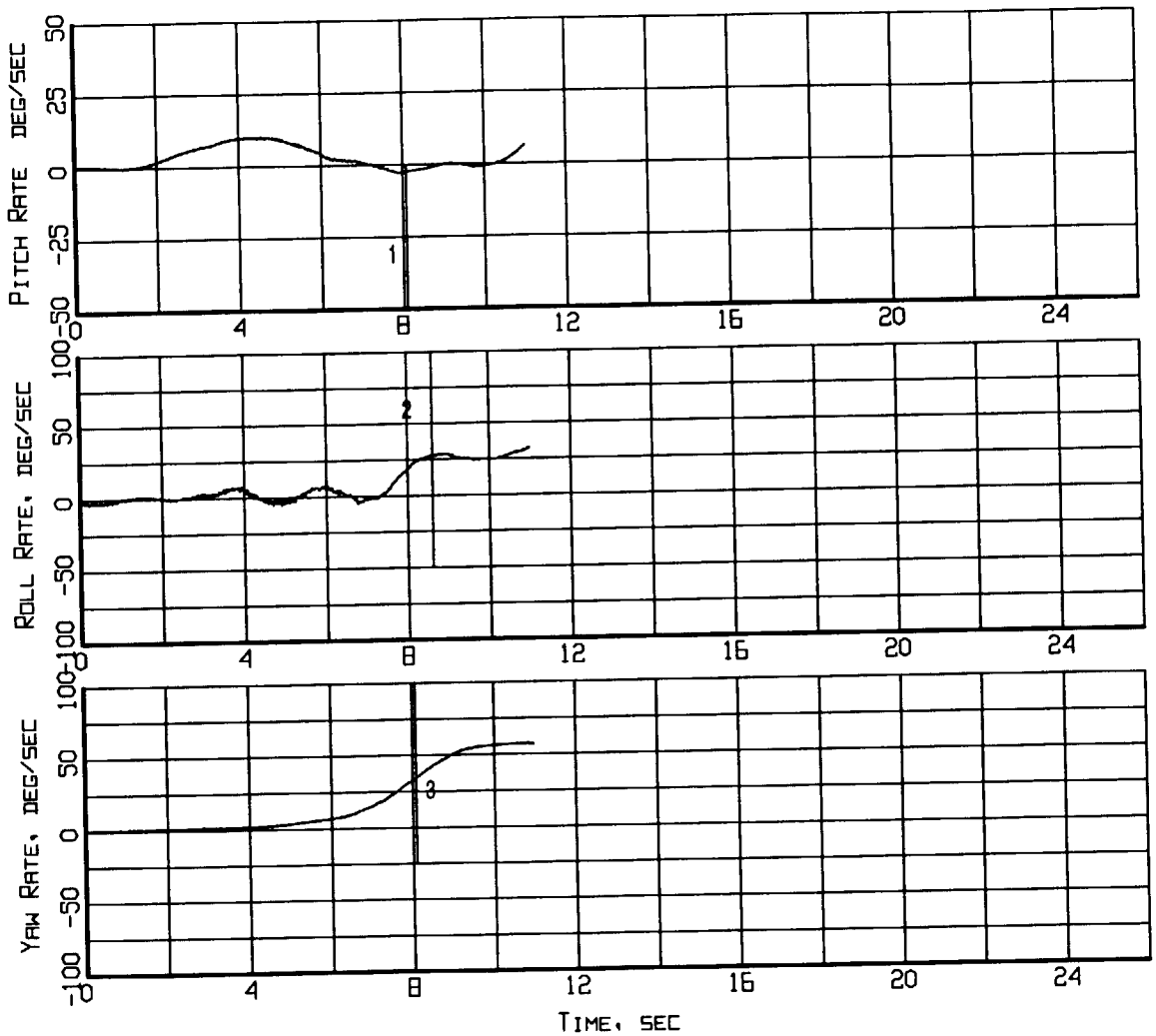

Event Marker

1 - Max DPRSF

2 - Max DPRSH

3 - Max DP/PC

Figure B8-9. Event markers superposed on the aircraft motion time histories (Flight 240, Test Point 41b).

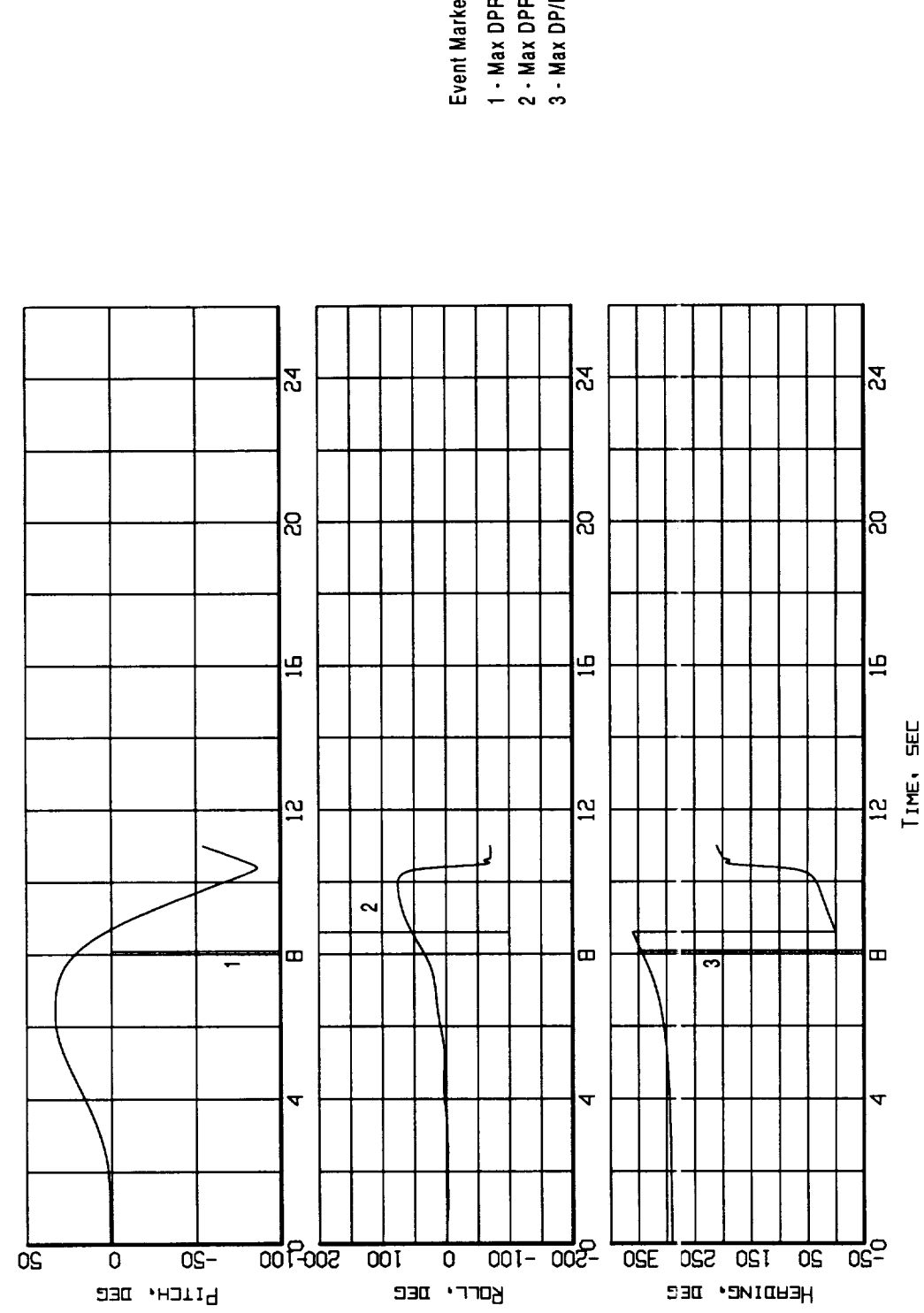

Figure B8-8. Event markers superposed on the aircraft attitude time histories (Flight 240, Test Point 41b).

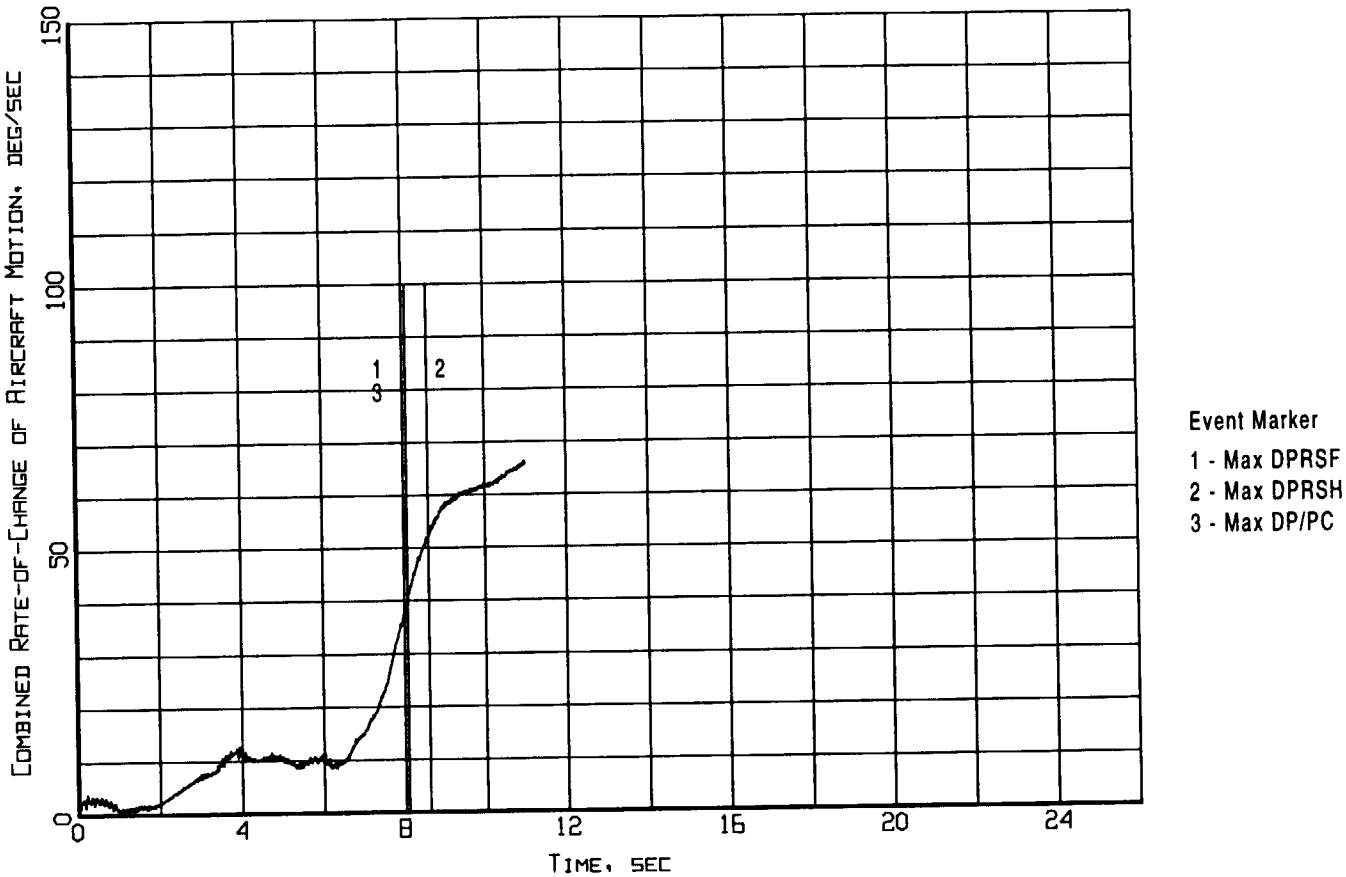

Figure B8-10. Event markers superposed on the combined of rate-of-change of aircraft motion time history (Flight 240, Test Point 41b).

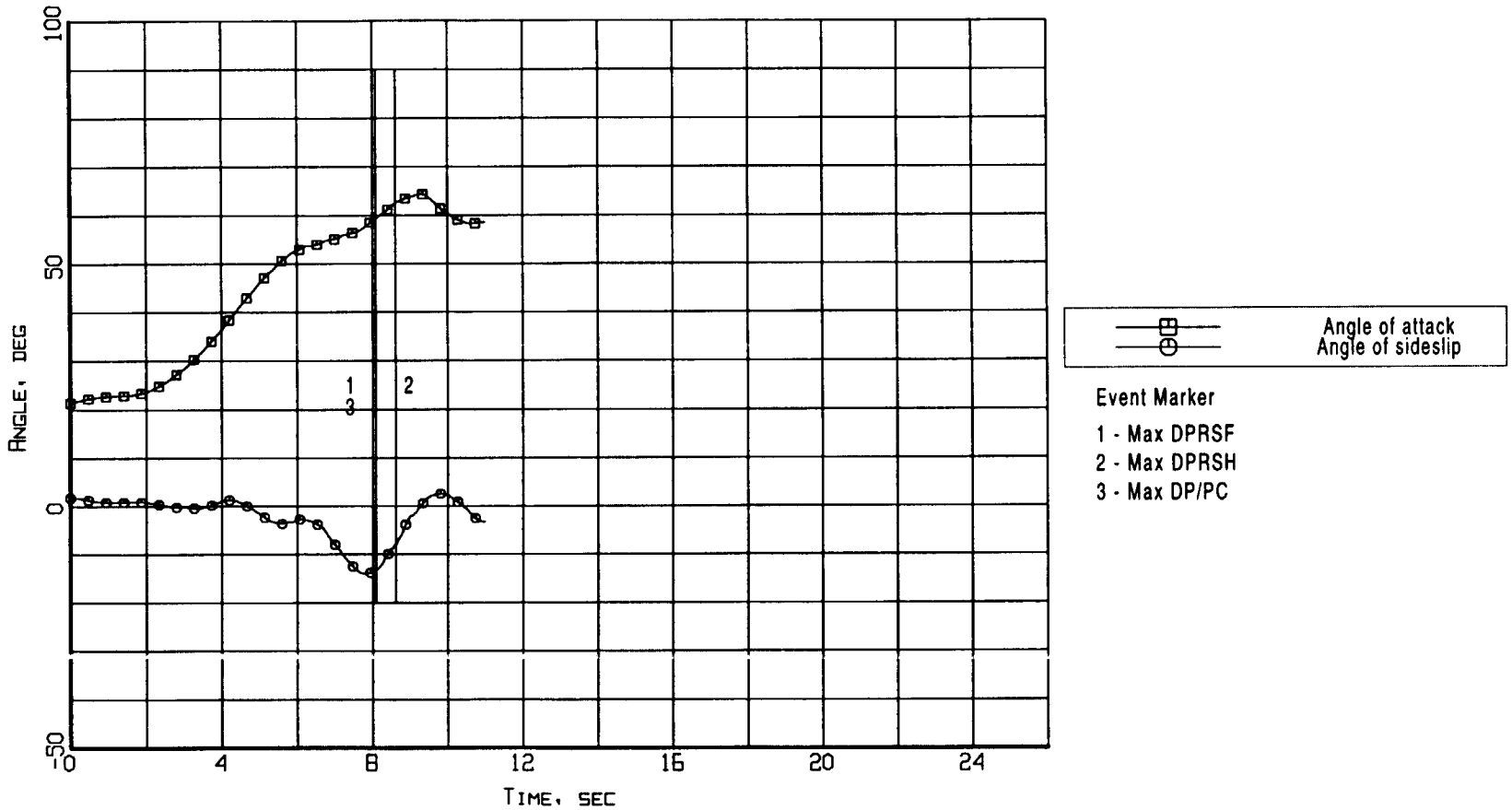

Figure B8-11. Event markers superposed on the aerodynamic flowstream descriptor time histories (Flight 240, Test Point 41b).

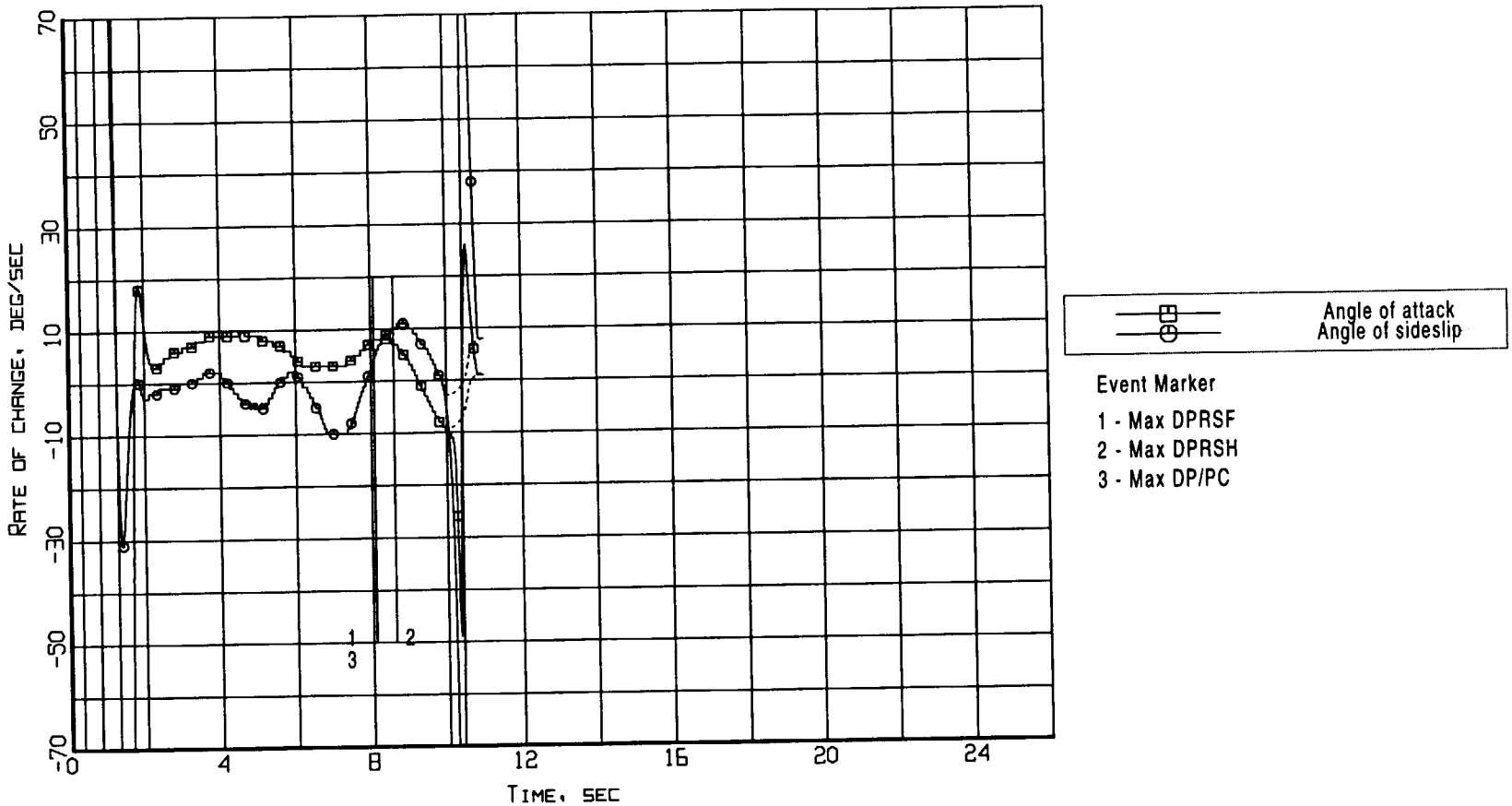

Figure B8-12. Event markers superposed on the aerodynamic flowstream descriptors rate-of-change time histories (Flight 240, Test Point 41b).

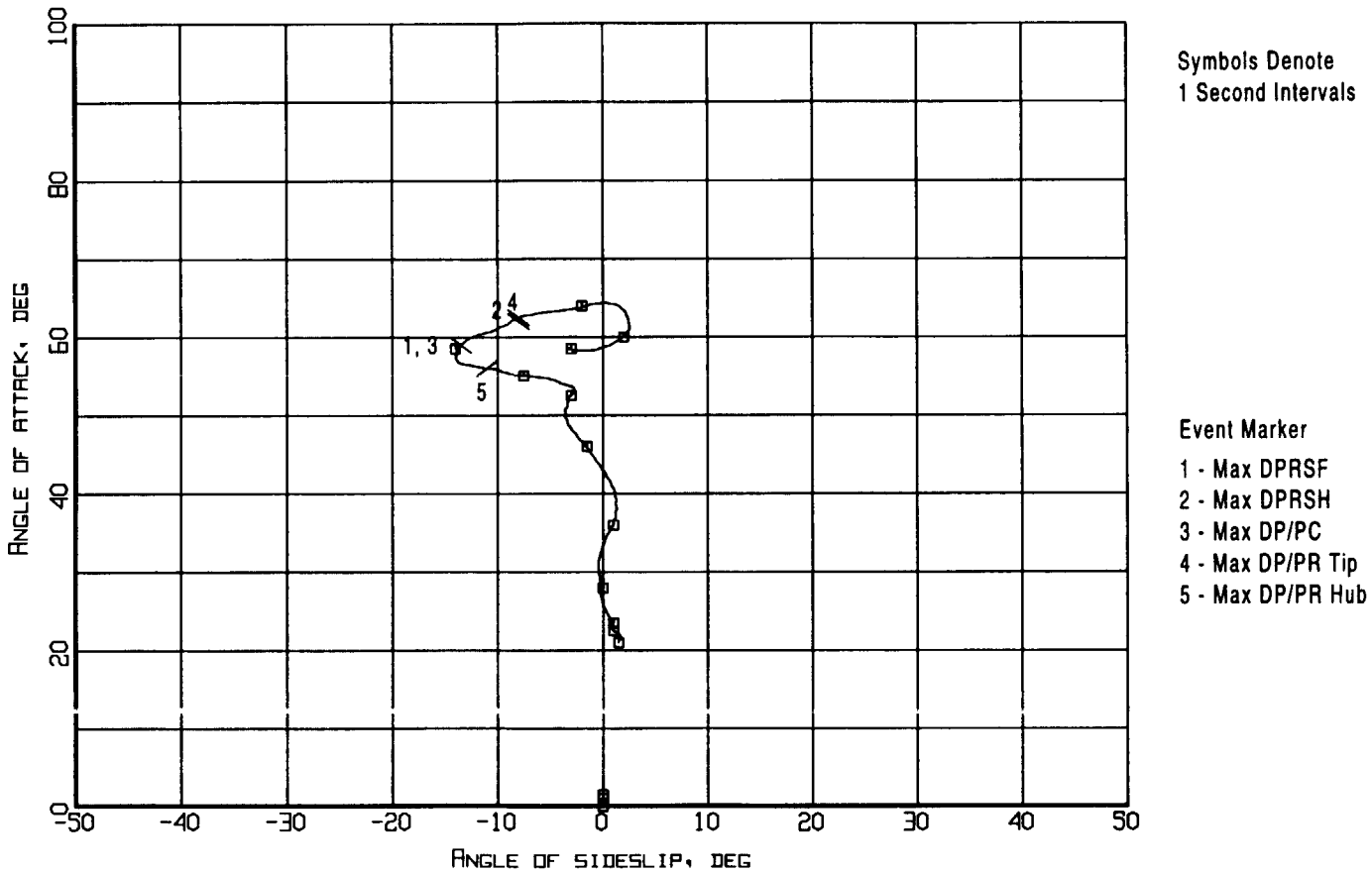

Figure B8-13. Event markers superposed on the aerodynamic flowstream descriptors trajectory (Flight 240, Test Point 41b).

Appendix B9 - Flight 238, Test Point 42b

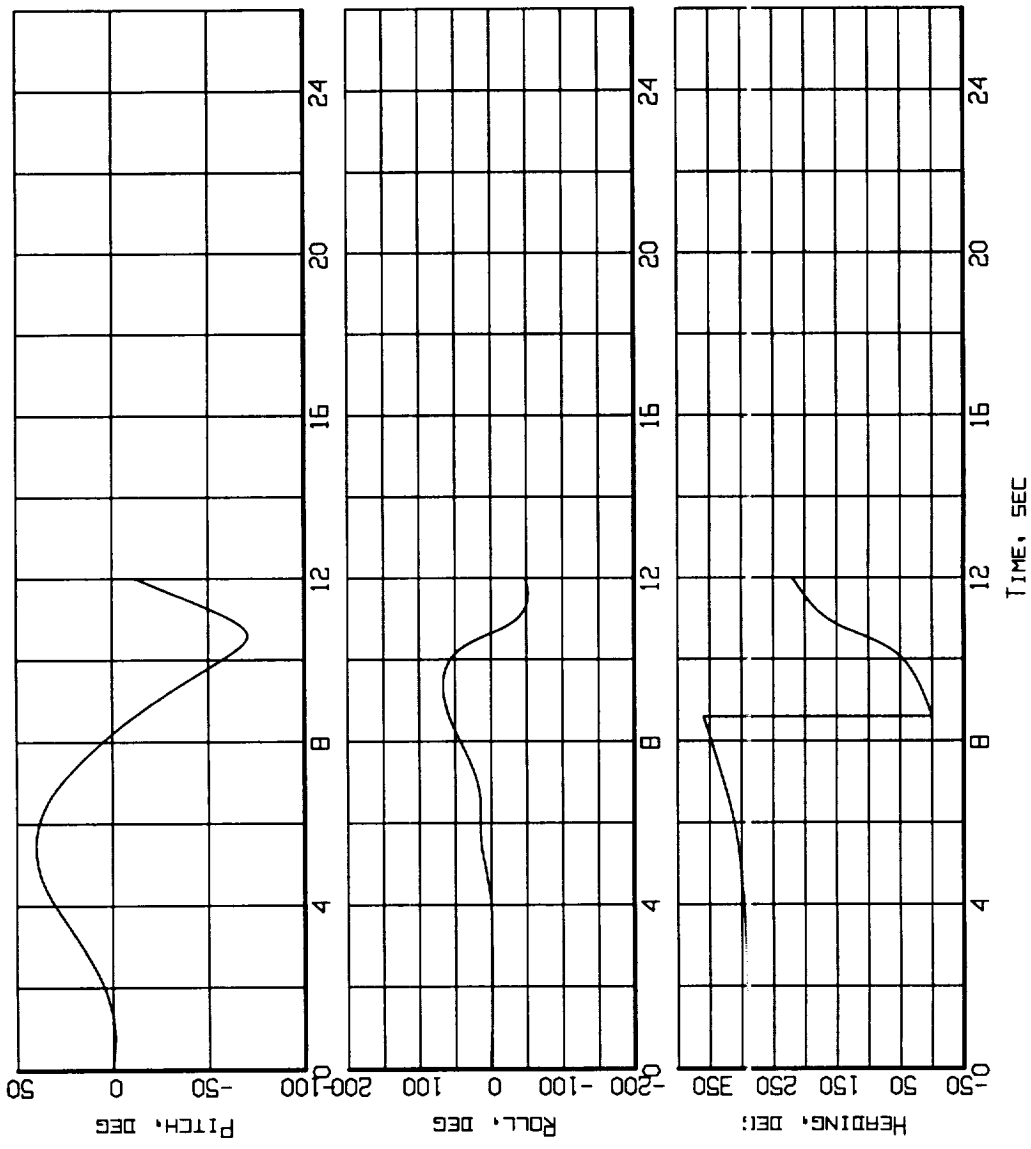

Figure B9-1. Aircraft attitude - Pitch, Roll, and Heading (Flight 238, Test Point 42b).

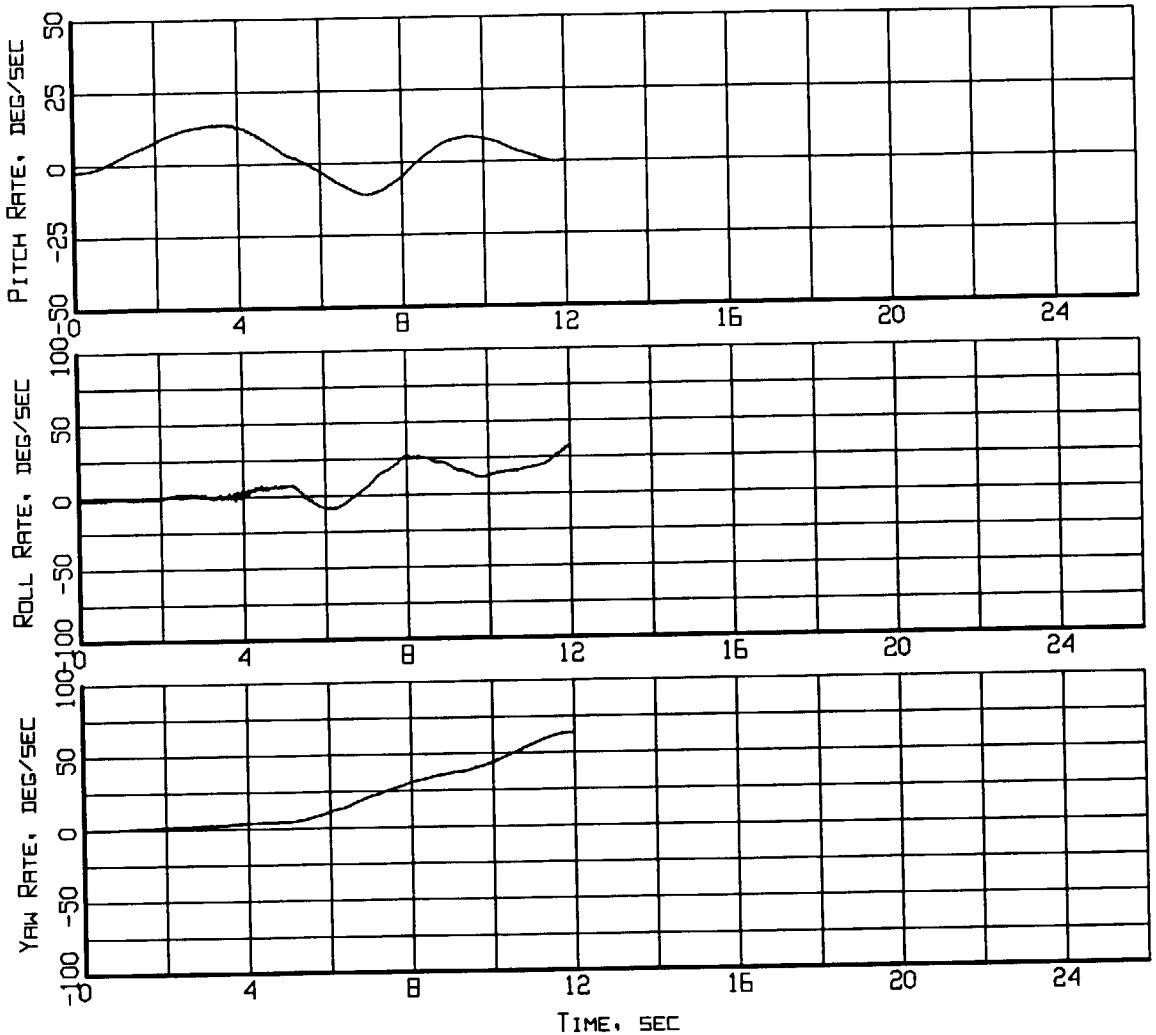

Figure B9-2. Aircraft Motion - Rate-of-Change of Pitch, Roll and Heading (Flight 238, Test Point 42b).

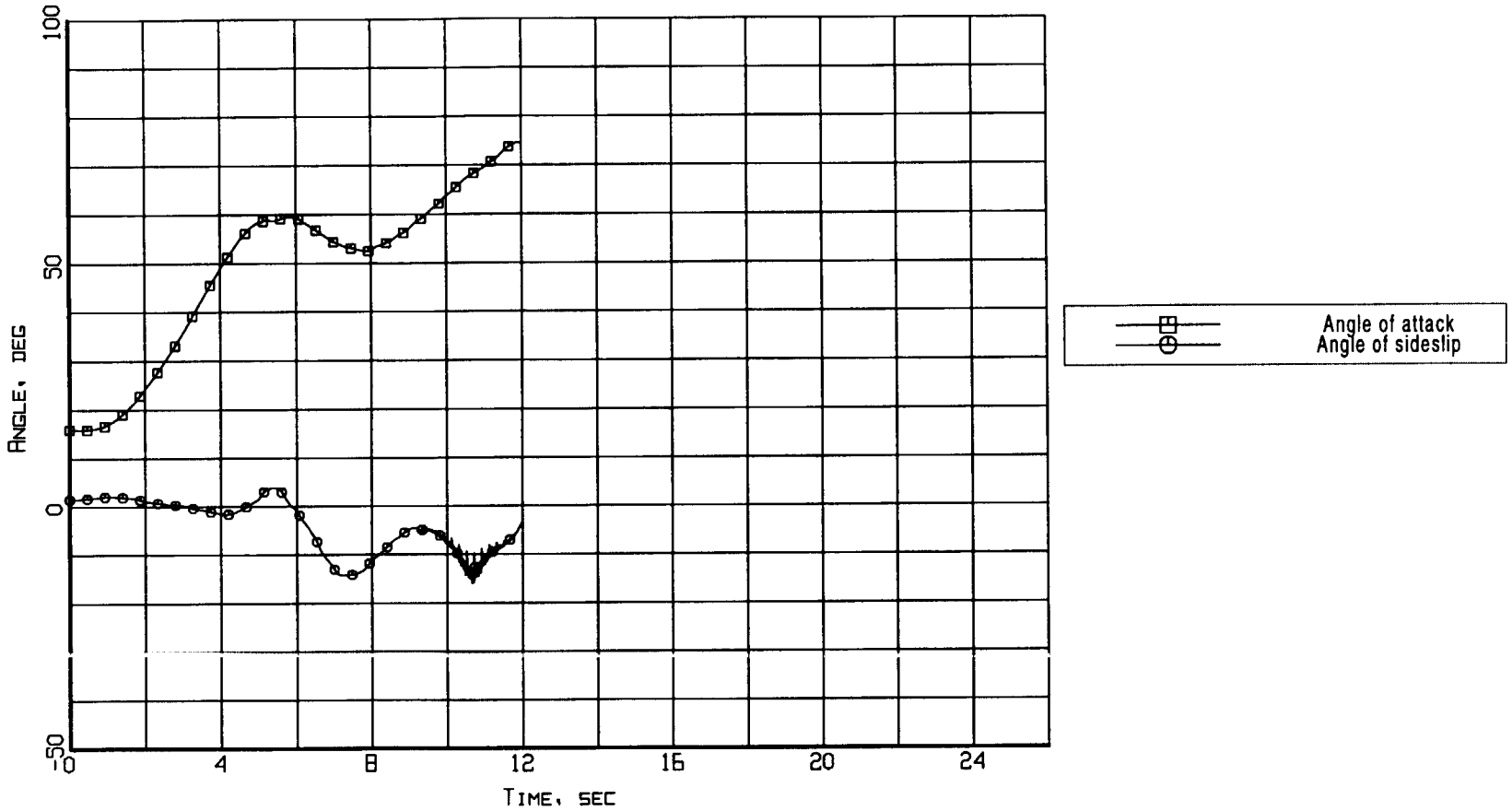

Figure B9-3. Aerodynamic flowstream descriptors - angle of attack and angle of sideslip (Flight 238, Test Point 42b).

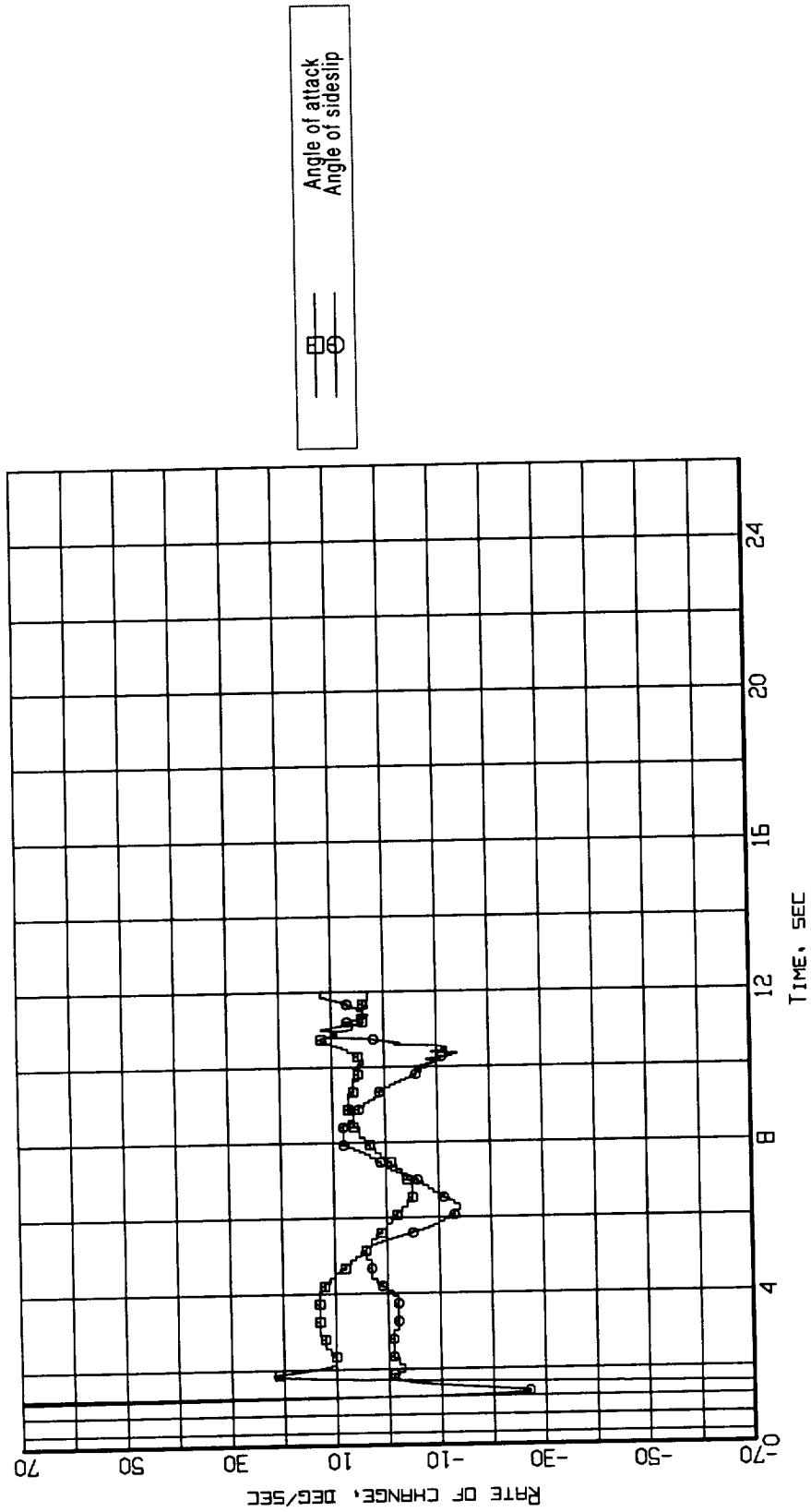

Figure B9-4. Aerodynamic flowstream descriptors - rate of change of angle of attack and angle of sideslip (Flight 238, Test Point 42b).

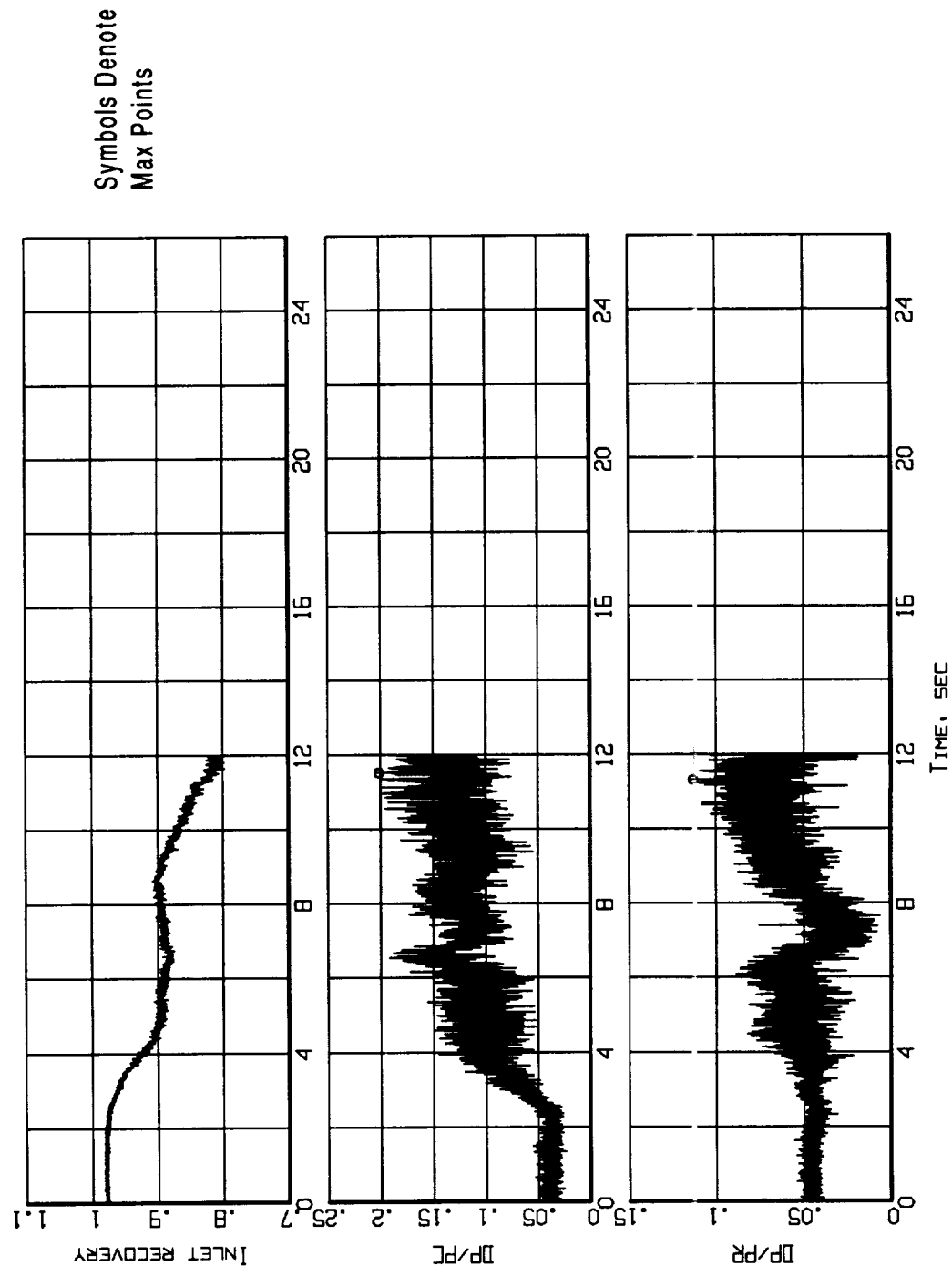

Figure B9-5. Time histories of inlet recovery and distortion descriptors (Flight 238, Test Point 42b).

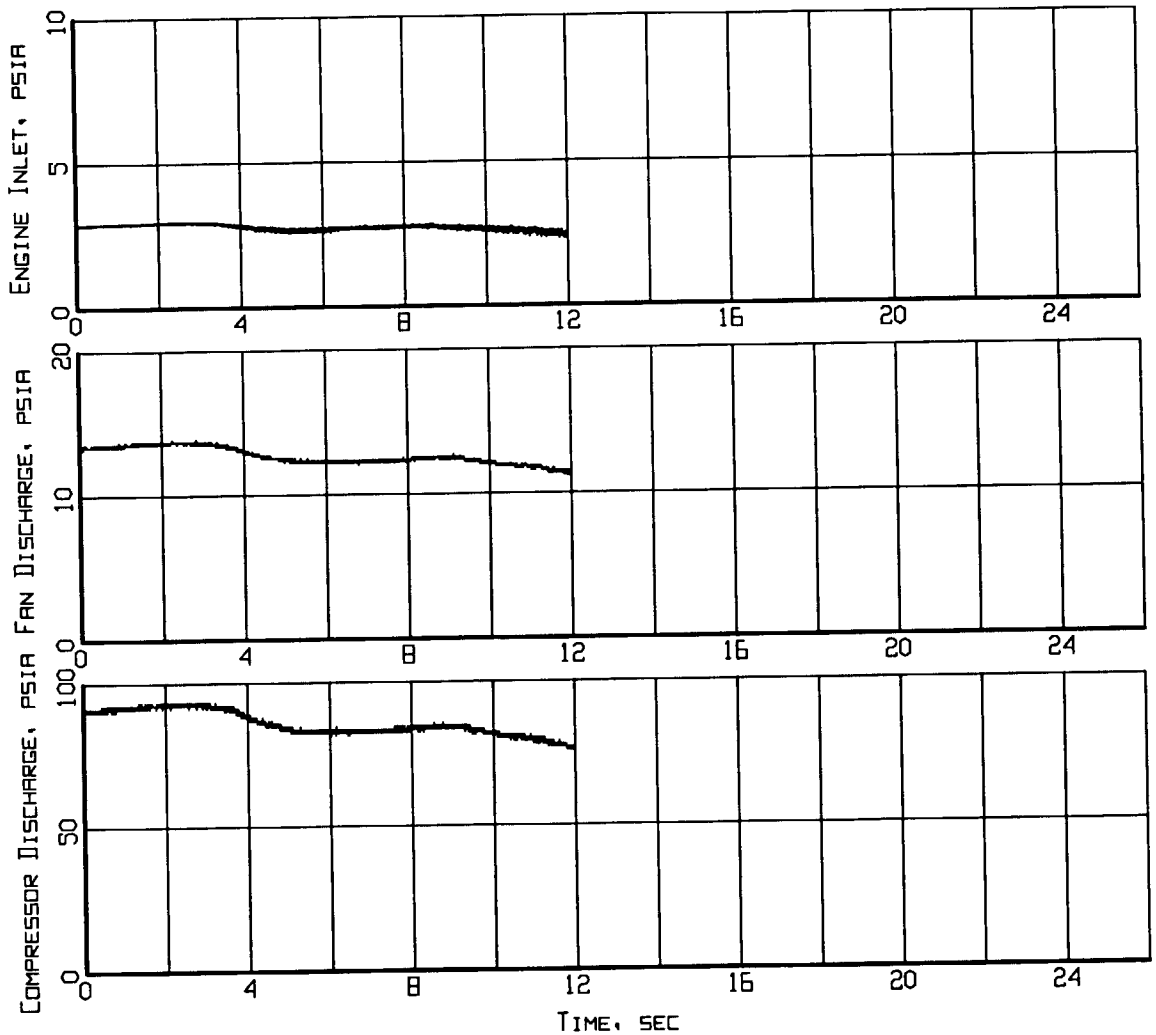

Figure B9-6. Measured inlet/engine entry and engine internal pressures time histories (Flight 238, Test Point 42b).

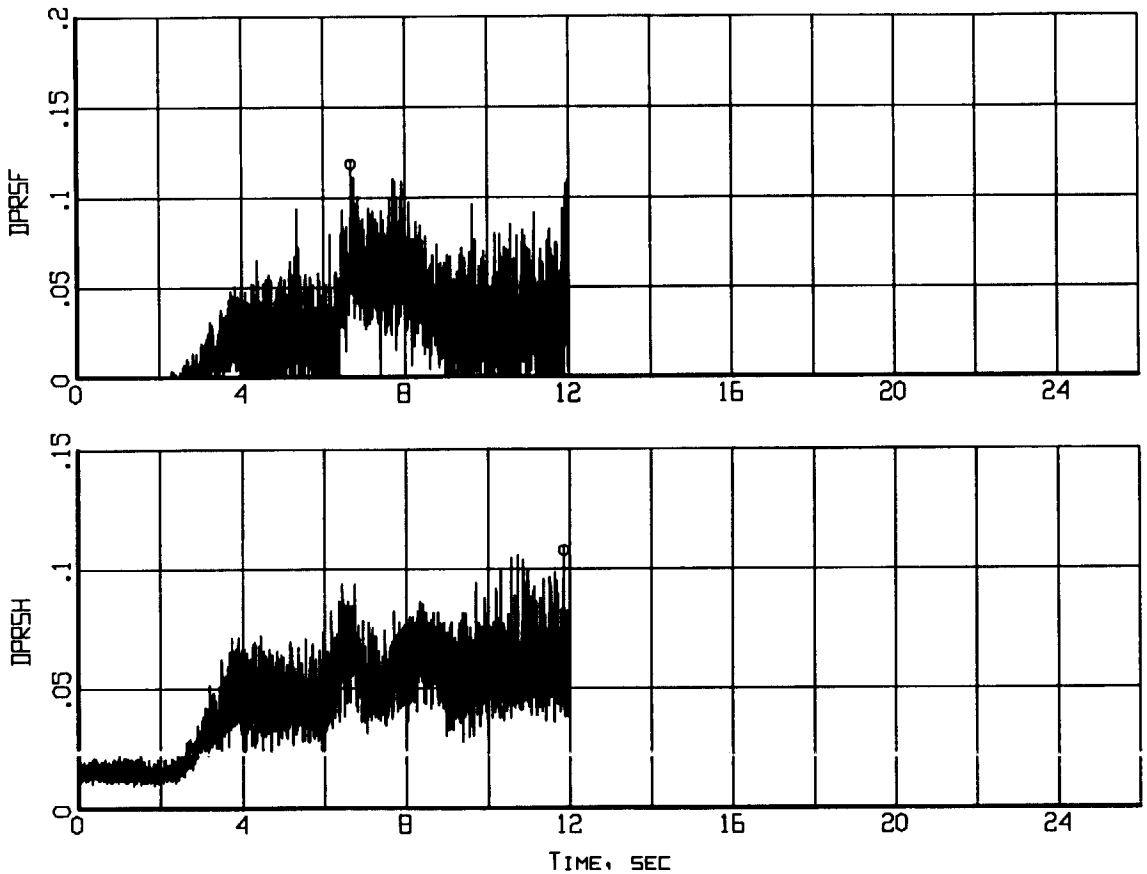

Symbols Denote
Max Points

Figure B9-7. Time histories of the predicted loss of stability pressure ratio for the fan and the compressor (Flight 238, Test Point 42b).

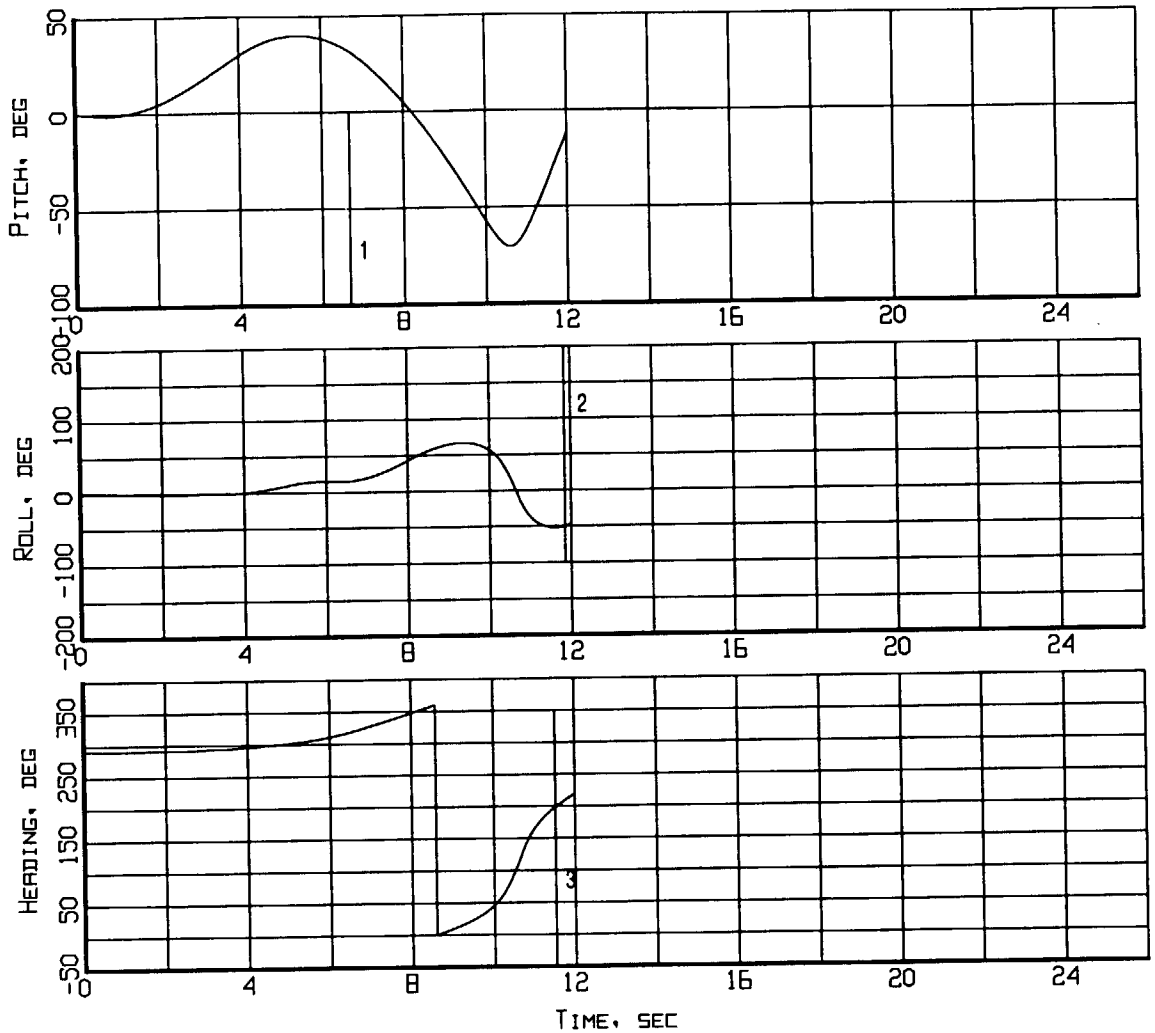

Event Marker

1 - Max DPRSF

2 - Max DPRSH

3 - Max DP/PC

Figure B9-8. Event markers superposed on the aircraft attitude time histories (Flight 238, Test Point 42b).

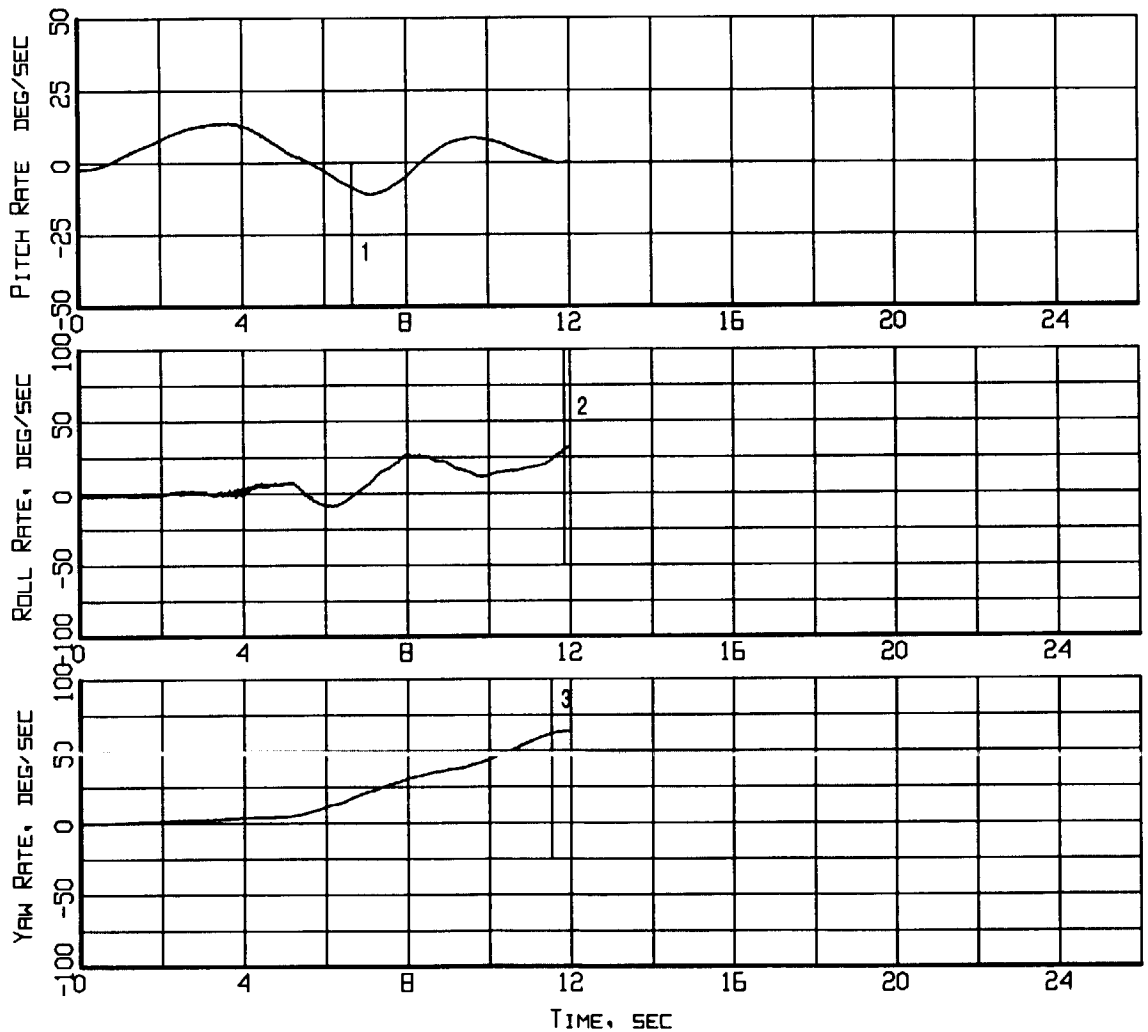

Figure B9-9. Event markers superposed on the aircraft motion time histories (Flight 238, Test Point 42b).

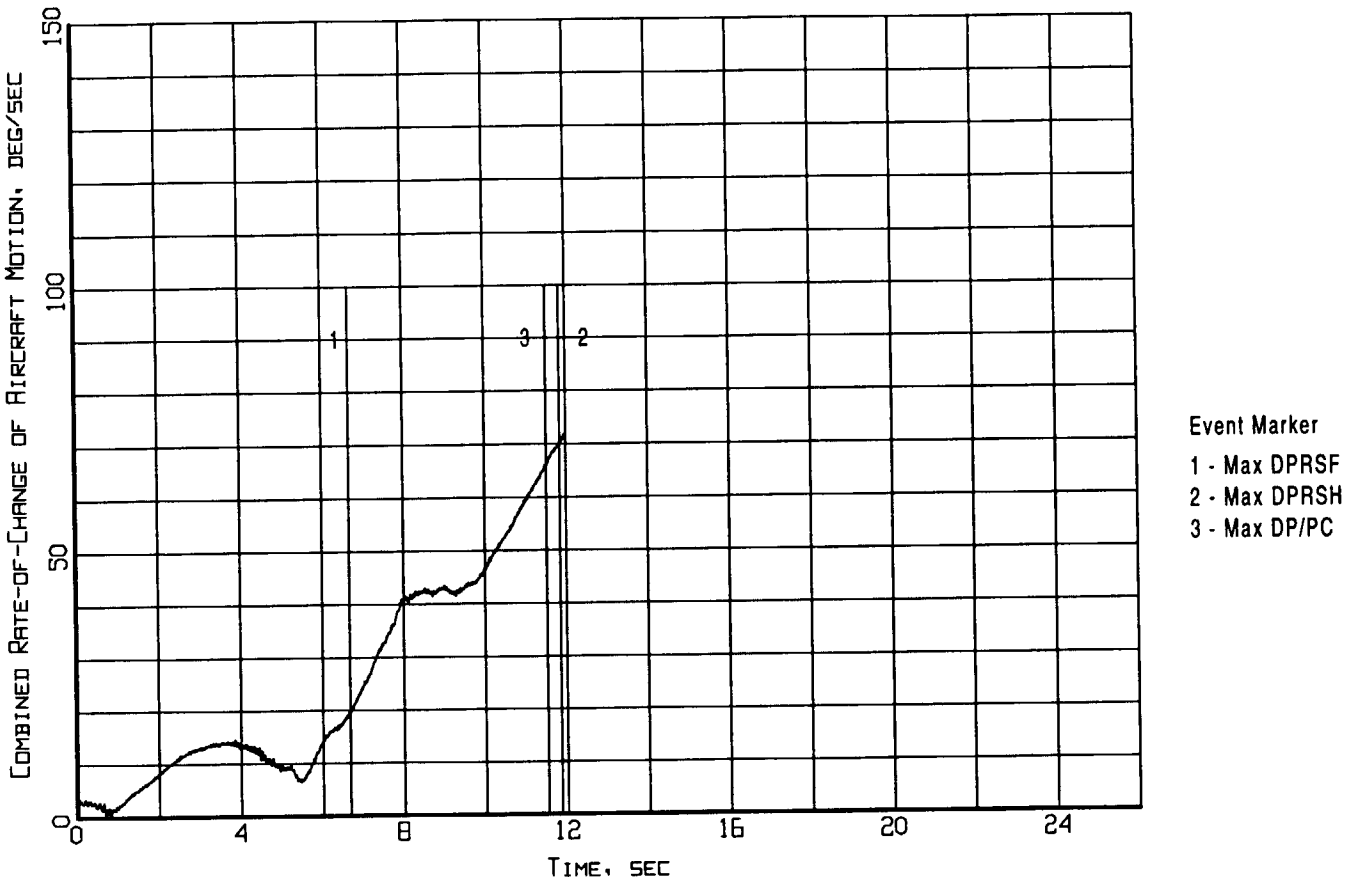

Figure B9-10. Event markers superposed on the combined of rate-of-change of aircraft motion time history (Flight 238, Test Point 42b).

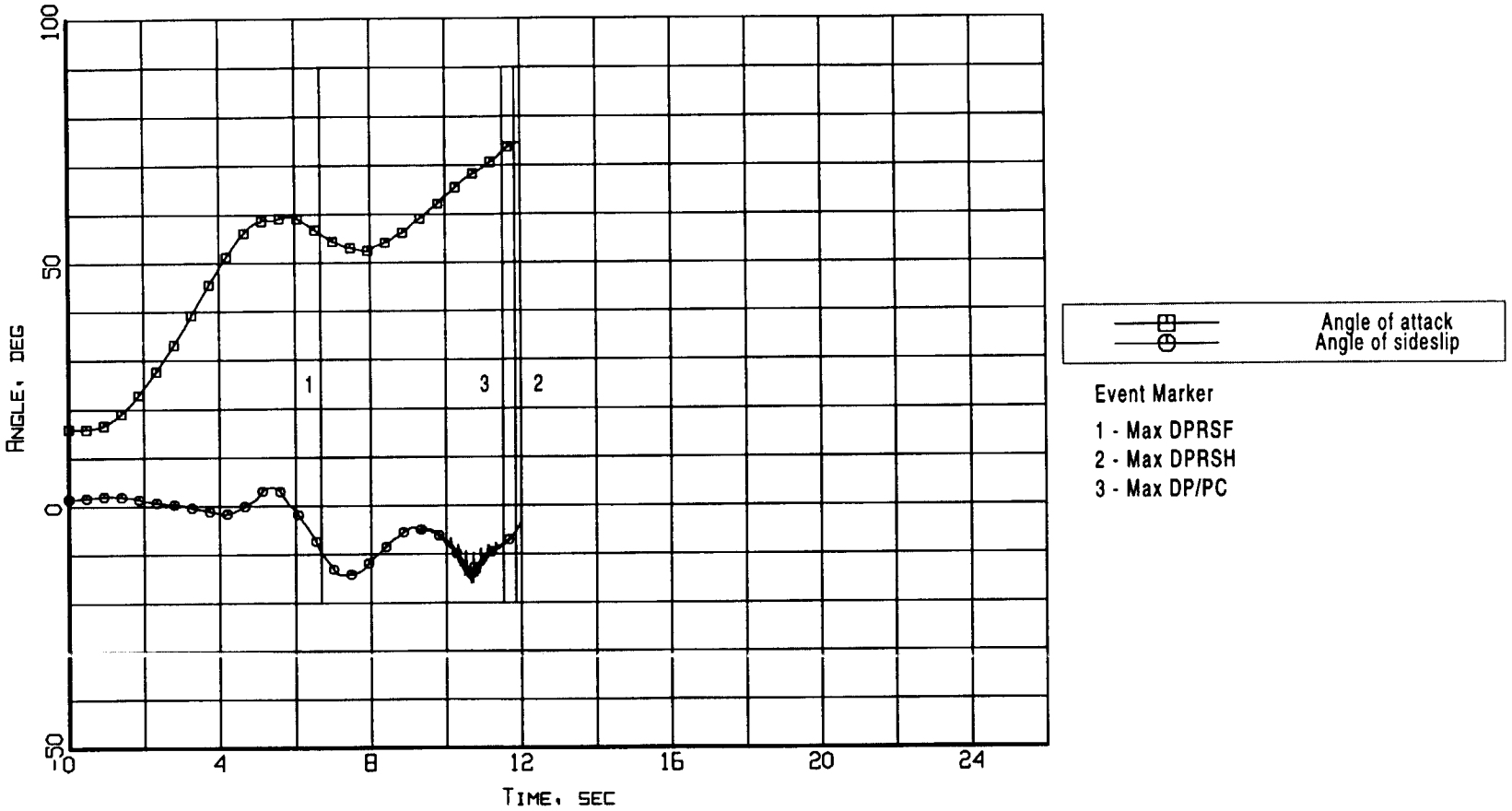

Figure B9-11. Event markers superposed on the aerodynamic flowstream descriptor time histories (Flight 238, Test Point 42b).

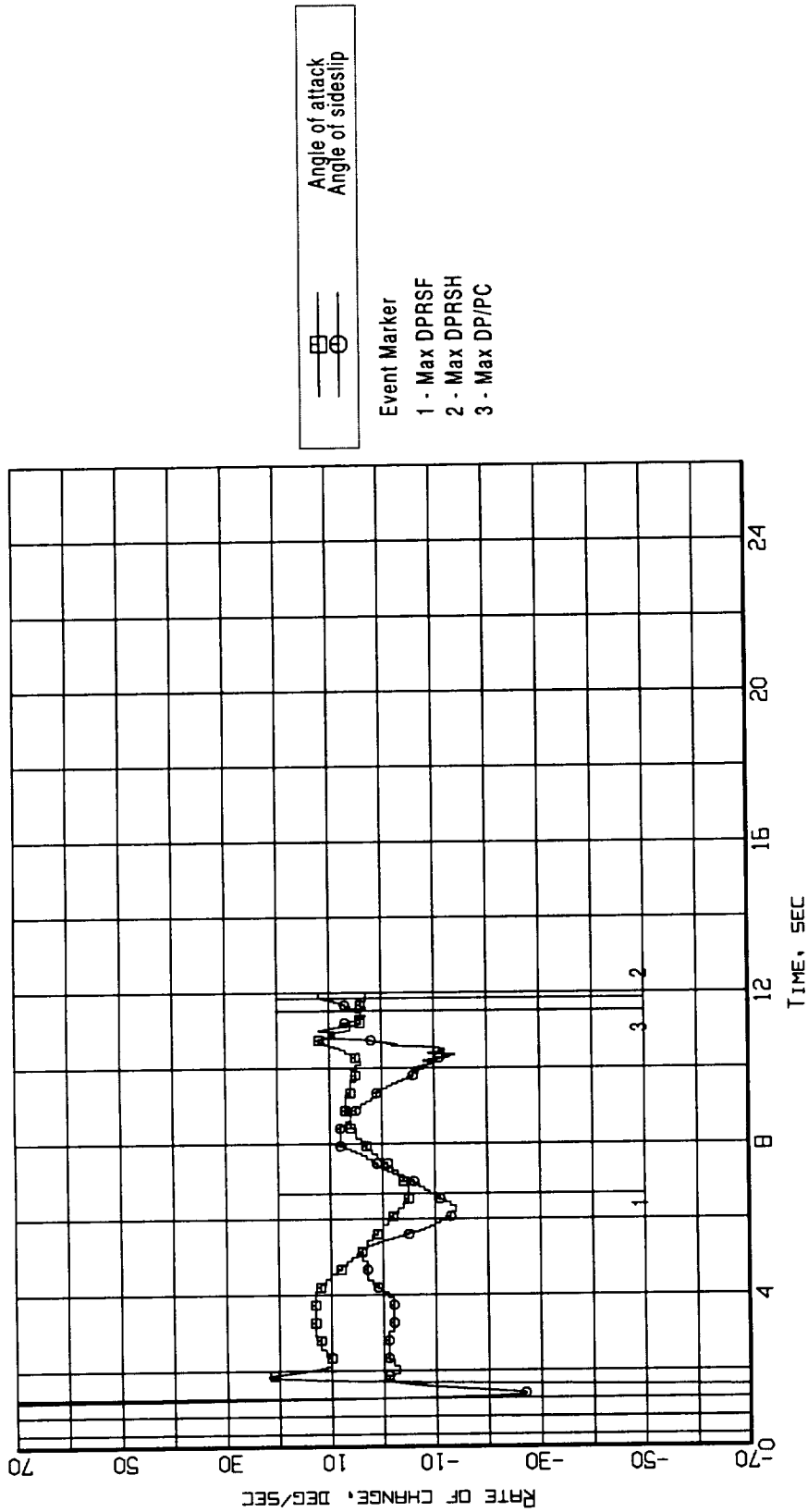

Figure B9-12. Event markers superposed on the aerodynamic flowstream descriptors rate-of-change time histories (Flight 238, Test Point 42b).

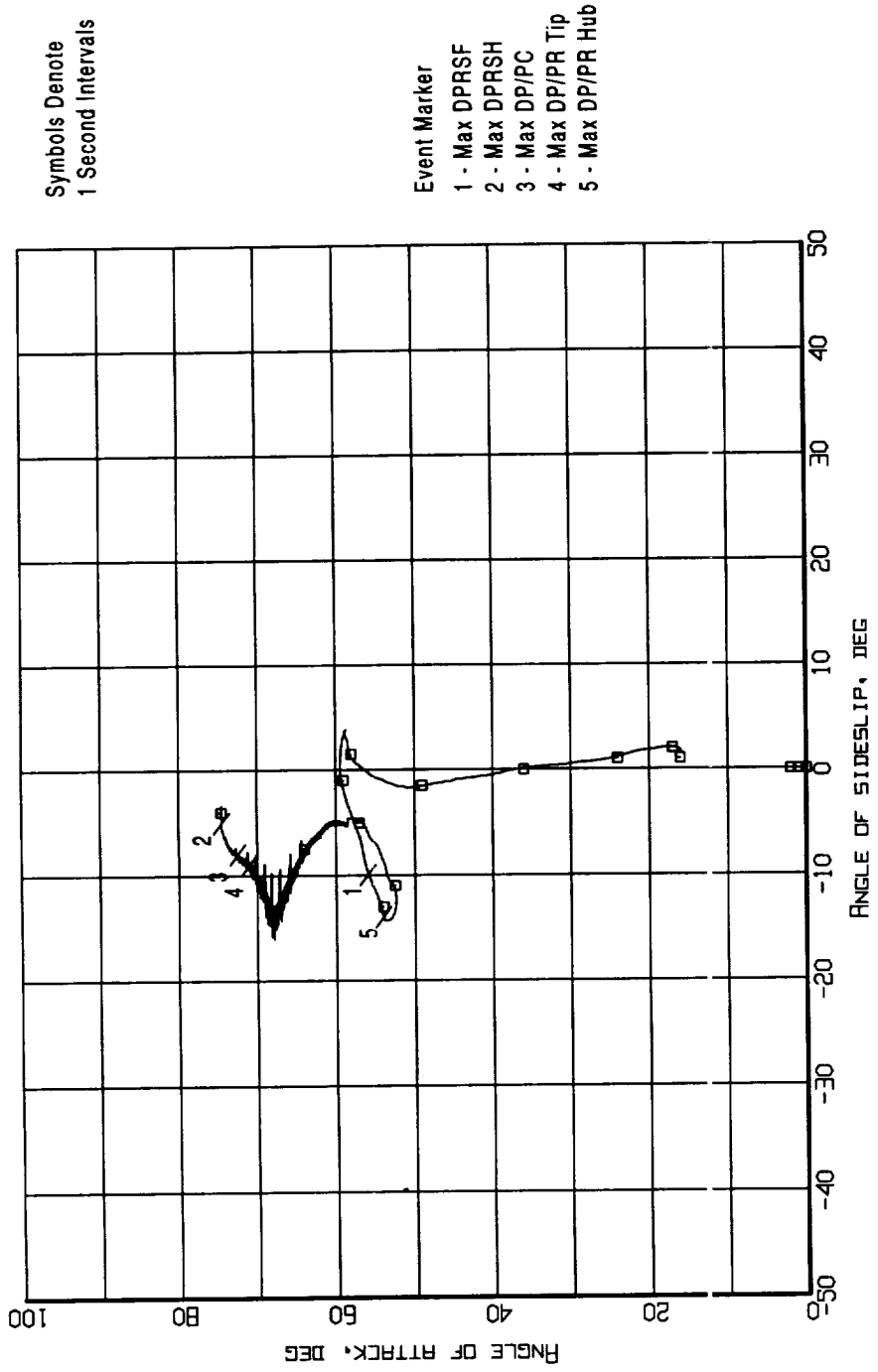

Figure B9-13. Event markers superposed on the aerodynamic flowstream descriptors trajectory (Flight 238, Test Point 42b).

Appendix B10 - Flight 240, Test Point 43b

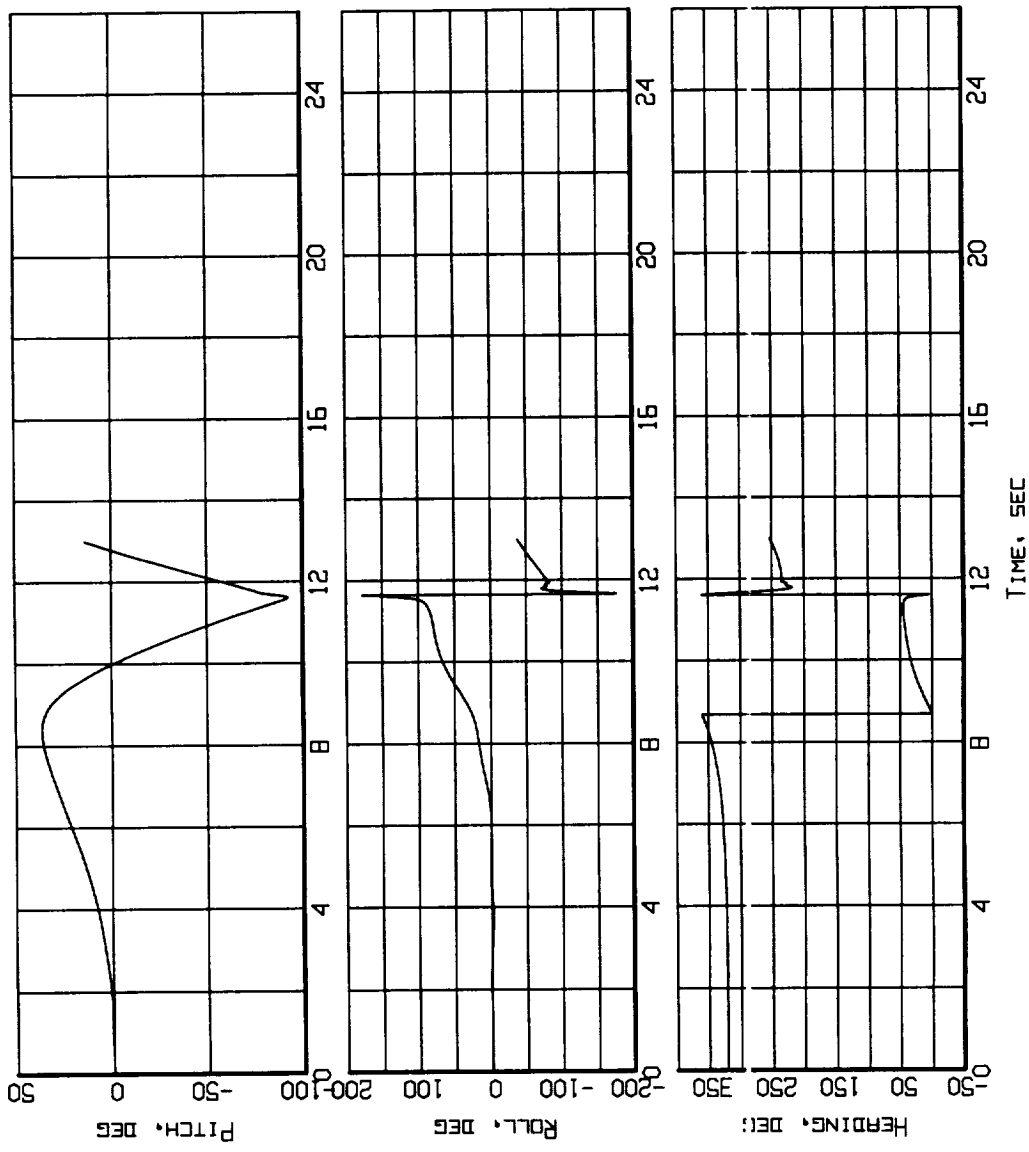

Figure B10-1. Aircraft attitude - Pitch, Roll, and Heading (Flight 240, Test Point 43b).

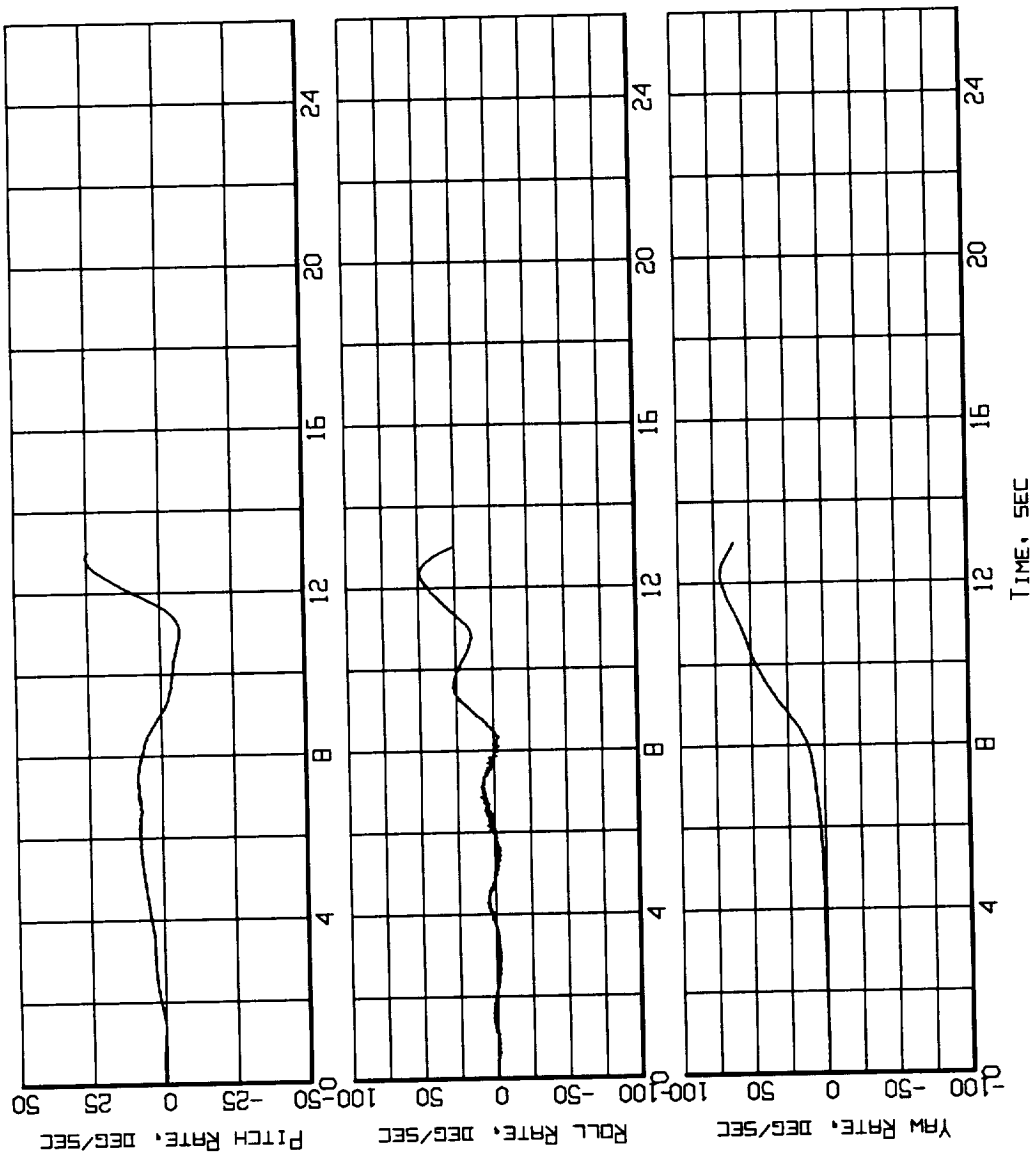

Figure B10-2. Aircraft Motion - Rate-of-Change of Pitch, Roll and Heading (Flight 240, Test Point 43b).

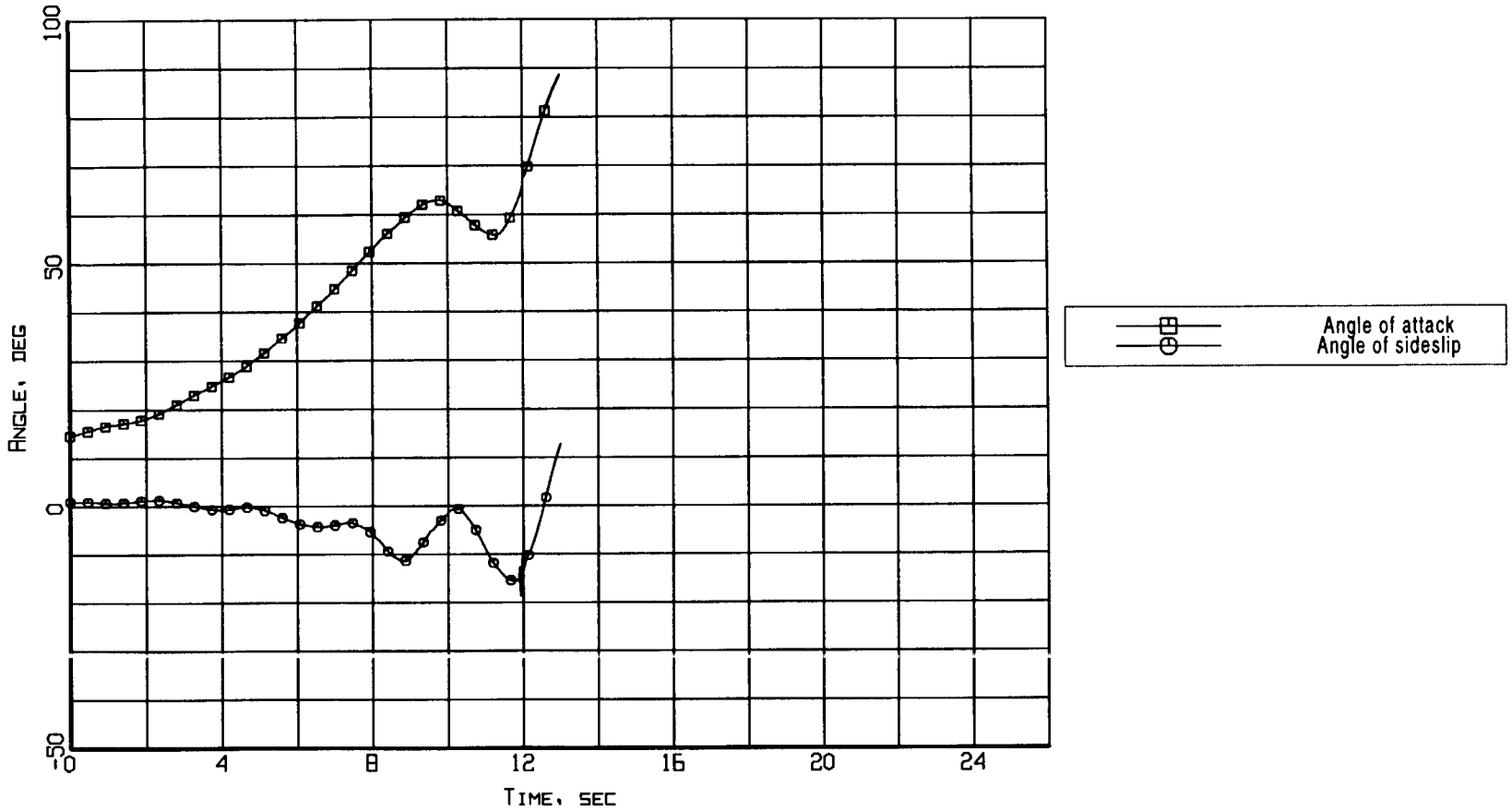

Figure B10-3. Aerodynamic flowstream descriptors - angle of attack and angle of sideslip (Flight 240, Test Point 43b).

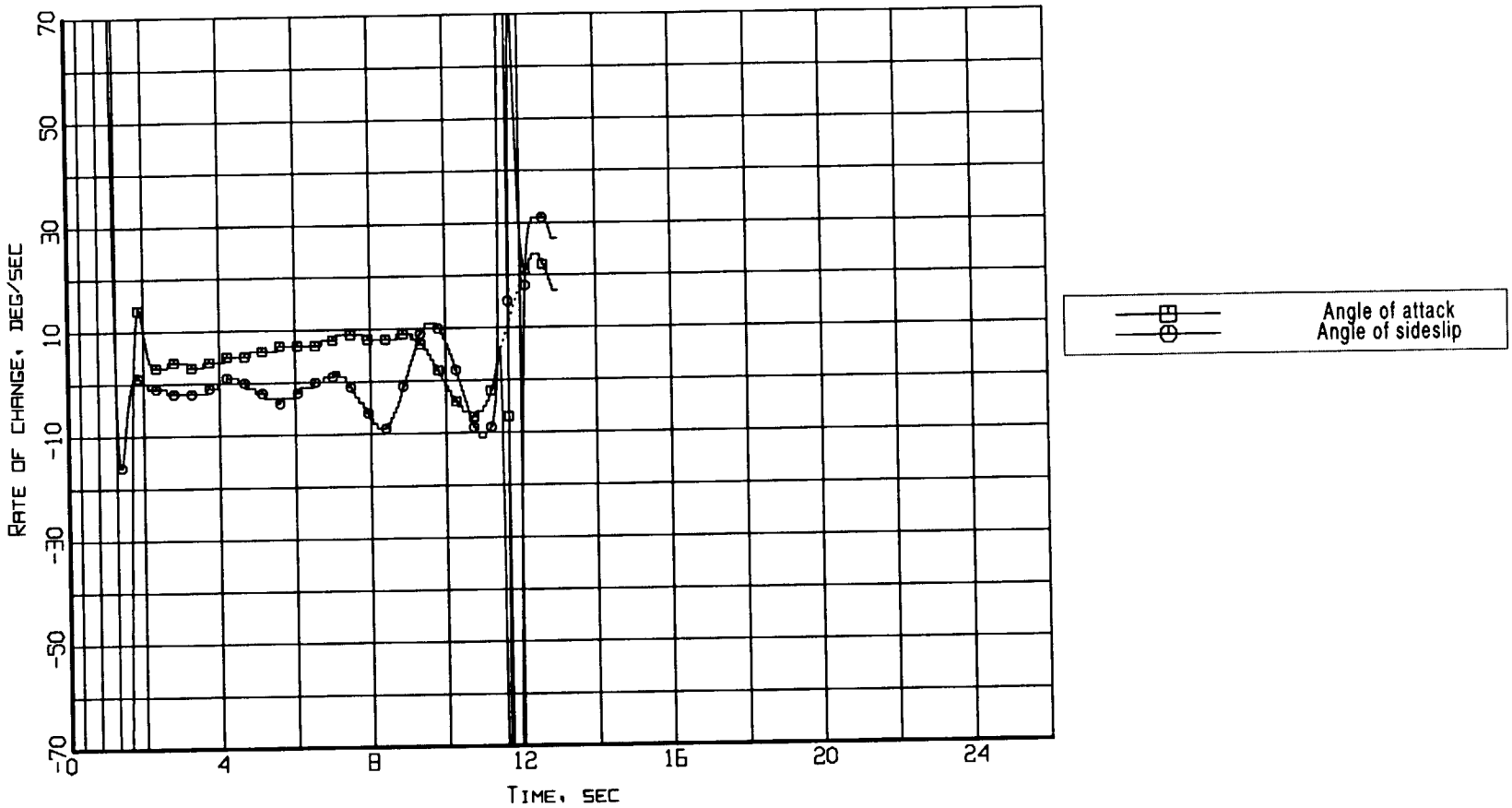

Figure B10-4. Aerodynamic flowstream descriptors - rate of change of angle of attack and angle of sideslip (Flight 240, Test Point 43b).

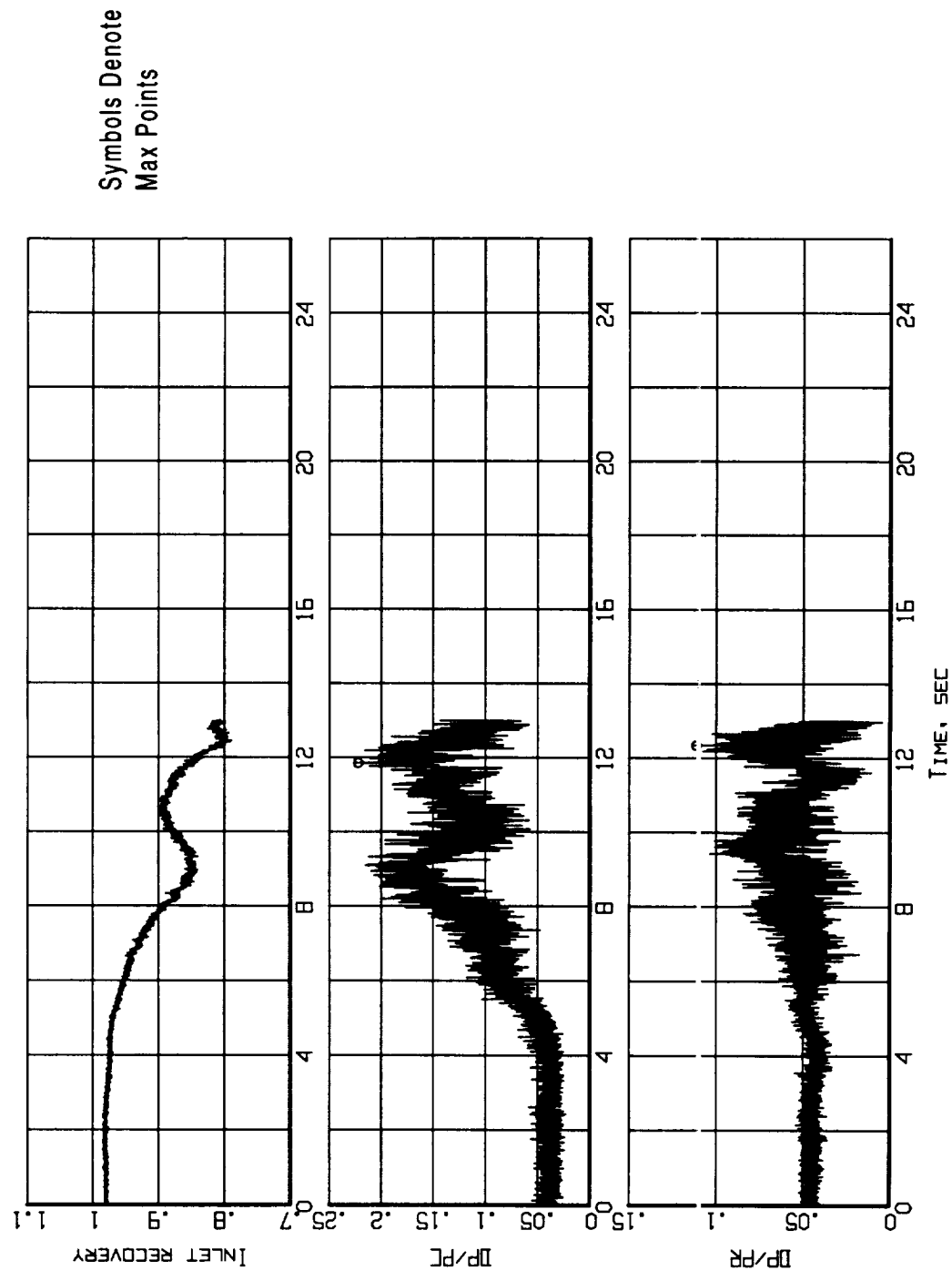

Figure B10-5. Time histories of inlet recovery and distortion descriptors (Flight 240, Test Point 43b).

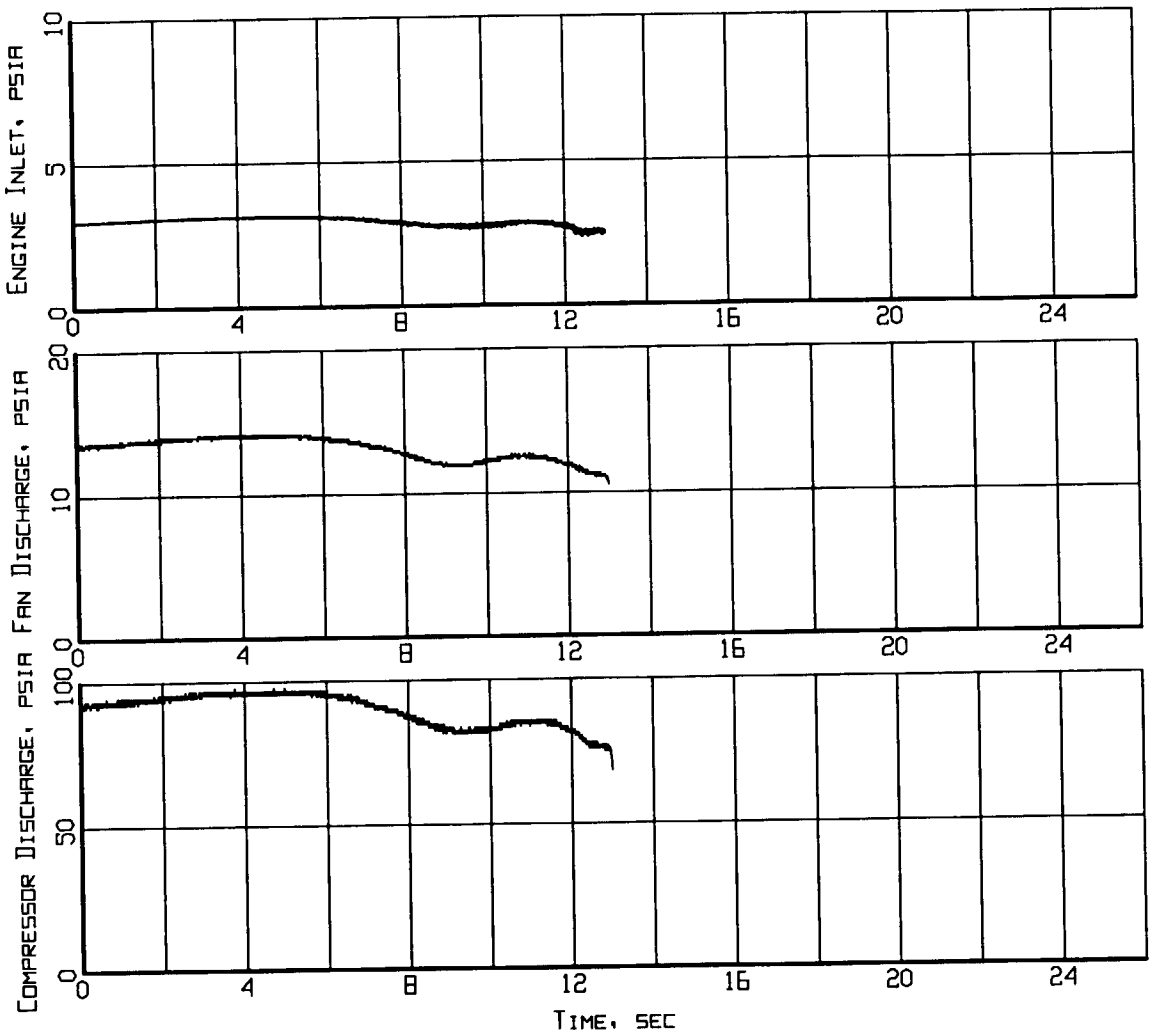

Figure B10-6. Measured inlet/engine entry and engine internal pressures time histories (Flight 240, Test Point 43b).

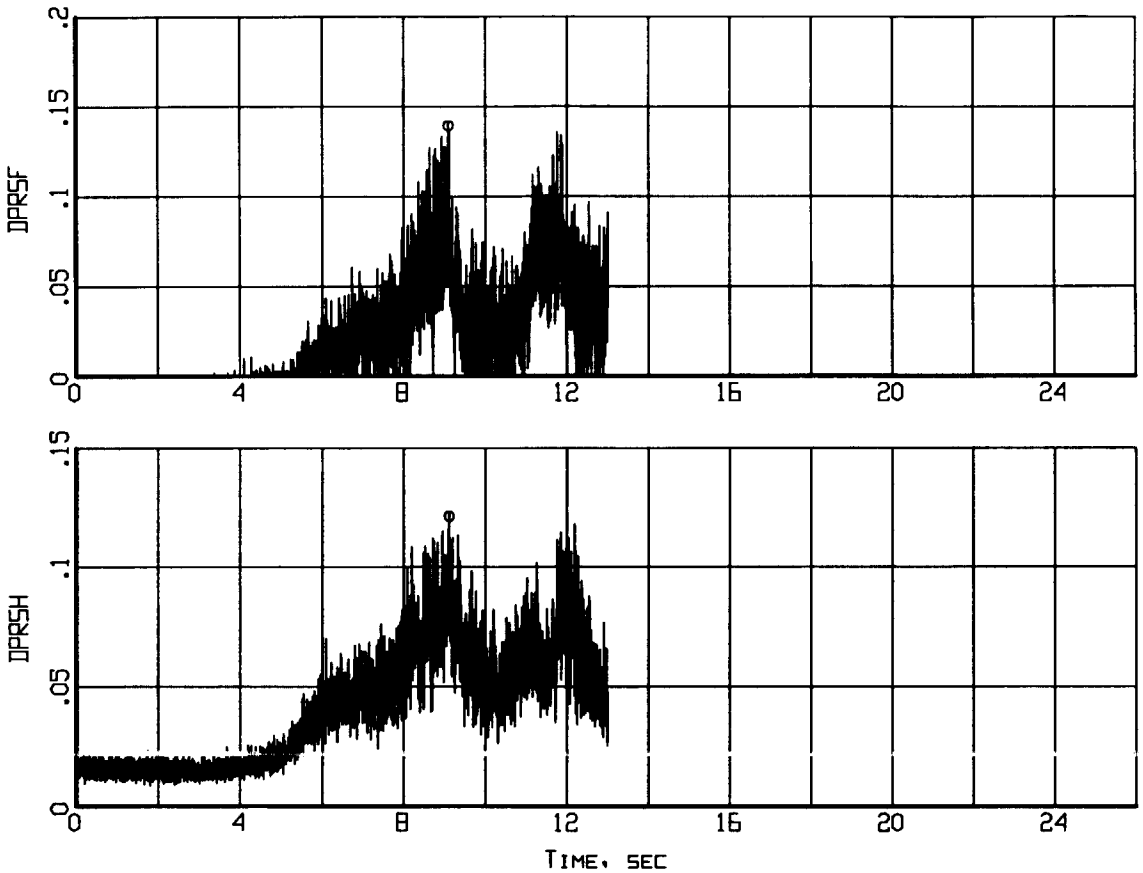

Figure B10-7. Time histories of the predicted loss of stability pressure ratio for the fan and the compressor (Flight 240, Test Point 43b).

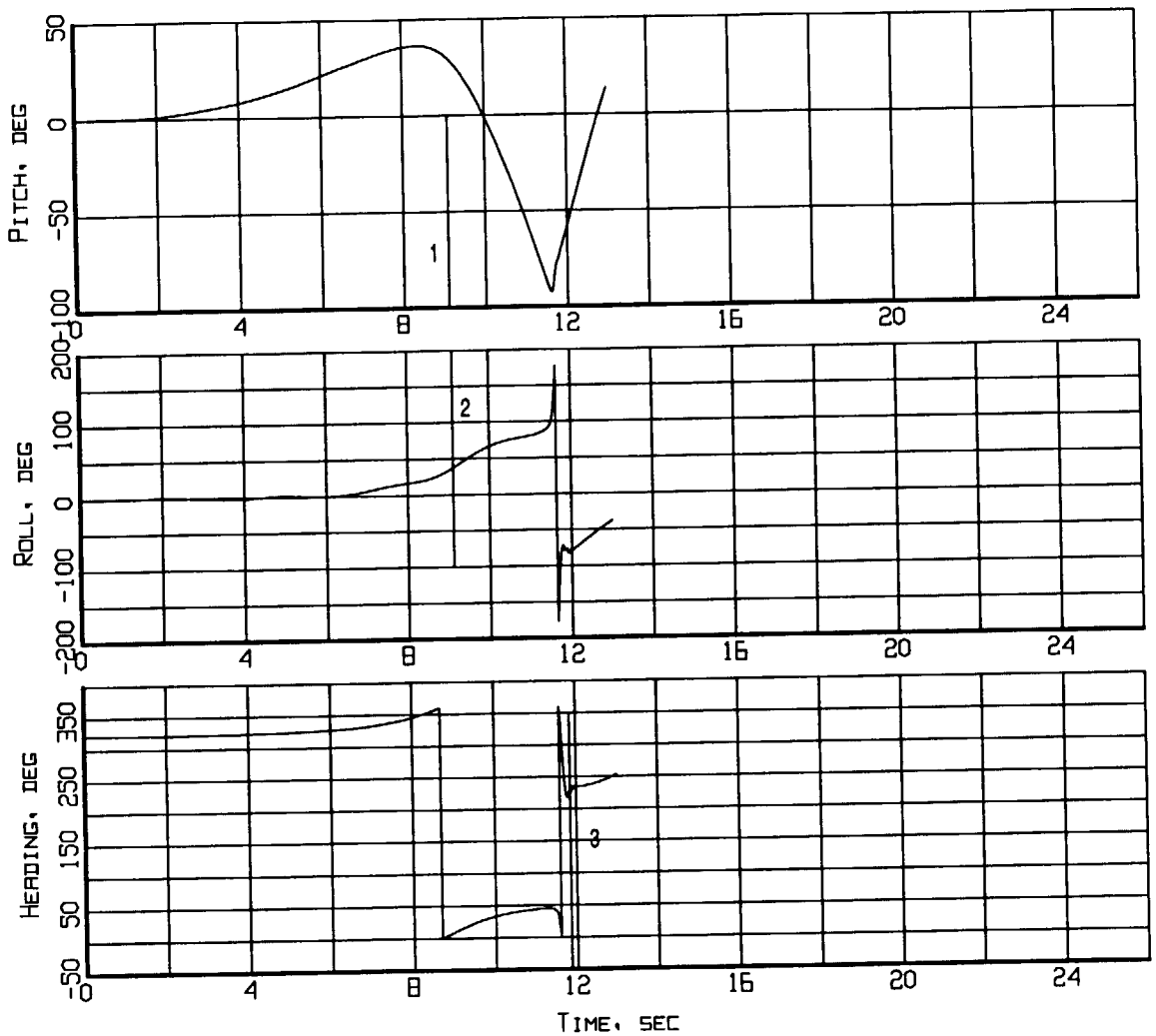

Event Marker

1 - Max DPRSF
2 - Max DPRSH
3 - Max DP/PC

Figure B10-8. Event markers superposed on the aircraft attitude time histories (Flight 240, Test Point 43b).

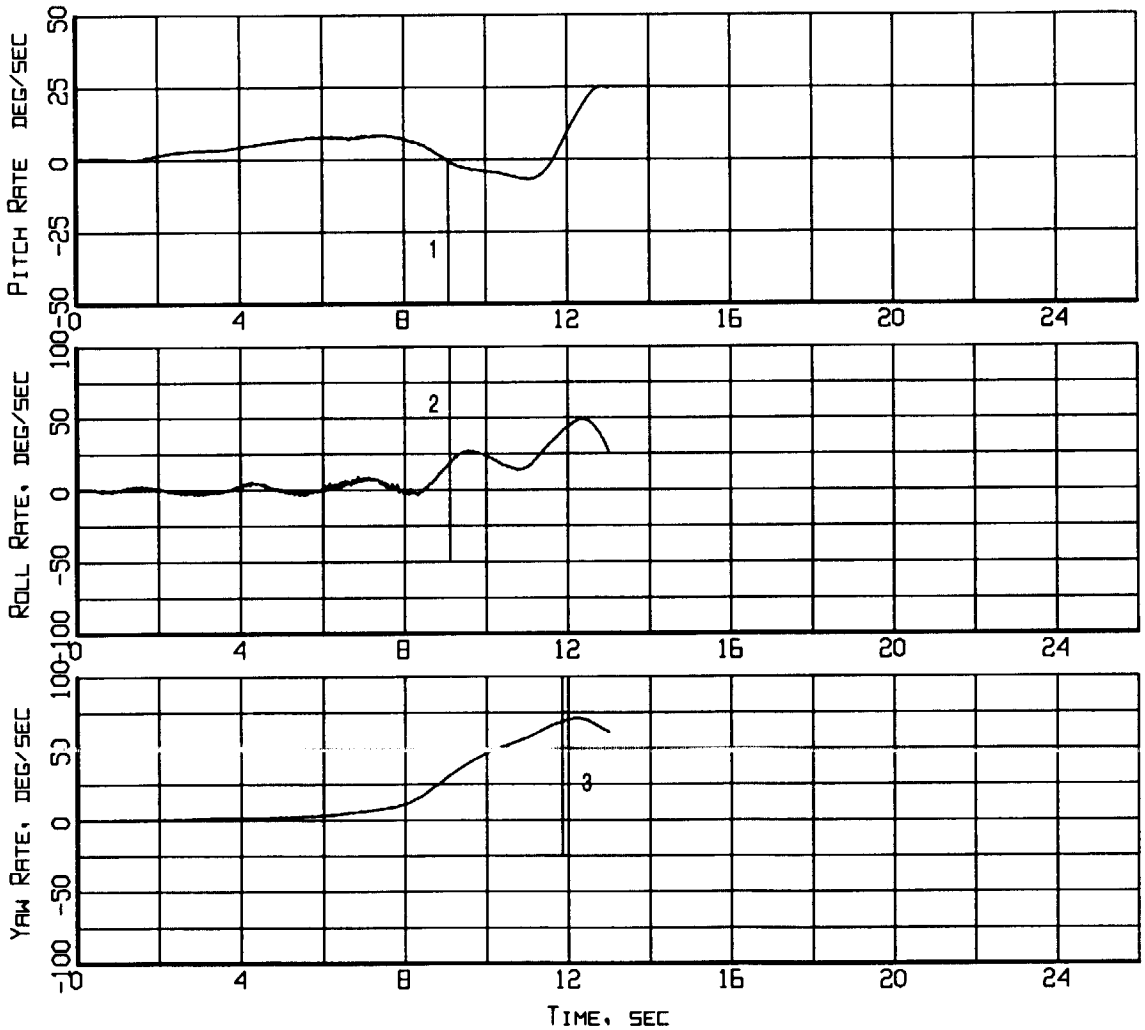

Figure B10-9. Event markers superposed on the aircraft motion time histories (Flight 240, Test Point 43b).

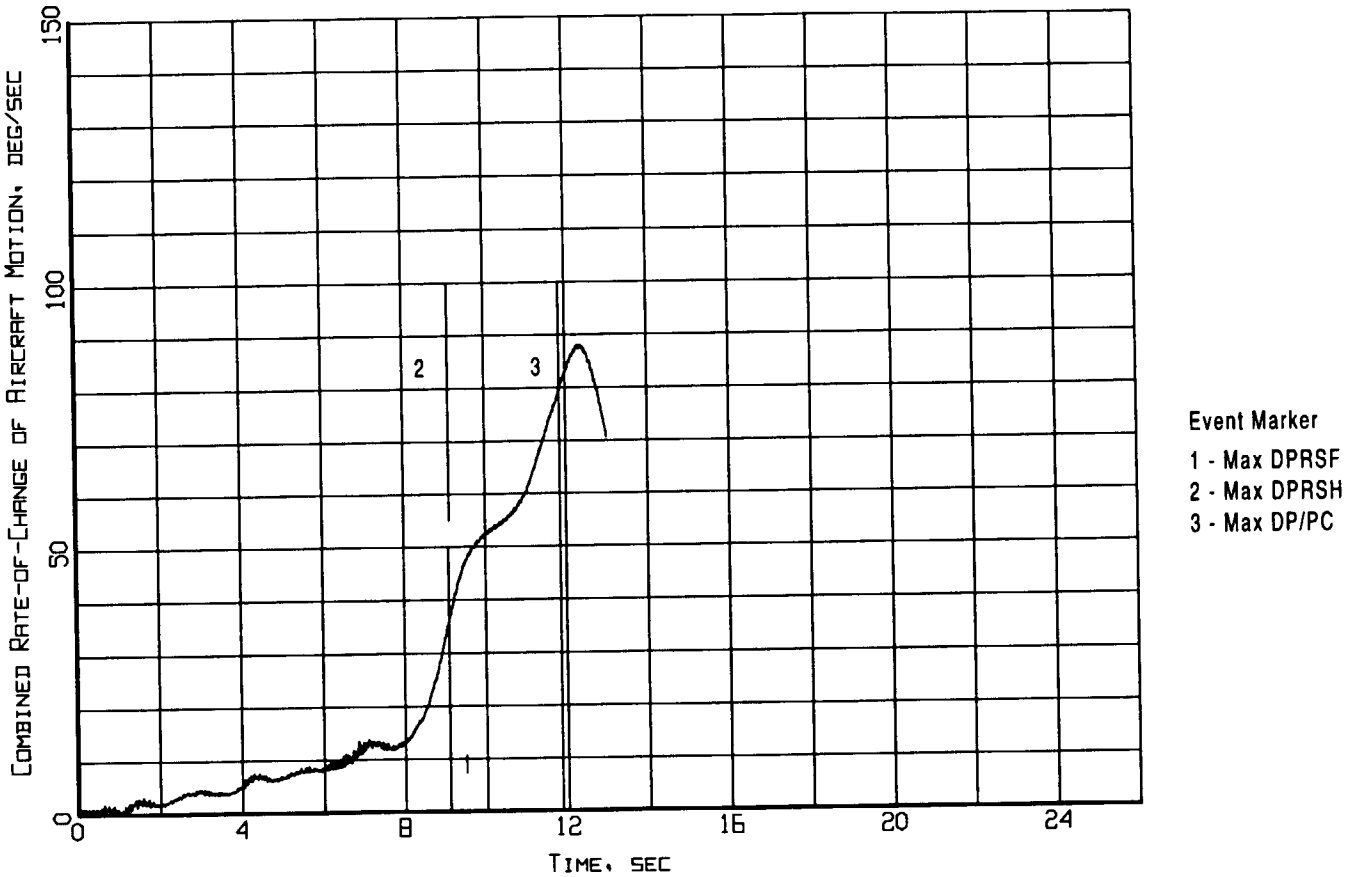

Figure B10-10. Event markers superposed on the combined of rate-of-change of aircraft motion time history (Flight 240, Test Point 43b).

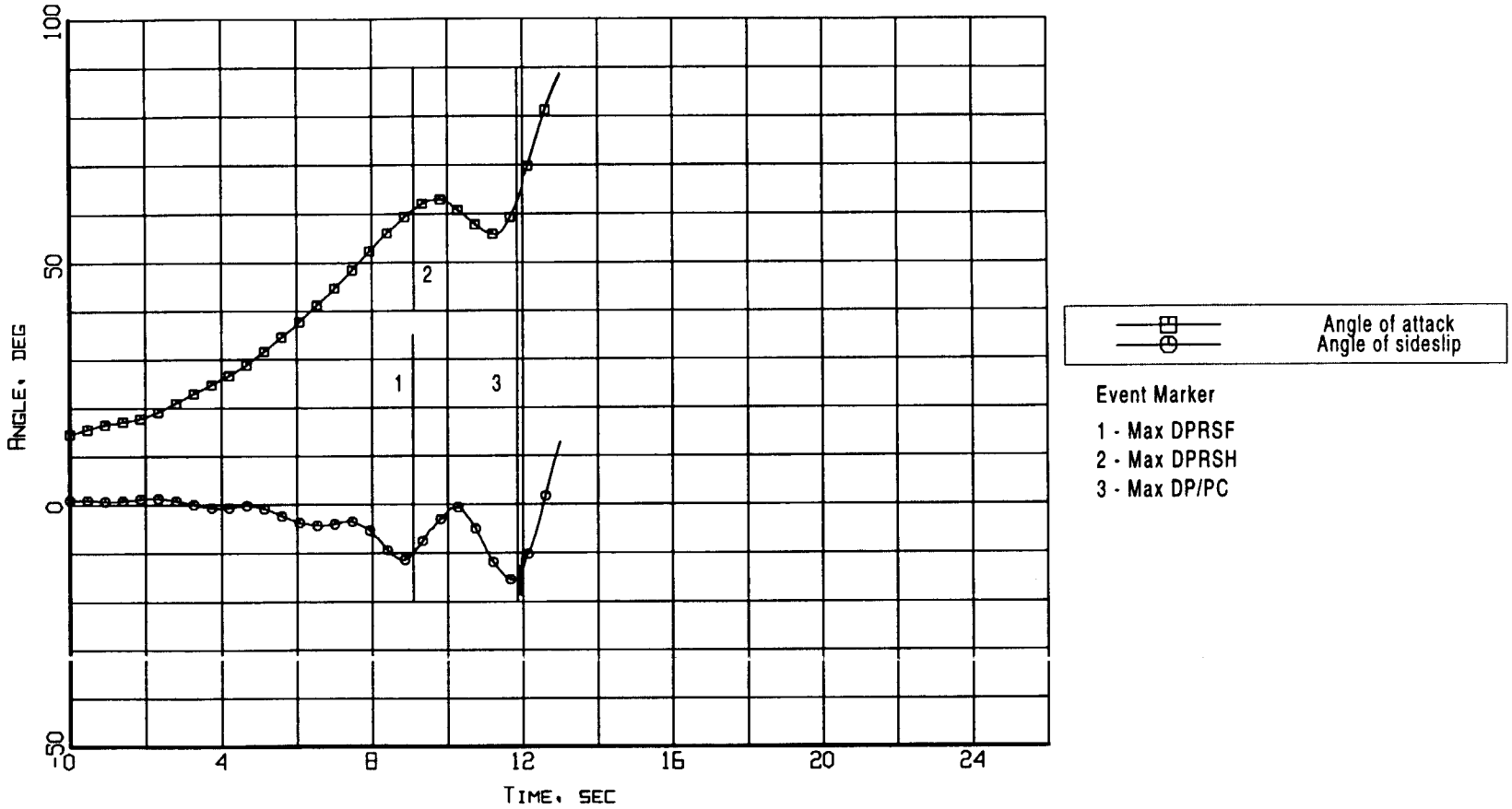

Figure B10-11. Event markers superposed on the aerodynamic flowstream descriptor time histories (Flight 240, Test Point 43b).

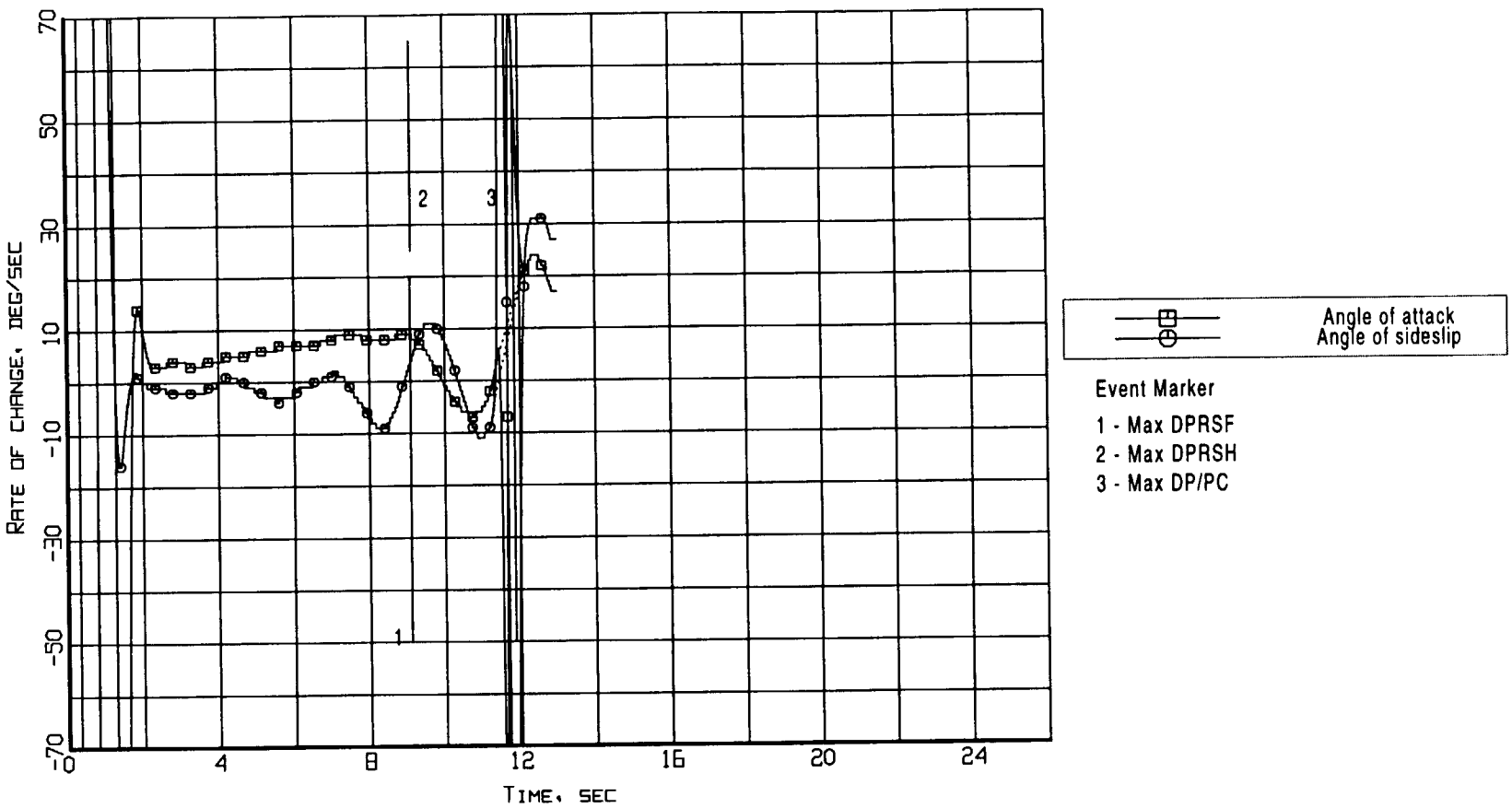

Figure B10-12. Event markers superposed on the aerodynamic flowstream descriptors rate-of-change time histories (Flight 240, Test Point 43b).

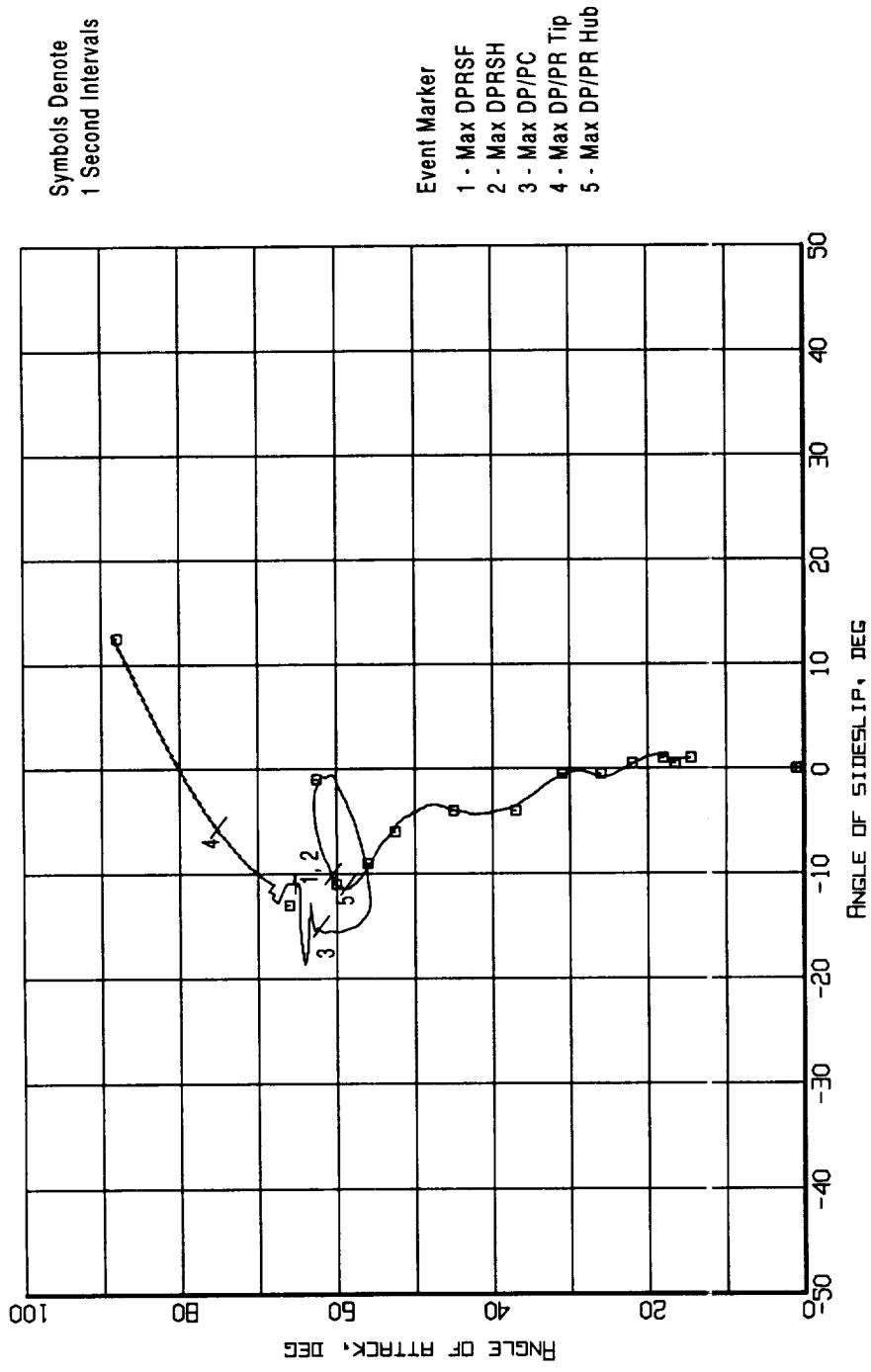

Figure B10-13. Event markers superposed on the aerodynamic flowstream descriptors trajectory (Flight 240, Test Point 43b).

Appendix B11 - Flight 238, Test Point 44b

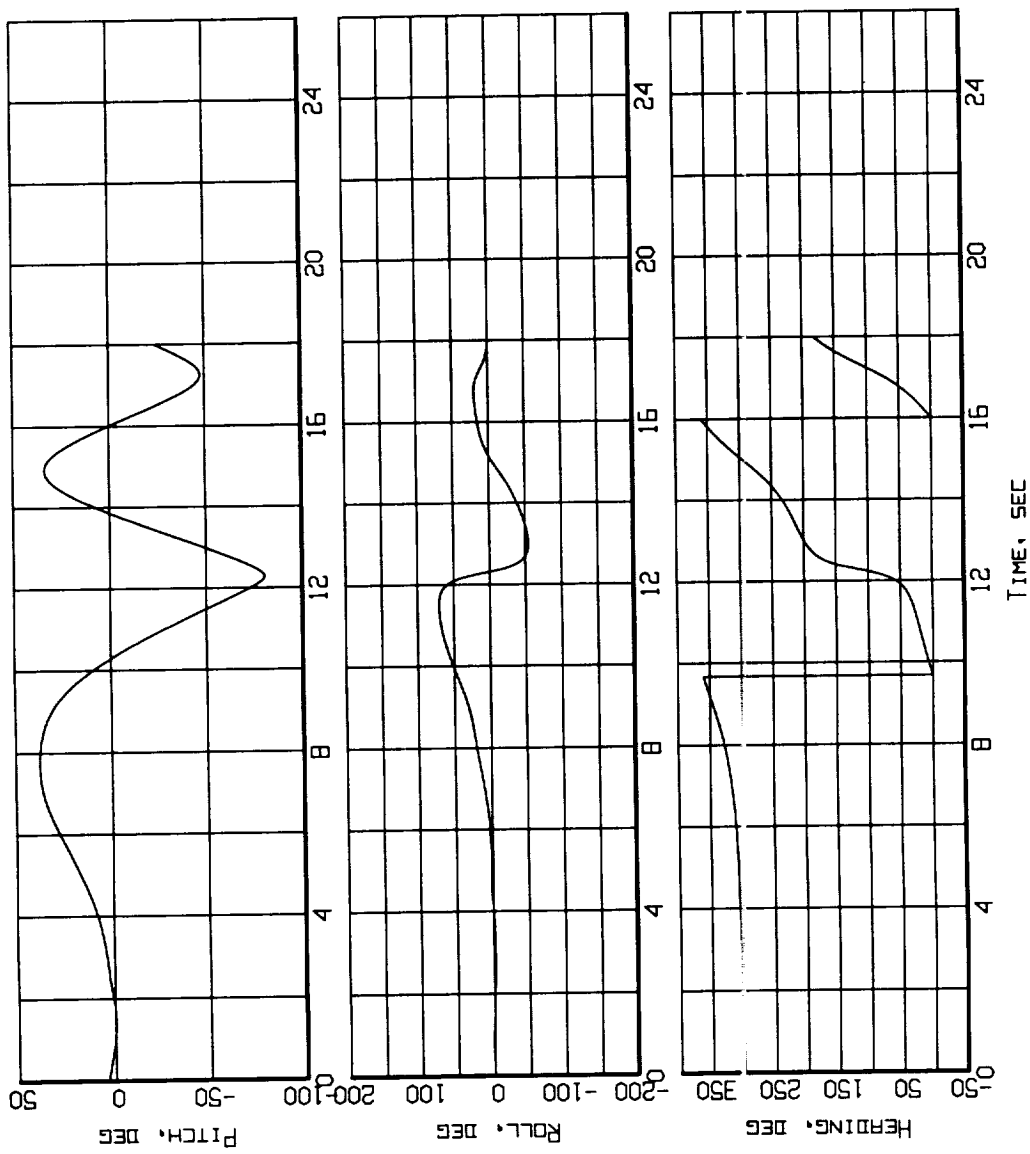

Figure B11-1. Aircraft attitude - Pitch, Roll, and Heading (Flight 238, Test Point 44b).

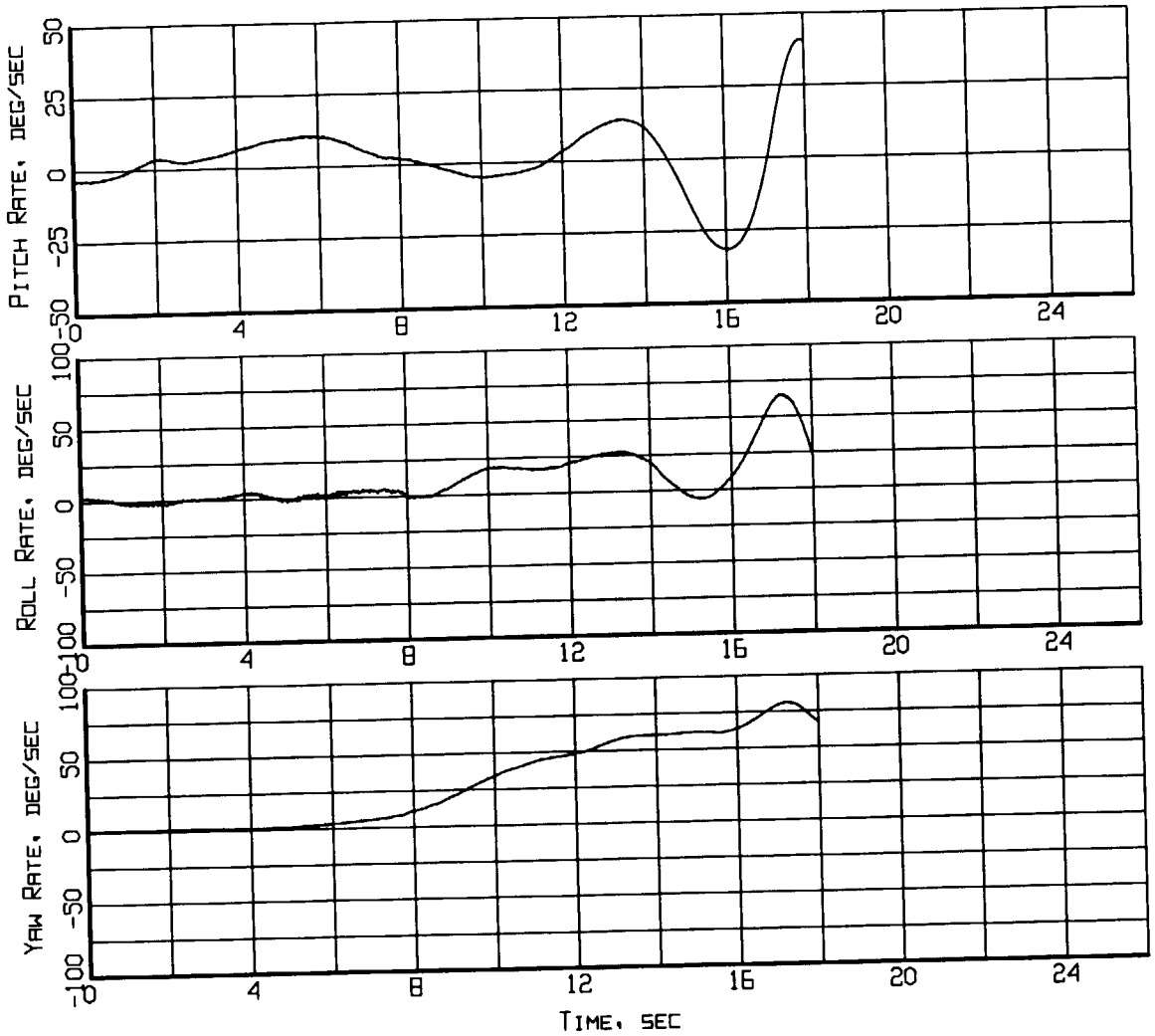

Figure B11-2. Aircraft Motion - Rate-of-Change of Pitch, Roll and Heading (Flight 238, Test Point 44b).

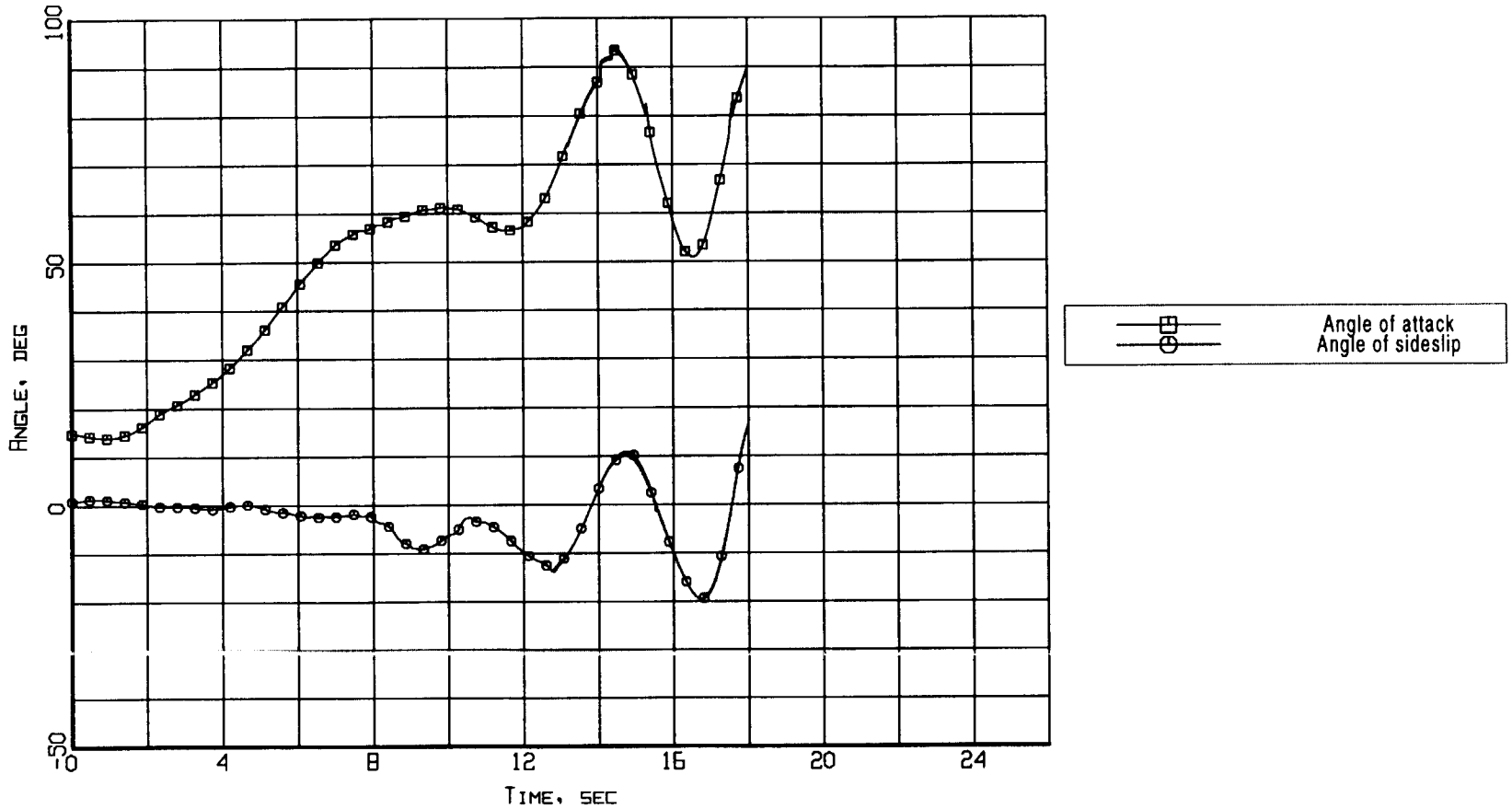

Figure B11-3. Aerodynamic flowstream descriptors - angle of attack and angle of sideslip (Flight 238, Test Point 44b).

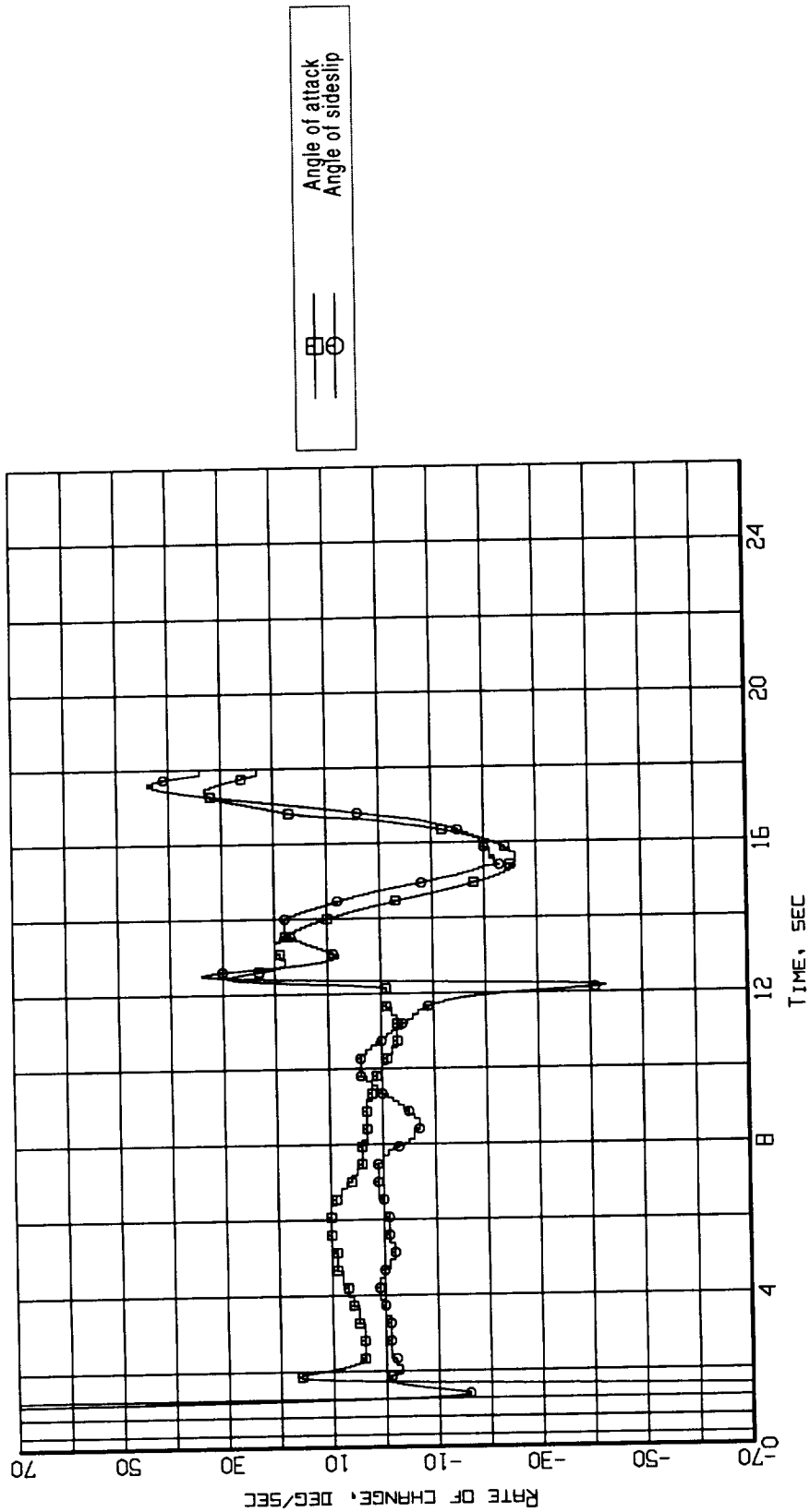

Figure B11-4. Aerodynamic flowstream descriptors - rate of change of angle of attack and angle of sideslip (Flight 238, Test Point 44b).

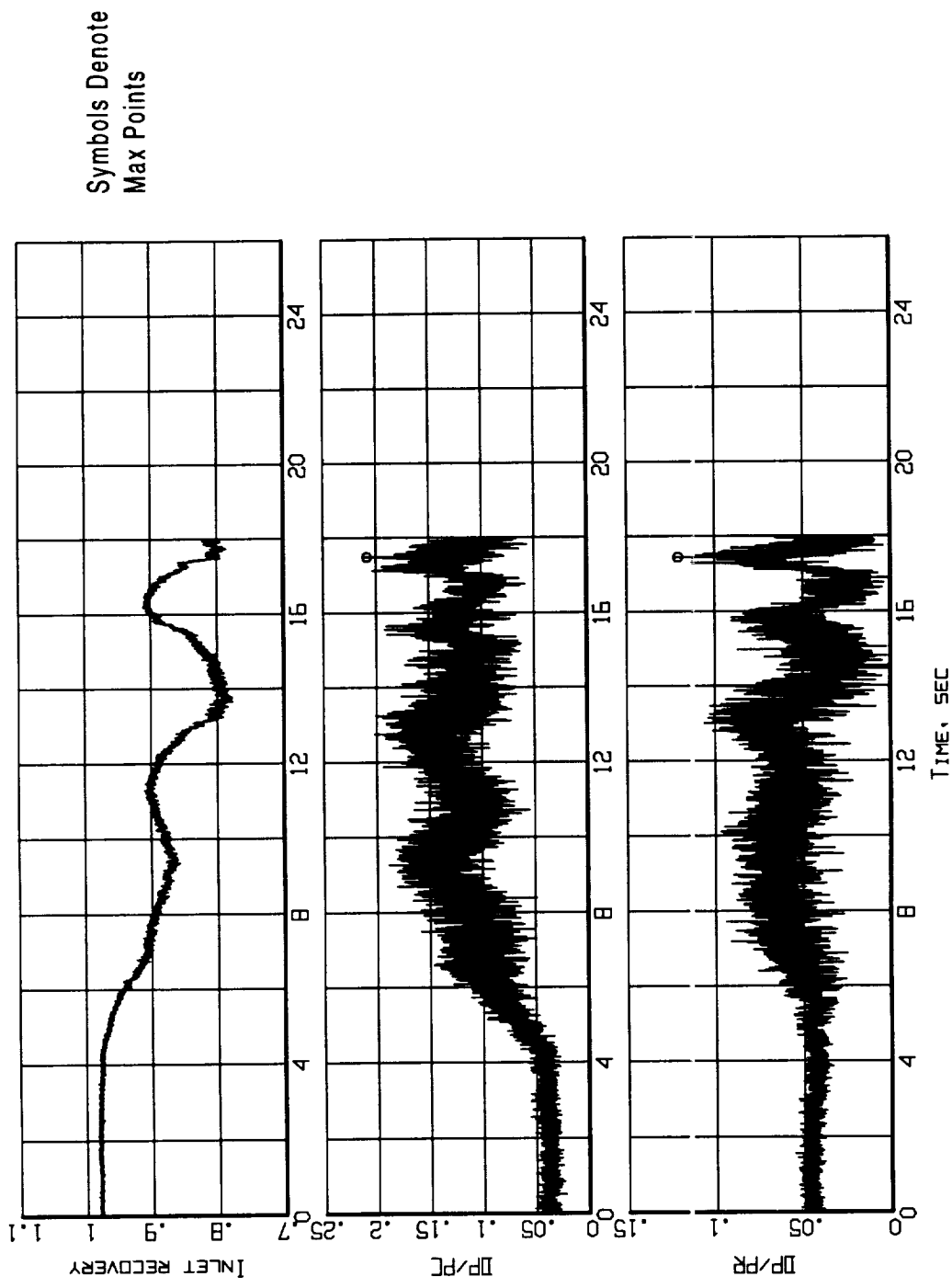

Figure B11-5. Time histories of inlet recovery and distortion descriptors (Flight 238, Test Point 44b).

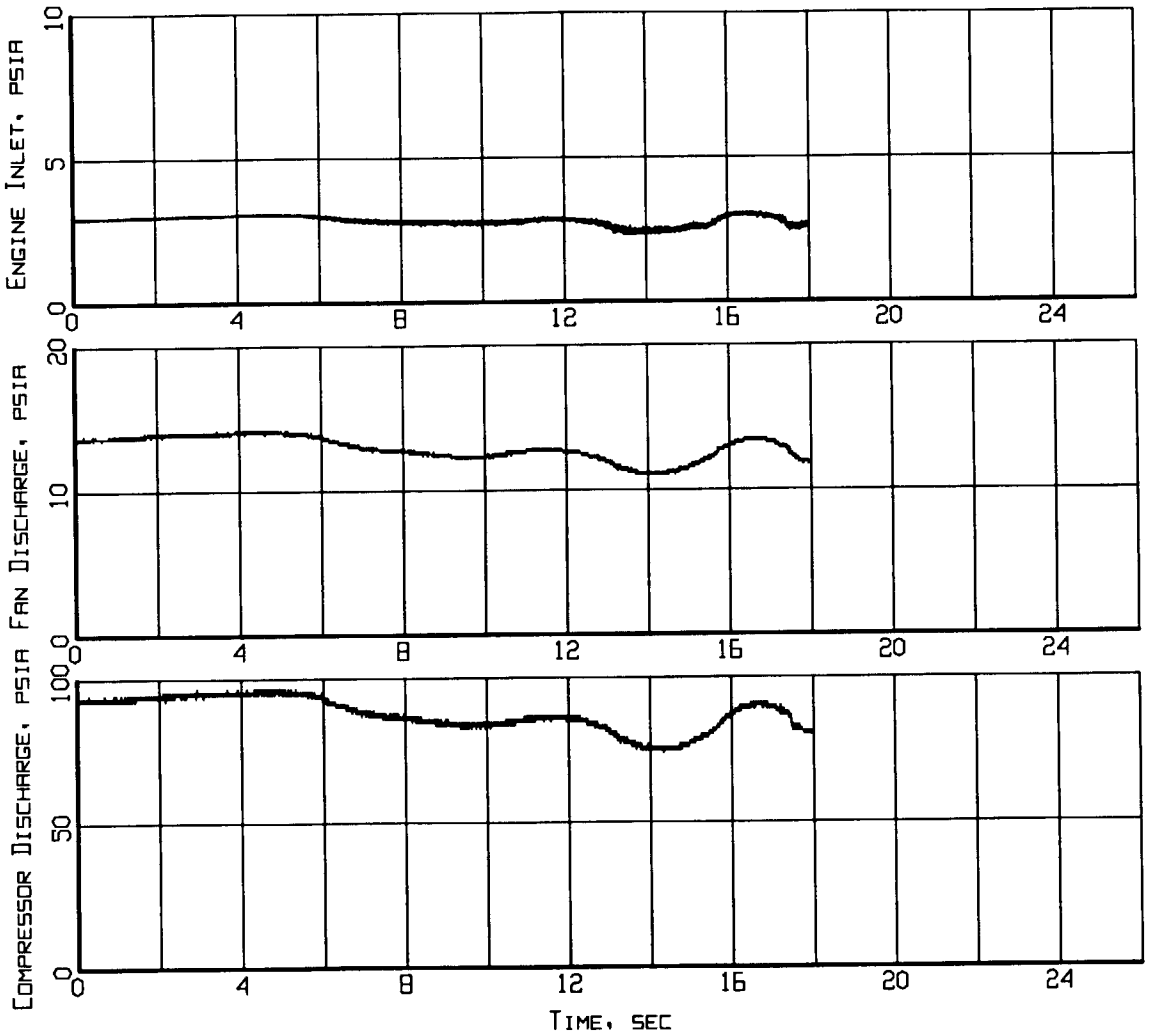

Figure B11-6. Measured inlet/engine entry and engine internal pressures time histories (Flight 238, Test Point 44b).

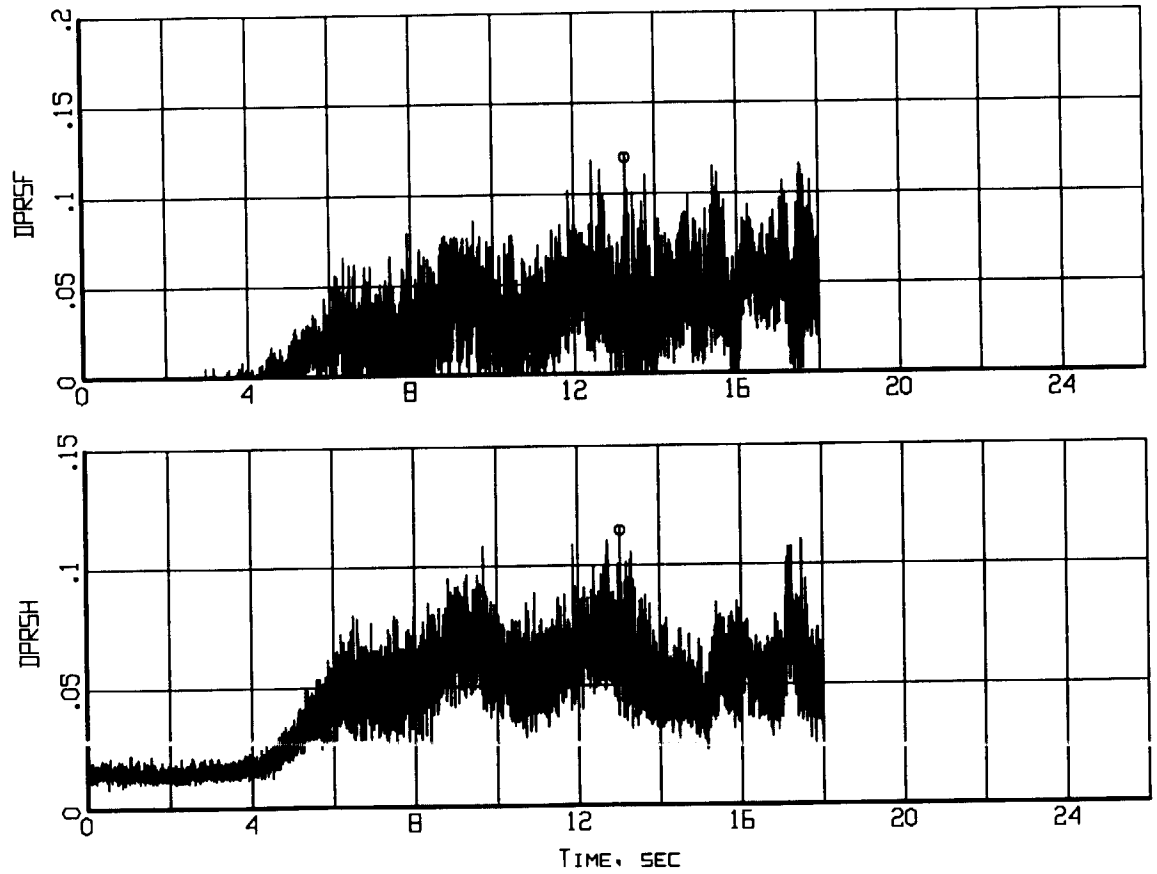

Symbols Denote
Max Points

Figure B11-7. Time histories of the predicted loss of stability pressure ratio for the fan and the compressor (Flight 238, Test Point 44b).

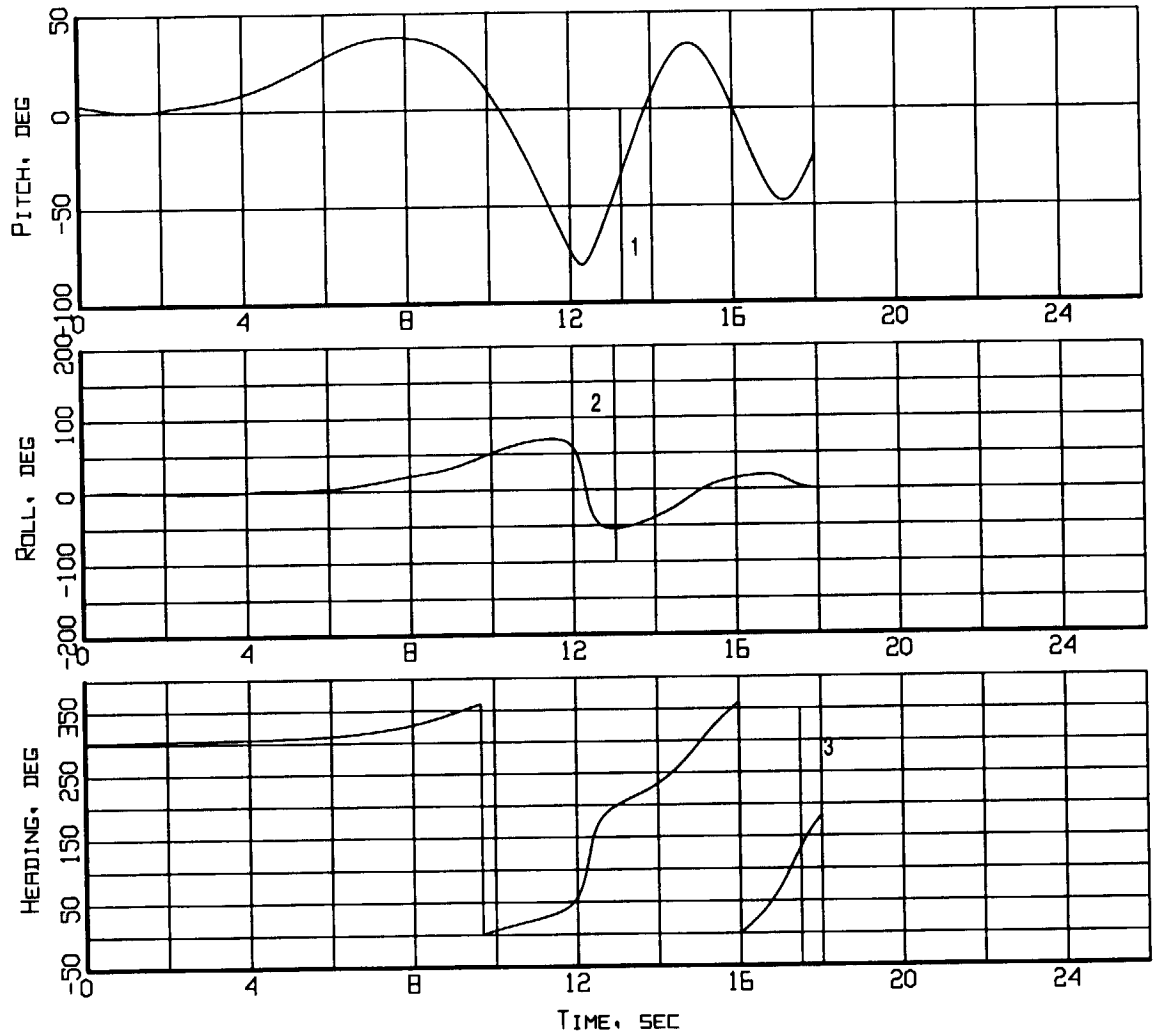

Event Marker

1 - Max DPRSF

2 - Max DPRSH

3 - Max DP/PC

Figure B11-8. Event markers superposed on the aircraft attitude time histories (Flight 238, Test Point 44b).

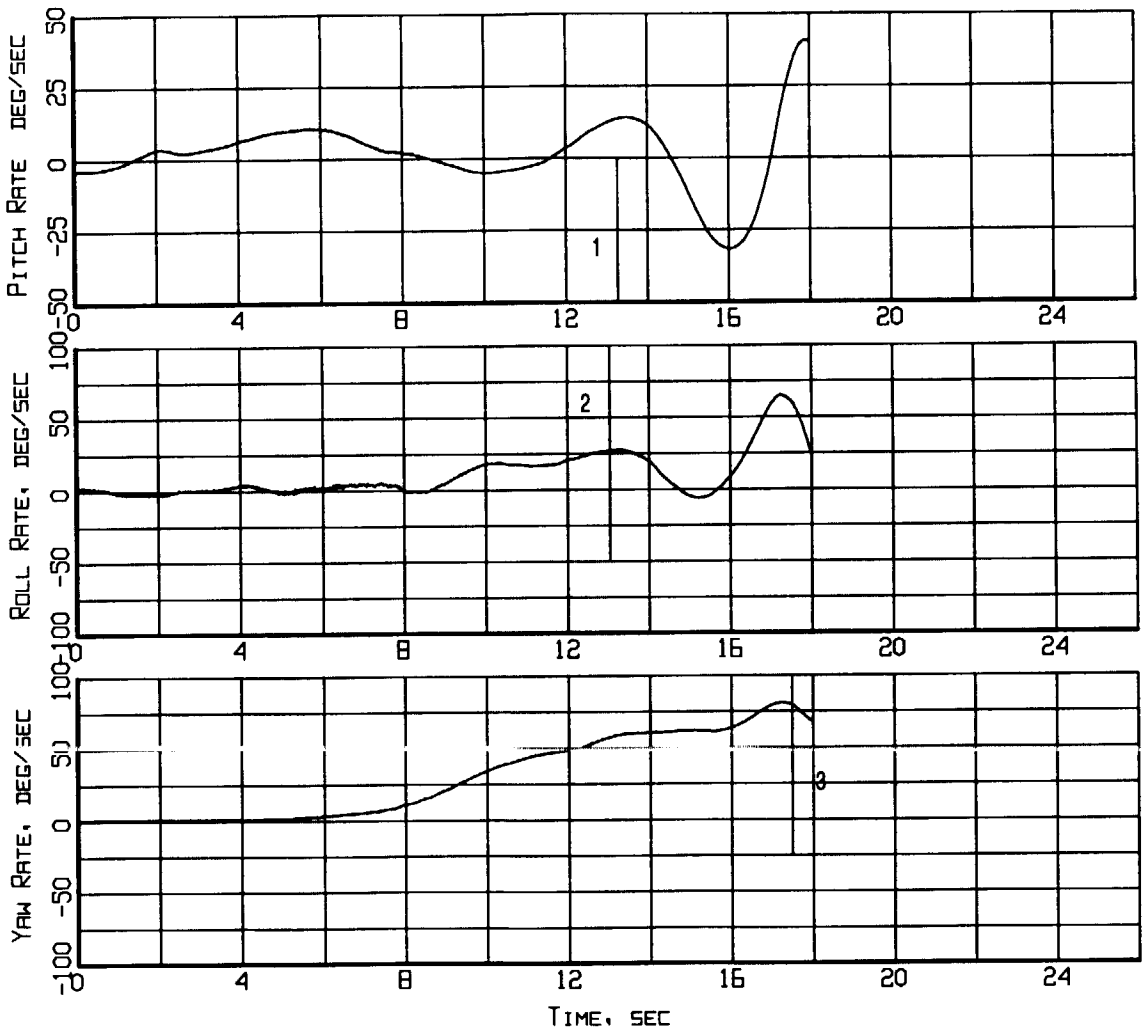

Figure B11-9. Event markers superposed on the aircraft motion time histories (Flight 238, Test Point 44b).

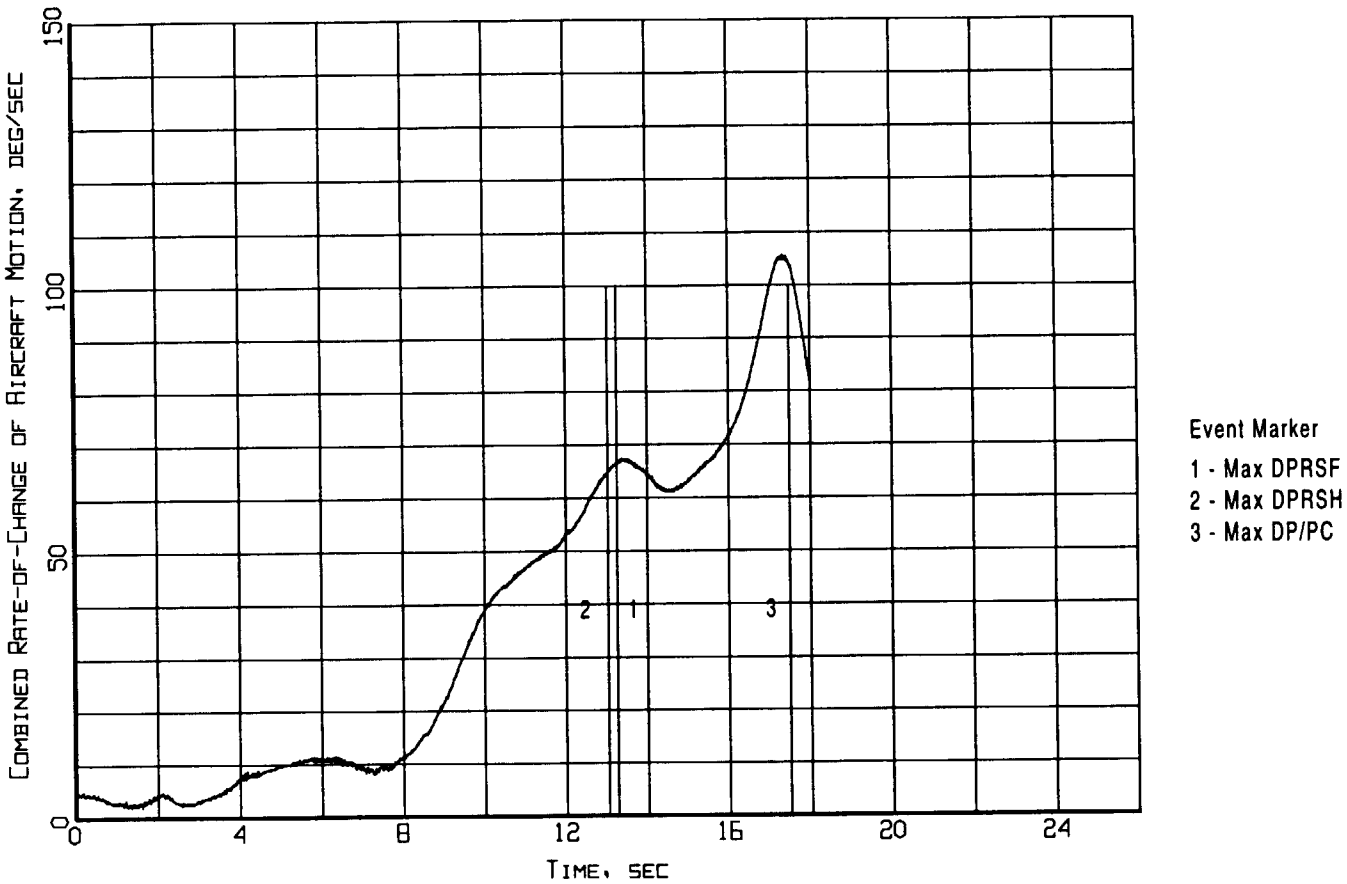

Figure B11-10. Event markers superposed on the combined of rate-of-change of aircraft motion time history (Flight 238, Test Point 44b).

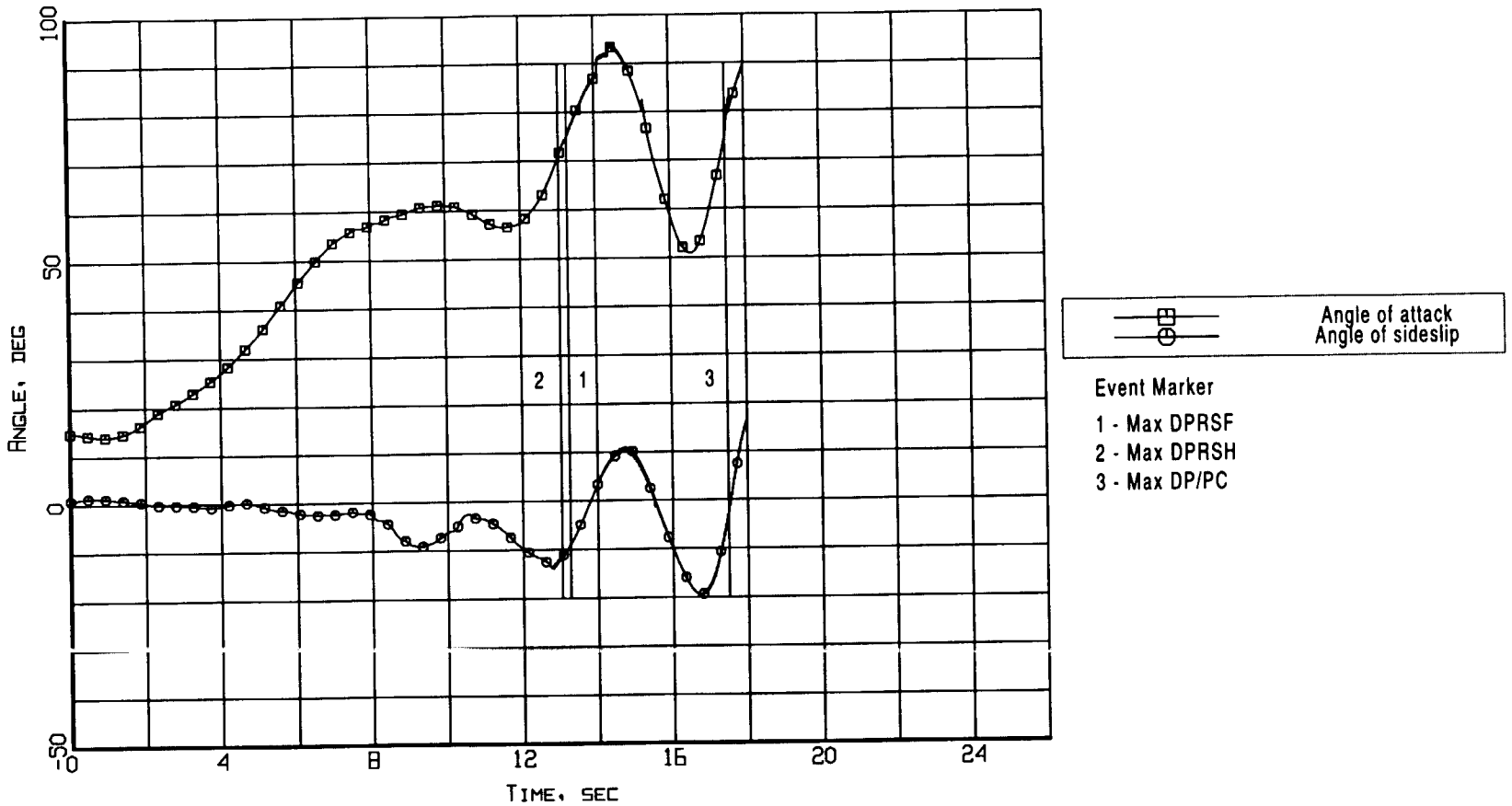

Figure B11-11. Event markers superposed on the aerodynamic flowstream descriptor time histories (Flight 238, Test Point 44b).

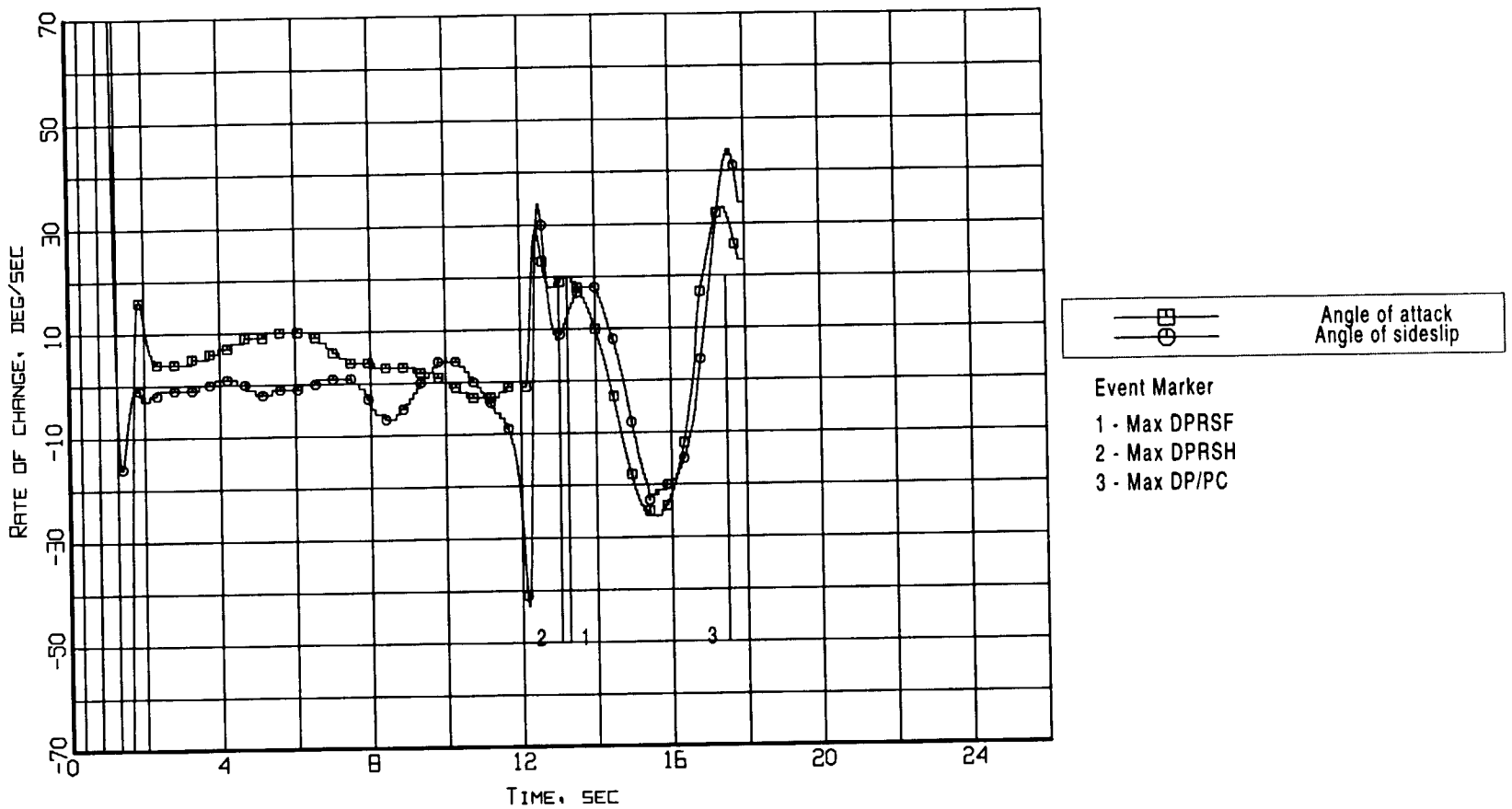

Figure B11-12. Event markers superposed on the aerodynamic flowstream descriptors rate-of-change time histories (Flight 238, Test Point 44b).

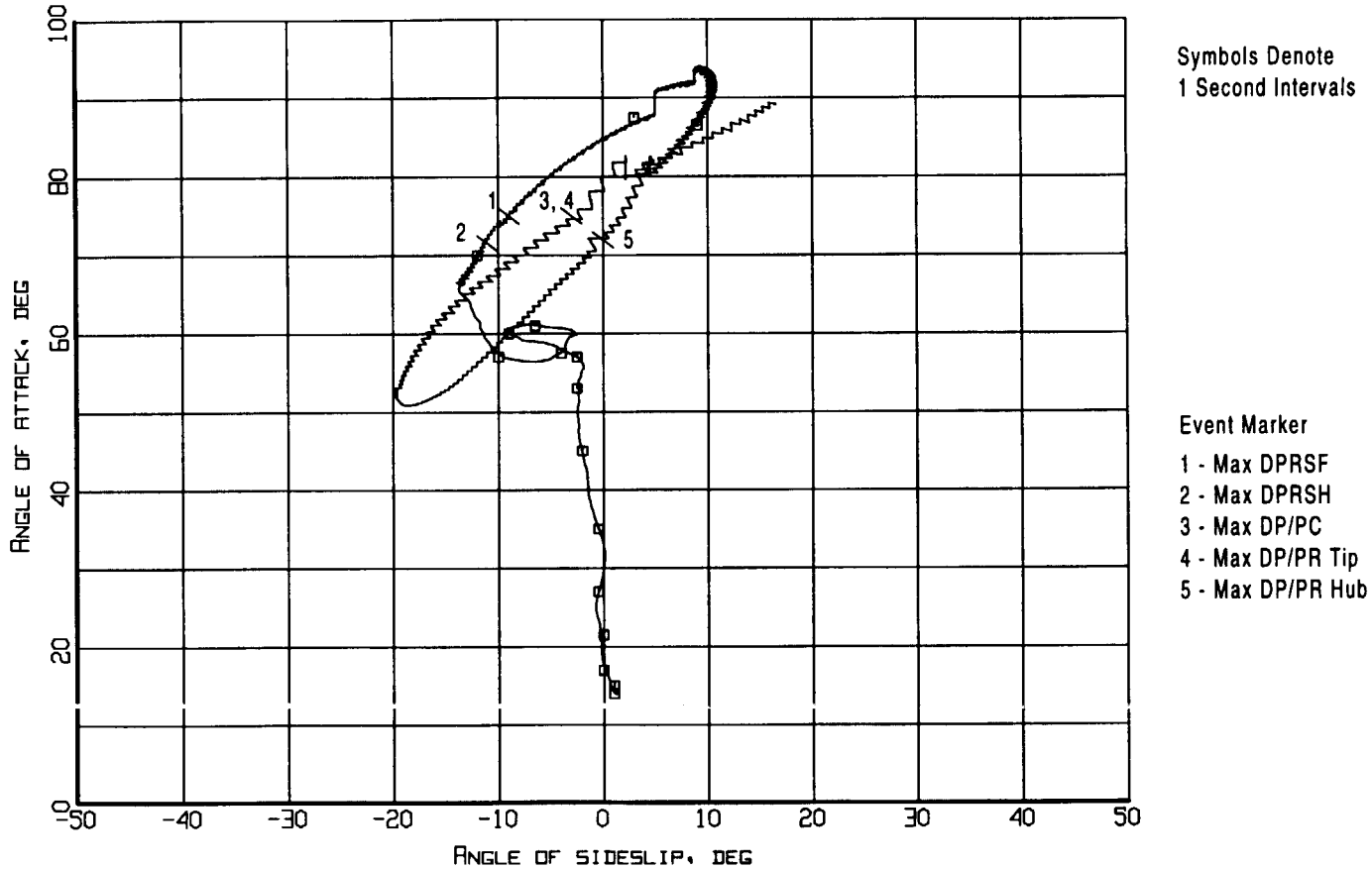

Figure B11-13. Event markers superposed on the aerodynamic flowstream descriptors trajectory (Flight 238, Test Point 44b).

Appendix B12 - Flight 240, Test Point 45b

The figures that could be contained in this appendix are already contained in Section 4 of this report.

REPORT DOCUMENTATION PAGE

Form Approved
OMB No. 0704-0188

Public reporting burden for this collection of information is estimated to average 1 hour per response, including th time for reviewing instructions, searching existing data sources, gathering and maintaining the data needed, and completing and reviewing the collection of information. Send comments rega ding this burden estimate or any other aspect of this collection of information, including suggestions for reducing this burden, to Washington Headquarters Services, Directorate for Information Operations and Reports, 1215 Jefferson Davis Highway, Suite 1204, Arlington, VA 22202-4302, and to the Office of Management and Budget, Paperwork Reduction Project (0704-0188), Wash ngton, DC 20503.

1. AGENCY USE ONLY (Leave blank)	2. REPORT DATE	3. REPORT TYPE AND DATES COVERED
	February 1999	Technical Memorandum

4. TITLE AND SUBTITLE

Factors Affecting Inlet-Engine Compatibility During Aircraft Departures at High Angle of Attack for an F/A-18A Aircraft

5. FUNDING NUMBERS

WU 529-31-04-00-37-00-F18

6. AUTHOR(S)

W. G. Steenken, J. G. Williams, A. J. Yuhas, and K. R. Walsh

7. PERFORMING ORGANIZATION NAME(S) AND ADDRESS(ES)

NASA Dryden Flight Research Center
P.O. Box 273
Edwards, California 93523-0273

8. PERFORMING ORGANIZATION REPORT NUMBER

H-2327

9. SPONSORING/MONITORING AGENCY NAME(S) AND ADDRESS(ES)

National Aeronautics and Space Administration
Washington, DC 20546-0001

10. SPONSORING/MONITORING AGENCY REPORT NUMBER

NASA/TM-1999-206572

11. SUPPLEMENTARY NOTES

W. G. Steenken and J. G. Williams, GE Aircraft Engines, Cincinnati, Ohio; A. J. Yuhas, Analytical Services and Materials, Inc., Edwards, California; and K. R. Walsh, Dryden Flight Research Center, Edwards, California. NASA Contract NAS3-26617.

12a. DISTRIBUTION/AVAILABILITY STATEMENT

Unclassified—Unlimited
Subject Category 07

12b. DISTRIBUTION CODE

13. ABSTRACT (Maximum 200 words)

The F404-GE-400 engine powered F/A-18A High Alpha Research Vehicle (HARV) was used to examine the quality of inlet airflow during departed flight maneuvers, that is, during flight outside the normal maneuvering envelope where control surfaces have little or no effectiveness. A series of six nose-left and six nose-right departures were initiated at Mach numbers between 0.3 and 0.4 at an altitude of 35 kft. The yaw rates at departure recovery were in the range of 40 to 90 degrees per second. Engine surges were encountered during three of the nose-left and one of the nose-right departures. Time-variant inlet-total-pressure distortion levels at the engine face were determined to not significantly exceed those measured at maximum angle-of-attack and -sideslip maneuvers during controlled flight. Surges as a result of inlet distortion levels were anticipated to initiate in the fan. Analysis revealed that the surges initiated in the compressor and were the result of a combination of high levels of inlet distortion and rapid changes in aircraft motion. These rapid changes in aircraft motion are indicative of a combination of engine mount and gyroscopic loads being applied to the engine structure that impact the aerodynamic stability of the compressor through changes in the rotor-to-case clearances.

14. SUBJECT TERMS

Aircraft departures, F-18 aircraft, F/A-18A, High angle of attack, Inlet distortion, Inlet-engine compatibility

15. NUMBER OF PAGES

197

16. PRICE CODE

A09

17. SECURITY CLASSIFICATION OF REPORT	18. SECURITY CLASSIFICATION OF THIS PAGE	19. SECURITY CLASSIFICATION OF ABSTRACT	20. LIMITATION OF ABSTRACT
Unclassified	Unclassified	Unclassified	Unlimited